Diamond Quantum Network Nodes with Open Microcavities

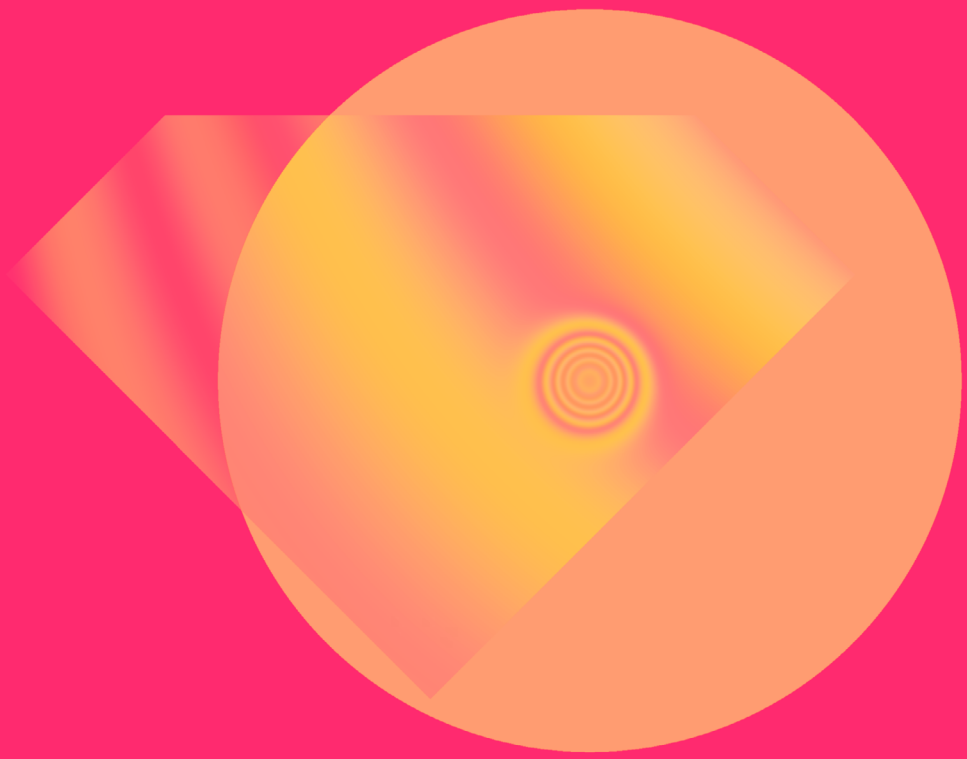

Julius Fischer

Diamond Quantum Network Nodes with Open Microcavities

Diamond Quantum Network Nodes with Open Microcavities

Dissertation

for the purpose of obtaining the degree of doctor
at Delft University of Technology,
by the authority of the Rector Magnificus, Prof. dr. ir. H. Bijl,
chair of the Board for Doctorates,
to be defended publicly on
Monday, 9th February 2026 at 12:30

by

Julius FISCHER

Master of Science in Physics,
Universität Stuttgart, Germany,
born in Gießen, Germany.

This dissertation has been approved by the promotor.

Composition of the doctoral committee:

Rector Magnificus	chairperson
Prof. dr. ir. R. Hanson	Technische Universiteit Delft, promotor
Dr. ir. T. H. Taminiau	Technische Universiteit Delft, copromotor
Independent members:	
Prof. dr. A. Kubanek	Universität Ulm, Germany
Prof. dr. S. Barz	Universität Stuttgart, Germany
Prof. dr. A. F. Otte	Technische Universiteit Delft
Dr. M. Rossi	Technische Universiteit Delft
Prof. dr. ir. L. M. K. Vandersypen	Technische Universiteit Delft, reserve member

ISBN 978-94-6518-198-1

Cover design by Julius Fischer. The illustrations are produced using numerical simulations. The visual patterns on the front and back cover arise from the reflection and transmission response of a mirror-bonded diamond membrane, which is confined by a laser-ablated circular optical fiber mirror.

An electronic version of this dissertation is available at
`https://repository.tudelft.nl/`.

Contents

Summary

The technology of building quantum networks by interconnecting multiple quantum nodes has the potential to revolutionize the world, much like its classical equivalent - the internet - did. The possibility of processing quantum information on a shared network promises exciting applications that are not possible with today's technologies. Quantum systems with stationary qubits and qubit-photon interfaces, like diamond color centers, are prime candidates for these quantum network nodes. Here, the qubit-photon interface efficiency is crucial for their connectivity, which propels the development of cavity systems that enhance this interface via the Purcell effect. This dissertation presents advances in coupling nitrogen-vacancy (NV) and tin-vacancy (SnV) centers in diamond to open microcavities and explores their capabilities for quantum networks.

The basis for experiments with cavity-coupled color centers is laid by the construction of a cryogenic fiber-based open microcavity system. This system uses a flat sample mirror opposite to a laser-ablated spherical fiber mirror to confine optical cavity modes. It is designed to achieve a low passive cavity length fluctuation level, microwave integration as well as full optical access through the fiber-mirror and free-space via the sample mirror. A closed-cycle optical cryostat hosts this system and enables continuous operation in a controlled high-vacuum environment.

Besides the microcavity developments, a novel patterning method for the fabrication of micrometer-thin diamond membranes is presented. The method involves laser-cutting to pattern diamonds with micrometer-scale feature sizes and subsequent bonding to a sample mirror. Comparing the laser-cutting method to established electron-beam lithography and a two-step transfer pattern process with a silicon nitride hard mask validates the fabrication of high-quality diamond devices for microcavity applications.

By integrating a diamond device hosting SnV centers into the cryogenic microcavity system, single cavity-coupled SnV centers are investigated. The coherent coupling regime is reached as a result of the achieved Purcell enhancement and the coherence of the optical transition. The coupled system of SnV center and cavity exhibits quantum nonlinear behavior, as evidenced by dips in the cavity transmission spectrum and changes in the photon statistics of the transmitted light. These effects can be exploited in remote entanglement protocols, underlining the potential of these systems to serve as quantum network nodes with Purcell-enhanced photonic interfaces.

Moreover, the cryogenic microcavity system is employed to equip NV centers with efficient qubit-photon interfaces. The cavity-coupling is used in combination with a cross-polarized resonant excitation and detection scheme to initialize and read out the NV center electron spin qubit. In addition, the electron spin is coherently controlled with on-chip delivered microwave pulses, and pulsed resonant excitation enables the generation of spin-photon correlated states. The quantum networking capabilities of the system are demonstrated by measuring heralded Z-basis correlations between photonic time-bin qubits and the spin qubit. In these experiments, a tenfold improvement in resonant photon

detection probability is achieved over state-of-the-art NV center quantum network nodes, paving the way for cavity-enhanced quantum networking with NV centers.

Samenvatting

De technologie voor het bouwen van kwantumnetwerken door meerdere kwantumknooppunten met elkaar te verbinden, heeft het potentieel om een nieuwe revolutie tot stand te brengen, net zoals zijn klassieke equivalent – het internet – dat heeft gedaan. De mogelijkheid om kwantuminformatie te verwerken op een gedeeld netwerk biedt interessante toepassingen die met de huidige technologieën onmogelijk zijn. Kwantumsystemen met stationaire qubits en qubit-fotoninterfaces, zoals diamantkleurcentra, zijn uitstekende kandidaten voor deze kwantumnetwerkknooppunten. Hier is de efficiëntie van de qubit-fotoninterface cruciaal voor hun connectiviteit, wat de ontwikkeling stimuleert van caviteitssystemen die deze interface verbeteren via het Purcell-effect. Dit proefschrift presenteert vorderingen op het gebied van het koppelen van stikstof-holte (NV) en tin-holte (SnV) centra in diamant aan open microcaviteiten en onderzoekt hun mogelijkheden voor kwantumnetwerken.

De basis voor experimenten met caviteit-gekoppelde kleurcentra wordt gelegd door de constructie van een cryogeen glasvezel-gebaseerd open microcaviteitsysteem. Dit systeem maakt gebruik van een vlakke sample spiegel tegenover een laser-geërodeerde sferische glasvezel spiegel om optische caviteitmodi te lokaliseren. Het is ontworpen voor een laag passief caviteitlengtefluctuatie niveau, microgolfintegratie en volledige optische toegang via de glasvezel spiegel en via de lucht door de sample spiegel. Een optische gesloten cyclus cryostaat omvat dit systeem en maakt continue werking mogelijk in een gecontroleerde hoogvacuümomgeving.

Naast de ontwikkelingen op het gebied van microcaviteiten wordt een nieuwe fabricagemethode voor het structureren van micrometer-dunne diamantmembranen gepresenteerd. De methode omvat lasersnijden om diamanten te structuren met micrometer-schaal kenmerken en vervolgens te hechten aan een sample spiegel. Een vergelijking van de lasersnijmethode met de bestaande methode gebaseerd op elektronenstraallithografie en een tweestaps-transferpatroonproces met een siliciumnitride masker bevestigt de fabricage van hoogwaardige diamant samples voor microcaviteitstoepassingen.

Door een diamanten sample met SnV-centra te integreren in het cryogene microcaviteitssysteem, worden enkelvoudige caviteit-gekoppelde SnV-centra onderzocht. Het coherente koppelingsregime wordt bereikt als gevolg van de bereikte Purcell-versterking en de coherentie van de optische transitie. Het gekoppelde systeem van SnV-centrum en caviteit vertoont kwantum-niet-lineair gedrag, wat blijkt uit dalen in het transmissiespectrum van de caviteit en veranderingen in de fotonstatistieken van het doorgelaten licht. Deze effecten kunnen worden benut in protocollen voor niet lokale verstrengeling, wat het potentieel van deze systemen benadrukt om te dienen als kwantumnetwerkknooppunten met Purcell-versterkte fotonische interfaces.

Bovendien wordt het cryogene microcaviteitssysteem gebruikt om NV-centra uit te rusten met efficiënte qubit-fotoninterfaces. De caviteitskoppeling wordt gebruikt in combinatie met een kruisgepolariseerd resonant excitatie- en detectiemethode om de elektronenspin-qubit van NV-centra te initialiseren en uit te lezen. Bovendien wordt de elektronenspin

coherent aangedreven met on-chip geleverde microgolfpulsen en maakt gepulseerde resonante excitatie het mogelijk om spin-fotongecorreleerde toestanden te genereren. De kwantumnetwerkcapaciteiten van het systeem worden aangetoond door het meten van aangekondigde Z-basiscorrelaties tussen fotonische time-bin qubits en de spin-qubit. In deze experimenten wordt een tienvoudige verbetering in de resonante foton detectiekans bereikt ten opzichte van de meest geavanceerde NV-centrum kwantumnetwerkknooppunten, wat de weg vrijmaakt voor caviteitsversterkte kwantumnetwerken met NV-centra.

Kurzfassung

Die Technologie zum Aufbau von Quantennetzwerken, durch das Zusammenschalten mehrerer Quantenknotenpunkte, hat das Potenzial die Welt zu revolutioniere. Ähnlich hat dies bereits ihre klassische Entsprechung – das Internet – getan. Die Möglichkeit Quanteninformationen in einem gemeinsamen Netzwerk zu verarbeiten verspricht aussichtsreiche Anwendungen, die mit heutigen Technologien nicht möglich sind. Quantensysteme mit stationären Qubits und Qubit-Photon-Schnittstellen, wie Diamant-Farbzentren, sind vielversprechende Kandidaten für diese Quantennetzwerkknoten. Die Effizienz der Qubit-Photon-Schnittstelle ist dabei entscheidend für ihre Konnektivität, was die Entwicklung von Hohlraumresonatoren vorantreibt, welche diese Schnittstelle mit Hilfe des Purcell-Effekt verbessern. Diese Dissertation präsentiert Fortschritte bei der Kopplung von Stickstoff-Fehlstellen (NV) und Zinn-Fehlstellen (SnV) Zentren in Diamanten an offene Mikroresonatoren und untersucht deren Eignung für Quantennetzwerke.

Die Grundlage für Experimente mit resonatorgekoppelten Farbzentren bildet die Konstruktion eines kryogenen, glasfaser-basierten, offenen Mikroresonatorsystems. Dieses System verwendet einen flachen Probenspiegel gegenüber einem laserabgetragenen sphärischen Glasfaserspiegel, um optische Resonatormoden zu begrenzen. Es ist so ausgelegt, dass es geringe passive Resonatorlängenschwankungen, Mikrowellenintegration sowie vollständigen optischen Zugang durch den Glasfaserspiegel und Freistrahl über den Probenspiegel erreicht. Dieses System ist in einem optischen Kryostat mit geschlossenem Kühlkreislauf eingebaut und ermöglicht einen kontinuierlichen Betrieb in einer kontrollierten Hochvakuumumgebung.

Neben den Entwicklungen im Bereich des Mikroresonators wird ein neuartiges Strukturierungsverfahren für die Herstellung von mikrometerdünnen Diamantmembranen vorgestellt. Das Verfahren umfasst das Laserschneiden zur Strukturierung von Diamanten im Mikrometerbereich und das anschließende Aufbringen auf einen Probenspiegel. Der Vergleich des Laserschneidverfahrens mit der etablierten Elektronenstrahllithografie und einem zweistufigen Transferstrukturverfahren mit einer Siliziumnitridmaske bestätigt die Herstellung hochwertiger Diamantproben für Mikroresonatoranwendungen.

Durch die Integration einer Diamantprobe mit SnV-Zentren in das kryogene Mikroresonatorsystems werden einzelne resonatorgekoppelte SnV-Zentren untersucht. Das kohärente Kopplungsregime wird als Ergebnis der erzielten Purcell-Verstärkung und der Kohärenz des optischen Übergangs erreicht. Das gekoppelte System aus SnV-Zentrum und Resonator zeigt quantenmechanisches nichtlineares Verhalten, das sich durch Senken im Transmissionsspektrum des Resonators und Veränderungen der Photonenstatistik des transmittierten Lichts zeigt. Diese Effekte können in Verschränkungsprotokollen genutzt werden, was das Potenzial dieser Systeme als Knotenpunkte in Quantennetzwerken mit Purcell-verstärkten photonischen Schnittstellen unterstreicht.

Darüber hinaus wird das kryogene Mikroresonatorsystem verwendet, um NV-Zentren mit effizienten Qubit-Photon-Schnittstellen auszustatten. Die Resonatorkopplung wird in

Kombination mit einer kreuzpolarisierten resonanten Anregungs- und Detektionsmethode verwendet, um das Elektronenspin-Qubit des NV-Zentrums zu initialisieren und auszulesen. Zudem wird der Elektronenspin mit on-chip Mikrowellenleitern kohärent kontrolliert und gepulste resonante Anregung ermöglicht die Erzeugung von Spin-Photon-korrelierten Zuständen. Die Quantennetzwerkfähigkeiten des Systems werden durch die Messung angekündigter Z-Basis Korrelationen zwischen photonischen time-bin Qubits und dem Spin-Qubit demonstriert. In diesen Experimenten wird eine zehnfache Verbesserung der resonanten Photonendetektionswahrscheinlichkeit gegenüber modernster NV-Zentren-Quantennetzwerkknoten erzielt, was den Weg für ein resonatorverstärktes Quantennetzwerk mit NV-Zentren ebnet.

1 Introduction

What began about sixty years ago with research efforts on internetworking of classical computer systems has evolved to a globe-spanning network that we now call the internet [1]. Nowadays, this technology processes a tremendous amount of information every day to provide us with services such as the World Wide Web.

More recently, research groups around the world have managed to isolate and control quantum systems, which are considered the first quantum computers as they can process quantum information [2]. These achievements stimulate research on quantum networks, which aims to interconnect quantum computers toward realizing a quantum internet in analogy to the 'classical' internet of today [3]. By harnessing quantum mechanical phenomena, novel services like quantum key distribution, blind quantum computing, and many more yet to be discovered applications can be implemented [4]. The prospect of executing network applications that are currently infeasible with existing technology drives research in this area.

At the core of quantum information technologies, quantum bits (qubits) are used to store and process quantum information. Compared to the 'classical' bit, qubits have two key differences due to their quantum nature. First, a qubit cannot only be in the bit state '0' or '1', but also in a superposition state of '0' and '1' at the same time. If the state of such a qubit is read out (measured) the outcome is either '0' or '1' with probabilities that are determined by the amplitudes of the superposition state. Second, qubits can be entangled with each other, which means that they share a common quantum state. The measurement of one of the qubits changes the state of the others, and hence influences their measurement outcome irrespective of their spatial separation. These quantum-mechanical properties make quantum information technologies fundamentally distinct from today's information technologies.

1.1 Quantum Networks

Figure 1.1 illustrates a quantum network of multiple quantum nodes with stationary qubits, that is capable of generating, processing and measuring shared quantum states. Next to classical communication channels, quantum nodes are connected via quantum channels, that enable the generation of shared (entangled) quantum states via middle stations. These

1

quantum channels are optical and can be implemented using optical fibers or free-space transmission lines.

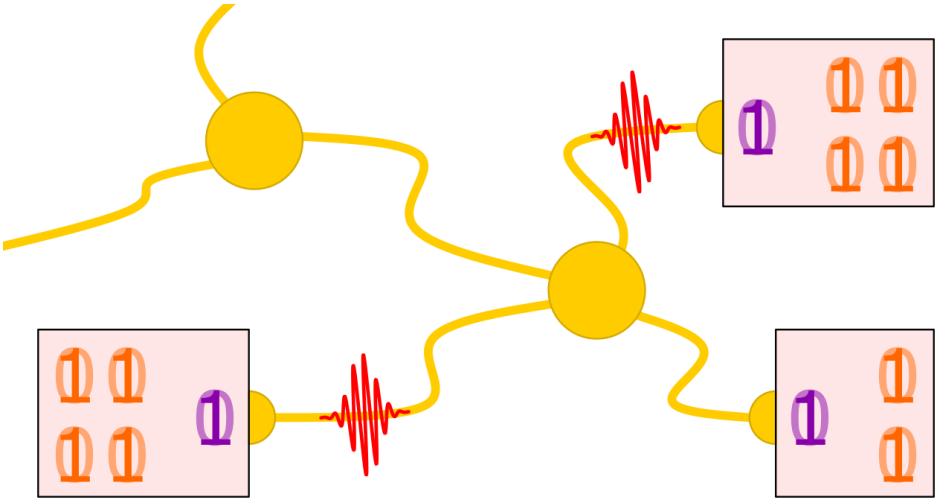

Figure 1.1: Quantum network illustration of quantum nodes with stationary qubits and optical interfaces. The quantum nodes (square boxes) exhibit memory qubits (in orange) and communication qubits (in purple). The communication qubit can be used to generate photons as flying qubits (red wave packets), which are sent over quantum channels and middle stations (yellow circles) to distribute entanglement in the quantum network.

The fundamental task of a quantum network is to distribute entanglement amoung quantum nodes. In this context, remote entanglement can be seen as a resource that, in combination with local processing and classical communication, can be used to realize quantum operations on a network. In these quantum networks, generating remote entanglement requires at least one qubit per quantum node with a qubit-photon interface. This interface enables local generation of an entangled state between the stationary qubit and a photon, which can be sent over a quantum channel to generate an entangled state with another node. The generated photons are referred to as flying qubits, and the stationary qubits with photonic interfaces are referred to as communication qubits.

Moreover, for many quantum network applications, additional stationary qubits are required as memory qubits to store quantum states, while, for example, the communication qubit establishes entanglement. The stored quantum states in stationary qubits decohere over time, which demands qubit-photon interfaces that efficiently generate entanglement in a network. In a final step, after generating and processing a shared quantum state on a quantum network, the qubits of the particpating quantum nodes can be measured to conclude the performed task.

In the last decades, many hardware platforms with stationary qubits and optical interfaces have been investigated for quantum networking, and multiple have achieved the generation of remote entanglement. These platforms include atomic clouds [5, 6], single atoms [7–10] and trapped ions [11–13] as well as solid-state systems like color centers in diamond [14–18], quantum dots [19, 20], rare-earth ion doped crystals [21], T centers in

silicon [22] and ytterbium ions in yttrium orthovanadate crystals [23].

1.2 Diamond Quantum Networks: State of the Art

Among the different qubit platforms, color centers in diamond have emerged as a very promising solid-state system for quantum networking. Diamond is a wide band gap semiconductor and can host quantum emitters with atom-like level structures within its band gap. These quantum emitters can show spin qubits with long coherence times and spin-selective optical transitions for remote entanglement generation. Up until now, systems based on the nitrogen-vacancy (NV) center [14] and the silicon-vacancy (SiV) center [17] have demonstrated the generation of entanglement between quantum network nodes. Moreover, in both systems nuclear spins in the color center's environment have been explored as memory qubits [24, 25].

Next to the first demonstration of heralded remote entanglement between solid-state qubits [14], the NV center platform has shown core quantum network capabilities like qubit teleportation [26], entanglement distillation [27] and deterministic entanglement delivery [15] between two quantum nodes as well as qubit teleportation between non-neighboring nodes [28] in a multinode quantum network [29]. Furthermore, the NV center platform has been used to develop and test a software control stack for quantum networks [30, 31]. In addition, the compatibility of the NV center platform with quantum frequency conversion to telecom wavelengths has been demonstrated [32, 33], which enabled the generation of heralded entanglement on a metropolitan scale [16].

In all of these experiments, NV centers in solid immersion lenses are used, which provide a sufficient spin-photon interface for these demonstrations. Compared to these non-resonant photonic structures, the SiV center has been successfully integrated in resonant diamond nanophotonic crystal cavities [34–36]. These structures can realize very efficient spin-photon interfaces and have enabled the exploration of different remote entanglement generation protocols [17, 18].

In the last years, also the tin-vacancy (SnV) center in diamond has emerged as a candidate for quantum networking due to its promising optical and spin properties [37, 38].

1.3 Next-Generation Quantum Network Nodes

Scaling quantum networks to more nodes and longer distances requires efficient spin-photon interfaces to mitigate photon loss and decoherence. Integrating color centers in resonant cavity structures is a very promising approach for this purpose [39]. Cavities benefit here in two ways: the color center's coherent photon emission probability can be enhanced via the Purcell effect, and the photons are emitted into a well-defined mode, enabling highly efficient collection. Cavities can equip color centers with almost deterministic spin-photon interfaces [40].

1.4 The Open Microcavity Platform

For the realization of diamond quantum network nodes with efficient spin-photon interfaces, open microcavities can be used [41]. An open microcavity consists of two mirrors that face each other at micrometer separations to confine photonic cavity modes between them. In

this work, we follow a fiber-based approach in which a spherical mirror on the tip of an optical fiber [42] and a flat sample mirror are used. As depicted in Fig. 1.2, the integration of color centers can be achieved by bonding micrometer-thin diamond devices to the sample mirror.

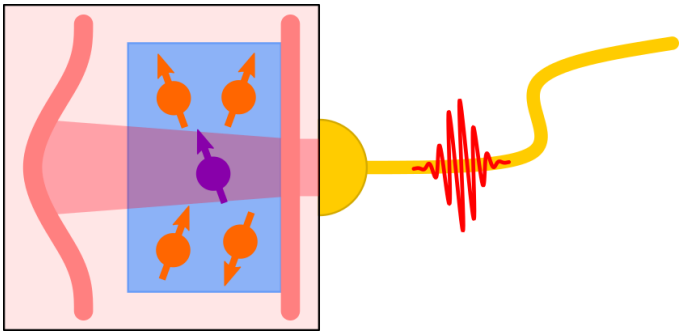

Figure 1.2: Quantum network node illustration of a microcavity-enhanced diamond color center in an open microcavity. The cavity mode is confined between the spherical and the flat sample mirror (light red lines). The electron spin of the color center (in purple) serves as the communication qubit and is coupled to the cavity mode. Nuclear spins (in orange) around the color center are used as memory qubits. The microcavity equips the color center with a spin-photon interface, enabling efficient generation and coupling of photons as flying qubits (red wave packets) to a quantum channel.

This cavity platform stands out for its great spatial and spectral tunability. Using a positioning system, the fiber mirror can be moved laterally over diamond devices, and a change in mirror separation (cavity length) can tune the cavity resonance over large wavelength ranges. Moreover, the cavity can be tailored to the optically active quantum emitter of interest by designing the center wavelengths, spectral bandwidths, and reflectivities of the mirrors. In addition, many solid-state sample types, like membranes [43], two-dimensional materials [44] or nanoparticles [45–47] can be integrated.

1.5 Thesis Overview

In this thesis, we address the challenge of using open microcavities to realize efficient spin-photon interfaces with NV and SnV centers in diamond and explore the open microcavity platform as a next-generation quantum network node. In the following, the thesis structure is outlined.

In Chapter 2, we present the basics about cavity-enhanced quantum network nodes with diamond color centers. First, the diamond NV center and the SnV center are introduced as qubit platforms, and their qubit control is summarized. Then, the Purcell enhancement of color centers in cavities and the generation of spin-photon entanglement as well as remote spin-spin entanglement are discussed.

In Chapter 3, a theoretical framework for diamond-air microcavities is introduced, that allows for quantifiying and optimizing the spin-photon interface performance. We investigate the cavity outcoupled coherent photon emission as well as the emitter-cavity

cooperativity, and discuss the optical interfacing of cavity-coupled color centers.

In Chapter 4, we present a cryogenic open microcavity setup featuring high passive stability and microwave integration. The passive stability is investigated by measuring cavity length fluctuations across multiple setup configurations, and the microwave integration is studied by performing optically detected magnetic resonance measurements of a microcavity-coupled NV center electron spin.

In Chapter 5, we introduce a novel patterning method for the fabrication of micrometer-thin diamond membranes utilizing laser-cutting. This method is used to fabricate diamond membranes for open microcavity applications and is compared with an established method that uses electron-beam lithography and a two-step transfer patterning with a silicon nitride hard mask. The diamond microdevices are characterized using scanning cavity microscopy, and the optical properties of color centers hosted in the diamond are studied using confocal photoluminescence excitation measurements.

In Chapter 6, the coherent coupling of a single SnV center to an open microcavity is studied. The Purcell enhancement is investigated with excited state lifetime and linewidth measurements. Moreover, the coherent interaction between the SnV center and the cavity is probed in cavity transmission, revealing its quantum nonlinear behavior.

In Chapter 7, a single NV center is microcavity-enhanced, and its electron spin is coherently controlled with microwave pulses. This efficient spin-photon interface is used in combination with short optical excitation pulses to generate spin-photon states. Finally, correlations between the photonic and the electron spin qubit states are measured.

In Chapter 8, the main results of this thesis are summarized, and an outlook about future microcavity experiments and research directions is provided.

1

References

[1] B. M. Leiner, V. G. Cerf, D. D. Clark, R. E. Kahn, L. Kleinrock, D. C. Lynch, J. Postel, L. G. Roberts, and S. Wolff, *A brief history of the internet,* ACM SIGCOMM Computer Communication Review **39** (2009).

[2] D. D. Awschalom, H. Bernien, R. Hanson, W. D. Oliver, and J. Vučković, *Challenges and opportunities for quantum information hardware,* Science **390**, 1004 (2025).

[3] H. J. Kimble, *The quantum internet,* Nature **453**, 1023 (2008).

[4] S. Wehner, D. Elkouss, and R. Hanson, *Quantum internet: A vision for the road ahead,* Science **362**, eaam9288 (2018).

[5] L.-M. Duan, M. D. Lukin, J. I. Cirac, and P. Zoller, *Long-distance quantum communication with atomic ensembles and linear optics,* Nature **414**, 413 (2001).

[6] J.-L. Liu, X.-Y. Luo, Y. Yu, C.-Y. Wang, B. Wang, Y. Hu, J. Li, M.-Y. Zheng, B. Yao, Z. Yan, D. Teng, J.-W. Jiang, X.-B. Liu, X.-P. Xie, J. Zhang, Q.-H. Mao, X. Jiang, Q. Zhang, X.-H. Bao, and J.-W. Pan, *Creation of memory–memory entanglement in a metropolitan quantum network,* Nature **629**, 579 (2024).

[7] S. Ritter, C. Nölleke, C. Hahn, A. Reiserer, A. Neuzner, M. Uphoff, M. Mücke, E. Figueroa, J. Bochmann, and G. Rempe, *An elementary quantum network of single atoms in optical cavities,* Nature **484**, 195 (2012).

[8] J. Hofmann, M. Krug, N. Ortegel, L. Gérard, M. Weber, W. Rosenfeld, and H. Weinfurter, *Heralded Entanglement Between Widely Separated Atoms,* Science **337**, 72 (2012).

[9] W. Zhang, T. van Leent, K. Redeker, R. Garthoff, R. Schwonnek, F. Fertig, S. Eppelt, W. Rosenfeld, V. Scarani, C. C.-W. Lim, and H. Weinfurter, *A device-independent quantum key distribution system for distant users,* Nature **607**, 687 (2022).

[10] T. Van Leent, M. Bock, F. Fertig, R. Garthoff, S. Eppelt, Y. Zhou, P. Malik, M. Seubert, T. Bauer, W. Rosenfeld, W. Zhang, C. Becher, and H. Weinfurter, *Entangling single atoms over 33 km telecom fibre,* Nature **607**, 69 (2022).

[11] D. L. Moehring, P. Maunz, S. Olmschenk, K. C. Younge, D. N. Matsukevich, L.-M. Duan, and C. Monroe, *Entanglement of single-atom quantum bits at a distance,* Nature **449**, 68 (2007).

[12] L. J. Stephenson, D. P. Nadlinger, B. C. Nichol, S. An, P. Drmota, T. G. Ballance, K. Thirumalai, J. F. Goodwin, D. M. Lucas, and C. J. Ballance, *High-Rate, High-Fidelity Entanglement of Qubits Across an Elementary Quantum Network,* Physical Review Letters **124**, 110501 (2020).

[13] V. Krutyanskiy, M. Galli, V. Krcmarsky, S. Baier, D. A. Fioretto, Y. Pu, A. Mazloom, P. Sekatski, M. Canteri, M. Teller, J. Schupp, J. Bate, M. Meraner, N. Sangouard, B. P. Lanyon, and T. E. Northup, *Entanglement of Trapped-Ion Qubits Separated by 230 Meters,* Physical Review Letters **130**, 050803 (2023).

[14] H. Bernien, B. Hensen, W. Pfaff, G. Koolstra, M. S. Blok, L. Robledo, T. H. Taminiau, M. Markham, D. J. Twitchen, L. Childress, and R. Hanson, *Heralded entanglement between solid-state qubits separated by three metres,* Nature **497**, 86 (2013).

[15] P. C. Humphreys, N. Kalb, J. P. J. Morits, R. N. Schouten, R. F. L. Vermeulen, D. J. Twitchen, M. Markham, and R. Hanson, *Deterministic delivery of remote entanglement on a quantum network,* Nature **558**, 268 (2018).

[16] A. J. Stolk, K. L. Van Der Enden, M.-C. Slater, I. Te Raa-Derckx, P. Botma, J. Van Rantwijk, J. J. B. Biemond, R. A. J. Hagen, R. W. Herfst, W. D. Koek, A. J. H. Meskers, R. Vollmer, E. J. Van Zwet, M. Markham, A. M. Edmonds, J. F. Geus, F. Elsen, B. Jungbluth, C. Haefner, C. Tresp, J. Stuhler, S. Ritter, and R. Hanson, *Metropolitan-scale heralded entanglement of solid-state qubits,* Science Advances **10**, eadp6442 (2024).

[17] C. M. Knaut, A. Suleymanzade, Y.-C. Wei, D. R. Assumpcao, P.-J. Stas, Y. Q. Huan, B. Machielse, E. N. Knall, M. Sutula, G. Baranes, N. Sinclair, C. De-Eknamkul, D. S. Levonian, M. K. Bhaskar, H. Park, M. Lončar, and M. D. Lukin, *Entanglement of nanophotonic quantum memory nodes in a telecom network,* Nature **629**, 573 (2024).

[18] P.-J. Stas, Y.-C. Wei, M. Sirotin, Y. Q. Huan, U. Yazlar, F. A. Arias, E. Knyazev, G. Baranes, B. Machielse, S. Grandi, D. Riedel, J. Borregaard, H. Park, M. Lončar, A. Suleymanzade, and M. D. Lukin, *Entanglement Assisted Non-local Optical Interferometry in a Quantum Network,* arXiv:2509.09464 (2025), https://arxiv.org/abs/2509.09464.

[19] A. Delteil, Z. Sun, W.-b. Gao, E. Togan, S. Faelt, and A. Imamoğlu, *Generation of heralded entanglement between distant hole spins,* Nature Physics **12**, 218 (2016).

[20] R. Stockill, M. J. Stanley, L. Huthmacher, E. Clarke, M. Hugues, A. J. Miller, C. Matthiesen, C. Le Gall, and M. Atatüre, *Phase-Tuned Entangled State Generation between Distant Spin Qubits,* Physical Review Letters **119**, 010503 (2017).

[21] I. Usmani, C. Clausen, F. Bussières, N. Sangouard, M. Afzelius, and N. Gisin, *Heralded quantum entanglement between two crystals,* Nature Photonics **6**, 234 (2012).

[22] F. Afzal, S. J. Beale, O. Bedroya, K. Bell, L. Bergeron, K. Bonsma-Fisher, P. Bychkova, Z. M. E. Chaisson, C. Chartrand, C. Clear, A. Darcie, A. DeAbreu, C. DeLisle, L. A. Duncan, C. D. Smith, J. Dunn, A. Ebrahimi, N. Evetts, D. F. Pinheiro, P. Fuentes, T. Georgiou, B. Guha, R. Haenel, D. Higginbottom, D. M. Jackson, N. Jahed, A. Khorshidahmad, P. K. Shandilya, A. T. K. Kurkjian, N. Lauk, N. R. Lee-Hone, E. Lin, R. Litynskyy, D. Lock, L. Ma, I. MacGilp, E. R. MacQuarrie, A. Mar, A. M. Khah, A. Matiash, E. Meyer-Scott, C. P. Michaels, J. Motira, N. K. Noori, E. Ospadov, E. Patel, A. Patscheider, D. Paulson, A. Petruk, A. L. Ravindranath, B. Reznychenko, M. Ruether, J. Ruscica, K. Saxena, Z. Schaller, A. Seidlitz, J. Senger, Y. S. Lee, O. Sevoyan, S. Simmons, O. Soykal, L. Stott, Q. Tran, S. Tserkis, A. Ulhaq, W. Vine, R. Weeks, G. Wolfowicz, and I. Yoneda, *Distributed Quantum Computing in Silicon,* arXiv:2406.01704 (2024), https://arxiv.org/abs/2406.01704.

[23] A. Ruskuc, C.-J. Wu, E. Green, S. L. N. Hermans, W. Pajak, J. Choi, and A. Faraon, *Multiplexed entanglement of multi-emitter quantum network nodes,* Nature **639**, 54 (2025).

[24] C. E. Bradley, S. W. De Bone, P. F. W. Möller, S. Baier, M. J. Degen, S. J. H. Loenen, H. P. Bartling, M. Markham, D. J. Twitchen, R. Hanson, D. Elkouss, and T. H. Taminiau, *Robust quantum-network memory based on spin qubits in isotopically engineered diamond,* npj Quantum Information **8**, 122 (2022).

[25] P.-J. Stas, Y. Q. Huan, B. Machielse, E. N. Knall, A. Suleymanzade, B. Pingault, M. Sutula, S. W. Ding, C. M. Knaut, D. R. Assumpcao, Y.-C. Wei, M. K. Bhaskar, R. Riedinger, D. D. Sukachev, H. Park, M. Lončar, D. S. Levonian, and M. D. Lukin, *Robust multi-qubit quantum network node with integrated error detection,* Science **378**, 557 (2022).

[26] W. Pfaff, B. J. Hensen, H. Bernien, S. B. van Dam, M. S. Blok, T. H. Taminiau, M. J. Tiggelman, R. N. Schouten, M. Markham, D. J. Twitchen, and R. Hanson, *Unconditional quantum teleportation between distant solid-state quantum bits,* Science **345**, 532 (2014).

[27] N. Kalb, A. A. Reiserer, P. C. Humphreys, J. J. W. Bakermans, S. J. Kamerling, N. H. Nickerson, S. C. Benjamin, D. J. Twitchen, M. Markham, and R. Hanson, *Entanglement distillation between solid-state quantum network nodes,* Science **356**, 928 (2017).

[28] S. L. N. Hermans, M. Pompili, H. K. C. Beukers, S. Baier, J. Borregaard, and R. Hanson, *Qubit teleportation between non-neighbouring nodes in a quantum network,* Nature **605**, 663 (2022).

[29] M. Pompili, *Multi-Node Quantum Networks with Diamond Qubits*, Ph.D. thesis, Delft University of Technology (2021).

[30] M. Pompili, C. Delle Donne, I. Te Raa, B. Van Der Vecht, M. Skrzypczyk, G. Ferreira, L. De Kluijver, A. J. Stolk, S. L. N. Hermans, P. Pawełczak, W. Kozlowski, R. Hanson, and S. Wehner, *Experimental demonstration of entanglement delivery using a quantum network stack,* npj Quantum Information **8**, 121 (2022).

[31] C. Delle Donne, M. Iuliano, B. Van Der Vecht, G. M. Ferreira, H. Jirovská, T. J. W. Van Der Steenhoven, A. Dahlberg, M. Skrzypczyk, D. Fioretto, M. Teller, P. Filippov, A. R.-P. Montblanch, J. Fischer, H. B. Van Ommen, N. Demetriou, D. Leichtle, L. Music, H. Ollivier, I. Te Raa, W. Kozlowski, T. H. Taminiau, P. Pawełczak, T. E. Northup, R. Hanson, and S. Wehner, *An operating system for executing applications on quantum network nodes,* Nature **639**, 321 (2025).

[32] A. Tchebotareva, S. L. N. Hermans, P. C. Humphreys, D. Voigt, P. J. Harmsma, L. K. Cheng, A. L. Verlaan, N. Dijkhuizen, W. de Jong, A. Dréau, and R. Hanson, *Entanglement between a Diamond Spin Qubit and a Photonic Time-Bin Qubit at Telecom Wavelength,* Physical Review Letters **123**, 063601 (2019).

[33] A. Stolk, K. van der Enden, M.-C. Roehsner, A. Teepe, S. Faes, C. Bradley, S. Cadot, J. van Rantwijk, I. te Raa, R. Hagen, A. Verlaan, J. Biemond, A. Khorev, R. Vollmer, M. Markham, A. Edmonds, J. Morits, T. Taminiau, E. van Zwet, and R. Hanson, *Telecom-Band Quantum Interference of Frequency-Converted Photons from Remote Detuned NV Centers,* PRX Quantum **3**, 020359 (2022).

[34] J. Riedrich-Möller, L. Kipfstuhl, C. Hepp, E. Neu, C. Pauly, F. Mücklich, A. Baur, M. Wandt, S. Wolff, M. Fischer, S. Gsell, M. Schreck, and C. Becher, *One- and two-dimensional photonic crystal microcavities in single crystal diamond,* Nature Nanotechnology **7**, 69 (2012).

[35] A. Sipahigil, R. E. Evans, D. D. Sukachev, M. J. Burek, J. Borregaard, M. K. Bhaskar, C. T. Nguyen, J. L. Pacheco, H. A. Atikian, C. Meuwly, R. M. Camacho, F. Jelezko, E. Bielejec, H. Park, M. Lončar, and M. D. Lukin, *An integrated diamond nanophotonics platform for quantum-optical networks,* Science **354**, 847 (2016).

[36] S. W. Ding, M. Haas, X. Guo, K. Kuruma, C. Jin, Z. Li, D. D. Awschalom, N. Delegan, F. J. Heremans, A. A. High, and M. Loncar, *High-Q cavity interface for color centers in thin film diamond,* Nature Communications **15**, 6358 (2024).

[37] A. E. Rugar, C. Dory, S. Sun, and J. Vučković, *Characterization of optical and spin properties of single tin-vacancy centers in diamond nanopillars,* Physical Review B **99**, 205417 (2019).

[38] J. Görlitz, D. Herrmann, G. Thiering, P. Fuchs, M. Gandil, T. Iwasaki, T. Taniguchi, M. Kieschnick, J. Meijer, M. Hatano, A. Gali, and C. Becher, *Spectroscopic investigations of negatively charged tin-vacancy centres in diamond,* New Journal of Physics **22**, 013048 (2020).

[39] M. Ruf, N. H. Wan, H. Choi, D. Englund, and R. Hanson, *Quantum networks based on color centers in diamond,* Journal of Applied Physics **130**, 070901 (2021).

[40] J. Borregaard, A. S. Sørensen, and P. Lodahl, *Quantum Networks with Deterministic Spin–Photon Interfaces,* Advanced Quantum Technologies **2**, 1800091 (2019).

[41] E. Janitz, M. K. Bhaskar, and L. Childress, *Cavity quantum electrodynamics with color centers in diamond,* Optica **7**, 1232 (2020).

[42] D. Hunger, T. Steinmetz, Y. Colombe, C. Deutsch, T. W. Hänsch, and J. Reichel, *A fiber Fabry–Perot cavity with high finesse,* New Journal of Physics **12**, 065038 (2010).

[43] E. Janitz, M. Ruf, M. Dimock, A. Bourassa, J. Sankey, and L. Childress, *Fabry-Perot microcavity for diamond-based photonics,* Physical Review A **92**, 043844 (2015).

[44] S. Vadia, J. Scherzer, H. Thierschmann, C. Schäfermeier, C. Dal Savio, T. Taniguchi, K. Watanabe, D. Hunger, K. Karraï, and A. Högele, *Open-Cavity in Closed-Cycle Cryostat as a Quantum Optics Platform,* PRX Quantum **2**, 040318 (2021).

[45] R. Albrecht, A. Bommer, C. Deutsch, J. Reichel, and C. Becher, *Coupling of a Single Nitrogen-Vacancy Center in Diamond to a Fiber-Based Microcavity,* Physical Review Letters **110**, 243602 (2013).

[46] T. Hümmer, J. Noe, M. S. Hofmann, T. W. Hänsch, A. Högele, and D. Hunger, *Cavity-enhanced Raman microscopy of individual carbon nanotubes,* Nature Communications **7**, 12155 (2016).

[47] B. Casabone, C. Deshmukh, S. Liu, D. Serrano, A. Ferrier, T. Hümmer, P. Goldner, D. Hunger, and H. De Riedmatten, *Dynamic control of Purcell enhanced emission of erbium ions in nanoparticles,* Nature Communications **12**, 3570 (2021).

2

Methods for Cavity-enhanced Quantum Network Nodes with Diamond Color Centers

In this chapter, the basics of cavity-enhanced quantum networking are outlined. First, the nitrogen-vacancy and the tin-vacancy center in diamond are introduced as the qubit platforms of this thesis. Next, an overview of the state-of-the-art microwave-based qubit control for quantum network nodes is provided for both platforms. Then, the Purcell enhancement of the color center's optical transitions and the resulting spin-photon interface efficiency are discussed. The chapter closes with the description of spin-photon and spin-spin entanglement generation using different remote entanglement protocols in a quantum network.

2.1 The Nitrogen-Vacancy Center in Diamond

The nitrogen-vacancy (NV) center in diamond is a crystallographic point defect that is formed by a substitutional nitrogen atom next to a vacant lattice site hosted in the diamond cubic crystal structure of carbon atoms, as shown in Fig. 2.1(a). The basis of the negatively charged NV center's electronic level structure is given by atomic orbitals of three electrons of the carbon dangling bonds, two electrons of the nitrogen atom, and an additional electron that is captured from the defect's environment [1]. The neutrally charged nitrogen vacancy center, with a total of five electrons, also forms an optically active defect. In general, crystal defects that exhibit optical transitions are called color centers. Since only the negatively charged NV center is studied in this thesis, we refer to it as the NV center in short. Following the C_{3v} point group symmetry of the defect, molecular orbitals are constructed as linear combinations of atomic orbitals [2]. Figure 2.1(b) shows the occupation of these molecular orbitals for the NV center's ground state within the band gap of diamond. Both the ground state and the first excited state of the NV center lie within the diamond band gap, which explains the atom-like behavior of the defect in a solid-state host.

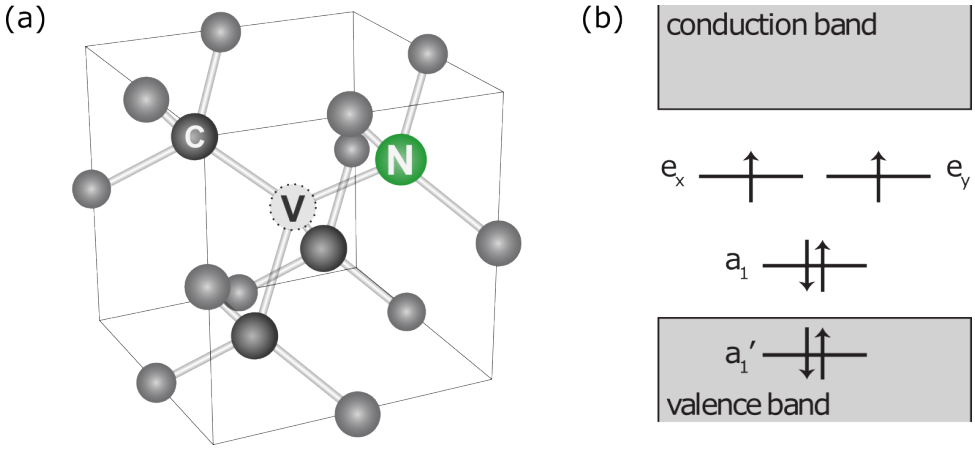

Figure 2.1: The nitrogen-vacancy center in diamond. (a) The crystallographic structure of the NV center in the diamond lattice unit cell, formed by a substitutional nitrogen atom (N) next to a lattice vacancy (V). (b) The molecular orbital states within the band gap of diamond. The electron occupation for the ground state of the negatively charged NV center is depicted. Figure (a) from Ruf [3] and Figure (b) from Bernien [4], Pfaff [5].

The NV center is a spin-1 system exhibiting spin-singlet and spin-triplet states. The ground states are formed by orbital-singlet spin-triplet states that are connected via spin-selective optical transitions to orbital-doublet spin-triplet excited states [1]. Next to the direct decay from the excited states to the ground states, the decay can also occur via the spin-singlet states as depicted in Fig. 2.2(a). At cryogenic temperatures, the individual optical transitions can be spectrally resolved, and the E_x and E_y transition show high cyclicities and hence lower decay rates into the spin-singlet states than the other excited states [6, 7]. The excited states are susceptible to crystal strain and electric fields, which can affect cyclicities of the optical transitions. Moreover, deliberately applied electric fields can be used to tune optical transitions in experiments via the Stark effect [8, 9].

Furthermore, the degeneracy of the ground states is lifted by an external magnetic field, and the (communication) qubit states are defined.

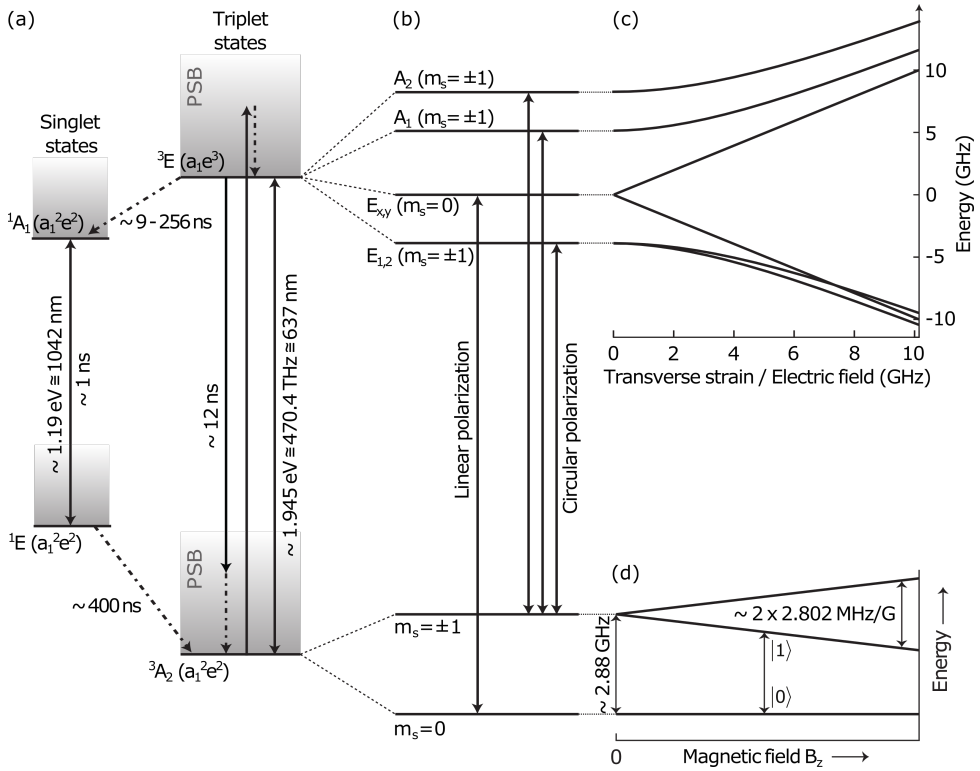

Figure 2.2: Electronic level structure of the negatively charged NV center. (a) The spin-triplet ground states $^3A_2$ are connected to the excited states ^3E via spin-selective optical transitions. The excitation and decay can occur either resonantly via the zero-phonon line (ZPL, solid arrows) or via the phonon sideband (PSB) involving phonon processes (dashed-dotted arrows). From the spin-triplet excited states, there is spin-dependent decay into the spin-singlet excited states $^1A_1$. The decay back into the spin-triplet manifold from the spin-singlet ground states ^1E favors the $m_s = 0$ ground state. (b) At cryogenic temperatures, the individual optical transitions between the spin-triplet states can be observed. (c) Transverse strain and electric fields change the excited states. (d) The $m_s = \pm 1$ ground state degeneracy is lifted by magnetic fields aligned with the NV center crystal axis. This allows one to define, for example, the spin states $m_s = 0$ and $m_s = -1$ as the $|0\rangle$ and $|1\rangle$ qubit states, respectively. Figure adapted from Ruf [3], Kalb [10], Bernien [4], Pfaff [5].

Optical excitation and decay can occur either resonantly via the zero-phonon line (ZPL) or via the phonon sideband (PSB) of the excited states and ground states, respectively. For the NV center decay, a ~ 3 % fraction [11] of the total radiative emission is emitted into the ZPL. Since only the ZPL emission is suitable for remote entanglement generation, as quantum information is lost when a phonon leaks into the environment, this constitues a limit of the remote entanglement generation efficiency.

For quantum networking applications the NV center must be operated at temperatures $< 10\,\mathrm{K}$ as this enables the observation of lifetime-limited linewidths of the optical transitions [12], which are needed for remote entanglement generation. The temperature requirements

on the electron spin qubit in the ground states are more relaxed with demonstrations of coherent spin dynamics at room temperature [13].

2.2 The Tin-Vacancy Center in Diamond

The diamond tin-vacancy (SnV) center is a crystallographic point defect and belongs to the group IV vacancy centers in diamond. As depicted in Fig. 2.3(a), these defects are formed by an interstitial atom of a group 14[1] element between two vacant carbon lattice sites, which is also known as a split-vacancy configuration. Optical studies have been performed with silicon-[14–17], germanium-[18–20], tin-[21–24] and lead-vacancy centers [25–27], that all show similar electronic level structures with differing energetic level spacings. The electronic level structure of the negatively-charged SnV center, or just SnV center in short, is based on the atomic orbitals of six electrons from the carbon dangling bonds, four electrons from the tin atom, and an additional electron that is captured from the defect's environment. Following the D_{3d} point group symmetry of the defect, molecular orbitals are constructed as linear combinations of atomic orbitals [28]. Figure 2.3(b) shows the occupation of these molecular orbitals for the SnV center ground state within the band gap of diamond. The e_u molecular orbitals are close to the valence band edge in the ground state and contribute in the excited state [29]. Furthermore, the point group symmetry includes an inversion symmetry around the position of the interstitial group IV atom, which leads to a vanishing permanent electric dipole moment of the defect. As a consequence, the optical transitions of SnV centers are first-order insensitive to electric fields, enabling their integration into nanophotonic diamond structures where fluctuating electric surface charges are in close proximity [30, 31].

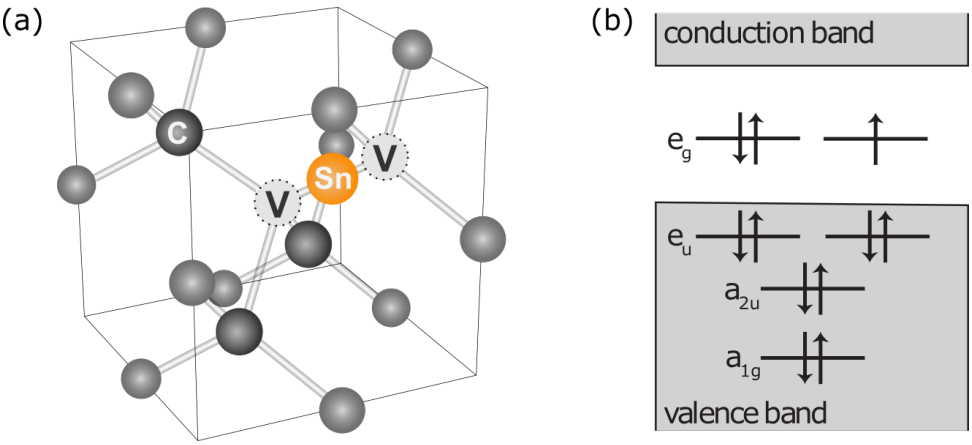

Figure 2.3: The tin-vacancy center in diamond. (a) The crystallographic structure of the SnV center in the diamond lattice unit cell, formed by an interstitial tin atom (Sn) between two lattice vacancies (V). (b) The molecular orbital states within the band gap of diamond. The electron occupation for the ground state of the negatively charged SnV center is depicted. Figure (a) adapted from Ruf [3], and Figure (b) adapted from Herrmann [32].

[1] Official IUPAC nomenclature.

The SnV center is a spin-1/2 system with an orbital-doublet spin-doublet ground and excited state. The ground and excited states are split into an orbital lower branch (LB) and upper branch (UB), each with a double spin degeneracy. All of these states are susceptible to crystal strain and magnetic fields, which can also mix their orbital and spin component, respectively [33]. In addition, phonon transitions are allowed between the LB and UB in the excited and ground states [34]. Figure 2.4 shows the electronic level structure of the SnV center with the relevant optical and phonon transitions. At cryogenic temperatures, effectively only the LBs are occupied, justifying the focus on the C transition, which splits into the $A1$, $A2$, $B1$, and $B2$ optical transitions as a result of the magnetic field [23]. The two states of the LB in the ground states can be used as a (communication) qubit. Without strain or off-axis magnetic fields, the qubit states have opposite orbital and spin components, which renders direct driving forbidden. This shows that engineering strain and magnetic fields is crucial for qubit driving with microwaves and opens up a parameter space to explore [35]. In experiments, strain can be used to facilitate qubit driving and, with smaller magnitudes, already be used for large-range tuning of the optical transitions [36]. Moreover, strain and magnetic fields affect the cyclicities of the optical transitions, which need to be considered for the photonic qubit interface [37].

As for the NV center, the optical excitation and decay can occur either resonantly via the ZPL or via the PSB of the excited states and ground states, respectively. For the SnV center decay, about 57 % [24] is attributed to ZPL emission, of which about 64 % [38] is emitted into the C transition. Compared to the NV center, with a remote entanglement suited emission fraction of 3 % [11], the SnV center exhibits an approximately tenfold more efficient optical interface.

To use the SnV center as a quantum network node, temperatures of $< 2\,\mathrm{K}$ are required to improve phonon-related spin coherence times to $> 1\,\mathrm{s}$ [39]. Further, SnV centers with strain magnitudes on the order of the spin-orbit coupling have been coherently controlled at temperatures of 4 K [40]. This constitutes a stricter requirement compared to the observation of lifetime-limited linewidths of the optical transitions, which is possible for temperatures $< 6\,\mathrm{K}$ [27].

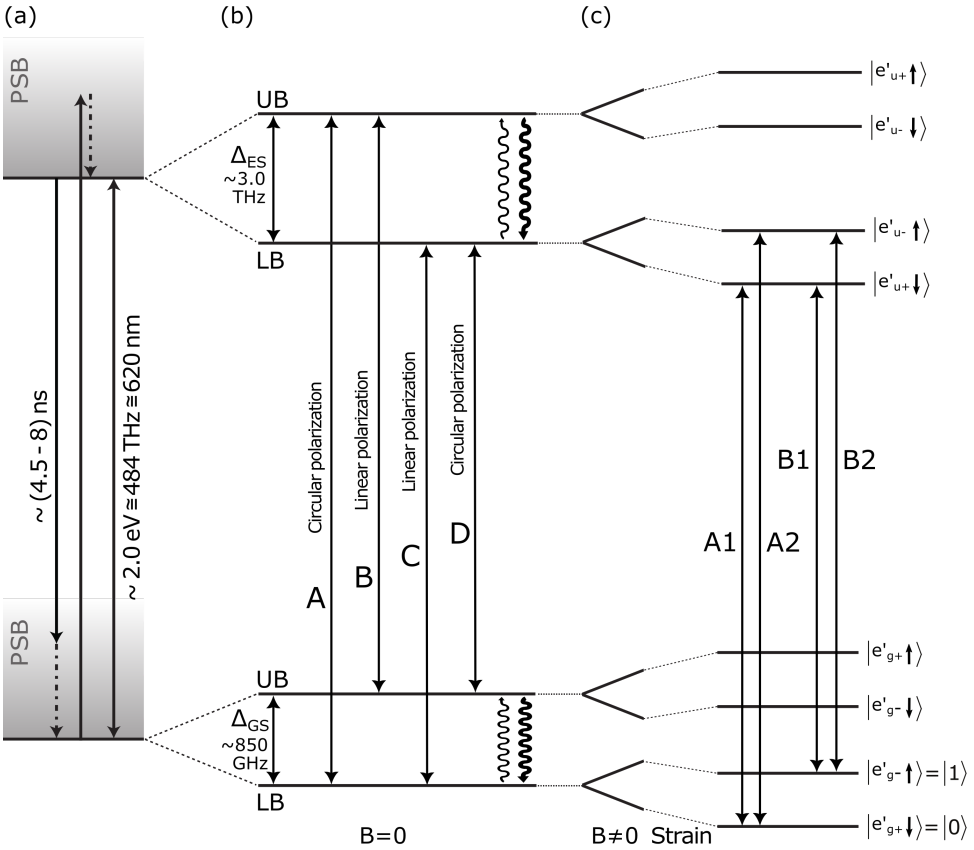

Figure 2.4: Electronic level structure of the negatively charged SnV center. (a) The excited and ground states are formed by an orbital-doublet spin-doublet and are connected via spin-selective optical transitions. The excitation and decay can occur either resonantly via the zero-phonon line (ZPL, solid arrows) or via the phonon sideband (PSB) involving phonon processes (dashed-dotted arrows). (b) The excited and ground states are split into a lower branch (LB) and an upper branch (UB), from which four optical transitions *A*, *B*, *C*, and *D* arise. Between the branches in the excited and ground states, phonon transitions (wavy arrows) are allowed. In (c), the effect of strain and magnetic fields on the ground and excited states is visualized. The application of a magnetic field can lift the degeneracy in all branches. This allows one to define the two qubit states $|0\rangle$ and $|1\rangle$ in the LB of the ground states, with their corresponding optical transitions *A*1, *A*2, *B*1, and *B*2 to the LB of the excited states. Figure adapted from Herrmann [32].

2.3 Communication and Memory Qubit Control: State of the Art

This section provides a brief overview of microwave qubit control of the electron spin (communication qubit) and of surrounding nuclear spins (memory qubits) with NV and SnV centers. In addition, timescales of their qubit coherence are summarized. Microwave-based qubit control is well studied for the NV center and has been adapted to the SnV center more recently.

For NV centers, extended electron spin coherence times [41] and high-fidelity quantum gates [42] have been demonstrated. Furthermore, the NV center has been used to realize a ten-qubit register with the nitrogen nuclear spin and surrounding carbon-13 nuclear spins [43]. In addition, a spin-qubit network consisting of 50 nuclear spins has been mapped out in the environment of a NV center [44].

In the last few years, microwave-based qubit control has been realized with the SnV center electron spin [37, 40, 45]. In addition, single-shot readout of the electron spin [46] and the coherent control of a carbon-13 nuclear spin in the vicinity of the SnV center have been achieved [47].

In these demonstrations, the microwave signals are delivered to the color center via striplines or wire bonds with typical qubit gate times of hundreds of ns for the electron spin and hundreds of µs for carbon-13 nuclear spins. Furthermore, the electron spin is initialized and read out via optical pumping with durations on the order of µs. To summarize, electron spin coherence times of $> 1\,\mathrm{s}$ have been achieved with a NV center [41], while for the SnV center, recent results have shown coherence times of $\sim 10\,\mathrm{ms}$ [45]. For carbon-13 nuclear spins as memory qubits, coherence times $\sim 50\,\mathrm{ms}$ for NV centers under remote entanglement generation [48] and $\sim 20\,\mathrm{ms}$ for SnV centers [47] have been demonstrated. Comparing the spin coherence times to reported attempt durations for heralded remote entanglement of $\sim 5\,\mu\mathrm{s}$ [49] in a meter-scale network and of $\sim 100\,\mu\mathrm{s}$ [50] in a metropolitan-scale network shows that multiple remote entanglement attempts can be executed within the spin coherence time. This underlines the potential of both color centers for quantum networking.

2.4 Purcell Enhancement of a Color Center's Optical Transition

In this section, the Purcell effect [51] as the underlying physical phenomenon to realize cavity-based spin-photon interfaces for diamond color centers is outlined. Therefore, the optical transition rate of a dipole emitter in a homogeneous medium and in an optical cavity is discussed.

Fermi's golden rule can be used to calculate the emitter transition rate from an excited state $|e\rangle$ to a ground state $|g\rangle$, considering external perturbations. For an emitter with electric dipole moment $\vec{\mu}_{eg}$, vacuum fluctuations of the electric field $\vec{E}_{\mathrm{vac}}$ perturb the emitter system, which leads to the transition rate [52, 53]

$$\Gamma_{e\to g}(\omega) = \frac{2\pi}{\hbar^2}\left|\vec{\mu}_{eg}\cdot\vec{E}_{\mathrm{vac}}\right|^2 D(\omega), \tag{2.1}$$

with the photonic density of states $D(\omega)$ at the emitter's optical transition frequency ω. The root mean square electric field amplitude of the vacuum fluctuations is given by [53]

$$\vec{E}_{\text{vac}} = \left|\vec{E}_{\text{vac}}\right| \cdot \hat{e} = \sqrt{\frac{\hbar\omega}{2\epsilon_0\epsilon_r V}} \cdot \hat{e}, \tag{2.2}$$

with the vacuum permittivity ϵ_0, the relative permittivity ϵ_r, the vacuum field quantization volume V and the polarization unit vector of the electric field $\hat{e}$. This results in the transition rate

$$\Gamma_{e\to g}(\omega) = \frac{\pi\omega}{\hbar\epsilon_0\epsilon_r V}\mu_{eg}^2 \left|\hat{d}\cdot\hat{e}\right|^2 D(\omega) = 2\pi g^2 \left|\hat{d}\cdot\hat{e}\right|^2 D(\omega), \tag{2.3}$$

with $\vec{\mu}_{eg} = \mu_{eg}\hat{d}$ and the introduction of the coupling constant between dipole emitter and vacuum electric field

$$g = \sqrt{\frac{\omega\mu_{eg}^2}{2\hbar\epsilon_0\epsilon_r V}}. \tag{2.4}$$

For a homogeneous medium, the photonic density of states is given by [53]

$$D_{\text{hom}}(\omega) = \frac{\omega^2 V}{\pi^2 (c/n)^3}, \tag{2.5}$$

with the refractive index n of the medium. This leads to the emitter optical transition rate

$$\Gamma_{\text{hom}}(\omega) = \frac{\omega^3 n^3 \mu_{eg}^2}{3\hbar\pi\epsilon_0\epsilon_r c^3}, \tag{2.6}$$

considering a random overlap between emitter dipole and electric field polarization in the medium with an average of $|\hat{d}\cdot\hat{e}|^2 = 1/3$. The resulting rate resembles the natural emission decay rate of the optical transition, that connects the excited state $|e\rangle$ to the ground state $|g\rangle$ of the emitter.

Integrating a dipole emitter in an optical cavity can lead to additional emission decay due to the interaction with the vacuum electric field of the cavity mode, which can exhibit a high photonic density of states $D_{\text{cav}}(\omega)$ at the emitter's optical transition frequency.

The photonic density of states around a cavity resonance ω_c follows a Lorentzian line shape and is given by [53]

$$D_{\text{cav}}(\omega) = \frac{2}{\pi\kappa} \cdot \frac{\kappa^2}{4(\omega-\omega_c)^2 + \kappa^2}, \tag{2.7}$$

with the cavity decay rate $\kappa = 2\pi\delta\nu$, which is connected to the Lorentzian full width at half maximum cavity linewidth $\delta\nu$. On resonance, the cavity density of states yields

$$D_{\text{cav}}(\omega = \omega_c) = \frac{2}{\pi\kappa} = \frac{2Q}{\pi\omega}, \tag{2.8}$$

with the definition of the cavity quality factor $Q = \omega/\kappa$. Finally, the emission decay rate into the cavity mode on resonance reads

$$\Gamma_{\text{cav}}(\omega = \omega_c) = \frac{2\mu_{eg}^2}{\hbar\epsilon_0\epsilon_r}\left|\hat{d}\cdot\hat{e}\right|^2 \frac{Q}{V}, \tag{2.9}$$

with the cavity electric field quantization volume V, given as the cavity mode volume. The Purcell factor is defined as the ratio of the coherent emission rate into the cavity to the natural emission rate

$$F_P = \frac{\Gamma_{\text{cav}}}{\Gamma_{\text{hom}}} = \frac{3}{4\pi^2}\left(\frac{\lambda_0}{n}\right)^3 \frac{Q}{V}, \tag{2.10}$$

where we assume a unity emitter dipole overlap with the polarization of the cavity electric field $|\hat{d}\cdot\hat{e}|^2 = \xi = 1$.

Diamond color centers exhibit multiple decay mechanisms from an excited state $|e\rangle$, which all contribute to a total natural emitter decay rate γ. These can involve non-radiative decay, phonon sideband decay via vibrational states, and resonant decay that branches into other ground states, which are specified by the quantum efficiency η, the Debye-Waller factor β_0, and the branching ratio α, respectively. Next to these emitter properties, the emitter dipole overlap with the cavity electric field polarization ξ and the spatial overlap between emitter and cavity mode ϵ must be considered. All these contributions lead to the definition of the cooperativity [38]

$$C = \frac{4g^2}{\kappa\gamma} = \frac{\gamma_{\text{cav}}}{\gamma} = \eta\beta_0\alpha\xi\epsilon F_P, \tag{2.11}$$

which describes the color centers coherent emission rate into the cavity mode γ_{cav} to its total natural emitter decay rate γ and by that the efficiency of the spin-photon interface [54]. The fraction of emission into the cavity mode is then given by

$$\beta_{\text{cav}} = \frac{\gamma_{\text{cav}}}{\gamma_{\text{cav}}+\gamma} = \frac{C}{C+1}. \tag{2.12}$$

The cavity mode is a well-defined optical mode, that enables efficient detection. In experiments, the cavity outcoupling efficiency must be considered to determine the actual fraction of emission available for detection. The outcoupling efficiency $\eta_{\text{out}} = \kappa_{\text{out}}/\kappa$ is given by the cavity loss rate into the detection mode κ_{out} to the total cavity loss rate κ. This leads to the cavity outcoupled coherent emission of $\beta_{\text{out}} = \eta_{\text{out}}\beta_{\text{cav}}$, which is the upper bound of the photon detection efficiency after optical excitation p_{det} in experiments.

Color centers can also show a pure dephasing rate γ_{d} in addition to their lifetime-limited emitter linewidth γ. This dephasing is taken into account in the coherent cooperativity

$$C_{\text{coh}} = C\frac{\gamma}{\gamma'} = \frac{4g^2}{\kappa\gamma'}, \tag{2.13}$$

with the linewidth-broadened emitter decay rate $\gamma' = \gamma + \gamma_{\text{d}}$. The coherent cooperativity ultimately determines the fidelity of a protocol [54].

2.5 Spin-Photon and Remote Spin-Spin Entanglement Generation

The generation of spin-photon and remote spin-spin entanglement requires a coherent spin-photon interface. Depending on the specific spin-photon interface, there are multiple

schemes to generate spin-photon entanglement and different protocols to generate spin-spin entanglement [55]. With NV centers in solid immersion lenses, the spin-photon emission scheme has been used in two different remote entanglement protocols [49, 56]. More recently, a spin-photon projector scheme with SiV centers in nanophotonic crystal cavities has been used in two reflection-based remote entanglement protocols [57, 58].

In the spin-photon emission scheme, the spin qubit is first prepared in a superposition state

$$\sqrt{\alpha}\,|0\rangle + \sqrt{1-\alpha}\,|1\rangle, \tag{2.14}$$

with the population α of the $|0\rangle$ spin state. Then, spin-selective optical excitation is used to address the $|0\rangle$ state, to generate coherent photons that are entangled with the spin state. The spin-photon state after coherent photon emission equals

$$\sqrt{\alpha}\,|0\rangle|1\rangle_\gamma + \sqrt{1-\alpha}\,|1\rangle|0\rangle_\gamma, \tag{2.15}$$

where the photonic qubit is encoded in the presence ($|1\rangle_\gamma$) and absence ($|0\rangle_\gamma$) of a photon. Spin-photon states of this form are used in the single photon protocol for remote entanglement generation [59, 60] with typical α values of $\lesssim 0.1$ [48, 61]. In the case of the two photon protocol for remote entanglement generation [62] the qubit state is flipped after the first (early) excitation pulse and a second (late) excitation pulse is applied which ultimately encodes the photonic qubit in the early ($|e\rangle_\gamma$) and late ($|l\rangle_\gamma$) time-bin basis

$$\sqrt{\alpha}\,|1\rangle|e\rangle_\gamma + \sqrt{1-\alpha}\,|0\rangle|l\rangle_\gamma. \tag{2.16}$$

Using an equal superposition state with $\alpha = 0.5$ results in a maximally entangled spin-photon state as used for the two photon protocol [56].

In both remote entanglement protocols, the indistinguishable photonic qubits of each spin-photon state are interfered at a beam splitter to remove the 'which path' information, and subsequent photon detection click patterns at the two beam splitter output ports herald the spins in one of the entangled states

$$|\Psi^\pm\rangle = \frac{|0\rangle|1\rangle \pm e^{i\Delta\theta}|1\rangle|0\rangle}{\sqrt{2}}. \tag{2.17}$$

The $\pm$ sign depends on the detector click pattern and can be taken into account by local qubit operations after remote entanglement generation.

The two photon protocol heralds the entangled states with $\Delta\theta = 0$ and, in principle, with unity fidelity, and a success probability per attempt of $0.5p_{\mathrm{det}}^2$, where p_{det} is the photon detection efficiency after optical excitation for both quantum network nodes. In experiments, this results in remote entanglement rates of $\sim 1\,\mathrm{mHz}$ [56] and fidelities ~ 0.9 [63]. Compared to that, the single photon protocol heralds the entangled state with a $\Delta\theta$ that is determined by the optical phase difference of the interfering photonic qubits, and a fidelity of $1-\alpha$ with a success probability per attempt that scales with $2p_{\mathrm{det}}\alpha$. In experiments, optical phase stabilization routines are used to control $\Delta\theta$ to a known set point [49]. The single photon protocol achieves higher remote entanglement generation rates in the high loss regime ($p_{\mathrm{det}}^2 \ll p_{\mathrm{det}}$) at the expense of a fidelity decrease by α. This leads to rates of $\sim 10\,\mathrm{Hz}$ and fidelities ~ 0.8 [49, 61].

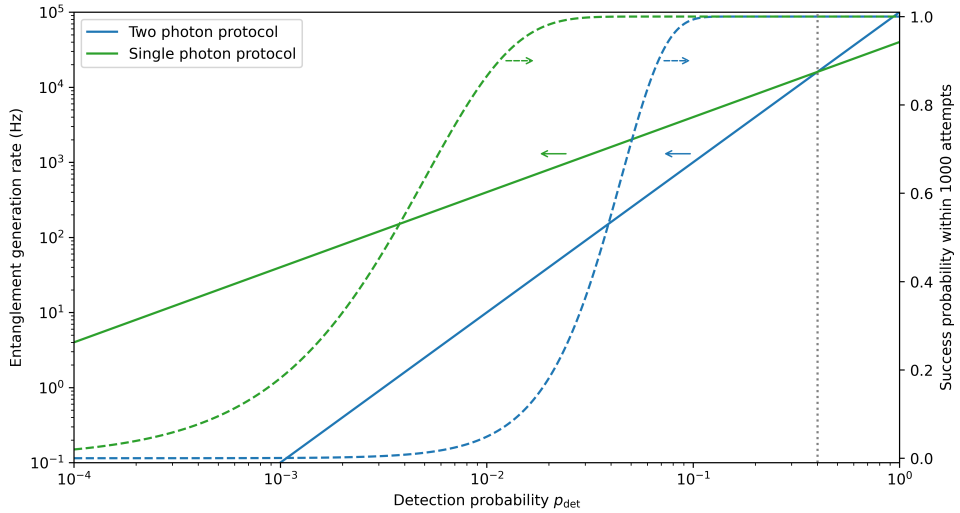

Figure 2.5: Comparing the remote entanglement generation of the two photon protocol (in blue) with the single photon protocol (in green), depending on the photon detection efficiency. The solid lines show the average remote entanglement generation rates for the single and two photon protocol, following $2\alpha p_{\text{det}}$ and $0.5 p_{\text{det}}^2$, respectively. A duration of 5 µs per entanglement attempt and $\alpha = 0.1$ is used. The dashed lines show the success probabilities for an implementation that performs at most 1000 remote entanglement generation attempts before starting over. The gray dotted line presents the threshold $p_{\text{det}} = 4\alpha$, from which on the two photon protocol outperforms the single photon protocol. The used system parameters are based on experimental values of state-of-the-art NV center quantum networks [48, 49, 61].

Figure 2.5 compares the single and two photon protocol for remote entanglement generation depending on the detection efficiency in a quantum network with realistic system parameters [48, 61]. State-of-the-art quantum network experiments with NV centers in solid immersion lenses achieve detection efficiencies of $\sim 5 \times 10^{-4}$ and employ the single photon protocol [48, 61]. To achieve similar remote entanglement rates with the two photon protocol, a detection efficiency of $\sim 2\,\%$ is needed, whereas the single photon protocol would already be capable of delivering an on average entangled state deterministically in 1000 generation attempts. This regime is reached for the two photon protocol only for detection efficiencies above $\sim 10\,\%$, and for $p_{\text{det}} > 4\alpha$ the two photon protocol outperforms the single photon protocol in the remote entanglement generation rate.

Moreover, Fig. 2.5 shows that for reported entanglement attempt durations of $\sim 5\,\mu s$ [49], remote entanglement generation rates are limited to a few kHz for a 10 dB photon loss. This is equivalent to optical fiber losses of $\sim 1\,km$ at the NV center emission wavelength [63] or $\sim 50\,km$ at a frequency-converted telecom wavelength [50] and further does not consider any additional communication times for distant quantum network nodes. Higher rates can be achieved by performing multiplexing with multiple qubits per quantum node.

For SiV centers in nanophotonic crystal cavities, two reflection-based protocols have been realized that use spin-dependent cavity reflection at both nodes to mediate entanglement generation in a serial [57] and a parallel [58] network configuration. In these

demonstrations, weak coherent states are used as photonic qubits and remote entangled states with fidelities ~ 0.8 at generation rates of $\sim 50\,\mathrm{mHz}$ [57] and $\sim 1\,\mathrm{Hz}$ [58] are achieved, respectively. These experiments establish the first quantum network demonstrations using cavity-enhanced diamond color centers and open up exciting avenues for exploring new types of remote entanglement generation protocols [55].

References

[1] M. W. Doherty, N. B. Manson, P. Delaney, F. Jelezko, J. Wrachtrup, and L. C. Hollenberg, *The nitrogen-vacancy colour centre in diamond,* Physics Reports **528**, 1 (2013).

[2] J. R. Maze, A. Gali, E. Togan, Y. Chu, A. Trifonov, E. Kaxiras, and M. D. Lukin, *Properties of nitrogen-vacancy centers in diamond: the group theoretic approach,* New Journal of Physics **13**, 025025 (2011).

[3] M. Ruf, *Cavity-enhanced quantum network nodes in diamond*, Ph.D. thesis, Delft University of Technology (2021).

[4] H. Bernien, *Control, measurement and entanglement of remote quantum spin registers in diamond*, Ph.D. thesis, Delft University of Technology (2014).

[5] W. Pfaff, *Quantum measurement and entanglement of spin quantum bits in diamond*, Ph.D. thesis, Delft University of Technology (2013).

[6] M. L. Goldman, A. Sipahigil, M. W. Doherty, N. Y. Yao, S. D. Bennett, M. Markham, D. J. Twitchen, N. B. Manson, A. Kubanek, and M. D. Lukin, *Phonon-Induced Population Dynamics and Intersystem Crossing in Nitrogen-Vacancy Centers,* Physical Review Letters **114**, 145502 (2015).

[7] M. L. Goldman, M. W. Doherty, A. Sipahigil, N. Y. Yao, S. D. Bennett, N. B. Manson, A. Kubanek, and M. D. Lukin, *State-selective intersystem crossing in nitrogen-vacancy centers,* Physical Review B **91**, 165201 (2015).

[8] P. Tamarat, T. Gaebel, J. R. Rabeau, M. Khan, A. D. Greentree, H. Wilson, L. C. L. Hollenberg, S. Prawer, P. Hemmer, F. Jelezko, and J. Wrachtrup, *Stark Shift Control of Single Optical Centers in Diamond,* Physical Review Letters **97**, 083002 (2006).

[9] L. C. Bassett, F. J. Heremans, C. G. Yale, B. B. Buckley, and D. D. Awschalom, *Electrical Tuning of Single Nitrogen-Vacancy Center Optical Transitions Enhanced by Photoinduced Fields,* Physical Review Letters **107**, 266403 (2011).

[10] N. Kalb, *Diamond-based quantum networks with multi-qubit nodes*, Ph.D. thesis, Delft University of Technology (2018).

[11] D. Riedel, I. Söllner, B. J. Shields, S. Starosielec, P. Appel, E. Neu, P. Maletinsky, and R. J. Warburton, *Deterministic Enhancement of Coherent Photon Generation from a Nitrogen-Vacancy Center in Ultrapure Diamond,* Physical Review X **7**, 031040 (2017).

[12] K.-M. C. Fu, C. Santori, P. E. Barclay, L. J. Rogers, N. B. Manson, and R. G. Beausoleil, *Observation of the Dynamic Jahn-Teller Effect in the Excited States of Nitrogen-Vacancy Centers in Diamond,* Physical Review Letters **103**, 256404 (2009).

[13] L. Childress, M. V. Gurudev Dutt, J. M. Taylor, A. S. Zibrov, F. Jelezko, J. Wrachtrup, P. R. Hemmer, and M. D. Lukin, *Coherent Dynamics of Coupled Electron and Nuclear Spin Qubits in Diamond,* Science **314**, 281 (2006).

[14] C. Wang, C. Kurtsiefer, H. Weinfurter, and B. Burchard, *Single photon emission from SiV centres in diamond produced by ion implantation,* Journal of Physics B: Atomic, Molecular and Optical Physics **39**, 37 (2005).

[15] E. Neu, D. Steinmetz, J. Riedrich-Möller, S. Gsell, M. Fischer, M. Schreck, and C. Becher, *Single photon emission from silicon-vacancy colour centres in chemical vapour deposition nano-diamonds on iridium,* New Journal of Physics **13**, 025012 (2011).

[16] L. Rogers, K. Jahnke, T. Teraji, L. Marseglia, C. Müller, B. Naydenov, H. Schauffert, C. Kranz, J. Isoya, L. McGuinness, and F. Jelezko, *Multiple intrinsically identical single-photon emitters in the solid state,* Nature Communications **5**, 4739 (2014).

[17] L. J. Rogers, K. D. Jahnke, M. W. Doherty, A. Dietrich, L. P. McGuinness, C. Müller, T. Teraji, H. Sumiya, J. Isoya, N. B. Manson, and F. Jelezko, *Electronic structure of the negatively charged silicon-vacancy center in diamond,* Physical Review B **89**, 235101 (2014).

[18] E. A. Ekimov, S. G. Lyapin, K. N. Boldyrev, M. V. Kondrin, R. Khmelnitskiy, V. A. Gavva, T. V. Kotereva, and M. N. Popova, *Germanium–vacancy color center in isotopically enriched diamonds synthesized at high pressures,* JETP Letters **102**, 701 (2015).

[19] Y. N. Palyanov, I. N. Kupriyanov, Y. M. Borzdov, and N. V. Surovtsev, *Germanium: a new catalyst for diamond synthesis and a new optically active impurity in diamond,* Scientific Reports **5**, 14789 (2015).

[20] P. Siyushev, M. H. Metsch, A. Ijaz, J. M. Binder, M. K. Bhaskar, D. D. Sukachev, A. Sipahigil, R. E. Evans, C. T. Nguyen, M. D. Lukin, P. R. Hemmer, Y. N. Palyanov, I. N. Kupriyanov, Y. M. Borzdov, L. J. Rogers, and F. Jelezko, *Optical and microwave control of germanium-vacancy center spins in diamond,* Physical Review B **96**, 081201 (2017).

[21] T. Iwasaki, Y. Miyamoto, T. Taniguchi, P. Siyushev, M. H. Metsch, F. Jelezko, and M. Hatano, *Tin-Vacancy Quantum Emitters in Diamond,* Physical Review Letters **119**, 253601 (2017).

[22] S. D. Tchernij, T. Herzig, J. Forneris, J. Küpper, S. Pezzagna, P. Traina, E. Moreva, I. P. Degiovanni, G. Brida, N. Skukan, M. Genovese, M. Jakšić, J. Meijer, and P. Olivero, *Single-Photon-Emitting Optical Centers in Diamond Fabricated upon Sn Implantation,* ACS Photonics **4**, 2580 (2017).

[23] A. E. Rugar, C. Dory, S. Sun, and J. Vučković, *Characterization of optical and spin properties of single tin-vacancy centers in diamond nanopillars,* Physical Review B **99**, 205417 (2019).

[24] J. Görlitz, D. Herrmann, G. Thiering, P. Fuchs, M. Gandil, T. Iwasaki, T. Taniguchi, M. Kieschnick, J. Meijer, M. Hatano, A. Gali, and C. Becher, *Spectroscopic investigations of negatively charged tin-vacancy centres in diamond,* New Journal of Physics **22**, 013048 (2020).

[25] P. Wang, T. Taniguchi, Y. Miyamoto, M. Hatano, and T. Iwasaki, *Low-Temperature Spectroscopic Investigation of Lead-Vacancy Centers in Diamond Fabricated by High-Pressure and High-Temperature Treatment,* ACS Photonics **8**, 2947 (2021).

[26] S. Ditalia Tchernij, T. Lühmann, T. Herzig, J. Küpper, A. Damin, S. Santonocito, M. Signorile, P. Traina, E. Moreva, F. Celegato, S. Pezzagna, I. P. Degiovanni, P. Olivero, M. Jakšić, J. Meijer, P. M. Genovese, and J. Forneris, *Single-Photon Emitters in Lead-Implanted Single-Crystal Diamond,* ACS Photonics **5**, 4864 (2018).

[27] P. Wang, L. Kazak, K. Senkalla, P. Siyushev, R. Abe, T. Taniguchi, S. Onoda, H. Kato, T. Makino, M. Hatano, F. Jelezko, and T. Iwasaki, *Transform-Limited Photon Emission from a Lead-Vacancy Center in Diamond above 10 K,* Physical Review Letters **132**, 073601 (2024).

[28] C. Hepp, *Electronic Structure of the Silicon Vacancy Color Center in Diamond*, Ph.D. thesis, Universität des Saarlandes (2014).

[29] G. Thiering and A. Gali, *Ab Initio Magneto-Optical Spectrum of Group-IV Vacancy Color Centers in Diamond,* Physical Review X **8**, 021063 (2018).

[30] A. E. Rugar, C. Dory, S. Aghaeimeibodi, H. Lu, S. Sun, S. D. Mishra, Z.-X. Shen, N. A. Melosh, and J. Vučković, *Narrow-Linewidth Tin-Vacancy Centers in a Diamond Waveguide,* ACS Photonics **7**, 2356 (2020).

[31] M. E. Trusheim, B. Pingault, N. H. Wan, M. Gündoğan, L. De Santis, R. Debroux, D. Gangloff, C. Purser, K. C. Chen, M. Walsh, J. J. Rose, J. N. Becker, B. Lienhard, E. Bersin, I. Paradeisanos, G. Wang, D. Lyzwa, A. R.-P. Montblanch, G. Malladi, H. Bakhru, A. C. Ferrari, I. A. Walmsley, M. Atatüre, and D. Englund, *Transform-Limited Photons From a Coherent Tin-Vacancy Spin in Diamond,* Physical Review Letters **124**, 023602 (2020).

[32] Y. Herrmann, *Good Vibrations: A Microcavity-based Diamond Spin-Photon Interface for Quantum Networking*, Ph.D. thesis, Delft University of Technology (2025).

[33] S. Meesala, Y.-I. Sohn, B. Pingault, L. Shao, H. A. Atikian, J. Holzgrafe, M. Gundogan, C. Stavrakas, A. Sipahigil, C. Chia, R. Evans, M. J. Burek, M. Zhang, L. Wu, J. L. Pacheco, J. Abraham, E. Bielejec, M. D. Lukin, M. Atatüre, and M. Lončar, *Strain engineering of the silicon-vacancy center in diamond,* Physical Review B **97**, 205444 (2018).

[34] K. D. Jahnke, A. Sipahigil, J. M. Binder, M. W. Doherty, M. Metsch, L. J. Rogers, N. B. Manson, M. D. Lukin, and F. Jelezko, *Electron–phonon processes of the silicon-vacancy centre in diamond,* New Journal of Physics **17**, 043011 (2015).

[35] G. Pieplow, M. Belhassen, and T. Schröder, *Efficient microwave spin control of negatively charged group-IV color centers in diamond,* Physical Review B **109**, 115409 (2024).

[36] J. M. Brevoord, L. G. C. Wienhoven, N. Codreanu, T. Ishiguro, E. van Leeuwen, M. Iuliano, L. De Santis, C. Waas, H. K. C. Beukers, T. Turan, C. Errando-Herranz,

K. Kawaguchi, and R. Hanson, *Large-range tuning and stabilization of the optical transition of diamond tin-vacancy centers by in situ strain control,* Applied Physics Letters **126**, 174001 (2025).

[37] E. I. Rosenthal, C. P. Anderson, H. C. Kleidermacher, A. J. Stein, H. Lee, J. Grzesik, G. Scuri, A. E. Rugar, D. Riedel, S. Aghaeimeibodi, G. H. Ahn, K. Van Gasse, and J. Vučković, *Microwave Spin Control of a Tin-Vacancy Qubit in Diamond,* Physical Review X **13**, 031022 (2023).

[38] Y. Herrmann, J. Fischer, J. M. Brevoord, C. Sauerzapf, L. G. C. Wienhoven, L. J. Feije, M. Pasini, M. Eschen, M. Ruf, M. J. Weaver, and R. Hanson, *Coherent Coupling of a Diamond Tin-Vacancy Center to a Tunable Open Microcavity,* Physical Review X **14**, 041013 (2024).

[39] H. Beukers, *Quantum Networks with Diamond Color Centers: Local Control and Multi-Node Entanglement*, Ph.D. thesis, Delft University of Technology (2025).

[40] X. Guo, A. M. Stramma, Z. Li, W. G. Roth, B. Huang, Y. Jin, R. A. Parker, J. Arjona Martínez, N. Shofer, C. P. Michaels, C. P. Purser, M. H. Appel, E. M. Alexeev, T. Liu, A. C. Ferrari, D. D. Awschalom, N. Delegan, B. Pingault, G. Galli, F. J. Heremans, M. Atatüre, and A. A. High, *Microwave-Based Quantum Control and Coherence Protection of Tin-Vacancy Spin Qubits in a Strain-Tuned Diamond-Membrane Heterostructure,* Physical Review X **13**, 041037 (2023).

[41] M. H. Abobeih, J. Cramer, M. A. Bakker, N. Kalb, M. Markham, D. J. Twitchen, and T. H. Taminiau, *One-second coherence for a single electron spin coupled to a multi-qubit nuclear-spin environment,* Nature Communications **9**, 2552 (2018).

[42] H. Bartling, J. Yun, K. Schymik, M. Van Riggelen, L. Enthoven, H. Van Ommen, M. Babaie, F. Sebastiano, M. Markham, D. Twitchen, and T. Taminiau, *Universal high-fidelity quantum gates for spin qubits in diamond,* Physical Review Applied **23**, 034052 (2025).

[43] C. E. Bradley, J. Randall, M. H. Abobeih, R. C. Berrevoets, M. J. Degen, M. A. Bakker, M. Markham, D. J. Twitchen, and T. H. Taminiau, *A Ten-Qubit Solid-State Spin Register with Quantum Memory up to One Minute,* Physical Review X **9**, 031045 (2019).

[44] G. L. Van De Stolpe, D. P. Kwiatkowski, C. E. Bradley, J. Randall, M. H. Abobeih, S. A. Breitweiser, L. C. Bassett, M. Markham, D. J. Twitchen, and T. H. Taminiau, *Mapping a 50-spin-qubit network through correlated sensing,* Nature Communications **15**, 2006 (2024).

[45] I. Karapatzakis, J. Resch, M. Schrodin, P. Fuchs, M. Kieschnick, J. Heupel, L. Kussi, C. Sürgers, C. Popov, J. Meijer, C. Becher, W. Wernsdorfer, and D. Hunger, *Microwave Control of the Tin-Vacancy Spin Qubit in Diamond with a Superconducting Waveguide,* Physical Review X **14**, 031036 (2024).

[46] E. I. Rosenthal, S. Biswas, G. Scuri, H. Lee, A. J. Stein, H. C. Kleidermacher, J. Grzesik, A. E. Rugar, S. Aghaeimeibodi, D. Riedel, M. Titze, E. S. Bielejec, J. Choi, C. P. Anderson,

and J. Vučković, *Single-Shot Readout and Weak Measurement of a Tin-Vacancy Qubit in Diamond,* Physical Review X **14**, 041008 (2024).

[47] H. K. C. Beukers, C. Waas, M. Pasini, H. B. Van Ommen, Z. Ademi, M. Iuliano, N. Codreanu, J. M. Brevoord, T. Turan, T. H. Taminiau, and R. Hanson, *Control of Solid-State Nuclear Spin Qubits Using an Electron Spin- 1 / 2,* Physical Review X **15**, 021011 (2025).

[48] S. L. N. Hermans, M. Pompili, H. K. C. Beukers, S. Baier, J. Borregaard, and R. Hanson, *Qubit teleportation between non-neighbouring nodes in a quantum network,* Nature **605**, 663 (2022).

[49] P. C. Humphreys, N. Kalb, J. P. J. Morits, R. N. Schouten, R. F. L. Vermeulen, D. J. Twitchen, M. Markham, and R. Hanson, *Deterministic delivery of remote entanglement on a quantum network,* Nature **558**, 268 (2018).

[50] A. J. Stolk, K. L. Van Der Enden, M.-C. Slater, I. Te Raa-Derckx, P. Botma, J. Van Rantwijk, J. J. B. Biemond, R. A. J. Hagen, R. W. Herfst, W. D. Koek, A. J. H. Meskers, R. Vollmer, E. J. Van Zwet, M. Markham, A. M. Edmonds, J. F. Geus, F. Elsen, B. Jungbluth, C. Haefner, C. Tresp, J. Stuhler, S. Ritter, and R. Hanson, *Metropolitan-scale heralded entanglement of solid-state qubits,* Science Advances **10**, eadp6442 (2024).

[51] E. M. Purcell, *Spontaneous emission probabilities at radio frequencies,* Physical Review **69**, 674 (1946).

[52] E. Fermi, *Quantum Theory of Radiation,* Reviews of Modern Physics **4**, 87 (1932).

[53] M. Fox, *Quantum optics: an introduction*, Oxford master series in physics No. 15 (Oxford University Press, Oxford, New York, 2006).

[54] J. Borregaard, A. S. Sørensen, and P. Lodahl, *Quantum Networks with Deterministic Spin–Photon Interfaces,* Advanced Quantum Technologies **2**, 1800091 (2019).

[55] H. K. Beukers, M. Pasini, H. Choi, D. Englund, R. Hanson, and J. Borregaard, *Remote-Entanglement Protocols for Stationary Qubits with Photonic Interfaces,* PRX Quantum **5**, 010202 (2024).

[56] H. Bernien, B. Hensen, W. Pfaff, G. Koolstra, M. S. Blok, L. Robledo, T. H. Taminiau, M. Markham, D. J. Twitchen, L. Childress, and R. Hanson, *Heralded entanglement between solid-state qubits separated by three metres,* Nature **497**, 86 (2013).

[57] C. M. Knaut, A. Suleymanzade, Y.-C. Wei, D. R. Assumpcao, P.-J. Stas, Y. Q. Huan, B. Machielse, E. N. Knall, M. Sutula, G. Baranes, N. Sinclair, C. De-Eknamkul, D. S. Levonian, M. K. Bhaskar, H. Park, M. Lončar, and M. D. Lukin, *Entanglement of nanophotonic quantum memory nodes in a telecom network,* Nature **629**, 573 (2024).

[58] P.-J. Stas, Y.-C. Wei, M. Sirotin, Y. Q. Huan, U. Yazlar, F. A. Arias, E. Knyazev, G. Baranes, B. Machielse, S. Grandi, D. Riedel, J. Borregaard, H. Park, M. Lončar, A. Suleymanzade, and M. D. Lukin, *Entanglement Assisted Non-local Optical Interferometry in a Quantum Network,* arXiv:2509.09464 (2025), https://arxiv.org/abs/2509.09464.

[59] C. Cabrillo, J. I. Cirac, P. García-Fernández, and P. Zoller, *Creation of entangled states of distant atoms by interference,* Physical Review A **59**, 1025 (1999).

[60] S. Bose, P. L. Knight, M. B. Plenio, and V. Vedral, *Proposal for Teleportation of an Atomic State via Cavity Decay,* Physical Review Letters **83**, 5158 (1999).

[61] M. Pompili, S. L. N. Hermans, S. Baier, H. K. C. Beukers, P. C. Humphreys, R. N. Schouten, R. F. L. Vermeulen, M. J. Tiggelman, L. dos Santos Martins, B. Dirkse, S. Wehner, and R. Hanson, *Realization of a multinode quantum network of remote solid-state qubits,* Science **372**, 259 (2021).

[62] S. D. Barrett and P. Kok, *Efficient high-fidelity quantum computation using matter qubits and linear optics,* Physical Review A **71**, 060310 (2005).

[63] B. Hensen, H. Bernien, A. E. Dréau, A. Reiserer, N. Kalb, M. S. Blok, J. Ruitenberg, R. F. L. Vermeulen, R. N. Schouten, C. Abellán, W. Amaya, V. Pruneri, M. W. Mitchell, M. Markham, D. J. Twitchen, D. Elkouss, S. Wehner, T. H. Taminiau, and R. Hanson, *Loophole-free Bell inequality violation using electron spins separated by 1.3 kilometres,* Nature **526**, 682 (2015).

3

A Theoretical Introduction to Diamond-Air Microcavities for Quantum Networks

The open microcavity platform is a promising approach to equip diamond color centers with efficient spin-photon interfaces for next-generation quantum network nodes. We use a one-dimensional transfer matrix model to study the properties of dielectric cavity mirrors and complete diamond-air microcavity systems. The different hybrid modes of the diamond-air cavity are outlined, and an analytical model of the Purcell enhancement with its susceptibility to cavity length fluctuations is derived. This enables the optimization of cavity parameters to maximize the Purcell factor and the cavity outcoupled zero-phonon line emission for diamond nitrogen-vacancy and tin-vacancy centers. Finally, the optical interfacing of microcavity-coupled color centers is discussed, and methods for resonant optical spin qubit readout are presented.

3.1 Introduction

The open microcavity platform has been used at cryogenic temperatures to Purcell-enhance the diamond nitrogen-vacancy (NV) center [1–3] as well as various diamond group IV color centers, like the silicon-vacancy (SiV) [4, 5], the germanium-vacancy (GeV) [6] and the tin-vacancy (SnV) center [7, 8]. The color centers can be integrated into the microcavity by micrometer-thin diamond membranes that are bonded to one of the cavity mirrors. This leads to hybridized cavity modes arising from a diamond part and an air gap between the two cavity mirrors [9]. To describe these cavity modes and their Purcell effect on color centers under experimental conditions, a detailed theoretical model is needed.

In this work, we derive an analytical expression for the Purcell factor of diamond-air microcavities and optimize cavity parameters for next-generation quantum network nodes with NV and SnV centers. Therefore, we consider a hemispherical plano-concave cavity geometry, consisting of a flat sample mirror with a bonded diamond membrane that faces a spherical fiber mirror. The used dielectric mirror coating parameters are designed for the NV center ZPL wavelength of 637 nm, which also serves as the reference for the refractive indices of the coating material. The cavity materials exhibit negligible absorption at this wavelength, and their refractive indices are 1.45 for fused silica, 1.48 for silicon dioxide, 2.10 for tantalum pentoxide, $n_d = 2.41$ for diamond, and $n_a = 1$ for air (vacuum). Since the SnV center ZPL wavelength of 619 nm is close to that of the NV center, the optimized cavity parameters for the NV center are used for the calculations with SnV centers as well.

3.2 Dielectric Mirrors and Bonded Diamond Membranes

The microcavity is built with highly reflective dielectric mirrors that are fabricated on fused silica substrates. For the spherical mirrors, cleaved optical fibers, and for the flat sample mirrors, wafers can be used. These substrates are coated with alternating layers of silicon dioxide and tantalum pentoxide, forming a Bragg mirror. All mirrors terminate with a tantalum pentoxide layer as the high refractive index material, and an anti-reflection coating is applied to the opposite surface of the sample mirror (not shown here). The fiber mirror shown in Fig. 3.1 (a) consists of quarter wavelength layers, whereas the sample mirror shown in Fig. 3.1 (c) uses quarter wavelength and three-quarter wavelength layers to realize a narrower stopband. Further, we consider the sample mirror to be terminated with diamond.

The optical properties of the dielectric mirrors are derived from electric field simulations based on a one-dimensional transfer matrix model [9–11]. In this formalism, the electric field $E = E^+ + E^-$ of a monochromatic plane wave is split into a forward E^+ and a backward E^- field describing the co-propagating and the counter-propagating component, respectively. These fields are translated along a propagation axis using matrices (see Appendix 3.8.1 for matrix definitions). By performing incremental propagation steps, the electric field $E(z) = E^+(z) + E^-(z)$ along the propagation axis z is calculated. The linear polarization $\hat{e}$ of the electric field is transverse with respect to the propagation axis ($\hat{e} \cdot \hat{z} = 0$). Further, we assume a harmonic time-dependence, leading to the position and time-dependent electric field $\hat{E}(z,t) = E(z)\hat{e}\exp(i\omega t)$ with angular frequency ω of the monochromatic plane wave. In addition, the magnetic field $\hat{B}(z,t) = (E^+(z) - E^-(z))(\hat{z} \times \hat{e})\exp(i\omega t)/c$ is directly linked

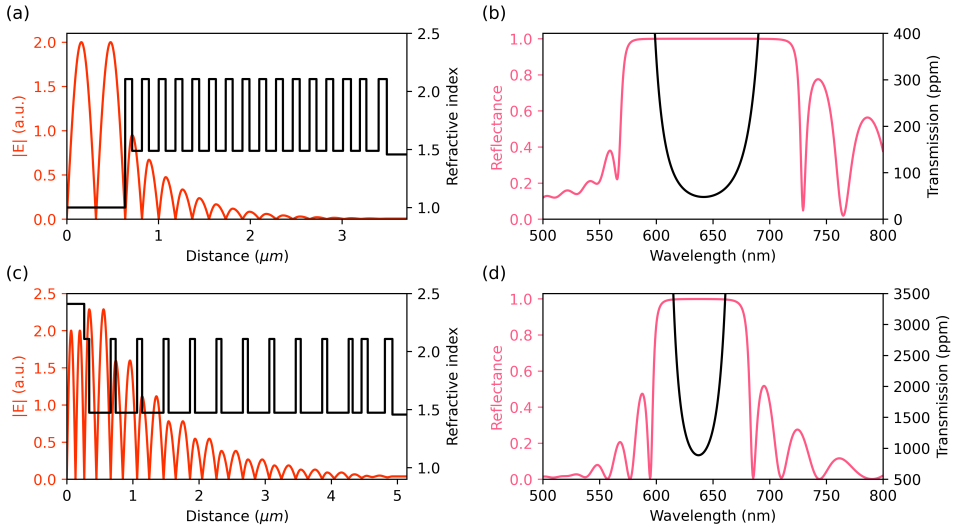

Figure 3.1: Simulations of the dielectric fiber and sample mirror using a one-dimensional transfer matrix model. (a) and (c) Refractive index mirror layers (solid black line) and corresponding electric field distribution (solid red line) for an incident monochromatic plane wave from the left side with wavelength $\lambda_0 = 637\,\text{nm}$ for the air-terminated fiber and diamond-terminated sample mirror. The rightmost layer resembles the fused silica substrate, and the leftmost layer is air or diamond, respectively. (b) and (d) Mirror reflectance (solid pink line) and transmission (solid black line) depending on the wavelength for the air-terminated fiber and diamond-terminated sample mirror. The mirror coating designs are developed by Laseroptik.

to the electric field and the physically observable fields are given by their corresponding real parts. In the following, we make use of subscripts x that reference the variable to the corresponding part of the refractive index n_x. A general optical system expressed by its transfer matrix M relates the electric field to its right (material with refractive index n_r) to its left (material with refractive index n_l) by

$$\begin{pmatrix} E_l^+ \\ E_l^- \end{pmatrix} = \begin{pmatrix} M_{0,0} & M_{0,1} \\ M_{1,0} & M_{1,1} \end{pmatrix} \begin{pmatrix} E_r^+ \\ E_r^- \end{pmatrix}. \tag{3.1}$$

We solve these electric field equations for the case that there is no incident electric field from the right side ($E_r^- = 0$). Figure 3.1 (a) and (c) show the simulated electric field distribution $|E(z)|$ of the mirrors for an incident monochromatic plane wave from the left side with a wavelength of $\lambda_0 = 637\,\text{nm}$ forming a standing wave. Based on the calculated electric fields, the mirror transmission T and reflectance R are calculated by

$$T = \frac{\text{Transmitted Power}}{\text{Incident Power}} = \frac{n_r |E_r^+|^2}{n_l |E_l^+|^2} = \frac{n_r}{n_l |M_{0,0}|^2} = \mathcal{L}_{M,l}, \tag{3.2}$$

$$R = \frac{\text{Reflected Power}}{\text{Incident Power}} = \frac{|E_l^-|^2}{|E_l^+|^2} = \frac{|M_{1,0}|^2}{|M_{0,0}|^2}. \tag{3.3}$$

Figure 3.1 (b) and (d) show the mirror reflectance depending on the wavelength of the incident plane wave. Both mirrors exhibit a stopband centered at $\lambda_0 = 637\,\text{nm}$ with a

transmission of $\mathcal{L}_{M,a} = 48\,\text{ppm}$ and $\mathcal{L}_{M,d} = 888\,\text{ppm}$ for the air-terminated fiber mirror and diamond-terminated sample mirror, respectively.

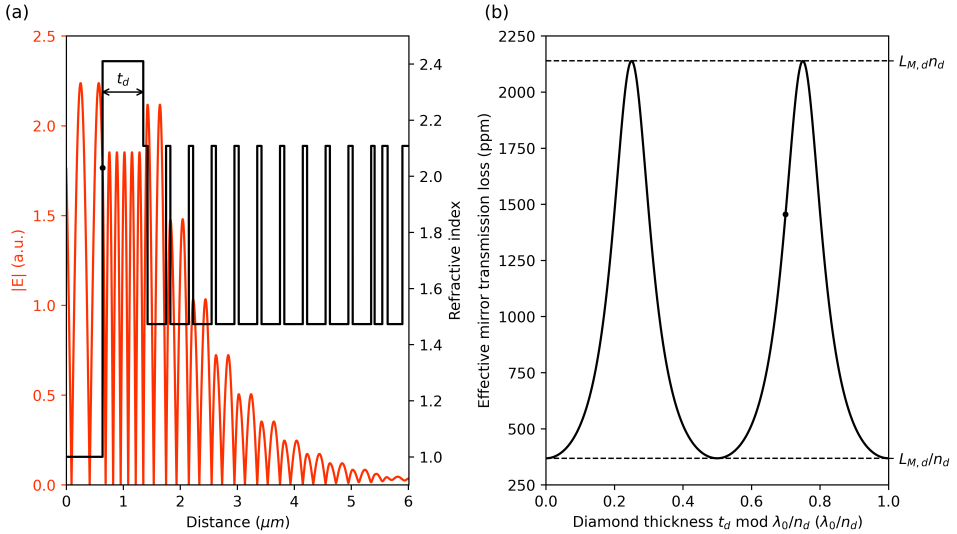

Figure 3.2: (a) Refractive index mirror layers (solid black line) and corresponding electric field distribution (solid red line) for an incident monochromatic plane wave from the left side with wavelength $\lambda_0 = 637\,\text{nm}$ of the sample mirror with a bonded diamond membrane. (b) Effective mirror transmission loss of the sample mirror as a function of the thickness of the bonded diamond membrane. The transmission of the sample mirror with diamond termination is $\mathcal{L}_{M,d} = 888\,\text{ppm}$ at $\lambda_0 = 637\,\text{nm}$. The black dot presents the effective mirror loss for the shown diamond thickness in (a) with the corresponding electric field at the air-diamond interface.

In the following, we study the influence of the bonded diamond sample on the optical properties of the mirror. First, the mirror transmission at a wavelength of $\lambda_0 = 637\,\text{nm}$ is investigated as a function of the thickness of the diamond sample. For that, the transition of the electric field at the air-diamond interface is of interest because it determines the transmission loss ultimately (see Fig. 3.2). The electric field intensity ratio between the air and the diamond part is given by

$$\frac{n_a|E_a^+|^2}{n_d|E_d^+|^2} = \frac{n_a|E_a^-|^2}{n_d|E_d^-|^2} = \frac{n_a|E_{\max,a}|^2}{n_d|E_{\max,d}|^2} = \frac{n_a}{n_d}\sin^2\left(\frac{2\pi n_d t_d}{\lambda_0}\right) + \frac{n_d}{n_a}\cos^2\left(\frac{2\pi n_d t_d}{\lambda_0}\right) = \alpha, \tag{3.4}$$

with the electric field E_a in air, E_d in diamond and the diamond thickness t_d (see Appendix 3.8.1 for the derivation). Together with equation (3.2), the effective mirror transmission loss is derived as

$$\frac{n_r|E_r^+|^2}{n_a|E_a^+|^2} = \frac{n_r|E_r^+|^2}{n_d|E_d^+|^2}\frac{n_d|E_d^+|^2}{n_a|E_a^+|^2} = \frac{\mathcal{L}_{M,d}}{\alpha}, \tag{3.5}$$

which shows the modulation of the mirror transmission $\mathcal{L}_{M,d}$ with the electric field intensity ratio α. As outlined in more detail in section 3.3, the effective mirror transmission loss with its diamond thickness dependence leads to a variation in the cavity finesse of diamond-air microcavities.

Moreover, the effects of the transmission loss modulations can be observed under a light microscope when broadband optical illumination is taken into account. We simulate the wavelength-dependent reflectance of the mirror-bonded diamond and convert it into an observable color using an illuminant spectrum. Figure 3.3 (a) shows the observable color depending on the thickness of the diamond. The color variations are substantial for diamond thicknesses below ~ 600 nm and fade to a uniform lighter color for larger diamond thicknesses.

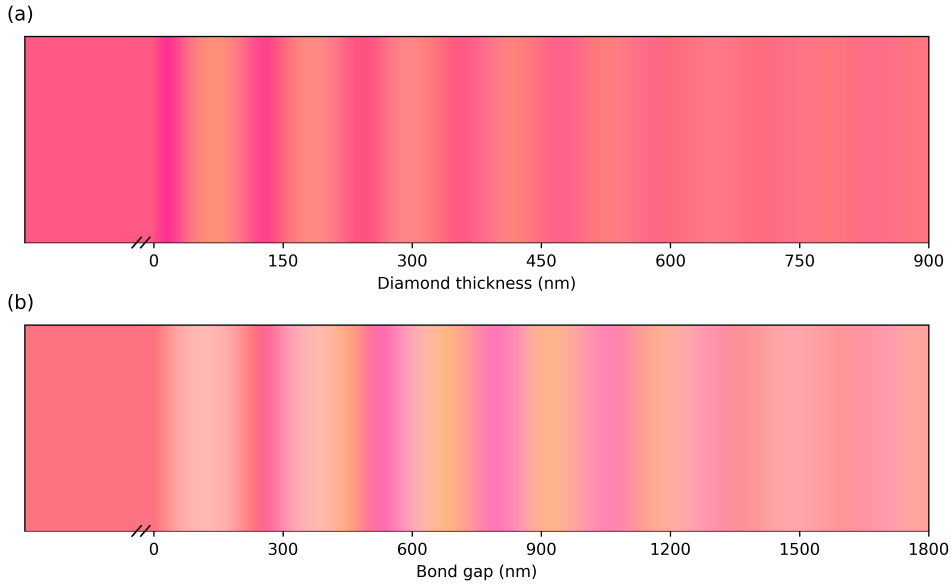

Figure 3.3: Simulated observable color of the sample mirror with bonded diamond membrane under broadband optical illumination. (a) Observable color depending on the thickness of the diamond membrane. (b) Observable color depending on the bond gap between the sample mirror and a 3.7 µm thick diamond membrane. For these simulations, the standard daylight illuminant D50 is used.

Furthermore, ill-bonded membranes can exhibit bond gaps between the mirror surface and the diamond, which cause interference patterns known as Newton rings [12]. Analogous to the diamond thickness-dependent color, we simulate the observable color as a function of the bond gap between the diamond membrane and the mirror. Figure 3.3 (b) shows the bond gap dependent color for a diamond with a thickness of 3.7 µm.

Note that the color variations simulated in Fig. 3.3 (a) and (b) do not follow a periodic oscillation with $\lambda_0/2n_d$ nor $\lambda_0/2n_a$ ($\lambda_0 = 637$ nm) for the diamond thickness and bond gap, respectively. This is a result of mirror-specific broadband interference and must be considered when interpreting light microscope images.

3.3 Diamond-Air Microcavity

A Fabry-Pérot microcavity is formed by placing the fiber mirror opposite to the sample mirror and adjusting the emerging air gap such that the cavity is on resonance with a

specific wavelength within the mirror stopbands. Figure 3.4 (a) and (c) show the electric field simulations at a wavelength of $\lambda_0 = 637\,\text{nm}$ for two particular diamond thicknesses, which cause a so-called air-like mode and diamond-like mode with an electric field node and antinode at the air-diamond interface, respectively.

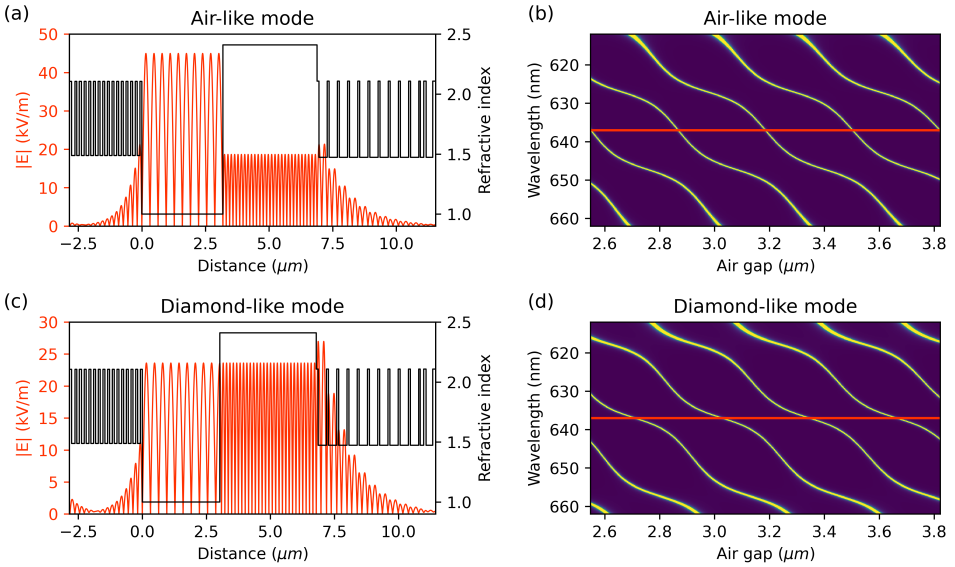

Figure 3.4: Simulations of the open microcavity using a one-dimensional transfer matrix model. (a) and (c) Refractive index mirror layers (solid black line) and corresponding electric field distribution (solid red line) for an incident monochromatic plane wave from the left side with wavelength $\lambda_0 = 637\,\text{nm}$ of a microcavity with an air-like mode and a diamond-like mode, respectively. The diamond membrane thickness is about 3.7 µm. The shown electric field distribution resembles the rms vacuum electric field amplitude, obtained by normalizing the stored cavity energy to the vacuum energy $h\nu/2$. (b) and (d) Open microcavity mode dispersion simulated as the cavity transmission depending on the air gap under broadband optical illumination for the cavity presented in (a) and (c), respectively. The horizontal red line represents the cavity resonance wavelength of $\lambda_0 = 637\,\text{nm}$.

The air-like and diamond-like modes are two special cases of the diamond-air hybrid cavity mode that obey the following resonance conditions [13]

$$t_d = m_d \frac{\lambda_0}{2n_d} \quad \text{and} \quad t_a = m_a \frac{\lambda_0}{2n_a} \quad \text{(air-like mode)}, \tag{3.6}$$

$$t_d = (2m_d - 1)\frac{\lambda_0}{4n_d} \quad \text{and} \quad t_a = (2m_a - 1)\frac{\lambda_0}{4n_a} \quad \text{(diamond-like mode)}, \tag{3.7}$$

with the positive integer numbers m_d and m_a defining the hybrid cavity mode number $m = m_d + m_a$. The electric field intensity ratio α simplifies to n_d/n_a for air-like modes and n_a/n_d for diamond-like modes. In general, for any diamond thickness and wavelength, the air gap can be adjusted to form a resonance mode. Figure 3.4 (b) and (d) show the corresponding simulated mode dispersions depending on the air gap. Air-like and diamond-like modes are identified by regions of steepest and flattest slope, respectively. Moreover,

the mode dispersion can be measured experimentally and allows for determining the diamond thickness and air gap of a hybrid microcavity via an analytical fit [9, 11].

For every wavelength and microcavity geometry, the two main cavity parameters, namely the mode volume V_x and the cavity loss rate $\kappa = 2\pi\nu/Q$, with the cavity resonance frequency $\nu = c/\lambda_0$ and the cavity quality factor Q, must be calculated to determine the Purcell factor. The mode volume is calculated as the volume integral of the normalized electric field energy density in the cavity. For the considered hemispherical plano-concave cavity geometry, the integral splits into the mode field area of the Gaussian cavity beam in the lateral dimensions multiplied by the integral over the normalized cavity electric field energy distribution in the vertical direction. Hence, the cavity mode volume is calculated by [11]

$$V_x = \frac{\pi w_0^2}{2} \frac{\int_{\text{cav}} \epsilon(z)|E(z)|^2 \,\mathrm{d}z}{\epsilon_x |E_{\text{max},x}|^2} = \frac{\pi w_0^2}{4} L_{\text{eff},x}, \tag{3.8}$$

with the permittivity $\epsilon(z) = \epsilon_0 n(z)^2$, the cavity beam waist w_0 and the maximum electric field $|E_{\text{max},x}| = \max(|E(z)|)$ for all z in the considered cavity part of refractive index n_x. Finally, this results in the definition of the effective cavity length $L_{\text{eff},x}$. Typically, the maximum electric field is chosen in the cavity part hosting the quantum emitter, as this defines the cavity mode volume used for the Purcell factor [11]. This is the diamond part of the cavity for diamond color centers. For now, we normalize to the air gap, as this provides insights into the cavity air gap dependence later. By definition, the effective cavity length normalized to the air gap compared to the diamond part relates by $L_{\text{eff},a}/L_{\text{eff},d} = n_d/n_a\alpha$ with the electric field intensity ratio of equation (3.4). Next, the cavity loss rate $\kappa = P_{\text{loss}}/E_{\text{cav}}$ describing the exponential energy decay of the cavity field is calculated by the ratio of power P_{loss} leaving the cavity and its stored energy E_{cav}. The stored energy of a microcavity is calculated by

$$E_{\text{cav}} = \frac{\pi w_0^2}{2} \int_{\text{cav}} \epsilon(z)|E(z)|^2 \,\mathrm{d}z = \frac{\pi w_0^2}{4} L_{\text{eff},a} \epsilon_a |E_{\text{max},a}|^2 = V_a \epsilon_a |E_{\text{max},a}|^2, \tag{3.9}$$

where the energy is equally stored in the electric and magnetic cavity field, which leads to the interpretation of $|E(z)|$ and $|E_{\text{max},a}|$ as root mean square (rms) electric field amplitudes. The power P_{loss} is determined by the carried energy of the Gaussian beams leaving the cavity on both cavity sides, which is described by the mode field area multiplied by their time-averaged Poynting vectors [10]. This leads to

$$P_{\text{loss}} = \frac{\pi w_0^2}{2} \left(\frac{c\epsilon_l}{2n_l} |E_l^-|^2 + \frac{c\epsilon_r}{2n_r} |E_r^+|^2 \right), \tag{3.10}$$

$$P_{\text{loss}} = \frac{\pi w_0^2}{2} \left(\frac{c\epsilon_l}{2n_l} \frac{n_a}{n_l} \frac{n_l |E_l^-|^2}{n_a |E_a^-|^2} |E_a^-|^2 + \frac{c\epsilon_r}{2n_r} \frac{n_a}{n_r} \frac{n_r |E_r^+|^2}{n_d |E_d^+|^2} \frac{n_d |E_d^+|^2}{n_a |E_a^+|^2} |E_a^+|^2 \right), \tag{3.11}$$

$$P_{\text{loss}} = \frac{\pi w_0^2}{4} \frac{c\epsilon_a}{n_a} \left(\mathcal{L}_{M,a} + \frac{\mathcal{L}_{M,d}}{\alpha} \right) \left| \frac{E_{\text{max},a}}{\sqrt{2}} \right|^2, \tag{3.12}$$

where inside the air gap the forward and backward field amplitudes relate to the maximum rms electric field amplitude by $|E_a^-| = |E_a^+| = |E_{\text{max},a}/\sqrt{2}|$. With the definition of the air

cavity finesse $\mathcal{F}_a = 2\pi/(\mathcal{L}_{M,a} + \mathcal{L}_{M,d}/\alpha)$, this leads to the final expression for the cavity loss rate of

$$\kappa = \frac{P_{\text{loss}}}{E_{\text{cav}}} = \frac{c}{2n_a L_{\text{eff},a}} \frac{2\pi}{\mathcal{F}_a}. \tag{3.13}$$

Solving equation (3.13) for the air cavity finesse leads to

$$\mathcal{F}_a = \frac{\frac{\lambda_0}{2n_a}}{\delta\nu \frac{L_{\text{eff},a}}{\nu}}, \tag{3.14}$$

with the Lorentzian full width at half maximum (FWHM) cavity linewidth $\delta\nu = \kappa/2\pi$. The air cavity finesse of equation (3.14) can be interpreted as the ratio of the cavity free spectral range in length $\lambda_0/2n_a$ to the FWHM cavity linewidth in length $\delta t_a = \delta\nu L_{\text{eff},a}/\nu$. For that reason, the air cavity finesse is also referred to as finesse in length [9]. The on resonance cavity slope s of the microcavity mode dispersion can thus be expressed as

$$s = \left|\frac{\partial\nu}{\partial t_a}\right| = \frac{\nu}{L_{\text{eff},a}}, \tag{3.15}$$

which describes the change in resonance frequency to the change in air gap. We note that the derivation of the cavity loss rate κ can also be carried out by normalizing to the diamond part of the cavity, which results in the same linewidth value and the formula

$$\kappa = \frac{c}{2n_d L_{\text{eff},d}} \frac{2\pi}{\mathcal{F}_d}, \tag{3.16}$$

with the definition of a diamond cavity finesse $\mathcal{F}_d = \mathcal{F}_a/\alpha$, which can also be referred to as finesse in frequency (see Appendix 3.8.2 for experimental considerations of these finesse definitions). Following this derivation, the deduced slope would describe the change in cavity resonance frequency to the change in diamond thickness (while keeping the air gap constant). This slope is experimentally challenging to probe compared to the straightforward accessible change in air gap for open microcavities. On the other hand, the diamond cavity finesse, as discussed earlier for the cavity mode volume V_d, is of importance for calculating the cavity Purcell factor for diamond color centers

$$F_P = \frac{3}{4\pi^2}\left(\frac{\lambda_0}{n_d}\right)^3 \frac{Q}{V_d} = \frac{6}{\pi^2}\left(\frac{\lambda_0}{n_d}\right)^2 \frac{\mathcal{F}_d}{\pi w_0^2}, \tag{3.17}$$

with the cavity quality factor $Q = 2n_d L_{\text{eff},d}\mathcal{F}_d/\lambda_0$ following from equation (3.16). The Purcell factor of equation (3.17) is a analytical formula considering the cavity beam waist [11]

$$w_0 = \sqrt{\frac{\lambda_0}{\pi n_a}}\left(\left(t_a + \frac{n_a t_d}{n_d}\right)\left(ROC - \left(t_a + \frac{n_a t_d}{n_d}\right)\right)\right)^{1/4}, \tag{3.18}$$

with the radius of curvature ROC of the spherical fiber mirror. Furthermore, we note that the effective length can be approximated by $L_{\text{eff},a} \approx t_a + t_d n_d/n_a\alpha$ if the electric field penetration depth into the mirrors is small compared to the air gap and diamond thickness. Moreover, scattering losses at the air-diamond interface $\mathcal{L}_{S,\text{eff},d}$ as well as absorption losses

inside the diamond $\mathcal{L}_{A,d}$ can be taken into account for the cavity finesse [9, 11, 12, 14]. These additional losses reduce the achievable Purcell factor in experiments and affect the cavity outcoupling efficiency. As an example, the outcoupling efficiency through the sample mirror $\eta_{\text{out}} = \mathcal{L}_{M,d}/(\alpha\mathcal{L}_{M,a} + \mathcal{L}_{M,d} + \mathcal{L}_{S,\text{eff},d} + \mathcal{L}_{A,d})$ is given by the ratios of the corresponding effective cavity losses.

In addition, cavity length fluctuations can average out the Purcell factor in experiments. Requiring that the standard deviation of cavity resonance frequencies caused by cavity length fluctuations should be smaller than the cavity linewidth results in the upper bound for the rms cavity length fluctuations of

$$\sigma_{\text{rms}} < \frac{\lambda_0}{2n_a\alpha\mathcal{F}_d}. \tag{3.19}$$

For typical finesse values of diamond-air microcavities, this imposes a cavity vibration level of tens of picometers or less [15]. In addition, for any finesse value, the α dependence in equation (3.19) shows that the microcavity is a factor of $n_d^2/n_a^2 \approx 5.8$ less susceptible to cavity length fluctuations in a diamond-like mode compared to an air-like mode. In general, it is challenging to achieve such low cavity vibration levels at cryogenic temperatures [15–17]. Therefore, we investigate and optimize cavity parameters as a function of the cavity vibration level in the next section.

3.4 Optimizing Microcavity Parameters

In this section, we optimize the cavity parameters for two quantities: the cooperativity and the outcoupled zero-phonon line (ZPL) emission. The first is proportional to the Purcell factor and describes the interaction strength between the quantum emitter and the cavity electric field. The second describes the probability for extracting the optical excitation of a cavity-coupled quantum emitter as a resonant photon from the cavity mode. In both cases, the properties of the quantum emitter must be taken into account. In general, the larger the ratio of the emitter's optical transition rate γ_{coupled} used for cavity-coupling to the total natural emitter decay rate γ, the higher the achievable cooperativity and outcoupled ZPL emission. We denote this ratio as $\beta_0^* = \gamma_{\text{coupled}}/\gamma$ and set it to 0.03 for diamond nitrogen-vacancy centers [1] and 0.36 for diamond tin-vacancy centers [7]. For easier comparison, a cavity resonance wavelength of $\lambda_0 = 637\,\text{nm}$ is used for both color centers.

We focus on the influence of cavity length fluctuations and tailor the mirror transmission loss values accordingly, as they can be well engineered for microcavities. In addition, we use a *ROC* value of 15.7 µm if not stated otherwise. Furthermore, we do consider scattering or absorption losses in the cavity and choose the sample mirror side of the cavity for excitation and detection, which typically leads to an overcoupled cavity due to our choice of a higher transmission loss for the sample mirror compared to the fiber mirror.

3.4.1 Cavity Length Fluctuations Model

We use the cavity length fluctuation mode as introduced in Ref. [15] to calculate vibration-averaged cavity quantities. The standard deviation of fluctuations in cavity length translates via the cavity slope into fluctuations in cavity frequency $\sigma_\nu = s\sigma_{\text{rms}}$, which are modeled by

the Gaussian probability density function [2]

$$f(\Delta\nu) = \frac{1}{\sqrt{2\pi\sigma_\nu^2}} e^{-\Delta\nu^2/2\sigma_\nu^2}, \tag{3.20}$$

with the emitter-cavity detuning $\Delta\nu$. In addition, for emitters with an optical linewidth much smaller than the cavity linewidth, the spectral overlap is given by [11]

$$\xi_s(\Delta\nu) = \frac{1}{1 + \frac{4Q^2}{\nu^2}\Delta\nu^2}, \tag{3.21}$$

with the cavity resonance frequency ν. By taking the spectral overlap for the Purcell factor into account and integrating the probability density function over the emitter-cavity detunings $\Delta\nu$, the vibration-averaged cooperativity and outcoupled ZPL emission are calculated.

3.4.2 Maximum Attainable Outcoupled ZPL Emission

We define the outcoupled ZPL emission $\beta_{\text{out}} = \eta_{\text{out}}\beta_0^* F_P/(\beta_0^* F_P + 1)$ with the outcoupling efficiency through the sample mirror η_{out}. Considering cavity length fluctuations, the maximum attainable outcoupled ZPL emission is calculated by

$$\beta_{\text{out,max}} = \max_{\mathcal{L}_{M,d}} \left(\eta_{\text{out}} \int_{-\infty}^{\infty} d(\Delta\nu) \frac{\beta_0^* F_P \xi_s(\Delta\nu)}{\beta_0^* F_P \xi_s(\Delta\nu) + 1} f(\Delta\nu) \right), \tag{3.22}$$

where η_{out} is a function of $\mathcal{L}_{M,d}$ as well as $\mathcal{L}_{M,a} = 48\,\text{ppm}$ and additionally F_P depends on the cavity beam waist w_0. Figure 3.5 shows the maximum attainable outcoupled ZPL emission for a NV and SnV center in a microcavity for the simulated air-like and diamond-like mode of Fig. 3.4. For vanishing cavity length fluctuations, the maximum attainable outcoupled ZPL emission is mainly determined by the fiber mirror loss $\mathcal{L}_{M,a} = 48\,\text{ppm}$. Figure 3.5 shows that the maximum attainable outcoupled ZPL emission decreases less in the diamond-like mode compared to the air-like mode with increasing vibrations. In addition, the maximum attainable outcoupled ZPL emission is generally larger for SnV centers as a consequence of the significantly larger β_0^* value compared to NV centers. Despite that, outcoupled ZPL emissions of tens of percent are feasible for both color centers, which presents a significant improvement compared to setups based on bulk or solid-immersion lens samples [18, 19].

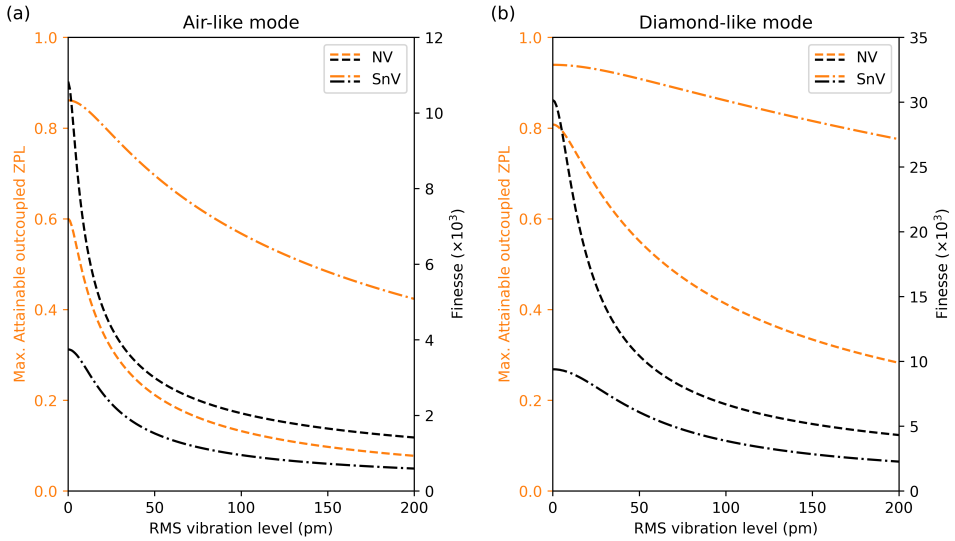

Figure 3.5: Maximum attainable outcoupled ZPL emission depending on the cavity vibration level for a microcavity-coupled NV (dashed orange lines) and SnV (dashed-dotted orange lines) center. The microcavity geometry of an air-like (a) and diamond-like (b) mode as introduced in Fig. 3.4 with a cavity beam waist of $w_0 = 1.2\,\mu\text{m}$ is considered. The diamond finesse values (black lines) correspond to the optimized mirror transmission losses. A fixed fiber mirror transmission loss of $\mathcal{L}_{M,a} = 48\,\text{ppm}$ is used.

3.4.3 Maximum Attainable Purcell Factor

Following Ref. [15] and combining it with the here derived cavity mode volume V_d and cavity slope $s = \nu n_a \alpha / L_{\text{eff},d} n_d$ leads to the maximum attainable Purcell factor

$$F_{P,\max} = \frac{3}{4\pi^2} \left(\frac{\lambda_0}{n_d} \right)^3 \frac{1}{\pi w_0^2} \sqrt{\frac{\pi}{2\sigma_{\text{rms}}^2}} \frac{2n_d}{\alpha n_a}. \tag{3.23}$$

We highlight that equation (3.23) is inversely proportional to α, and since w_0 is almost independent of the hybrid cavity mode, the maximum attainable Purcell factor is $n_d^2/n_a^2 \approx 5.8$ higher in a diamond-like mode compared to an air-like mode. The maximum attainable cooperativity is then given by $C = \beta_0^* F_{P,\max}$. Figure 3.6 shows these maximum attainable Purcell factors as well as the corresponding cooperativities for a NV and SnV center in the microcavity as considered in Fig. 3.5.

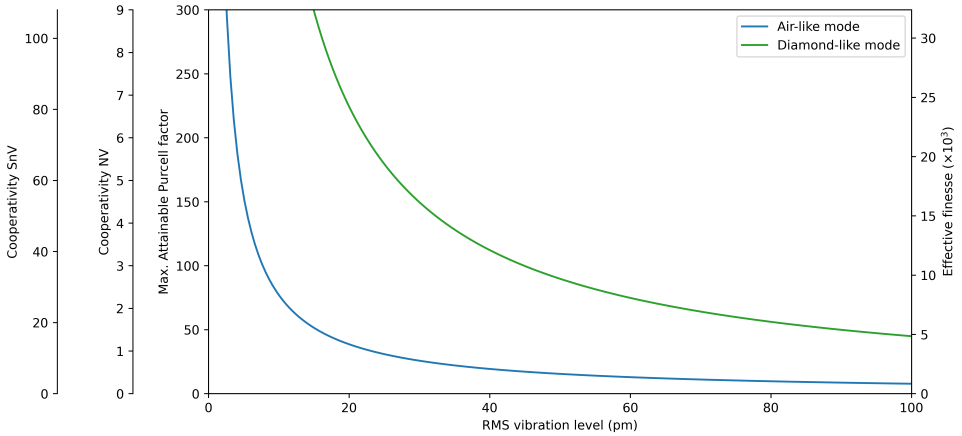

Figure 3.6: Maximum attainable Purcell factor and corresponding cooperativities for a microcavity-coupled NV and SnV center depending on the cavity vibration level. For the air-like and diamond-like mode as introduced in Fig. 3.4, the cavity beam waist is $w_0 = 1.2\,\mu\text{m}$. The stated effective finesse is the back-calculated value of the maximum attainable Purcell factor for vanishing cavity length fluctuations. It serves as an estimate of the experimentally required diamond cavity finesse.

The cooperativity of the SnV to the NV center differs by their ratio in β_0^*, and Fig. 3.6 shows that a strong coupling ($C > 1$) can be reached for both color centers. Furthermore, since SnV centers preserve their optical coherence in very thin ($\sim 150\,\text{nm}$) diamond membranes [20], shorter cavity length and fiber mirrors with smaller *ROC* of $\sim 4\,\mu\text{m}$ [21, 22] can be used. This adjustment promises cavity geometries with a two-fold reduction in cavity beam waist w_0 and consequently a four-fold increase in Purcell factor and cooperativity compared to the data shown in Fig. 3.6. This presents a route to strongly coupled SnV centers ($C \gg 1$) in open microcavities with moderate requirements on the cavity finesse.

3.5 Optical Interfacing of Microcavity-coupled Color Centers

In this section, we outline the resonant optical interfacing of microcavity-coupled color centers and present two optical qubit readout methods. The optical transitions used for cavity-coupling connect a ground state to an excited state of the color center, where we consider the ground state to be one of the electron spin qubit states. Given that, a resonant laser pulse can be used to probe the optical transition spin-selectively, enabling the optical qubit readout.

For a cavity-coupled optical transition, resonant addressing is mediated by the cavity mode, which can be modeled with cavity quantum electrodynamics. In this framework, the emitter-cavity system is described by the cavity loss rate κ, the total natural emitter decay rate γ, and the single-photon Rabi frequency g, which is determined by the cooperativity $C = 4g^2/\kappa\gamma$. In the following, we use this framework and the parameters of the microcavity of Fig. 3.4(c), with a FWHM cavity linewidth of 1.87 GHz, an outcoupling efficiency of 98 % and maximum cooperativities of about 2 for NV and 23 for SnV centers.

We note that the optical readout of the electron spin relies on a measurable difference in the detected photon counts depending on the spin qubit state. The better the two distributions of detected photons are separated, the higher the readout fidelity. This means that, in addition to the readout methods discussed here, the emitter transition cyclicity and the detection efficiency also affect the readout fidelity.

3.5.1 Optical Readout via Resonance Fluorescence

The first readout method is based on detecting emitter resonance fluorescence (ZPL emission) while driving the readout transition. This method requires filtering of resonant laser light from the resonance fluorescence signal. For microcavities, this can be done by polarization filtering via the two orthogonal linear polarization cavity modes [3, 23], to both of which the emitter's transition electric dipole is coupled. This enables excitation and detection in two orthogonal modes, and subsequent polarization filtering retrieves the desired resonance fluorescence signal. To estimate the required cooperativity per cavity mode, we simulate the detected ratio of resonance fluorescence to the laser photon count rate leaking through the polarization filtering. Figure 3.7 shows simulated ratios as a function of the cooperativity using a Lindblad master equation approach [7, 24]. In addition, the influence of an exemplary pure dephasing rate of 5γ and a frequency splitting between the two polarization cavity modes of $5\kappa/2\pi$ is investigated. In recent experiments, laser polarization suppression ratios of > 60 dB [3] have been demonstrated, which enables spin qubit state readouts with high signal to laser background ratios (> 100) for moderate cooperativities on the percent level (see Fig. 3.7). This means that for the considered cavity, the cooperativity can be split asymmetrically between the polarization cavity modes to realize efficient excitation, while preserving an efficient spin-photon interface in the detection cavity mode, as discussed in section 3.4. If sufficient cooperativities are not achieved in experiments, pulsed resonant excitation, combined with detection time filtering, can also be used to filter the excitation laser light from the resonance fluorescence signal in the time domain [3].

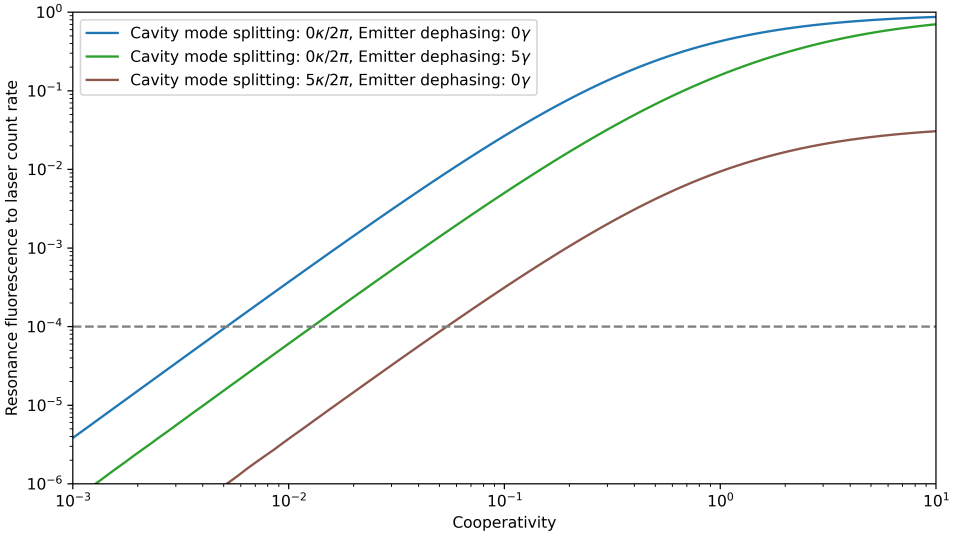

Figure 3.7: Simulated emitter resonance fluorescence to excitation laser count rate for an emitter that is equally coupled to both polarization microcavity modes. The cooperativity is stated per polarization cavity mode, and the simulations are performed in the linear excitation regime, where the resonance fluorescence count rate increases linearly with laser power. In addition, the cavity reflection is assumed to be unity for the excitation cavity polarization mode. Furthermore, an emitter decay rate $\gamma = 12.8\,\mathrm{MHz}$ [25] of the NV center is used, albeit the results are virtually identical for a SnV center decay rate. The dashed gray line indiactes a threshold that, with laser polarization suppression ratios of $> 60\,\mathrm{dB}$, yields high signal to laser background ratios of > 100.

3.5.2 Optical Readout via Cavity Reflection

The second readout method is based on detecting resonant laser light that is reflected off the cavity with a spin state-dependent coefficient. This method requires a relatively large cooperativity ($C \gtrsim 1$) and good optical coherence of the emitter, such that the cavity-coupled optical transitions significantly modulate the cavity reflection. Figure 3.8 shows the cavity reflection for a SnV center with an exemplary optical spin state transition splitting of 500 MHz and a cooperativity of $C = 1$. In addition, the detuning between the emitter and the cavity resonance frequency is chosen such that the reflection vanishes at a specific frequency for one of the spin states. Probing the cavity with resonant laser light at this frequency can enable spin state readout with high contrast [26]. For a NV center, the cavity reflection of the readout transition is qualitatively similar, but achieving the considered cooperativity of $C = 1$ in experiments is more challenging.

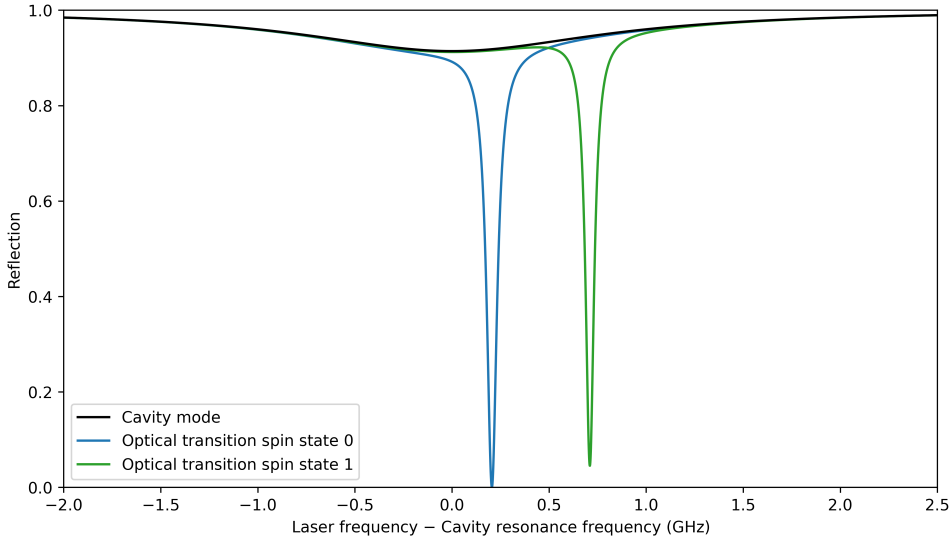

Figure 3.8: Cavity reflection of a cavity-coupled SnV center, derived from an analytical model [27]. In the simulations, an optical spin state transition splitting of 500 MHz and a cooperativity of $C = 1$ are used. In addition, the optical transition frequency of spin state 0 is intentionally detuned by about 200 MHz from the cavity resonance to achieve a vanishing reflection for that spin state. Furthermore, an emitter decay rate $\gamma = 32$ MHz [7] of the SnV center is used.

3.6 Summary and Discussion

In summary, we have introduced a one-dimensional transfer matrix model to describe dielectric mirrors with bonded diamond membranes and diamond-air microcavities, including their hybridized cavity modes. An analytical model for the Purcell factor of diamond color centers in microcavities is derived, which provides insights into different finesse definitions and the susceptibility of the open microcavity to cavity length fluctuations. We optimize the cavity parameters to maximize the outcoupled ZPL emission and the cooperativity. Cavity outcoupled ZPL emission values of tens of percent are feasible for the NV and the SnV center, with, in general, higher values in diamond-like modes. Considering the cooperativity, SnV centers exhibit approximately a factor of 10 higher values than NV centers due to their natively larger decay ratio into the cavity-coupled optical transition. Moreover, in the presence of cavity length fluctuations, the cooperativity in a diamond-like mode is a factor of $n_d^2/n_a^2 \approx 5.8$ larger than in an air-like mode, which follows from different susceptibilities to cavity length fluctuations. This highlights the diamond-like mode as the preferred cavity mode under cavity length fluctuations. However, in diamond-like modes, additional scattering losses can occur due to their electric field antinode at the air-diamond interface. This can reduce the cavity finesse and the cavity outcoupling efficiency in experiments, such that air-like modes are again more favorable. Purcell-enhanced diamond color centers have not been reported in diamond-like modes, but high diamond cavity finesse values $\sim 10^4$ [28] similar to air-like modes [29] have been achieved.

Finally, the optical interfacing of microcavity-coupled diamond color centers is dis-

cussed, and cavity quantum electrodynamics calculations are used to present two resonant optical readout methods for the color center's electron spin. The first readout method is based on the detection of resonance fluorescence signal in a cross-polarized scheme using the two cavity polarization modes of the microcavity. We show that, with a laser polarization suppression ratio $> 60\,\mathrm{dB}$ and cooperativities on the percent level, high resonance fluorescence to laser background ratios > 100 can be achieved. This shows that efficient optical qubit readout is possible with moderate cooperativities in the polarization cavity mode used for excitation, without sacrificing an efficient spin-photon interface with high cooperativity in the cavity polarization mode used for detection. The second readout method relies on a rather strongly cavity-coupled optical transition ($C \gtrsim 1$), which alters the cavity reflection response. Depending on the spin qubit state, the light from a probe laser is reflected off the cavity with different amplitudes, allowing the two qubit states to be distinguished. This readout technique is particularly interesting for microcavity-coupled SnV centers, as they can achieve the required cooperativities more easily than NV centers.

3.7 Acknowledgment

We thank Yanik Herrmann and Daniel Bedialauneta Rodriguez for feedback on this work. We thank Tobias Groß from Laseroptik for providing the dielectric mirror coating parameters.

3.7.1 Data Availability

The simulation code that supports this work is available at 4TU.ResearchData [30].

3.8 Appendix

3.8.1 Transfer Matrix Model: Definitions and Derivations

The transfer matrices used in this work are composed of matrices to describe the propagation of the electric field in a homogeneous medium and boundary matrices to describe the transition of the electric field between two media of different refractive index. The propagation matrix is defined as [10]

$$M_{\text{propagation}} = \begin{pmatrix} e^{ikz} & 0 \\ 0 & e^{-ikz} \end{pmatrix}, \tag{3.24}$$

with the wave vector $k = 2\pi n/\lambda_0$, the refractive index n of the homogeneous medium and the propagation distance z. The boundary matrix is defined as [10]

$$M_{\text{boundary}} = \frac{1}{\tau} \begin{pmatrix} 1 & \rho \\ \rho & 1 \end{pmatrix}, \tag{3.25}$$

with the coefficient $\tau = 2n_l/(n_l + n_r)$ and $\rho = (n_l - n_r)/(n_l + n_r)$.

Electric field intensity ratio of air-diamond interfaces

We consider the reflection of a monochromatic plane wave of wavelength λ_0 at the sample mirror with bonded diamond membrane as depicted in Fig. 3.2(a). Using equation (3.25), we translate the electric fields at the air-diamond interface from its right side with $n_r = n_d$

to its left side with $n_l = n_a$. This yields the relation between the forward and backward electric fields

$$E_a^+ = \frac{E_d^+ + \rho E_d^-}{\tau}, \tag{3.26}$$

$$E_a^- = \frac{\rho E_d^+ + E_d^-}{\tau}, \tag{3.27}$$

at the air-diamond interface. Assuming a highly reflective sample mirror ($R = 1$) results in a standing wave in front of the mirror with $|E_a^+| = |E_a^-|$ and $|E_d^+| = |E_d^-|$ at any position. Further, the ratio of the backward to the forward electric field in diamond at the air-diamond interface $E_d^-/E_d^+ = \exp(i\varphi)$ relates by the phase $\varphi = k2t_d + \pi$ with $k = 2\pi n_d/\lambda_0$, which originates from the propagation in the diamond of thickness t_d and a π phase shift from the mirror reflection. In combination with equation (3.26), the squared electric field ratio of the air side to the diamond side is

$$\frac{|E_a^+|^2}{|E_d^+|^2} = \frac{|1+\rho e^{i\varphi}|^2}{\tau^2} = \frac{1+\rho^2+2\rho\cos(\varphi)}{\tau^2}, \tag{3.28}$$

$$= \frac{1}{2}(1+\cos(\varphi)) + \frac{n_d^2}{2n_a^2}(1-\cos(\varphi)). \tag{3.29}$$

This finally leads to the electric field intensity ratio

$$\frac{n_a|E_a^+|^2}{n_d|E_d^+|^2} = \frac{n_a}{n_d}\sin^2\left(\frac{2\pi n_d t_d}{\lambda_0}\right) + \frac{n_d}{n_a}\cos^2\left(\frac{2\pi n_d t_d}{\lambda_0}\right) = \frac{n_a|E_a^-|^2}{n_d|E_d^-|^2} = \frac{n_a|E_{\max,a}|^2}{n_d|E_{\max,d}|^2}, \tag{3.30}$$

which also holds for the backward electric fields and the maximum electric fields.

3.8.2 Finesse Measurements of Diamond-Air Microcavities

In this work, we introduce the air cavity finesse $\mathcal{F}_a$ (finesse in length) and the diamond cavity finesse $\mathcal{F}_d$ (finesse in frequency). These two definitions arise from considering the air gap or the diamond part of the microcavity as the cavity medium, as reflected in the derived formulas by normalizing to the air gap or the diamond part. In the first consideration, the air gap is the cavity medium, confined on one side by an air-terminated dielectric mirror and on the other by a dielectric mirror with an additional diamond layer (the diamond membrane). In the second consideration, the diamond part is the cavity medium, confined on onse side by a diamond-terminated dielectric mirror and on the other by a dielectric mirror with an additional air layer (the air gap). These two cavity views and their corresponding finesse definitions must be distinguished in experiments, as they provide different measures and are related by $\mathcal{F}_d = \mathcal{F}_a/\alpha$, where α is the electric field intensity ratio. In the following, we summarize experimental methods for determining both cavity finesse quantities.

Air cavity finesse (finesse in length)

The air cavity finesse for a wavelength λ_0 can be measured experimentally by the following methods:

- The microcavity is probed in transmission or reflection with a narrowband laser of wavelength λ_0, while scanning the air gap over two subsequent resonance modes (scan range $> \lambda_0/2n_a$) and measuring the probe laser intensity [12]. The intensity signal is recorded over the air gap, which allows the width of the studied resonance mode and the distance between the two subsequent modes (equal to $\lambda_0/2n_a$) to be extracted. Following equation (3.14), the ratio of the subsequent mode distance to the FWHM width of the resonance mode yields the air cavity finesse.

- The cavity quality factor $Q = \nu/\delta\nu$ is determined for subsequent cavity modes at the cavity resonance frequency $\nu = c/\lambda_0$ by measuring the FWHM cavity linewidth $\delta\nu$ [28]. This can be done by scanning a frequency-stabilized narrowband probe laser over the cavity resonance mode and extracting the FWHM cavity linewidth $\delta\nu$ from the laser intensity signal in cavity transmission or reflection [3, 7]. Alternatively, the probe laser can be frequency modulated with sidebands, or two probe lasers with a known frequency offset can be used, while scanning the air gap over the studied cavity resonance and measuring the laser intensity [12, 15]. Taking the sideband modulation frequency or the frequency offset as a reference enables the extraction of the cavity linewidth from the probe laser intensity signal. Following equation (3.13), the cavity quality factor can be expressed as $Q = 2n_a L_{\mathrm{eff},a} \mathcal{F}_a/\lambda_0$. Further, the effective cavity length normalized to the air gap can be decomposed to $L_{\mathrm{eff},a} = t_a + L_{\mathrm{rest}}$, where L_{rest} is the remaining integral of the normalized cavity electric field energy distribution over the diamond part and the mirrors. Translating the air gap t_a to the air mode number m_a with equations (3.7) yields the cavity quality factor $Q = m_a \mathcal{F}_a + Q_0$ with an air gap independent offset value Q_0. This shows that the air cavity finesse $\mathcal{F}_a$ can be calculated as the cavity quality factor difference between two subsequent cavity modes with air mode numbers m_a and $m_a + 1$.

Diamond cavity finesse (finesse in frequency)

The diamond cavity finesse for a wavelength λ_0 can be measured experimentally by the following method:

- The FWHM cavity linewidth $\delta\nu$ of the studied resonance mode is measured and following equation (3.16) the diamond cavity finesse $\mathcal{F}_d = c/2n_d L_{\mathrm{eff},d}\delta\nu$ is determined with the effective cavity length $L_{\mathrm{eff},d}$ [3, 7]. The cavity linewidth can be measured using a narrowband probe laser of wavelength λ_0, as outlined for the air cavity finesse. The effective cavity length normalized to the diamond part can be calculated by the integral of the normalized cavity electric field energy distribution, which requires knowledge of the dielectric mirrors as well as the air gap and diamond membrane thickness. The parameters of the dielectric mirrors are known from the mirror coating design, whereas the air gap and diamond thickness must be determined experimentally. This can be done by measuring the cavity mode dispersion and fitting an analytical model [9, 11].

References

[1] D. Riedel, I. Söllner, B. J. Shields, S. Starosielec, P. Appel, E. Neu, P. Maletinsky, and R. J. Warburton, *Deterministic Enhancement of Coherent Photon Generation from a Nitrogen-Vacancy Center in Ultrapure Diamond,* Physical Review X **7**, 031040 (2017).

[2] M. Ruf, M. Weaver, S. van Dam, and R. Hanson, *Resonant Excitation and Purcell Enhancement of Coherent Nitrogen-Vacancy Centers Coupled to a Fabry-Perot Microcavity,* Physical Review Applied **15**, 024049 (2021).

[3] J. Fischer, Y. Herrmann, C. F. J. Wolfs, S. Scheijen, M. Ruf, and R. Hanson, *Spin-photon correlations from a Purcell-enhanced diamond nitrogen-vacancy center coupled to an open microcavity,* Nature Communications **16**, 11680 (2025).

[4] M. Salz, Y. Herrmann, A. Nadarajah, A. Stahl, M. Hettrich, A. Stacey, S. Prawer, D. Hunger, and F. Schmidt-Kaler, *Cryogenic platform for coupling color centers in diamond membranes to a fiber-based microcavity,* Applied Physics B **126**, 131 (2020).

[5] G. Bayer, R. Berghaus, S. Sachero, A. B. Filipovski, L. Antoniuk, N. Lettner, R. Waltrich, M. Klotz, P. Maier, V. Agafonov, and A. Kubanek, *Optical driving, spin initialization and readout of single SiV^- centers in a Fabry-Perot resonator,* Communications Physics **6**, 300 (2023).

[6] R. Zifkin, C. D. Rodríguez Rosenblueth, E. Janitz, Y. Fontana, and L. Childress, *Lifetime Reduction of Single Germanium-Vacancy Centers in Diamond via a Tunable Open Microcavity,* PRX Quantum **5**, 030308 (2024).

[7] Y. Herrmann, J. Fischer, J. M. Brevoord, C. Sauerzapf, L. G. C. Wienhoven, L. J. Feije, M. Pasini, M. Eschen, M. Ruf, M. J. Weaver, and R. Hanson, *Coherent Coupling of a Diamond Tin-Vacancy Center to a Tunable Open Microcavity,* Physical Review X **14**, 041013 (2024).

[8] S. Sachero, R. Berghaus, F. Feuchtmayr, N. Lettner, P. Maier, E. N. Hernandez, S. D. Tchernij, and A. Kubanek, *Tunable cavity coupling of a single SnV^- center in nanodiamond across the bad-emitter and bad-cavity regimes,* Physical Review Applied **24**, 054063 (2025).

[9] E. Janitz, M. Ruf, M. Dimock, A. Bourassa, J. Sankey, and L. Childress, *Fabry-Perot microcavity for diamond-based photonics,* Physical Review A **92**, 043844 (2015).

[10] S. J. Orfanidis, *Electromagnetic Waves and Antennas* (Rutgers University, New Brunswick, 2016).

[11] S. B. van Dam, M. Ruf, and R. Hanson, *Optimal design of diamond-air microcavities for quantum networks using an analytical approach,* New Journal of Physics **20**, 115004 (2018).

[12] Y. Herrmann, J. M. Brevoord, J. Fischer, S. Scheijen, C. Sauerzapf, N. Codreanu, L. G. C. Wienhoven, Y. M. Q. Van Der Graaf, C. F. J. Wolfs, R. Méjard, M. Ruf, N. De Jong, and R. Hanson, *Laser-cut patterned, micrometer-thin diamond membranes with coherent*

color centers for open microcavities, Materials for Quantum Technology **5**, 035001 (2025).

[13] S. van Dam, *Optical cavities, coherent emitters, and protocols for diamond-based quantum networks*, Ph.D. thesis, Delft University of Technology (2019).

[14] J. Körber, M. Pallmann, J. Heupel, R. Stöhr, E. Vasilenko, T. Hümmer, L. Kohler, C. Popov, and D. Hunger, *Scanning Cavity Microscopy of a Single-Crystal Diamond Membrane,* Physical Review Applied **19**, 064057 (2023).

[15] Y. Herrmann, J. Fischer, S. Scheijen, C. F. J. Wolfs, J. M. Brevoord, C. Sauerzapf, L. G. C. Wienhoven, L. J. Feije, M. Eschen, M. Ruf, M. J. Weaver, and R. Hanson, *A low-temperature tunable microcavity featuring high passive stability and microwave integration,* AVS Quantum Science **6**, 041401 (2024).

[16] Y. Fontana, R. Zifkin, E. Janitz, C. D. Rodríguez Rosenblueth, and L. Childress, *A mechanically stable and tunable cryogenic Fabry–Pérot microcavity,* Review of Scientific Instruments **92**, 053906 (2021).

[17] M. Pallmann, T. Eichhorn, J. Benedikter, B. Casabone, T. Hümmer, and D. Hunger, *A highly stable and fully tunable open microcavity platform at cryogenic temperatures,* APL Photonics **8**, 046107 (2023).

[18] H. K. C. Beukers, C. Waas, M. Pasini, H. B. Van Ommen, Z. Ademi, M. Iuliano, N. Codreanu, J. M. Brevoord, T. Turan, T. H. Taminiau, and R. Hanson, *Control of Solid-State Nuclear Spin Qubits Using an Electron Spin- 1 / 2,* Physical Review X **15**, 021011 (2025).

[19] B. Hensen, H. Bernien, A. E. Dréau, A. Reiserer, N. Kalb, M. S. Blok, J. Ruitenberg, R. F. L. Vermeulen, R. N. Schouten, C. Abellán, W. Amaya, V. Pruneri, M. W. Mitchell, M. Markham, D. J. Twitchen, D. Elkouss, S. Wehner, T. H. Taminiau, and R. Hanson, *Loophole-free Bell inequality violation using electron spins separated by 1.3 kilometres,* Nature **526**, 682 (2015).

[20] X. Guo, A. M. Stramma, Z. Li, W. G. Roth, B. Huang, Y. Jin, R. A. Parker, J. Arjona Martínez, N. Shofer, C. P. Michaels, C. P. Purser, M. H. Appel, E. M. Alexeev, T. Liu, A. C. Ferrari, D. D. Awschalom, N. Delegan, B. Pingault, G. Galli, F. J. Heremans, M. Atatüre, and A. A. High, *Microwave-Based Quantum Control and Coherence Protection of Tin-Vacancy Spin Qubits in a Strain-Tuned Diamond-Membrane Heterostructure,* Physical Review X **13**, 041037 (2023).

[21] A. A. P. Trichet, P. R. Dolan, D. M. Coles, G. M. Hughes, and J. M. Smith, *Topographic control of open-access microcavities at the nanometer scale,* Optics Express **23**, 17205 (2015).

[22] D. Najer, M. Renggli, D. Riedel, S. Starosielec, and R. J. Warburton, *Fabrication of mirror templates in silica with micron-sized radii of curvature,* Applied Physics Letters **110**, 011101 (2017).

[23] V. Yurgens, Y. Fontana, A. Corazza, B. J. Shields, P. Maletinsky, and R. J. Warburton, *Cavity-assisted resonance fluorescence from a nitrogen-vacancy center in diamond,* npj Quantum Information **10**, 112 (2024).

[24] A. Sipahigil, R. E. Evans, D. D. Sukachev, M. J. Burek, J. Borregaard, M. K. Bhaskar, C. T. Nguyen, J. L. Pacheco, H. A. Atikian, C. Meuwly, R. M. Camacho, F. Jelezko, E. Bielejec, H. Park, M. Lončar, and M. D. Lukin, *An integrated diamond nanophotonics platform for quantum-optical networks,* Science **354**, 847 (2016).

[25] S. L. N. Hermans, M. Pompili, L. D. Santos Martins, A. R-P Montblanch, H. K. C. Beukers, S. Baier, J. Borregaard, and R. Hanson, *Entangling remote qubits using the single-photon protocol: an in-depth theoretical and experimental study,* New Journal of Physics **25**, 013011 (2023).

[26] M. K. Bhaskar, R. Riedinger, B. Machielse, D. S. Levonian, C. T. Nguyen, E. N. Knall, H. Park, D. Englund, M. Lončar, D. D. Sukachev, and M. D. Lukin, *Experimental demonstration of memory-enhanced quantum communication,* Nature **580**, 60 (2020).

[27] P.-J. Stas, Y. Q. Huan, B. Machielse, E. N. Knall, A. Suleymanzade, B. Pingault, M. Sutula, S. W. Ding, C. M. Knaut, D. R. Assumpcao, Y.-C. Wei, M. K. Bhaskar, R. Riedinger, D. D. Sukachev, H. Park, M. Lončar, D. S. Levonian, and M. D. Lukin, *Robust multi-qubit quantum network node with integrated error detection,* Science **378**, 557 (2022).

[28] S. Flågan, D. Riedel, A. Javadi, T. Jakubczyk, P. Maletinsky, and R. J. Warburton, *A diamond-confined open microcavity featuring a high quality-factor and a small mode-volume,* Journal of Applied Physics **131**, 113102 (2022).

[29] S. Bogdanović, S. B. van Dam, C. Bonato, L. C. Coenen, A.-M. J. Zwerver, B. Hensen, M. S. Z. Liddy, T. Fink, A. Reiserer, M. Lončar, and R. Hanson, *Design and low-temperature characterization of a tunable microcavity for diamond-based quantum networks,* Applied Physics Letters **110**, 171103 (2017).

[30] J. Fischer, *Data underlying the dissertation "Diamond Quantum Network Nodes with Open Microcavities",* 4TU.ResearchData (2026), https://doi.org/10.4121/032fe578-6933-45da-ba7a-f7da2b186bcd.

4

A Low-Temperature Tunable Microcavity featuring High Passive Stability and Microwave Integration

Y. Herrmann*, J. Fischer*, S. Scheijen, C. F. J. Wolfs, J. M. Brevoord, C. Sauerzapf, L. G. C. Wienhoven, L. J. Feije, M. Eschen, M. Ruf, M. J. Weaver and R. Hanson

Open microcavities offer great potential for the exploration and utilization of efficient spin-photon interfaces with Purcell-enhanced quantum emitters, thanks to their large spectral and spatial tunability combined with high versatility of sample integration. However, a major challenge for this platform is the sensitivity to cavity length fluctuations in the cryogenic environment, which leads to cavity resonance frequency variations and thereby a lowered averaged Purcell enhancement. This work presents a closed-cycle cryogenic fiber-based microcavity setup, which is in particular designed for a low passive vibration level, while still providing large tunability and flexibility in fiber and sample integration, and high photon collection efficiency from the cavity mode. At temperatures below 10 *kelvin, a stability level of around* 25 *picometer is reproducibly achieved in different setup configurations, including the extension with microwave control for manipulating the spin of cavity-coupled quantum emitters, enabling a bright photonic interface with optically active qubits.*

The results of this chapter have been published in AVS Quantum Science **6**, 041401 (2024).
* Equally contributed authors.

4.1 Microcavities with Single Quantum Emitters

The strength of the light-matter interaction is a key parameter for the realization of efficient interfaces between single quantum emitters and optical photons. Optically active quantum emitters are interesting testbeds for quantum science and are promising candidates for realizing stationary qubits [1–3], but the bare coupling to optical photons in bulk materials is generally weak. This coupling can be greatly improved by integrating the emitter into an optical resonator [4–7]. In the simplest form, two highly reflective mirrors facing each other can be used to realize such a cavity. The cavity can be utilized to efficiently couple quantum emitters to an optical photon mode, thereby selectively enhancing their emission, known as the Purcell effect. When used with solid-state host materials, a hemispherical plano-concave cavity geometry with a low radius of curvature and a micrometer short length can be used to minimize the mode volume. Such open optical microcavities have proven to be a versatile tool in quantum optics, due to their high spectral and spatial tunability and their compatibility with a broad spectrum of quantum systems. The cavity design allows the incorporation of quantum emitters in various ways: quantum dots can be directly grown on top of the mirror [8–11] or emitters in layered materials [12–14] can be bonded onto the mirror surface. Furthermore, the spatial tunability can be used to optimize on localized emitters on the mirror like carbon nanotubes [15, 16], rare-earth ions in nanoparticles [17] or color centers in nanodiamonds [18–21]. And (sub) micrometer thin membranes can integrate color centers in host materials like diamond [22–24], silicon carbide [25, 26], yttrium orthosilicate [27] or organic crystals [28] into the cavity. This approach is especially advantageous for emitters like the nitrogen-vacancy center in diamond, which are notoriously hard to integrate coherently into nanostructures due to the presence of a permanent electric dipole, but maintain good optical properties in micrometer-thin membranes [29].

The optical access of the microcavity can conveniently benefit from the realization of the mirrors on the tip of optical fibers [30, 31], enabling direct fiber coupling. Furthermore, high cavity quality factors can be realized by commercially available mirror coatings, including the purposely design of symmetric or single-sided cavities.

The high spectral tunability makes the cavity sensitive to fluctuations in length, leading to variations in the resonance frequency. These perturbations lower the effective coupling of the emitter to the cavity and lead to a reduced averaged Purcell enhancement. This can be expressed with the spectral overlap of the resonance frequency of the emitter and the cavity frequency [32]. Assuming a Gaussian distribution of the varying cavity length [33], we can find a bound for the maximum attainable (effective) Purcell factor

$$F_{P,max} = \frac{3}{4\pi^2}\left(\frac{c}{n\nu}\right)^3 \frac{1}{V}\sqrt{\frac{\pi}{2(s\sigma)^2}}\frac{\nu}{2}, \tag{4.1}$$

which depends on the cavity resonance frequency ν, mode volume V, mode dispersion slope s, and root mean square (RMS) cavity length fluctuations σ with the refractive index in diamond n and the speed of light c. The derivation of equation (4.1) can be found in Appendix 4.8.1. For a hybrid cavity consisting of an air part and a diamond membrane, certain modes of a fixed frequency become more air- or diamond-like [34]. The mode type depends only on the diamond thickness. Due to a smaller slope in the cavity dispersion relation, diamond-like modes are less sensitive to vibrations [32]. Note that for a given

membrane thickness and air length, the cavity mode dispersion slope s can be calculated with an analytic expression [32]. Figure 4.1 (a) shows the maximum attainable Purcell factor depending on the RMS cavity length fluctuations for different cavity parameters realized in other works. To reach a large Purcell enhancement, a vibration level on the order of tens of picometer RMS vibrations is required. This poses a technical challenge, as most quantum systems need to be operated in high vacuum at cryogenic temperatures. For a closed-cycle cryostat configuration, which enables continuous operation and reduced experimental overhead, the vicinity of a running cryostat cold head inevitably introduces vibrations.
Setups with high stability levels have been reported in quiet helium bath cryostats [35] or with limited spatial control in closed-cycle cryostats [27]. Recently, systems with large spatial tunability and passive stability levels at the tens of picometer level have been reported in closed-cycle cryostats [36–39].

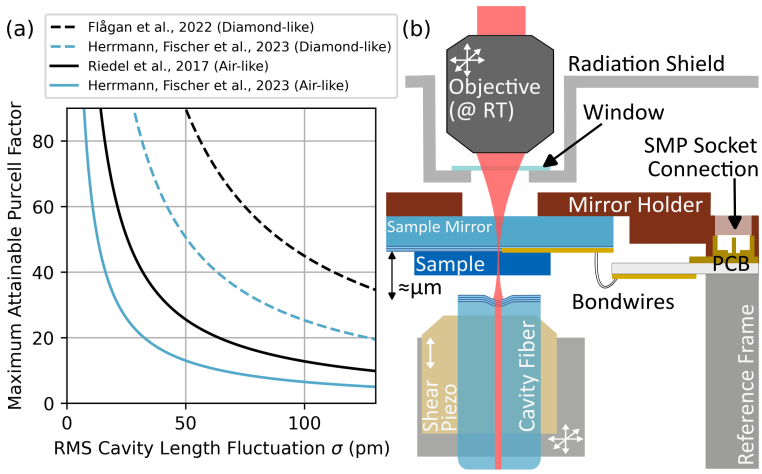

Figure 4.1: (a) Maximum attainable Purcell factor depending on RMS cavity length fluctuations. The black lines show simulations for a microcavity with an around 0.8 µm thin diamond membrane, achieved in Ref. [40] for an air-like mode (mode volume $V = 9\ \lambda^3$, cavity dispersion $s = 139$ MHz/pm for 637 nm) and in Ref. [41] for a diamond-like mode (mode volume $V = 4\ \lambda^3$, cavity dispersion $s = 89$ MHz/pm for 637 nm). The blue lines show simulations for an around 3.7 µm thin diamond membrane, achieved in Ref. [42] for an air-like mode (mode volume $V = 55\ \lambda^3$, cavity dispersion $s = 46$ MHz/pm for 619 nm) and for the diamond-like case (mode volume $V = 31\ \lambda^3$, cavity dispersion $s = 21$ MHz/pm for 619 nm). For a cavity without the diamond membrane, the maximum attainable Purcell factor follows approximately the air-like modes. (b) Sketch of the experimental setup design. The microcavity is composed of a flat sample mirror and a curved microscopic mirror, fabricated on the tip of an optical fiber. Optical access to the sample mirror side of the cavity is provided with a movable objective. The optical cavity axis is changed by moving the cavity fiber and the outcoupling objective over the sample mirror. The objective is kept at room temperature and thermally shielded by an aluminum cone with a thin window for optical access. The sample mirror has embedded gold striplines, which are connected over a support printed circuit board (PCB), to deliver microwaves close to the cavity spot.

In the following, we present a low-temperature fiber-based Fabry-Pérot microcavity setup inside a closed-cycle cryostat, which is designed to maintain a high passive stability level. We present the operation of the cavity together with an analysis of the passive stability. We showcase the functionality of this tunable platform by demonstrating the

coupling of two different diamond color centers, the tin-vacancy center and the nitrogen-vacancy center, to the cavity at temperatures below 10 K. Furthermore, we show that the integration of microwave delivery lines into our system, to address the spin states of cavity-enhanced nitrogen-vacancy centers, does not change the passive stability level.

4.2 Setup Design

A schematic drawing of the cavity geometry and the setup design is shown in Fig. 4.1 (b). The microcavity is mounted in an optical cryostat (Montana Instruments HILA) with an off-table cold head design and a base temperature of 5.6 K. The cold head is a two-stage Gifford-McMahon cryocooler, which is suspended inside a rack-mounted cooling tower assembly, hovering above the optical table. To minimize the vibration transfer, the cold head tower is connected over a loose bellow for vacuum and flexible braiding for cooling to the main chamber (see photograph in Appendix Fig. 4.10).

A computer-aided design (CAD) software drawing of the cryostat baseplate with the microcavity insert is shown in Fig. 4.2 (a) and a photograph in Appendix Fig. 4.9 (a). The baseplate is integrated into an auto-leveling floating stage acting as a low-pass filter for mechanical vibrations with a cutoff frequency of about 1 Hz. The baseplate is separated into three parts: an outer ring, kept at room temperature to mount the objective cone. An intermediate ring, which is connected to stage one of the cold head, reaching about 90 K. This ring is used for connecting the electrical cables and mounting the radiation shield separating microcavity and room temperature objective. The microcavity insert is placed on the central part, connected to stage two of the cold head, reaching the base temperature. The cryostat chamber (photograph shown in Appendix Fig. 4.9 (b)) is constantly pumped to a pressure in the range of 1×10^{-6} mbar, by an integrated turbopump and a differentially pumped outer vacuum.

The flexibility of moving the fiber over a millimeter-large range usually comes with the drawback of lower mechanical resonance frequencies, making the positioning system more susceptible to vibrations [43]. With a microcavity, where the fiber is placed on an orthogonal XYZ nanopositioning stage (JPE CS021), we measure a vibration level of about 0.5 nm directly on the baseplate at room temperature. A possible explanation for this is the low mechanical resonance frequencies of the nanopositioner stack (typically on the order of several 100 Hz), which are less suppressed by the isolation system.

To improve the vibration level, a different positioning system with a high internal resonance frequency is chosen. This is provided by the cryo positioning stage high resonance (JPE CPSHR1-a) placed on a passive vibration isolator (JPE CVIP1). The cross-section through the stage is shown in Fig. 4.2 (b). An optimized stiffness due to parallel kinematics results in a high resonance frequency of about 4 kHz along the cavity axis [44]. Three linear actuators (JPE CLA2201) move the fiber in situ in a tripod configuration over a range of more than 2 mm laterally and 1 mm along the cavity length axis, with a minimum step size of 1 nm at low temperatures. Additionally, each tripod axis is equipped with a fine scanning piezo element, with sub-nanometer resolution. This allows continuous cavity length detuning with frequencies up to 5 kHz over a range of up to 0.5 µm at low temperatures (all specifications of the CPSHR1-a stage can be found online [44]).

We employ two different ways of mounting the fiber, displayed in Fig. 4.2 (d): directly glued on a titanium holder or onto a shear piezo element featuring a high resonance frequency

(Noliac CSAP02). The latter enables high-bandwidth fine control of the cavity length, allowing for active cavity length stabilization [45]. In both settings, we use a two-component epoxy (Stycast 2850FT with catalyst LV 24) to glue the fiber. To guide the cavity fiber into the vacuum chamber, we make use of a 1/8 in stainless steel tube fitting (Swagelok male connector) with a custom-made Teflon ferrule. This ferrule has a borehole of 0.17 mm to fit the cavity fiber (Coherent FUD-4519 S630-P single-mode fiber) with a polyimide protection coating. Furthermore, we use a 0.25 mm thin polytetrafluoroethylene (PTFE) film (Reichelt Chemietechnik), cut to pieces of approximately 5 mm width and 25 mm length to further damp the fiber movement. This film connects the fiber mount and the reference frame (not shown in Fig. 4.2, see photograph in Appendix Fig. 4.8 (a)). We see that the additional damping by the film can improve the vibration level.
The sample mirror is mounted on top of the positioning system, separated by $> 100\,\mu m$ to the fiber. To ensure a good thermalization of the sample mirror to the baseplate, three flexible links made out of highly conductive copper (Montana Instruments custom-design) are used (not shown in the drawing, see Appendix Fig. 4.9 (a)). Each link is composed of multiple flat braids to ensure a good thermal connection in combination with a low transfer of vibrations from the baseplate to the cavity. This keeps the temperature difference between the mirror holder and baseplate to about 0.2 K. On the mirror holder, we monitor the temperature with a temperature sensor (Lake Shore Cryotronics Cernox 1050). To further ensure that the sample mirror reaches a low temperature, a 0.2 mm thin window (Edmond Optics Ultra-Thin N-BK7, with anti-reflection coating for 425 nm to 675 nm) glued into the radiation shield is used. This considerably reduces the heat load stemming from the black-body radiation of the room temperature objective that is about 4 mm away. The sample mirror is glued with silver conductive paint to the mirror holder, shown in Fig. 4.2 (c). In a test cooldown, we measure the temperature directly on the center of the sample mirror with a temperature sensor (Lake Shore Cryotronics Cernox Thin Film RTD), glued onto it with GE low-temperature varnish. Without the window, a temperature of around 20 K on the sample mirror is measured, while a temperature of about 8 K is reached with the window. This temperature is consistent with the measured linewidth of cavity-integrated diamond tin-vacancy centers in previous work [42].
To control the spin state of quantum emitters inside the cavity, microwaves are delivered to the cavity spot with gold striplines, embedded into the sample mirror [46]. The striplines are interfaced with 25 µm thin standard wire bonds to a support PCB, glued onto the cryostat insert (see Fig. 4.2 (b),(c) and Appendix Fig. 4.8 (b)). The PCB is connected with flexible coax cables (Montana Instruments LF-5 with SMP female ends) to semi-rigid coax cables (Montana Instruments C-20) on the baseplate, which are interfaced over a vacuum microwave feedthrough.
Optical access to the sample mirror side of the cavity is provided by a standard objective (Zeiss LD EC Epiplan-Neofluar, 100x magnification, 0.75 numerical aperture, 4 mm working distance). The objective can be positioned in a tripod configuration with three linear actuators (Physik Instrumente Q-545), mounted on an encircling stainless steel cone shown in Appendix Fig. 4.9 (b).

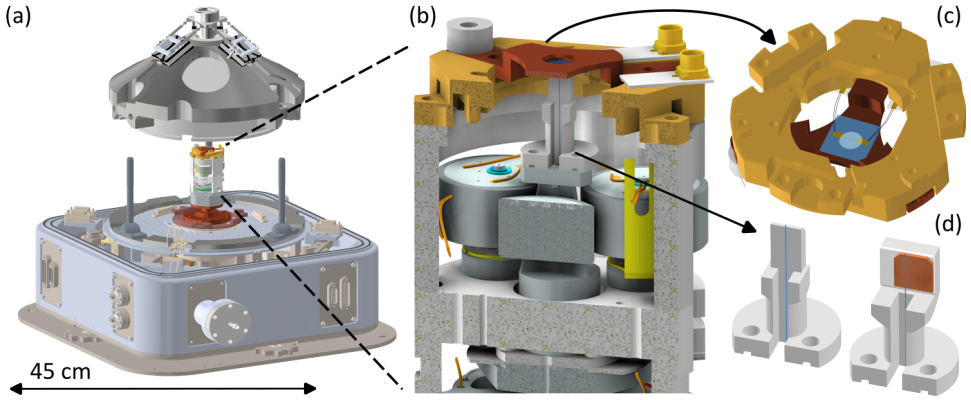

Figure 4.2: CAD drawing of the full setup with detailed individual parts. The drawing of the HILA cryostat in (a) is made by Montana Instruments, and the drawings of the positioner stage in (a) and (b) and the adapter piece in (c) are from JPE, used with permission and available under Ref. [47]. The drawing of the linear actuators in (a) is made by Physik Instrumente, used with permission, and is available under Ref. [48]. The drawing of the temperature sensor in (a) and (b) is made by Lakeshore, used with permission, and is available under Ref. [49]. (a) Floating cryostat baseplate with microcavity insert inside the vacuum chamber. The front part shows the fiber, microwave, and electrical feedthroughs. The insert is mounted on the copper-colored inner part of the baseplate, reaching a base temperature of 5.6 K. Two D-Sub 19 feedthroughs on the baseplate are used to connect the actuators, piezo elements, and temperature sensor to the control and readout electronics. The middle ring of the baseplate mounts the radiation shield (at about 90 K), while the outer part is used for the objective cone (at room temperature). (b) Cross-section of the microcavity insert. The fiber mount is positioned by three linear actuators in a tripod configuration. The sample mirror is glued on a copper holder, which is directly connected with flexible thermal links to the baseplate (not shown here, see photograph of the setup in the Appendix Fig. 4.9 (a)). The sample mirror has a thickness of about 0.5 mm, and is placed at a distance of $> 100\,\mu$m to the fiber, which can be compensated by the positioning system (a detailed sketch of the full microcavity insert can be found in Appendix Fig. 4.7). Each moving axis has an additional piezo element for fine positioning. We monitor the sample temperature with a sensor mounted on top of the microcavity insert. Furthermore, a support PCB is glued onto the stack to connect the mirror striplines to flexible coax cables. (c) Sample mirror on the copper holder with an adapter piece (JPE I2-CPSHR1) connecting to the reference frame. The gold striplines embedded into the mirror coating are connected with standard wire bonds to the support PCB. (d) Mounting of the cavity fiber: the fiber is glued either directly on a titanium mount (left) or onto a shear piezo element for fast fine control (right). The length of the fiber sticking out is kept as short as possible (between 100 µm and 200 µm) to avoid possible resonances associated with the overhanging fiber tip [45].

4.3 Microcavity Operation

The setup is controlled via a PC and the Python 3 framework QMI [50]. We use a real-time microcontroller (Jäger Computergesteuerte Messtechnik Adwin Pro II) for analog voltage control of the fine piezo element offset. Cavity scans with a frequency of up to 5 kHz are accomplished with a signal generator, connected to the fine piezo via a bias-T. The signal is amplified (JPE Piezo Scanning Module) and filtered afterward with a home-built voltage-controlled, switchable lowpass filter (cutoff frequency in the range of 30 Hz). Without filtering, we see that the noise from the amplifier can excite the resonance frequencies and increase the vibration level by a factor of up to two. The driving voltage of the linear actuators is also filtered and controlled by a high voltage amplifier (JPE Cryo Actuator Driver Module 2).

The microcavity is characterized by linewidth and length (or air length and membrane

thickness). With these parameters, important properties like finesse, quality factor, and mode volume can be calculated, and the sensitivity to vibrations can be determined. To measure the linewidth, we probe the cavity in transmission with two resonant lasers (Newfocus Velocity TLB-6300-LN and Toptica DL Pro), which are frequency-stabilized to a reference wavemeter (High Finesse WS-U). The cavity transmission signal is measured with a free-space photodiode (Thorlabs APD130A2). In Fig. 4.3 (a) we scan the cavity resonance over the two laser frequencies by applying a voltage to one of the fine piezo elements, moving the fiber. The difference in laser frequency is used to transform the scanning voltage into a change in cavity resonance frequency and to fit the two transmission peaks in the frequency domain. The use of two lasers with an arbitrary detuning allows the determination of a narrow, but also broader (> 10 GHz) cavity linewidth. This contrasts the use of a single laser with sidebands imprinted by an electrooptic phase modulator [33], in which case the range is limited by the frequency spacing of sidebands. To determine the cavity length, we probe the cavity in transmission with a supercontinuum white light source (NKT Photonics SC-450-2), filtered to 600 nm to 700 nm, which fully covers the cavity stopband (Fig. 4.3 (b)). The transmission signal is sent to a fiber-coupled spectrometer (Princeton Instruments SP-2500i). The cavity acts as a spectral filter, where fundamental modes appear as bright peaks in transmission. These modes are spaced by the free spectral range, which is directly related to the cavity length.

During cooling to the base temperature, the microcavity insert shrinks in height by about 550 µm (measured by the difference in the focal position of the objective), and the cavity length is reduced by about 50 µm.

Imaging through the objective with an LED and camera provides accurate observation of the cavity fiber position and the sample. The high magnification of the objective makes it possible to move the fiber with micrometer precision laterally over the sample mirror.

The cavity length stability, as a crucial system parameter, needs to be studied for different system configurations. For a given cavity length, the measured spectral cavity linewidth can be translated into a spatial linewidth, which allows direct measurement of the cavity length fluctuations. We use the same method as used in earlier work [33], where the cavity transmission signal is recorded and mapped to a change in cavity lengths (Fig. 4.3 (c)). The length is monitored with the cavity transmission signal, measured on a photodiode (50 MHz bandwidth) over a time of 10 s. This time trace is used to calculate the RMS vibrations, and a Fourier transform gives insights into the corresponding mechanical resonance frequencies. The cavity is operated in the low Finesse regime (1000 to 4000) to make sure that the transmission signal is fully caught on one half of the Lorentzian linewidth. Overshooting would lead to an underestimated cavity vibration level. To avoid this, we make sure that all points of the acquired length displacement trace follow an approximate Gaussian distribution (inset in Fig. 4.3 (c)).

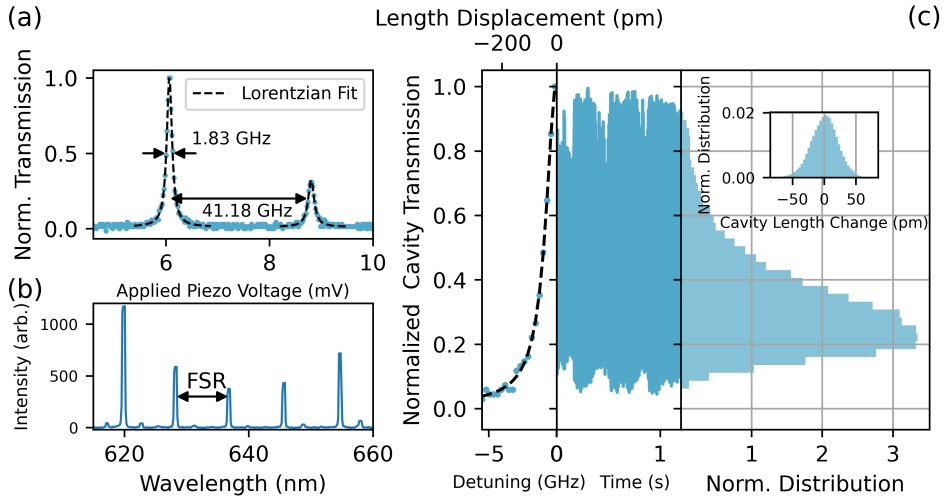

Figure 4.3: Characterizing the microcavity properties and the vibration level. (a) Cavity linewidth measurement with two detuned resonant lasers. The cavity transmission is probed by applying a voltage to one of the fine piezo elements to scan the cavity length (scan frequency of 2.33 kHz). (b) Cavity length measurement by probing the transmission of a broadband supercontinuum white light source. The visible fundamental modes directly determine the free spectral range and the cavity length. (c) Exemplary cavity vibration measurement: the cavity transmission signal (center panel) is mapped on half of the Lorentzian cavity resonance (left panel). The spatial linewidth of the cavity allows for translating the transmission signal into a change in length. The right panel shows a histogram of the transmission for the full measurement (10 s). The insert shows the corresponding distribution of the cavity length values.

4.4 Performance of System at Low Temperatures

At ambient temperature under vacuum of typically 1×10^{-6} mbar, we measure a vibration level less than 4 pm. At low temperatures, we see an increase to about 25 pm. This level is consistently reached for several setup configurations, including different fiber and sample mounting and the integrated electronics for applying microwaves. Figure 4.4 (a) shows the integrated noise spectrum of the measured length fluctuations, and Fig. 4.4 (b) an individual frequency spectrum. The length fluctuations show a small low-frequency contribution, which we attribute to the cold head cycle of the cryostat, running with a speed of about 1.4 Hz (settings: 25 Hz compressor and 70 Hz cold head). For all configurations, the spectrum shows a jump between 2 kHz and 4 kHz, which fits the first resonance of the fiber positioning system along the cavity axis. Most configurations show an almost flat spectrum for frequencies higher than 5 kHz.

Another measure of the vibration level is a resonant laser scan over the cavity transmission, shown in Fig. 4.4 (c). The cavity is probed with a resonant 637 nm laser from the fiber side and the transmission signal is recorded with a fiber-coupled single photon detector (Laser Components COUNT-10C-FC). With the cavity length, we determine a dispersion of 20 MHz/pm. In the previous measurement in Fig. 4.3 (a) the linewidth is measured by scanning the cavity with a high scan speed to 'freeze' the vibrations, revealing the intrinsic cavity linewidth (shown in Fig. 4.3 (a)). In contrast, the cavity is at a fixed length

in Fig. 4.4 (c), but the resonant laser frequency is swept to measure the linewidth. The data is fitted with a Voigt profile with a fixed Lorentzian part set to the intrinsic cavity linewidth. Vibrations lead to a Gaussian broadening, which can be transformed into an RMS vibration level with the dispersion relation. For the scans shown in Fig. 4.4 (c), we measure a vibration level of $(25.1 \pm 1.1)\,\mathrm{pm}$, which is close to the 22 pm measured in Fig. 4.4 (a).
We want to emphasize that the low vibration level is reproducibly reached for different configurations, in which the fiber or sample mounting is changed. Furthermore, it is also independent of the additional integration of microwave cables, a support PCB, and wire bonds to the sample mirror. The microcavity insert was reassembled in between different configurations, and thermally cycled for more than 50 times over two years without a degradation in performance. We do not see a vibration dependence on the exact wiring of cables used to connect the piezo elements or the microwave wires. Moreover, the vibration level did not change after exchanging the cold head.
In addition to vibrations $> 1\,\mathrm{Hz}$, the cavity can show drifts on longer timescales. When operated with higher incident laser power ($> 1\,\mu\mathrm{W}$) or microwave power ($> 25\,\mathrm{dBm}$ measured before the input of the cryostat, see next section for the transmission losses), cavity length drifts of more than one linewidth can be observed. However, after some time (order of minutes), the drifts reduce to a new equilibrium.
The closed-cycle operation of the cryostat allows to operate the cavity at a constant temperature (cryostat temperature stability $< 25\,\mathrm{mK}$) and to maintain the exact cavity spot for a longer time. In previous work [42], measurements with the same cavity-coupled diamond tin-vacancy center were conducted for more than two months with preserved cavity parameters.

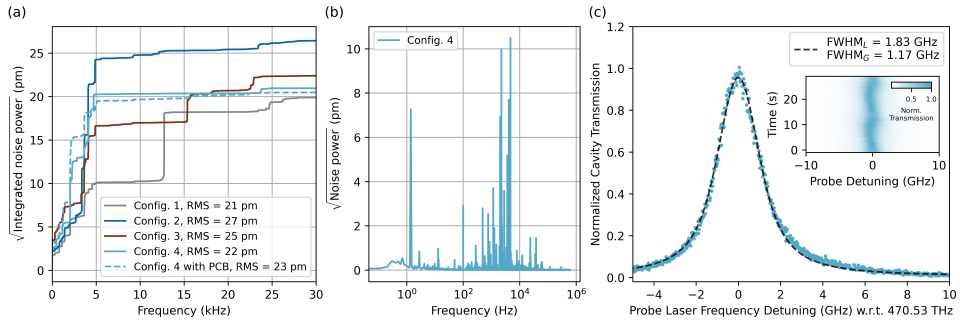

Figure 4.4: System performance at low temperatures for different setup configurations. (a) A comparable vibration level is reached for different settings: for the first three configurations, the fiber is mounted on a shear piezo element (right side of Fig. 2 (d)), while configuration four is without (left side of Fig. 2 (d)). All configurations use different cavity fibers and sample mirrors; configuration two was used in previous work with diamond tin-vacancy centers [42]. The extended PCB for microwave control in configuration four does not influence the vibration level. (b) Resonance spectrum of configuration four, revealing a typical resonance at 1.4 Hz corresponding to the cold head cycle and resonances up to 5 kHz attributed to the fiber positioning system. (c) Resonant cavity transmission scan for configuration four. The cavity is probed with a scan speed of about 10 GHz/s. The data is fitted with a Voigt profile, in which the Lorentzian part is fixed to the cavity linewidth. The Gaussian component can be used to calculate the vibration level. The inset shows 15 consecutive scans.

The same microcavity insert (JPE CVIP 1 with CPSHR1-a) was operated in earlier work [33] in a standard optical cryostation (Montana Instruments C2). Thanks to the similarity in setup design, it is instructive to compare both performances, see Fig. 4.5. The much better vibration isolation of the HILA leads to an almost six times improved RMS vibration level and a much smaller dependence on the cryostat cycle.
There are several further improvements of the vibration level possible: the damping with the PTFE film as explained in Section 4.2 can be optimized. Furthermore, the stability of the system would benefit from an increased mechanical resonance frequency of the positioning system, which can be achieved by further engineering. For example, a higher resonance frequency might be achievable by removing the fine piezo element and losing the ability for precise positioning and scanning of the fiber. Along the cavity axis, this could be compensated by using the shear piezo element with a scanning range of about 300 nm at low temperatures. Another possibility would be to increase the temperature of the positioning system. At room temperature, under vacuum, and with a running cold head, we observe a much better vibration level. An explanation could be that temperature-dependent material properties lead to an increased vibration level at low temperatures. Thus, putting the fiber positioning system at a higher temperature (for example, on stage one of the cold head at 90 K) might further improve the stability.
Furthermore, if it is compatible with the sample, it might be beneficial to operate the fiber in contact with the sample mirror. In a similar setup with a fiber-based microcavity in a closed-cycle cryostat [38], this resulted in a vibration level improved by a factor of six.
So far, we have only discussed the passive stability of the system. Most mechanical resonance frequencies are present below 10 kHz, which makes active length stabilization appealing. The use of a high bandwidth piezo element in a similar system enabled a locking bandwidth of 44 kHz [45], which would be sufficient to compensate for the resonance frequencies present in our system. Active stabilization would require some experimental overhead, like an additional laser and a broad (or second) cavity stopband, to find a cavity resonance that can be used to generate the error signal. This is especially challenging for a short cavity with a large free spectral range. Furthermore, the locking laser could lead to stimulated emission of the cavity-coupled emitters [51]. To avoid this, a second cavity formed by an additional fiber dimple can be utilized for active length stabilization [52].

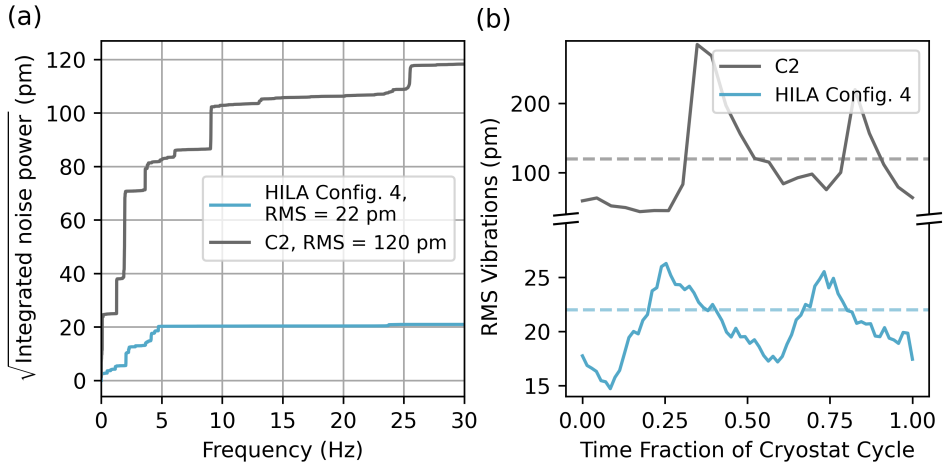

Figure 4.5: Comparison of vibration level achieved in configuration four with the HILA cryostat (light blue) versus the C2 optical cryostation (grey), used in an earlier experiment [33]. (a) Integrated noise spectra show that the mechanical resonance frequencies of the positioning system are excited in both cryostats, although at a much lower level in the HILA. Frequencies larger than 5 kHz are almost completely suppressed in the HILA. (b) RMS vibration level scaled to the time fraction of the cryostat cycle (about 0.7 s for the HILA and 1.2 s for the C2). The HILA shows a much smaller susceptibility to 'kicks' within the cold head cycle.

4.5 Cavity-coupled Diamond Color Centers with Microwave Control

We showcase the versatility of our platform by coupling two types of diamond color centers to the cavity, namely tin-vacancy (SnV) and nitrogen-vacancy (NV) centers, shown in Fig. 4.6 (a) and (b), respectively. The SnV sample is a $70\,\mathrm{x}\,70\,\mu\mathrm{m}^2$ square diamond device with a thickness of about 2.2 µm bonded to the sample mirror via Van der Waals force [40]. SnV centers are created by ion implantation in the range of the first intracavity electric field antinode. The NV sample is a $2\,\mathrm{x}\,2\,\mathrm{mm}^2$ and about 50 µm thick diamond membrane, with a central part thinned down to a thickness of about 5.8 µm, used in earlier work [33]. NV centers are created by electron irradiation and annealing [29]. The cavity spot shown in the inset of Fig. 4.6 (b) is formed in the thinned-down region.

To demonstrate that diamond color centers are coupled to the cavity at low temperature, we use off-resonant 515 nm excitation light (Hübner Photonics Cobolt MLD515) sent into the cavity via the fiber. The detection signal is collected from the sample mirror side by collimating the Gaussian beam leaving the cavity with the objective. The detection is filtered with a 600 nm longpass filter and measured with a spectrometer. The cavity resonance frequency is tuned around the emitter zero-phonon line by scanning the voltage of the three fine piezo elements. Once the cavity becomes resonant with an emitter, enhanced photoluminescence at that frequency is observed. An individual emitter can then be selectively coupled to the cavity by adjusting the fine piezo element voltage to the corresponding resonance frequency.

An essential capability for quantum information applications is qubit control, which can

be efficiently achieved through driving the corresponding spin states with microwaves. To deliver microwaves close to the cavity spot, 65 nm thin gold striplines are partly embedded into the sample mirror with nano-fabrication methods [46]. The striplines are connected as described in Section 4.2. With a vector network analyzer, we measure around 6.5 dB transmission loss including the PCB at a frequency of 2.88 GHz. The total cryostat transmission losses add up to about 25 dB due to several cable connections. To demonstrate the ability to address the spin states of the NV center, we measure an optically detected magnetic resonance (ODMR) spectrum without and with a static magnetic field, shown in Fig. 4.6 (c) and (d). The NV centers are excited with off-resonant green light sent in via the cavity fiber. Cavity-enhanced zero-phonon light is detected from the free space side with a single photon detector. This light is filtered with a 600 nm longpass filter, a (640 ± 5) nm bandpass filter and an angle-tunable etalon filter (LightMachinery custom coating, full width at half maximum ≈ 100 GHz). The cavity is kept on resonance during the ODMR measurement by interleaved probing of the cavity transmission with a reference laser and a voltage feedback on the fine piezo element. An external magnetic field is provided by a neodymium disc magnet (Supermagnete S-70-35-N), which is mounted on top of the cryostat vacuum chamber lid. Microwaves are delivered by a single-sideband modulated vector signal generator (Rohde & Schwarz SMBV100A) with an output power of -5 dBm (-3 dBm for the higher-frequency transition), which is amplified by 35 dB (MiniCiruits ZVE-6W-83+). A reduction in NV photoluminescence is observed when the microwave driving is on resonance with one of the ground-state spin transitions.

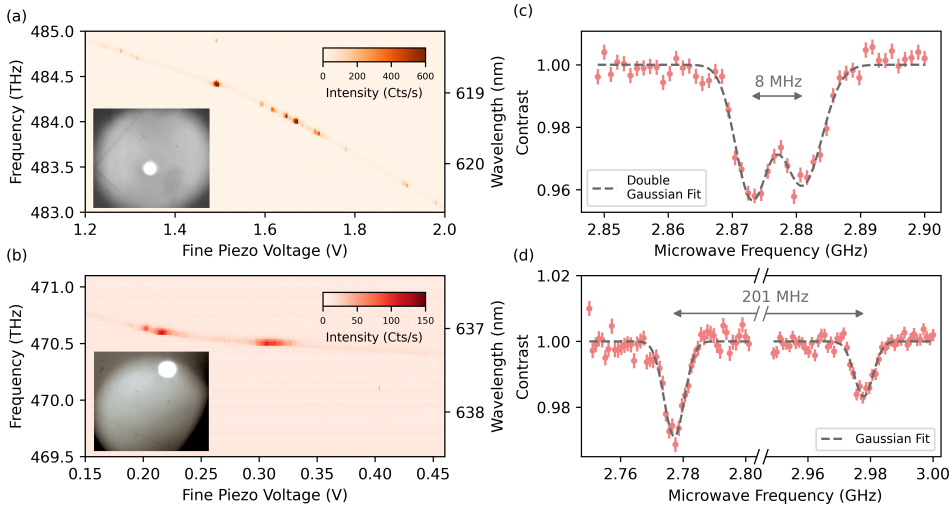

Figure 4.6: Platform versatility and microwave spin addressing. The insets of (a) and (b) show an about $50\,\mathrm{x}\,50\,\mu\mathrm{m}^2$ large section. (a) Cavity-coupled SnV centers under off-resonant excitation. The cavity mode (faint straight line) is scanned over the 619 nm and 620 nm zero-phonon line transitions of several SnV centers within the mode volume, which appear as bright spots. The inset shows the diamond device hosting the color centers bonded to the sample mirror. The position of the cavity on the sample is indicated by the bright laser spot, stemming from a green laser for which the cavity is mostly transparent. (b) Cavity-coupled NV centers. Under green excitation, the NV center is mostly initialized into the spin ground state. When the cavity becomes resonant, it enhances the E_x or E_y zero-phonon line transitions. The inset shows the thinned-down diamond membrane bonded to the sample mirror and the approximately 30 µm distant gold stripline. The nonlinearity in the cavity resonance in (a) and (b) stems from a small cavity length drift during the data acquisition. (c) ODMR measurement of a cavity-coupled NV center without an applied magnetic field. The NV zero field splitting around 2.87 GHz can be observed as a resonance. The splitting of 8 MHz can originate from a residual magnetic field or a strongly coupled carbon nuclear spin in the vicinity of the NV center. (d) ODMR measurement of a cavity-coupled NV center with an external static magnetic field. In the presence of the magnetic field, the two resonances associated with the NV electron spin are separated by the Zeeman splitting $2\gamma_e B_z$, with the NV electron spin gyromagnetic ratio γ_e and the magnetic field B_z. The splitting of 201 MHz corresponds to $B_z \approx 36\,\mathrm{G}$. The lower contrast for the high-frequency transition is caused by increased microwave losses at this frequency. Note that the ODMR measurements were acquired at a cavity spot around 20 µm distant to the stripline, which is a different spot than shown in (b). All measurements are performed at a sample temperature of about 8 K.

4.6 Conclusion

We present the design, assembly, and operation of a fiber-based microcavity platform with high passive stability and demonstrate the cavity coupling of diamond color centers together with the ability to address the spin of cavity-coupled NV centers with microwaves. The key elements for achieving high passive stability are the combination of a low-noise cryostat with incorporated vibration suppression and a positioning system with a high mechanical resonance frequency. The resulting separation of noise frequencies and the positioning system resonance frequencies leads to the high cavity length stability. Our system shows robustness and reproducibility over many thermal cycles with varied setup configurations. Moreover, the passive stability seems to be independent of experimental imperfections such as the exact wiring of cables or the tightness of screws. The vibrations in our system are mainly caused by the cold head, and we do not observe any influences on the vibration level of other external sources, like acoustic noise.

With improvements such as demonstrated by a related system [38] or by active cavity length stabilization [53], it might be possible to further reduce the vibration level. A stability improvement by another order of magnitude would render the effect of the vibrations on the maximum attainable Purcell factor almost negligible.

Notably, all parts for achieving the high passive vibration level, such as the floating baseplate cryostat and the fiber positioning system, are commercial.

For the estimated values for diamond color centers in Fig. 4.1 (a), the achieved passive stability would allow for an air-like Purcell factor up to about 25, with even higher values possible for a diamond-like cavity, in conjunction with good collection efficiency. With the integration of microwaves for full qubit control, this system provides a promising platform for testing and utilizing efficient qubit-photon interfaces.

4.7 Acknowledgement

We thank Arian Stolk and Kai-Niklas Schymik for feedback on the manuscript, Matteo Pasini for helpful discussions, Siebe Visser for technical support, Jason Mensingh and Olaf Benningshof for cryogenic engineering support, Nico Alberts and Tim Hiep for machining the custom parts, Raymond Vermeulen and Raymond Schouten for development of custom electronics, and Henri Ervasti for software development and support.

We thank Robbert Voorhoeve, Tom Duivenvoorde, Teun van den Dool, and Gert Witvoet from TNO for support on the setup design. Furthermore, we thank Hans Spierdijk and Jan de Vreugd from TNO for the design of the objective stage. We acknowledge support on device fabrication from Hans van den Berg, Jasper Flipse, and Nick de Jong from TNO. We thank Bart van Bree and Huub Janssen from JPE for helpful discussions and support on the cryo positioning stage. We thank Matt Ballinger and Alex Crane from Montana Instruments and Robert Janz and David Appel from Quantum Design for helpful discussions and the installation and support of the HILA cryostat.

We acknowledge funding from the Dutch Research Council (NWO) through the Spinoza Prize 2019 (project number SPI 63-264). We further acknowledge financial support from the EU Flagship on Quantum Technologies through the project Quantum Internet Alliance (EU Horizon 2020, grant agreement no. 820445). This research is supported by the Early Research Programme of the Netherlands Organisation for Applied Scientific Research

(TNO). Additional support from the Top Sector High Tech Systems and Materials is highly appreciated.

4.7.1 Author Contributions

Y. H. and J. F. contributed equally to this work. Y. H. and J. F. conducted the experiments and analyzed the data. S. S. characterized the cavity fibers and measured the data for one of the setup configurations. C. W. developed the ODMR measurements. M. R. developed parts of the device fabrication process and designed together with M. J. W., Y. H. and J. F. the setup. Y. H., J. F., L. J. F. and M. J. W. built the setup. J. M. B., C. S. and Y. H. fabricated the tin-vacancy diamond device. L. G. C. W. characterized the tin-vacancy diamond device and cavity fibers in a room-temperature cavity. M. R. fabricated the nitrogen-vacancy diamond device. M. E. fabricated the cavity fibers. Y. H., J. F., and R. H. wrote the manuscript with input from all authors. R. H. supervised the experiments.

4.7.2 Data Availability

The data that support the findings of this study are openly available on 4TU.ResearchData: 'Data underlying the publication "A Low-Temperature Tunable Microcavity featuring', at `https://www.doi.org/10.4121/451152e2-a4d4-4e42-96e0-4147afb1e45c` under reference number [54].

4.8 Appendix

4.8.1 Derivation of the Maximum Attainable Purcell Factor

The Purcell factor is defined as [55]

$$F_P = \frac{3}{4\pi^2}\left(\frac{c}{n\nu}\right)^3 \frac{Q}{V}, \tag{4.2}$$

with the cavity resonance frequency ν, refractive index n, cavity quality factor Q, cavity mode volume V, refractive index of diamond n and the speed of light c.

The spectral overlap of an emitter with a linewidth much smaller than the cavity linewidth is given by [32]

$$\xi_s(\Delta\nu) = \frac{1}{1+\frac{4Q^2}{\nu^2}\Delta\nu^2}, \tag{4.3}$$

with the cavity resonance frequency ν and the emitter-cavity detuning $\Delta\nu$.

The cavity frequency fluctuations can be modeled by a Gaussian distribution, where the probability density function reads [33]

$$f(\Delta\nu) = \frac{1}{\sqrt{2\pi\sigma_\nu^2}} e^{-\Delta\nu^2/2\sigma_\nu^2}, \tag{4.4}$$

with the RMS value of the cavity frequency fluctuations $\sigma_\nu = s\sigma$, where s is the cavity mode dispersion slope and σ the RMS cavity length fluctuations.

For an emitter on cavity resonance, the effective vibration-averaged Purcell factor can be calculated with

$$F_{P,vib} = F_P \int_{-\infty}^{\infty} d(\Delta\nu)\xi_s(\Delta\nu)f(\Delta\nu). \tag{4.5}$$

For a given cavity geometry, which determines the cavity mode volume V and the cavity mode dispersion slope s, the maximum attainable Purcell factor follows as

$$F_{P,max} = \max_{Q>0} F_{P,vib} = \frac{3}{4\pi^2}\left(\frac{c}{n\nu}\right)^3 \frac{1}{V}\sqrt{\frac{\pi}{2(s\sigma)^2}}\frac{\nu}{2}. \tag{4.6}$$

To obtain equation (4.6) we make use of

$$\int_{-\infty}^{\infty} dx \frac{e^{-x^2/B}}{1+Ax^2} = \frac{\pi e^{1/AB}\mathrm{erfc}\left(1/\sqrt{AB}\right)}{\sqrt{A}}, \tag{4.7}$$

with $A > 0$, $B > 0$ and the complementary error function $\mathrm{erfc}(x) = 1 - \mathrm{erf}(x)$ as well as

$$\max_{x>0}\left(e^{1/x^2}\mathrm{erfc}(1/x)\right) = 1. \tag{4.8}$$

4.8.2 Cavity Fiber Positioning System

Fig. 4.7 shows a sketch of the full microcavity insert, which is presented in the main text as a rendered CAD drawing in Fig. 4.2 (b).

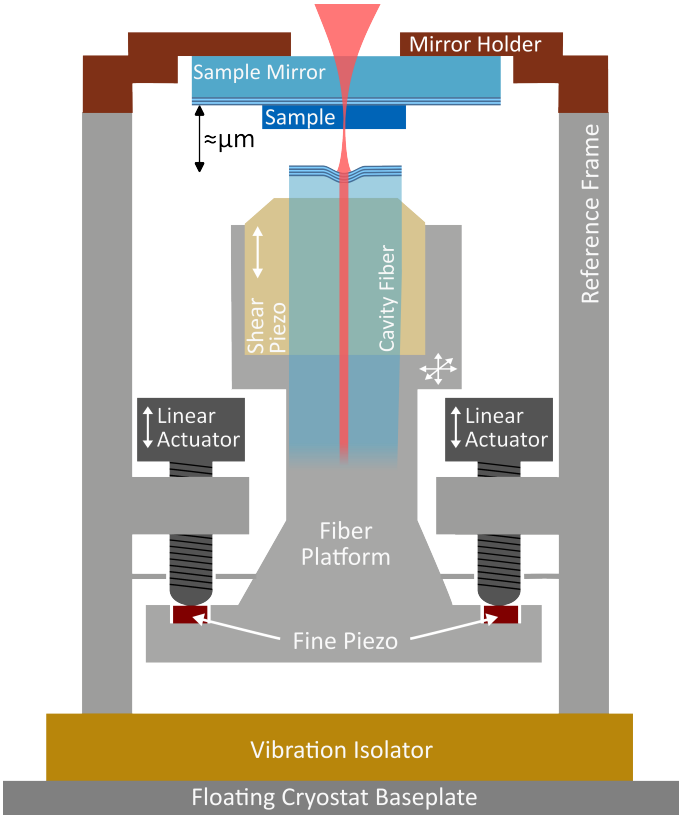

Figure 4.7: Sketch of the microcavity insert. Three linear actuators (JPE CLA2201) position the cavity fiber in front of the sample mirror: moving all three actuators simultaneously changes the cavity length in axial direction, while a single actuator movement changes the lateral position (together with a small change in the fiber angle). Each axis can additionally be controlled with a fine scanning piezo, which is clamped between the fiber platform and the linear actuators. Optionally, the fiber can be glued on a shear piezo for axial cavity length control. A passive vibration isolator (JPE CVIP1) is placed underneath the positioning system (JPE CPSHR1-a).

4.8.3 Photographs of the Setup

Photographs of individual parts of the setup and the cryostat can be found in Fig. 4.8 to Fig. 4.10.

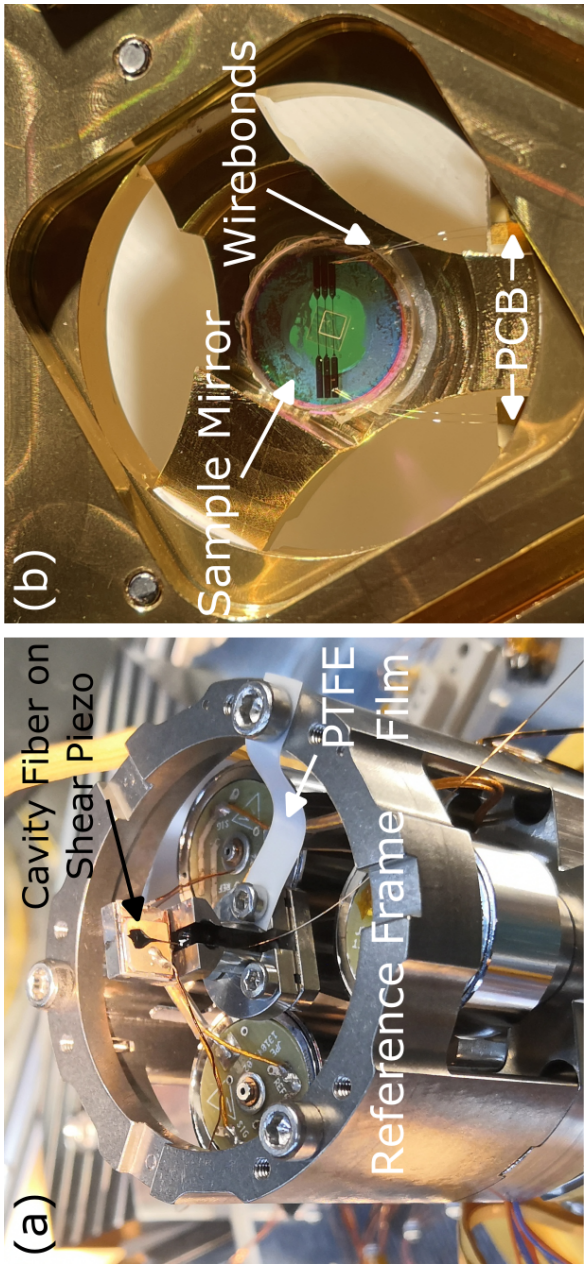

Figure 4.8: Photograph of the fiber and sample mounting. (a) The lower half of the cavity: cavity fiber glued to the shear piezo element for fast cavity length control. A 0.25 mm thin PTFE film is used to introduce additional damping, which can improve the passive stability. The platform with the fiber mount is moved in situ by the positioning system. (b) The upper half of the cavity: the sample mirror with embedded microwave stripline and a partially thinned-down diamond membrane. A support PCB is glued to the mirror holder adapter to connect the microwave lines via wire bonds.

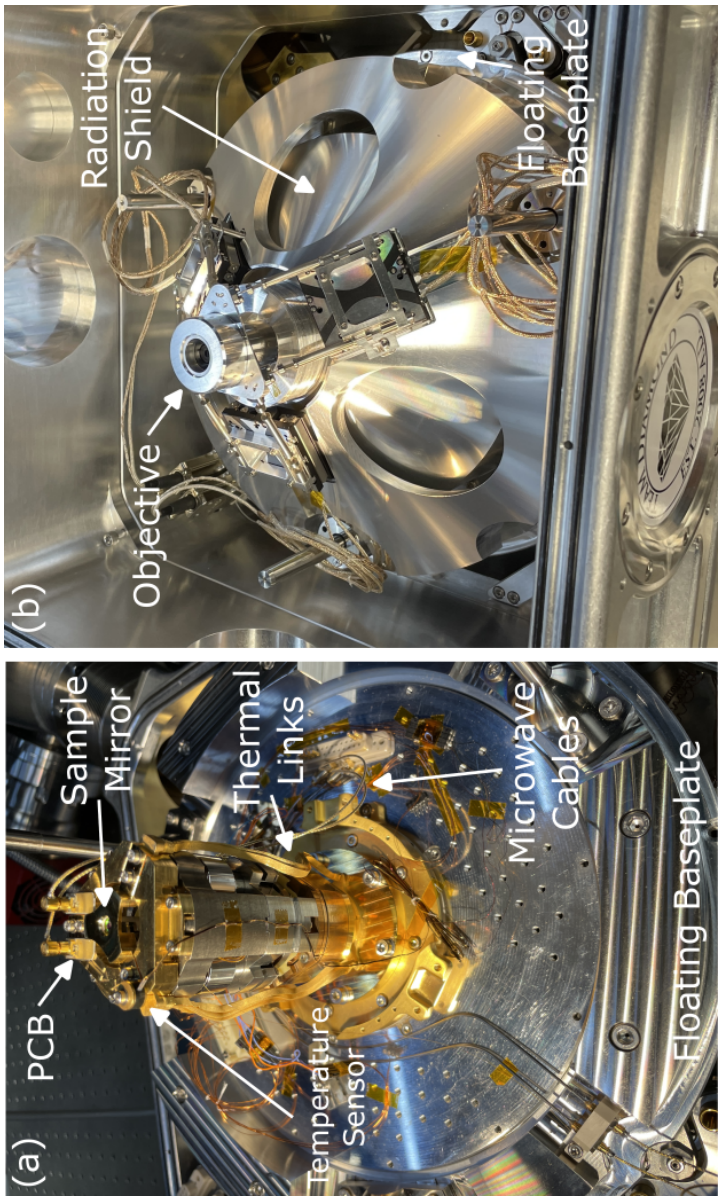

Figure 4.9: Photograph of the microcavity insert and the enclosing objective cone. (a) The insert is placed on the 5.6 K platform of the cryostat baseplate. Three thermal links ensure a good thermalization of the mirror holder to the baseplate. The temperature reached on top of the stack is monitored with a temperature sensor. The microwave lines of the PCB are connected with flexible coax cables to the baseplate to minimize the transfer of vibrations. On the baseplate, microwaves are guided by rigid cables to the vacuum feedthrough. (b) The insert is enclosed by a radiation shield and a stainless steel cone mounting the objective with linear actuators in a tripod setting. The radiation shield is made of a lower cone and an upper cylinder with an opening fitting the objective. The upper part is screwed into the lower part. The cone and objective are at room temperature inside the cryostat vacuum chamber.

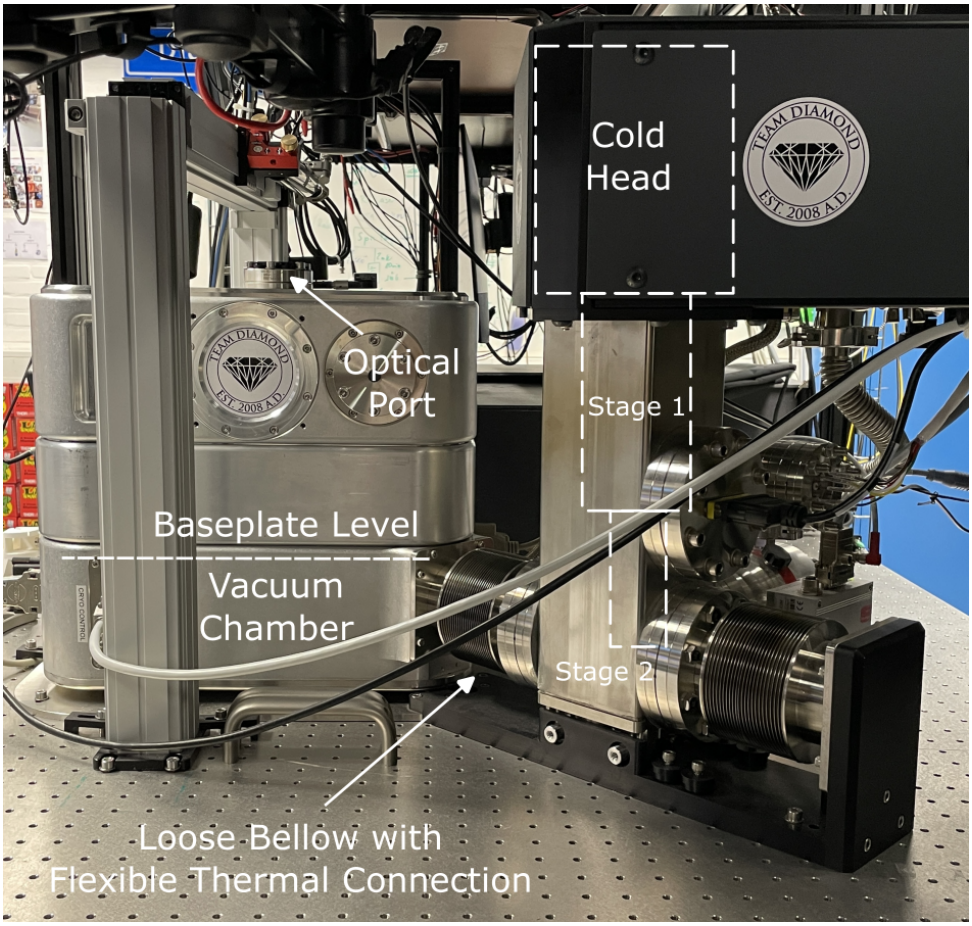

Figure 4.10: Photograph of the HILA cryostat vacuum chamber with the off-table cold head inside the tower assembly, mounted by a rack next to the optical table. Both stages of the cold head are connected over flexible thermal links with the floating baseplate inside the vacuum chamber.

References

[1] D. D. Awschalom, R. Hanson, J. Wrachtrup, and B. B. Zhou, *Quantum technologies with optically interfaced solid-state spins,* Nature Photonics **12**, 516 (2018).

[2] M. Atatüre, D. Englund, N. Vamivakas, S.-Y. Lee, and J. Wrachtrup, *Material platforms for spin-based photonic quantum technologies,* Nature Reviews Materials **3**, 38 (2018).

[3] G. Wolfowicz, F. J. Heremans, C. P. Anderson, S. Kanai, H. Seo, A. Gali, G. Galli, and D. D. Awschalom, *Quantum guidelines for solid-state spin defects,* Nature Reviews Materials **6**, 906 (2021).

[4] K. J. Vahala, *Optical microcavities,* Nature **424**, 839 (2003).

[5] A. Reiserer and G. Rempe, *Cavity-based quantum networks with single atoms and optical photons,* Reviews of Modern Physics **87**, 1379 (2015).

[6] E. Janitz, M. K. Bhaskar, and L. Childress, *Cavity quantum electrodynamics with color centers in diamond,* Optica **7**, 1232 (2020).

[7] M. Ruf, N. H. Wan, H. Choi, D. Englund, and R. Hanson, *Quantum networks based on color centers in diamond,* Journal of Applied Physics **130**, 070901 (2021).

[8] A. Muller, E. B. Flagg, M. Metcalfe, J. Lawall, and G. S. Solomon, *Coupling an epitaxial quantum dot to a fiber-based external-mirror microcavity,* Applied Physics Letters **95**, 173101 (2009).

[9] Z. Di, H. V. Jones, P. R. Dolan, S. M. Fairclough, M. B. Wincott, J. Fill, G. M. Hughes, and J. M. Smith, *Controlling the emission from semiconductor quantum dots using ultra-small tunable optical microcavities,* New Journal of Physics **14**, 103048 (2012).

[10] D. Najer, I. Söllner, P. Sekatski, V. Dolique, M. C. Löbl, D. Riedel, R. Schott, S. Starosielec, S. R. Valentin, A. D. Wieck, N. Sangouard, A. Ludwig, and R. J. Warburton, *A gated quantum dot strongly coupled to an optical microcavity,* Nature **575**, 622 (2019).

[11] N. O. Antoniadis, M. R. Hogg, W. F. Stehl, A. Javadi, N. Tomm, R. Schott, S. R. Valentin, A. D. Wieck, A. Ludwig, and R. J. Warburton, *Cavity-enhanced single-shot readout of a quantum dot spin within 3 nanoseconds,* Nature Communications **14**, 3977 (2023).

[12] T. Vogl, R. Lecamwasam, B. C. Buchler, Y. Lu, and P. K. Lam, *Compact Cavity-Enhanced Single-Photon Generation with Hexagonal Boron Nitride,* ACS Photonics **6**, 1955 (2019).

[13] S. Vadia, J. Scherzer, H. Thierschmann, C. Schäfermeier, C. Dal Savio, T. Taniguchi, K. Watanabe, D. Hunger, K. Karraï, and A. Högele, *Open-Cavity in Closed-Cycle Cryostat as a Quantum Optics Platform,* PRX Quantum **2**, 040318 (2021).

[14] L. B. Tan, O. K. Diessel, A. Popert, R. Schmidt, A. Imamoglu, and M. Kroner, *Bose Polaron Interactions in a Cavity-Coupled Monolayer Semiconductor,* Physical Review X **13**, 031036 (2023).

[15] T. Hümmer, J. Noe, M. S. Hofmann, T. W. Hänsch, A. Högele, and D. Hunger, *Cavity-enhanced Raman microscopy of individual carbon nanotubes,* Nature Communications **7**, 12155 (2016).

[16] A. Borel, T. Habrant-Claude, F. Rapisarda, J. Reichel, S. K. Doorn, C. Voisin, and Y. Chassagneux, *Telecom Band Single-Photon Source Using a Grafted Carbon Nanotube Coupled to a Fiber Fabry–Perot Cavity in the Purcell Regime,* ACS Photonics **10**, 2839 (2023).

[17] B. Casabone, C. Deshmukh, S. Liu, D. Serrano, A. Ferrier, T. Hümmer, P. Goldner, D. Hunger, and H. De Riedmatten, *Dynamic control of Purcell enhanced emission of erbium ions in nanoparticles,* Nature Communications **12**, 3570 (2021).

[18] R. Albrecht, A. Bommer, C. Deutsch, J. Reichel, and C. Becher, *Coupling of a Single Nitrogen-Vacancy Center in Diamond to a Fiber-Based Microcavity,* Physical Review Letters **110**, 243602 (2013).

[19] S. Johnson, P. R. Dolan, T. Grange, A. A. P. Trichet, G. Hornecker, Y. C. Chen, L. Weng, G. M. Hughes, A. A. R. Watt, A. Auffèves, and J. M. Smith, *Tunable cavity coupling of the zero phonon line of a nitrogen-vacancy defect in diamond,* New Journal of Physics **17**, 122003 (2015).

[20] J. Benedikter, H. Kaupp, T. Hümmer, Y. Liang, A. Bommer, C. Becher, A. Krueger, J. M. Smith, T. W. Hänsch, and D. Hunger, *Cavity-Enhanced Single-Photon Source Based on the Silicon-Vacancy Center in Diamond,* Physical Review Applied **7**, 024031 (2017).

[21] G. Bayer, R. Berghaus, S. Sachero, A. B. Filipovski, L. Antoniuk, N. Lettner, R. Waltrich, M. Klotz, P. Maier, V. Agafonov, and A. Kubanek, *Optical driving, spin initialization and readout of single SiV^- centers in a Fabry-Perot resonator,* Communications Physics **6**, 300 (2023).

[22] V. Yurgens, Y. Fontana, A. Corazza, B. J. Shields, P. Maletinsky, and R. J. Warburton, *Cavity-assisted resonance fluorescence from a nitrogen-vacancy center in diamond,* npj Quantum Information **10**, 112 (2024).

[23] R. Berghaus, S. Sachero, G. Bayer, J. Heupel, T. Herzig, F. Feuchtmayr, J. Meijer, C. Popov, and A. Kubanek, *Cavity-enhanced emission and absorption of color centers in a diamond membrane with selectable strain,* Physical Review Applied **23**, 034050 (2025).

[24] R. Zifkin, C. D. Rodríguez Rosenblueth, E. Janitz, Y. Fontana, and L. Childress, *Lifetime Reduction of Single Germanium-Vacancy Centers in Diamond via a Tunable Open Microcavity,* PRX Quantum **5**, 030308 (2024).

[25] D. M. Lukin, M. A. Guidry, and J. Vučković, *Integrated Quantum Photonics with Silicon Carbide: Challenges and Prospects,* PRX Quantum **1**, 020102 (2020).

[26] J. Heiler, J. Körber, E. Hesselmeier, P. Kuna, R. Stöhr, P. Fuchs, M. Ghezellou, J. Ul-Hassan, W. Knolle, C. Becher, F. Kaiser, and J. Wrachtrup, *Spectral stability of V2 centres in sub-micron 4H-SiC membranes,* npj Quantum Materials **9**, 34 (2024).

[27] B. Merkel, A. Ulanowski, and A. Reiserer, *Coherent and Purcell-Enhanced Emission from Erbium Dopants in a Cryogenic High- Q Resonator,* Physical Review X **10**, 041025 (2020).

[28] D. Wang, H. Kelkar, D. Martin-Cano, D. Rattenbacher, A. Shkarin, T. Utikal, S. Götzinger, and V. Sandoghdar, *Turning a molecule into a coherent two-level quantum system,* Nature Physics **15**, 483 (2019).

[29] M. Ruf, M. IJspeert, S. van Dam, N. de Jong, H. van den Berg, G. Evers, and R. Hanson, *Optically Coherent Nitrogen-Vacancy Centers in Micrometer-Thin Etched Diamond Membranes,* Nano Letters **19**, 3987 (2019).

[30] D. Hunger, T. Steinmetz, Y. Colombe, C. Deutsch, T. W. Hänsch, and J. Reichel, *A fiber Fabry–Perot cavity with high finesse,* New Journal of Physics **12**, 065038 (2010).

[31] D. Hunger, C. Deutsch, R. J. Barbour, R. J. Warburton, and J. Reichel, *Laser micro-fabrication of concave, low-roughness features in silica,* AIP Advances **2**, 012119 (2012).

[32] S. B. van Dam, M. Ruf, and R. Hanson, *Optimal design of diamond-air microcavities for quantum networks using an analytical approach,* New Journal of Physics **20**, 115004 (2018).

[33] M. Ruf, M. Weaver, S. van Dam, and R. Hanson, *Resonant Excitation and Purcell Enhancement of Coherent Nitrogen-Vacancy Centers Coupled to a Fabry-Perot Microcavity,* Physical Review Applied **15**, 024049 (2021).

[34] E. Janitz, M. Ruf, M. Dimock, A. Bourassa, J. Sankey, and L. Childress, *Fabry-Perot microcavity for diamond-based photonics,* Physical Review A **92**, 043844 (2015).

[35] L. Greuter, S. Starosielec, D. Najer, A. Ludwig, L. Duempelmann, D. Rohner, and R. J. Warburton, *A small mode volume tunable microcavity: Development and characterization,* Applied Physics Letters **105**, 121105 (2014).

[36] Y. Fontana, R. Zifkin, E. Janitz, C. D. Rodríguez Rosenblueth, and L. Childress, *A mechanically stable and tunable cryogenic Fabry–Pérot microcavity,* Review of Scientific Instruments **92**, 053906 (2021).

[37] T. Ruelle, D. Jaeger, F. Fogliano, F. Braakman, and M. Poggio, *A tunable fiber Fabry–Perot cavity for hybrid optomechanics stabilized at 4 K,* Review of Scientific Instruments **93**, 095003 (2022).

[38] M. Pallmann, T. Eichhorn, J. Benedikter, B. Casabone, T. Hümmer, and D. Hunger, *A highly stable and fully tunable open microcavity platform at cryogenic temperatures,* APL Photonics **8**, 046107 (2023).

[39] M. Fisicaro, M. Witlox, H. Van Der Meer, and W. Löffler, *Active stabilization of an open-access optical microcavity for low-noise operation in a standard closed-cycle cryostat,* Review of Scientific Instruments **95**, 033101 (2024).

[40] D. Riedel, I. Söllner, B. J. Shields, S. Starosielec, P. Appel, E. Neu, P. Maletinsky, and R. J. Warburton, *Deterministic Enhancement of Coherent Photon Generation from a Nitrogen-Vacancy Center in Ultrapure Diamond,* Physical Review X **7**, 031040 (2017).

[41] S. Flågan, D. Riedel, A. Javadi, T. Jakubczyk, P. Maletinsky, and R. J. Warburton, *A diamond-confined open microcavity featuring a high quality-factor and a small mode-volume,* Journal of Applied Physics **131**, 113102 (2022).

[42] Y. Herrmann, J. Fischer, J. M. Brevoord, C. Sauerzapf, L. G. C. Wienhoven, L. J. Feije, M. Pasini, M. Eschen, M. Ruf, M. J. Weaver, and R. Hanson, *Coherent Coupling of a Diamond Tin-Vacancy Center to a Tunable Open Microcavity,* Physical Review X **14**, 041013 (2024).

[43] Y. K. Yong, S. O. R. Moheimani, B. J. Kenton, and K. K. Leang, *Invited Review Article: High-speed flexure-guided nanopositioning: Mechanical design and control issues,* Review of Scientific Instruments **83**, 121101 (2012).

[44] JPE, *CPSHR1 Datasheet,* (2024), https://www.jpe-innovations.com/wp-content/uploads/CPSHR1_Datasheet.pdf.

[45] E. Janitz, M. Ruf, Y. Fontana, J. Sankey, and L. Childress, *High mechanical bandwidth fiber-coupled Fabry-Perot cavity,* Optics Express **25**, 20932 (2017).

[46] S. Bogdanović, M. S. Z. Liddy, S. B. van Dam, L. C. Coenen, T. Fink, M. Lončar, and R. Hanson, *Robust nano-fabrication of an integrated platform for spin control in a tunable microcavity,* APL Photonics **2**, 126101 (2017).

[47] JPE, *CPSHR1 Website,* (2024), https://www.jpe-innovations.com/cryo-uhv-products/cryo-positioning-stage-high-resonance/.

[48] P. I. P. G. . C. KG., *Q-545 Website,* (2024), https://www.physikinstrumente.com/en/products/linear-stages/miniature-linear-stages/q-545-q-motion-precision-linear-stage-103170.

[49] I. Lake Shore Cryotronics, *Lakeshore Website,* (2024), https://www.lakeshore.com/products/categories/downloads/temperature-products/cryogenic-temperature-sensors/cernox.

[50] I. T. Raa, H. K. Ervasti, P. J. Botma, L. C. Visser, R. Budhrani, J. F. van Rantwijk, S. P. Cadot, J. Vermeltfoort, M. Pompili, A. J. Stolk, M. J. Weaver, K. L. van der Enden, D. de Leeuw Duarte, M. Teng, J. van Zwieten, and F. Grooteman, *QMI - Quantum Measurement Infrastructure, a Python 3 framework for controlling laboratory equipment,* 4TU.ResearchData (2023), https://data.4tu.nl/datasets/6d39c6db-2f50-4a49-ad60-5bb08f40cb52.

[51] S. Raman Nair, L. J. Rogers, X. Vidal, R. P. Roberts, H. Abe, T. Ohshima, T. Yatsui, A. D. Greentree, J. Jeske, and T. Volz, *Amplification by stimulated emission of nitrogen-vacancy centres in a diamond-loaded fibre cavity,* Nanophotonics **9**, 4505 (2020).

[52] A. Ulanowski, J. Früh, F. Salamon, A. Holzäpfel, and A. Reiserer, *Spectral Multiplexing of Rare-Earth Emitters in a Co-Doped Crystalline Membrane,* Advanced Optical Materials **12**, 2302897 (2024).

[53] J. F. S. Brachmann, H. Kaupp, T. W. Hänsch, and D. Hunger, *Photothermal effects in ultra-precisely stabilized tunable microcavities,* Optics Express **24**, 21205 (2016).

[54] Y. Herrmann, J. Fischer, S. Scheijen, C. F. J. Wolfs, J. M. Brevoord, C. Sauerzapf, L. G. C. Wienhoven, L. J. Feije, M. Eschen, M. Ruf, M. J. Weaver, and R. Hanson, *Data underlying the publication "A Low-Temperature Tunable Microcavity featuring High Passive Stability and Microwave Integration",* 4TU.ResearchData (2024), https://doi.org/10.4121/451152e2-a4d4-4e42-96e0-4147afb1e45c.

[55] M. Fox, *Quantum optics: an introduction*, Oxford master series in physics No. 15 (Oxford University Press, Oxford, New York, 2006).

5

Laser-cut Patterned, Micrometer-thin Diamond Membranes with Coherent Color Centers for Open Microcavities

Y. Herrmann*, J. M. Brevoord*, J. Fischer*, S. Scheijen, N. Codreanu, L .G. C. Wienhoven, Y. M. Q. van der Graaf, C. F. J. Wolfs, R. Méjard, M. Ruf, N. de Jong and R. Hanson.

Micrometer-scale thin diamond devices are key components for various quantum sensing and networking experiments, including the integration of color centers into optical microcavities. In this work, we introduce a laser-cutting method for patterning microdevices from millimeter-sized diamond membranes. The method can be used to fabricate devices with micrometer thicknesses and edge lengths of typically 10 µm to 100 µm. We compare this method with an established nanofabrication process based on electron-beam lithography, a two-step transfer pattern utilizing a silicon nitride hard mask material, and reactive ion etching. Microdevices fabricated using both methods are bonded to a cavity Bragg mirror and characterized using scanning cavity microscopy. We record two-dimensional cavity finesse maps over the devices, revealing insights about the variation in diamond thickness, surface quality, and strain. The scans demonstrate that devices fabricated by laser-cutting exhibit similar properties to devices obtained by the conventional method. Finally, we show that the devices host optically coherent tin- and nitrogen-vacancy centers suitable for applications in quantum networking.

The results of this chapter have been published in Materials for Quantum Technology **5**, 035001 (2025).

5.1 Introduction

Single-crystal (sub) micrometer-thin diamond samples hosting coherent color centers are relevant for several quantum technology applications spanning from quantum networking to sensing. In quantum networking, such platforms can be used to engineer the photonic environment of color centers for enhanced photon collection [1–4]. This includes photonic crystal cavities, fabricated directly into the diamond [5–8] and thinned-down membranes, coated from both sides with a dielectric layer, which can function as an optical antenna [9]. Furthermore, such platforms can be incorporated into open microcavities [10–12] and they facilitate the manufacturing of heterogeneous photonic structures such as solid immersion lenses [13], nanophotonic resonators [14, 15] or plasmonic nanogap cavities [16].

In quantum sensing, chemically inert and biocompatible, thin diamond samples can bring color centers near other materials, while still providing optical access. This can be used in sensing of living cells [15], wide-field microscopy of electrical currents [17], or magnetic fields [18–22].

In this work, our main focus is on the fabrication of diamond microdevices for open microcavities to Purcell-enhance color centers hosted inside the device. While pioneering work made use of color centers in nanodiamonds [23–25], a micrometer-thin diamond sample is beneficial to maintain good optical coherence, especially in the case of nitrogen-vacancy centers [26, 27]. Such diamond samples have been used to couple nitrogen-vacancy and group-IV vacancy centers to open microcavities [28–31]. The coupling of color centers to the cavity is quantified by the Purcell factor, which is proportional to Q/V, where Q denotes the cavity quality factor and V is the cavity mode volume. To demonstrate significant Purcell enhancement of color centers, the following microdevice properties must be taken into consideration: (1) A thickness of a few micrometers (or less) is desired to minimize the cavity mode volume. (2) A smooth surface (roughness $R_q \lessapprox 1\,\mathrm{nm}$) is needed to maintain a high cavity quality factor (finesse). (3) Large lateral dimensions (tens of micrometers) with a small wedge are beneficial to provide an area to probe several cavity spots (cavity beam waist is on the order of a micrometer). (4) Bonding to a cavity Bragg mirror at a micrometer distance to a stripline for delivering microwaves [32] or static electric fields [33] is necessary. (5) The sample should contain color centers with good optical properties for quantum science and technology applications. While these criteria are relevant for the microcavity platform, they are also relevant to most of the applications mentioned.

Several fabrication methods have been developed to realize (sub) micrometer-thin diamond samples. These include the fabrication methods listed in the following: smart cut makes use of the implantation of light ions (like carbon [34] or helium [35]) to produce a sacrificial layer of amorphous carbon, which can be removed electrochemically [6, 36]. Additional overgrowth is necessary for a high crystalline quality thin film diamond released from the sacrificial layer [37]. In a diamond-on-insulator approach, a thin diamond membrane is bonded to a host (e.g. silicon) substrate and subsequently thinned down to the required thickness [5, 7, 38–40]. Furthermore, $\sim 50\,\mu\mathrm{m}$ diamond microdevices can be patterned in a one-step (e.g. with a hydrogen silsesquioxane (HSQ) mask [41]) or two-step pattern

* Equally contributed authors.

The authors Y. H., J. M. B., J. F., C. S., M. R., N. d. J., and R. H. filed a patent for the method of laser-cutting device fabrication used in this chapter.

transfer process (e.g. with a silicon nitride (Si_xN_y) hard mask [42]) and thinned down by dry etching and a heterogeneously integrated mask (e.g. a fused quartz mask [43]). Alternatively, such diamond membranes can be first bonded to the cavity mirror and then thinned down with a fused quartz [26] or diamond [44] mask. Other methods start from bulk diamond and use an undercutting process (via angled plasma etching [45] or quasi-isotropic plasma etching [46]). Moreover, the production of free-standing diamond nanoslabs with a Chromium protection mask and dry etching has been demonstrated [47]. These fabrication methods are typically complex, labor-intensive, and necessitate additional equipment for the pattern transfer, lithography tools, and deposition tools to define microstructures in lateral dimensions.

In this work, we present a fabrication method for patterning microdevices of different sizes and shapes using laser-cutting to engrave ~ 50 µm thick diamond membranes. This approach utilizes only two fabrication tools (a femtosecond pulsed laser writer and a reactive ion etcher), significantly simplifying the process, reducing its duration, and increasing accessibility. The method allows to achieve feature sizes of approximately 3 µm, limited by the laser spot size. We compare this new fabrication method with an already established method of patterning the diamond membrane with electron-beam lithography (EBL) based on two-step patterning: the desired design is EBL patterned into a resist, followed by a reactive ion etch (RIE) to transfer the pattern into a hard mask material. Next, the hard mask pattern is transferred into the diamond membrane via RIE [42]. Diamond microdevices obtained from both fabrication methods are then subsequently bonded to a cavity Bragg sample mirror, equipped with striplines for microwave delivery, see Fig. 5.1 (a) and (b). To demonstrate that the laser-cut microdevices are suitable for microcavity applications, we characterize the microdevices by scanning cavity microscopy (SCM) [48–50], see Fig. 5.1 (d). This demonstrates that both methods lead to microdevices with comparable cavity quality factors (cavity finesses). Furthermore, we study the optical properties of negatively charged tin-vacancy (SnV) and negatively charged nitrogen-vacancy (NV) centers embedded in diamond microdevices at low temperatures. Both methods result in devices suitable for microcavity applications in quantum networking.

5.2 Fabrication of Diamond Microdevices

The two fabrication methods are compared and described in detail in the following. The process flow of both methods can be divided into five steps: sample preparation, patterning, color center creation, device release etch, and bonding. Specifically, the two methods majorly differ in the patterning fabrication step, where the method presented here foresees a design pattern transfer via laser-cutting. In contrast, the conventional fabrication method foresees a two-step transfer pattern based on EBL. The laser-cut method with SnV center creation is schematically summarized in Fig. 5.1 (c). The conventional EBL-based fabrication method is detailed in [42]. Detailed fabrication steps and parameters can be found in the Appendix Tab. 5.1.

5.2.1 Sample Preparation

For both methods, we follow the sample preparation step outlined in Ref. [26]. We start with commercially available single-crystal, electronic-grade bulk diamonds, measuring

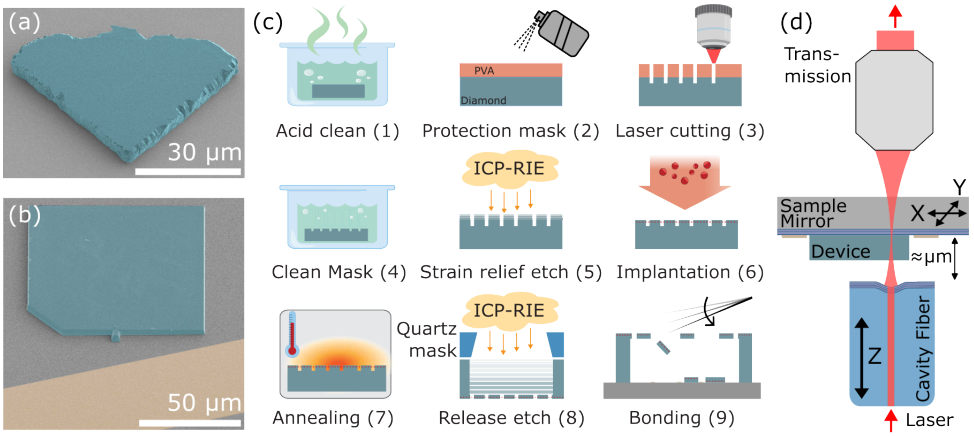

Figure 5.1: False-colored (cyan) scanning electron microscope (SEM) images of diamond microdevices obtained by laser-cutting (device originated from a parent diamond membrane named: *Vincent Vega*) in (a) and electron-beam lithography, and dry etching with a silicon nitride hard mask (*Pai Mei*) in (b). The devices are bonded to the cavity mirror. A gold stripline (yellow false-colored) can be used for microwave delivery. (c) Process flow to fabricate laser-cut diamond microdevices with tin-vacancy centers bonded to the cavity mirror. PVA: polyvinyl alcohol, ICP-RIE: inductively coupled plasma reactive ion etching. (d) Schematic of the scanning cavity microscope. The cavity is optically probed from the fiber side, and the transmission is detected. The sample mirror with the bonded diamond microdevices is scanned laterally in front of the fiber.

$(2\times2)\,\mathrm{mm}^2$ and 0.5 mm in thickness with a face-orientation of $\langle 100\rangle$, grown by chemical vapor deposition. The diamonds are laser-sliced into three ~ 50 µm thick membranes and polished on both sides (Almax Easylab). The roughness of the polished surface is typically $R_q < 1\,\mathrm{nm}$. Before patterning, the membranes are cleaned by fuming nitric acid (65 %) at room temperature (step (1) in Fig. 5.1 (c)).

5.2.2 Patterning

Patterns of arbitrary microdevice designs are transferred into the ~ 50 µm thick diamond membrane via the two methods by selectively removing diamond material. In the case of the laser-cutting method, the diamond membrane is coated with a polyvinyl alcohol (PVA) mask using standard PVA-based hairspray (step (2)). Next, approximately 10 µm to 15 µm deep trenches are created with a femtosecond-pulsed laser (Lasertec), transferring an arbitrary design into the diamond membrane (step (3)) [51]. After patterning, the PVA mask is removed via an ultrasonic bath in de-ionized (DI) water (H_2O) and acetone for 10 min each at room temperature (step (4)), followed by inorganic wet cleaning in a Piranha mixture (ratio 3:1 of H_2SO_4 (95 %) : H_2O_2 (31 %)) at 80 °C for 20 min. In the next step, the surface is treated with a strain relief etch for cleaning and to remove the residual polishing-induced strain from the membrane surface (step (5)) [41]. The membrane is mounted with PMMA495 A4 on a fused quartz carrier wafer and etched with inductively coupled plasma reactive ion etching (ICP/RIE) for 35 min in Ar/Cl_2 plasma chemistry, followed by 7 min etch in O_2 plasma chemistry (Oxford Instruments, Plasmalab System 100). This removes ~ 1.4 µm and ~ 2.1 µm, respectively, of diamond material from the surface. Alternatively, the strain relief etch can also be performed with a cyclic Ar/Cl_2 and O_2 recipe to improve

surface roughness, as demonstrated in Ref. [44].
The EBL method starts with processing the diamond membrane with a strain relief etch as described above (with different etching times). After the color center creation (described below), a ~ 320 nm thin Si_xN_y layer hard mask material is deposited on the top diamond surface by plasma-enhanced chemical vapor deposition (PECVD, Oxford Instruments Plasmalab 80 Plus). Next, CSAR-13 (AR-P 6200.13) positive tone resist is spin-coated, followed by the spin coating of Electra 92 (AR-PC 5090) conductive polymer to prevent charging effects during EBL exposure (Raith EPBG-5200). Before the development step, the Electra 92 is removed in deionized water and blow-dried with nitrogen. The resist is then developed by immersing the sample for 1 min in pentyl acetate, 5 s in ortho-xylene, 1 min in isopropyl alcohol (IPA), and blow-drying with nitrogen. The pattern is transferred into the Si_xN_y hard mask layer via ICP/RIE (Adixen AMS 100 I-speeder) in a CHF_3/O_2 based plasma chemistry [52]. The resist is removed in a two-fold step: first, a coarse resist removal is executed by immersing the sample in a PRS 3000 positive resist stripper solution, followed by a second fine resist removal in a Piranha mixture clean, which is executed two times. Next, the pattern is transferred from the Si_xN_y hard mask into the diamond membrane by ICP/RIE with an O_2 plasma (Oxford Instruments, Plasmalab System 100), resulting in a trench depth of around 6 µm to 10 µm. The Si_xN_y hard mask is then removed by wet inorganic etch in hydrofluoric (HF) acid (40 %) for 15 min at room temperature.
The patterning step in the EBL method accounts for at least half of the total processing time, which can be saved with the laser-cutting method, especially when outsourced.

5.2.3 Color Center Creation

SnV centers are created in the diamond membrane by ion implantation of tin (^{120}Sn) at an implantation energy of 350 keV and a dose of 3×10^{10} ions/cm^2 under an implantation angle of 7° (step (6)). The desired implantation energy is determined using Stopping Range of Ions in Matter (SRIM) simulations [53], resulting in an implantation depth of ~ 90 nm (straggle of ~ 17 nm), and the implantation angle is adopted to prevent ion channeling effects. For laser-cut samples, ion implantation is performed after patterning and strain relief etch. For EBL samples, the ion implantation is performed after the strain relief etch, but before the patterning step.
For the generation of NV centers with high optical coherence, we employ electron irradiation with minimal crystal damage to generate NV centers from the native nitrogen concentration [26, 33, 54]. We irradiate and anneal the bulk diamonds before laser-slicing into membranes, but this step can also be performed later in the process. Irradiation is realized at the Reactor Institute in Delft with an electron-beam acceleration energy of 2 MeV and a dose of 4×10^{13} e$^-$/cm^2. The energy leads to penetration of electrons through the full diamond (for both substrates used in this study, the 0.5 mm thick bulk and ~ 50 µm membranes). This results in lattice vacancies formed over the full thickness extent of the diamond substrates.
After the implantation and the irradiation steps, the diamond substrates are processed with a tri-acid clean (mixture of 1:1:1 ratio of H_2SO_4(97 %):HNO_3(65 %):$HClO_4$(60 %)) at 120 °C for one hour. To enable vacancy migration and to activate color centers, as well as to remove defects (such as divacancies from the lattice), the samples are high-temperature annealed (at a pressure of ~ 1×10^{-6} mbar) with a temperature of up to 1100 °C (step (7)),

followed by a tri-acid clean to remove any created graphite during the annealing step. We use the same annealing recipe as presented in former work [26]. Both ways to create color centers (implantation and electron irradiation) are compatible with the two demonstrated fabrication methods.

5.2.4 Device Release Etch

To release the structures, the membrane with the patterned side facing down is placed on a fused quartz wafer. A 0.5 mm thick fused quartz mask with a 1.4 mm rectangular central opening and angled sidewalls (30°) is positioned and aligned on top of the back surface of the diamond membrane [26]. The mask allows the etching plasma to access the back surface of the diamond membrane over the entire opening area, whereas areas of the membrane covered yield a supporting diamond frame. The center part of the membrane is etched with an ICP/RIE process (Oxford Instruments, Plasmalab System 100) composed of Ar/Cl_2 for 45 min for cleaning and smoothening the surface, followed by consecutive multiple rounds of O_2 plasma deep etching (step (8), depending on the diamond membrane thickness). Between etching rounds, the membrane is inspected under an optical light microscope to assess the progressing thickness and verify the release of the microdevices, connected to the parent membrane by a small tether by design. The device release etch step is concluded when the target thickness is reached.

5.2.5 Bonding

Prior to the diamond microdevice bonding to the cavity sample mirrors [12], microwave striplines can be fabricated on top of the mirrors. These are produced by an EBL and lift-off fabrication process, resulting in 5 nm titanium and 75 nm thick, 50 µm wide gold striplines. A wet inorganic Piranha clean concludes the microwave stripline fabrication, improving the bonding quality of the diamond microdevices. The stripline fabrication process does not reduce the cavity mirror reflectivity, as demonstrated in Ref. [32].

The bonding is performed by a four-degrees-of-freedom, piezo micromanipulator (Imina Technologies SA, miBots), used to controllably break the tether and release the diamond microdevices from the parent membrane (shown in Appendix Fig. 5.7 (a), see also Supplementary Video 1, which can be found on Ref. [55]). As a result, the microdevices land on the cavity mirror, aligned and positioned under the parent diamond membrane such that proximity to the microwave striplines is ensured (step (9)). The micromanipulator is equipped with a 0.6 µm fine tungsten needle (Ted Pella, Ultrafine Tungsten Manipulator Probe). To increase the probability of obtaining well-bonded devices, the surface of the cavity mirror can be activated for 30 min inside an Ozone chamber (BioForce Nanosciences UV/Ozone ProCleaner), which removes organic contamination on the molecular level. In addition, the overall parent diamond membrane with the released microdevices can be cleaned in HF (40 %) at room temperature. A well-bonded device exhibits a color matching with the mirror surface and does not show any interference patterns. Furthermore, these devices do not move when a lateral force with the micromanipulator tip is applied. Bonded microdevices from both fabrication methods are shown in Fig. 5.1 (a) and (b), measured with an SEM, and in Fig. 5.2 (a) and (c) with a light microscope.

In contrast, devices that are not fully bonded are typically identified by wave-like interference patterns (Newton's rings) or an opaque appearance (see Appendix Fig. 5.7 (b) and (c)).

Unbonded devices can be repositioned on the mirror surface for alignment, such as placement near the stripline. For some devices, gentle force or tapping with the micromanipulator has resulted in bonding. Both fabrication methods, laser-cutting (Fig. 5.2 (a)) and EBL (Fig. 5.2 (c)), produce well-bonded devices.

5.2.6 Fabrication Results

Representative examples of bonded microdevices fabricated with the two methods presented in the previous sections are shown in Fig. 5.2. A laser-cut $(70 \times 70)\,\mu m^2$, $\sim 2.5\,\mu m$ thin microdevice shown in Fig. 5.2 (a) hosts SnV centers. The corresponding height map in Fig. 5.2 (b) is measured by a white light interferometer (Bruker ContourX-500) and yields a wedge with a slope of $\sim 0.7\,\mu m/100\mu m$. The second microdevice, fabricated by EBL is $(90 \times 90)\,\mu m^2$ in size and around $3.5\,\mu m$ thin, shown in Fig. 5.2 (c) and contains NV centers. The height maps (Fig.5.2 (d)) shows a wedge of $\sim 1.4\,\mu m/100\mu m$. The higher gradient wedge indicates that this device originated from the outer region of the parent diamond membrane, where the etched profile is less homogeneous, because of the proximity effect due to the fused quartz mask. The determined wedge of both microdevices enables the investigation of the two different mode types, which are formed in the diamond-microcavity system (air-like and diamond-like, see next section).

The laser-cutting method yields devices with a significantly higher surface roughness for an extent of $\sim 10\,\mu m$ from the edges when compared to the EBL method obtained devices (compare Fig. 5.2 (a) to (c)). Beyond the high surface roughness extent of $\sim 10\,\mu m$, the inner area of the laser-cut microdevice shows a comparable surface quality to the devices fabricated by EBL.

Both methods lead to the successful fabrication of microdevices with high-quality surfaces in the center, suitable for microcavity experiments (next section).

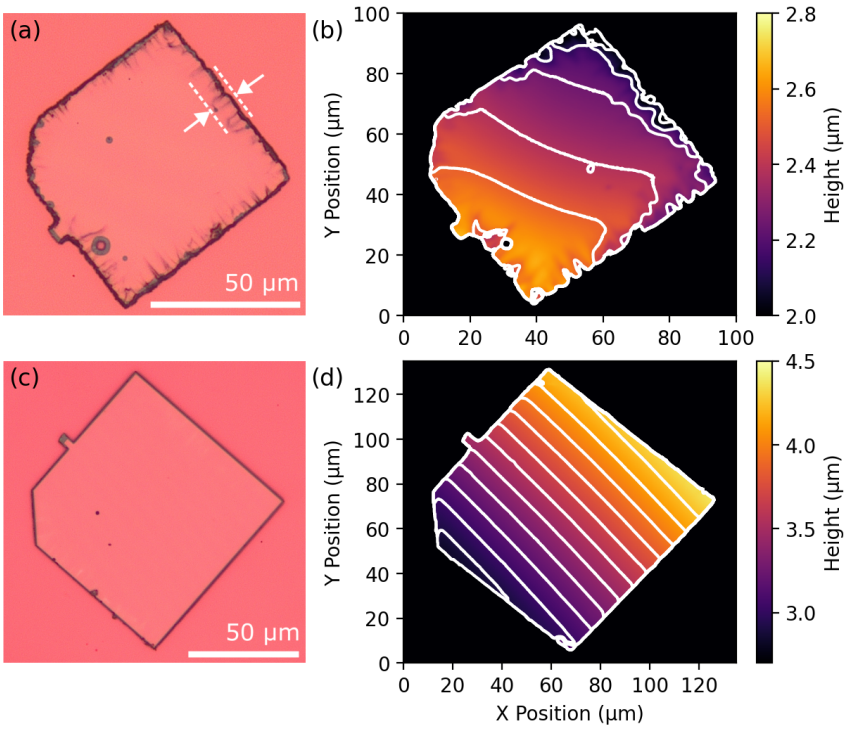

Figure 5.2: Comparison of diamond microdevices fabricated by laser-cutting and EBL. (a) Optical light microscope picture of the laser-cut microdevice (*Vincent Vega*). The rougher edge (indicated by the 10 µm spaced, dashed lines) of the laser-cut microdevice is visible. (b) The corresponding height map is measured with a white light interferometer. The white lines are overlayed and indicate a microdevice thickness matching air-like modes with $q = 16$ to $q = 19$, calculated by equation (5.1). (c) Optical light microscope picture of the EBL microdevice (*Pai Mei*). (d) Corresponding height map with diamond thicknesses leading to an air-like mode of $q = 22$ to $q = 32$, calculated by equation (5.1). Both devices are well-bonded to the underlying (pink) cavity mirror. The height data of the white light interferometer is stated with respect to the mirror surface.

5.3 Scanning Cavity Microscopy

In this section, we use SCM (see Supplementary Video 2, which can be found on Ref. [55]) to study the quality of the bonded diamond microdevices. The experiments involve finesse measurements of the microcavity that give insights into cavity losses and allow us to conclude the diamond device surface wedge and quality. For this, we first introduce a cavity loss model to describe the finesse determined in length, as done in our cavity finesse measurements.

5.3.1 Cavity Loss Model

We consider a hemispherical plano–concave microcavity, where both Bragg mirrors are terminated with a high refractive index material and the diamond microdevices are bonded to the (flat) sample mirror (see Fig. 5.1 (d)). The cavity finesse $\mathcal{F} = 2\pi/\mathcal{L}_{\text{eff}}$ is inversely

proportional to the sum of the effective losses $\mathcal{L}_{\text{eff}}$. Together with the known mirror transmission loss values, this results in a complete understanding of the system. Most fundamentally, the diamond devices change the sample mirror transmission loss for a given probe laser wavelength depending on their thickness. Hereby so-called air-like and diamond-like mode [10, 56] thicknesses can be defined:

$$t_d = q\frac{\lambda}{2n_d} \quad (\text{air}-\text{like}), \qquad t_d = (2q+1)\frac{\lambda}{4n_d} \quad (\text{diamond}-\text{like}), \tag{5.1}$$

with a corresponding fundamental mode number q and the refractive index of diamond $n_d = 2.41$ [57] (for our laser wavelength of $\lambda = 637\,\text{nm}$). For the air-like (diamond-like) modes, the mirror transmission loss is minimal (maximal). This phenomenon is associated with the electric field intensity ratio of the air and the diamond part of the cavity. A consecutive air-like and diamond-like mode is separated by a diamond thickness of $\lambda/(4n_d) \approx 66\,\text{nm}$ and hence can indicate a device thickness wedge.
To include further diamond-related loss mechanisms, we can model the effective losses for the here conducted finesse measurements with:

$$\mathcal{L}_{\text{eff}} = \mathcal{L}_{M,a} + \frac{n_d E^2_{\text{max,d}}}{E^2_{\text{max,a}}}\left(\mathcal{L}_{M,d} + \mathcal{L}_{A,d} + \mathcal{L}_{S,\text{eff,d}}\right) + \mathcal{L}_{\text{add}}. \tag{5.2}$$

In this equation, $\mathcal{L}_{M,a}$ accounts for the loss through the air-side mirror and $\mathcal{L}_{\text{add}}$ considers any additional losses. The fraction $n_d E^2_{\text{max,d}}/E^2_{\text{max,a}}$ describes the electric field intensity ratio between the air and diamond part, and can be calculated by [56]:

$$\left(\frac{n_d E^2_{\text{max,d}}}{E^2_{\text{max,a}}}\right)^{-1} = \frac{1}{n_d}\sin^2\left(\frac{2\pi n_d t_d}{\lambda}\right) + n_d\cos^2\left(\frac{2\pi n_d t_d}{\lambda}\right). \tag{5.3}$$

The ratio depends on the diamond thickness and leads to the modulation of the finesse values between air-like ($n_d E^2_{\text{max,d}}/E^2_{\text{max,a}} = 1/n_d$) and diamond-like modes ($n_d E^2_{\text{max,d}}/E^2_{\text{max,a}} = n_d$). The modulated losses are: the diamond-side sample mirror loss $\mathcal{L}_{M,d}$, the absorption losses $\mathcal{L}_{A,d}$, and the scattering losses at the air-diamond interface $\mathcal{L}_{S,\text{eff,d}}$. The absorption losses can be calculated with the diamond absorption coefficient α to $\mathcal{L}_{A,d} \approx 2\alpha t_d$, while the scattering losses can be calculated by [56]:

$$\mathcal{L}_{S,\text{eff,d}} \approx \sin^2\left(\frac{2\pi n_d t_d}{\lambda}\right)\frac{(n_d+1)(n_d-1)^2}{n_d}\left(\frac{4\pi\sigma_{DA}}{\lambda}\right)^2. \tag{5.4}$$

Here, σ_{DA} includes the device surface roughness at the air-diamond interface. For an air-like mode, the scattering losses are zero, while they become maximal in a diamond-like mode. The cavity finesse on the diamond is thus also a measure of the surface roughness.

5.3.2 Cavity Finesse Measurements

We characterize the diamond microdevices by two-dimensional scans, in which the cavity finesse is measured on each lateral spot with a room temperature fiber-based Fabry-Pérot microcavity, schematically depicted in Fig. 5.1(d) (scanning cavity microscopy [58]). The $(1\times 1)\,\text{cm}^2$ sample mirror, on which the diamond devices are bonded, is scanned laterally with

a piezo nanopositioning stage in steps of 0.2 µm. Technical details about the microcavity setup can be found in 5.7.3. An individual finesse measurement is performed by scanning the cavity length over two fundamental modes while probing the cavity transmission with a resonant laser, shown in Appendix Fig. 5.9 (a). We record all measurements with cavity lengths below 15 µm, to ensure that the cavity finesse is not limited by clipping losses (see Appendix Fig. 5.9 (b) for characterization of the cavity fiber). A scan of the two devices fabricated by laser-cutting and EBL is presented in Fig. 5.3 (a) and (c).
The mirror coatings (Laseroptik) are designed to be maximally reflective for 637 nm light with $\mathcal{L}_{M,a} = 50\,\text{ppm}$ ($\mathcal{L}_{M,d} = 670\,\text{ppm}$ for diamond termination) losses for the fiber tip (sample) mirror. As follows from equation (5.2), in a bare cavity ($t_d = 0\,\mu\text{m}$), scattering and absorption losses vanish and the sample mirror transmission losses translate to the air-terminated value of $1/n_d \times \mathcal{L}_{M,d} = 280\,\text{ppm}$. The measured finesse around 8000 (see green distributions in Fig. 5.3 (b) and (d)) indicates additional losses around $\mathcal{L}_{\text{add}} = 470\,\text{ppm}$. We attribute these additional losses to the quality of the concave fiber tip.
On both diamond microdevices in Fig. 5.3 (a) and (c), the finesse shows a clear modulation with the same pattern as in the diamond thickness variation from Fig. 5.2 (b) and (d). We associate the variation in finesse values with the alternation between air-like modes (higher finesse) and diamond-like modes (lower finesse). In the air-like modes, only a slight reduction of the cavity finesse compared to the bare cavity is observed. For the diamond-like modes, the finesse is much reduced. The cavity transmission on the EBL device (*Pai Mei*) is reduced around diamond-like mode regions so much that no finesse can be determined. Some thin lines with reduced finesse are visible in the scan in Fig. 5.3 (c), which are attributed to transverse-mode mixing [58].

To study the effect of the diamond microdevices more quantitatively, we investigate the finesse depending on the device thickness. This data is obtained by overlaying the white light interferometer data from Fig. 5.2 (b) and (d) with the finesse scans from Fig. 5.3 (a) and (c). The interferometer data has a sufficient lateral resolution of about 0.13 µm per step. For every measured finesse value, within the white rectangle in the scan, we take the corresponding diamond thickness from the interferometer data. This is shown in Fig. 5.4 for both diamond devices.
We notice that the absolute thickness values from the white light interferometer do not directly match the expected positions of the air-like and diamond-like modes according to equation (5.1). The measured values might be distorted due to the multilayer Bragg mirror on which the devices are bonded. We compensate for this by measuring the diamond thickness using the cavity mode dispersion (Appendix Fig. 5.10) on an air-like mode on the diamond (indicated in Fig. 5.3) to determine an offset for the diamond thickness values. The absolute thickness from the white light interferometer and the thickness determined by the cavity dispersion differ by 0.16 µm to 0.32 µm.
We fit the measured finesse values depending on the diamond thickness in Fig. 5.4 with the effective losses from equation (5.2). In the fit, we use the known mirror losses from the coating design as stated above, and a small diamond thickness translation of $< 20\,\text{nm}$ is allowed. Furthermore, for the used high-purity, electronic-grade diamonds grown by chemical vapor deposition, no absorption losses are expected [59]. This leaves the additional losses $\mathcal{L}_{\text{add}}$ and the diamond surface roughness σ_{DA} as free parameters in the fit.

For the laser-cut microdevice, the fit yields a diamond surface roughness value of

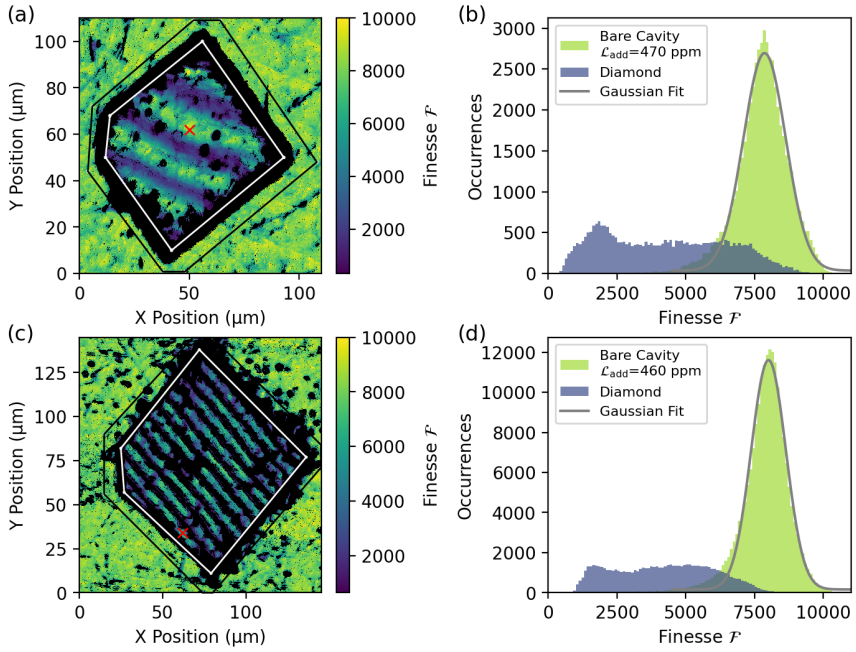

Figure 5.3: Scanning cavity microscopy of the diamond microdevices. Both devices show a clear modulation of the finesse due to the alternation between air-like and diamond-like modes. (a) Measured two-dimensional finesse scan on a laser-cut diamond microdevice (*Vincent Vega*). (b) Histogram of the finesse values measured in (a). Values on the diamond (bare cavity) are taken from inside the white rectangle (outside the black rectangle). (c) Measured two-dimensional finesse scan on an EBL diamond microdevice (*Pai Mei*). (d) Histogram of finesse values measured in (c). Finesse values on the diamond (bare cavity) are taken from inside the white rectangle (outside the black rectangle). For the bare cavity, a finesse centered around 8000 is determined by the Gaussian fits in (b) and (d). The red crosses in (a) and (c) indicate the positions where the cavity length measurements presented in 5.7.5 are taken. The histograms are plotted in bins of 100.

0.9 nm and additional losses of 610 ppm. The EBL device fit yields values of 1.2 nm surface roughness and 820 ppm additional losses. For both devices, a distribution of finesse values for a fixed diamond thickness is observed, leading to the band-like structure in Fig. 5.4. This means that for a specific diamond thickness, lateral cavity positions with varying surface quality are found. To quantify the spread in surface roughness of the data presented in Fig. 5.4, we use the following procedure: the finesse values for a thickness segment of 10 nm are binned into a histogram, which is fitted with a Gaussian function. This fit determines for every thickness segment a mean value and a standard deviation. We fit the mean plus (minus) the standard deviation values of all segments with the model losses of equation (5.2), to determine the upper yellow (lower bright green) curves in Fig. 5.4. With that, we find that our laser-cut (EBL) device exhibits areas with surface roughness values as low as 0.6 nm (1.1 nm), which are common values for these fabrication methods. For both samples finesse values similar to the bare cavity are reached in the air-like modes, whereas in the diamond-like modes scattering losses of $\mathcal{L}_{S,\mathrm{eff,d}} = 390\,\mathrm{ppm}$ (1330 ppm) limit the achievable finesse in the laser-cut (EBL) device.

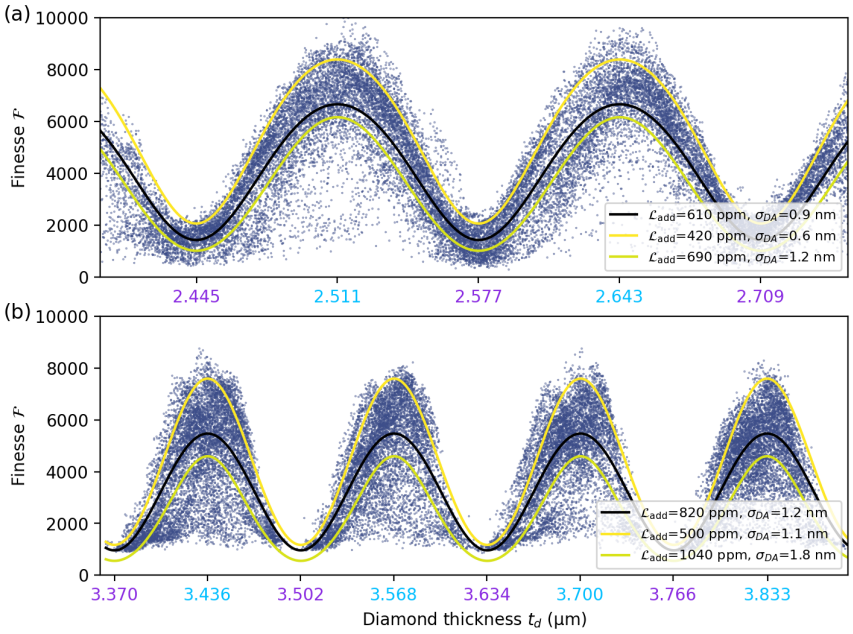

Figure 5.4: Diamond thickness dependent finesse values observed by SCM. Finesse values are taken from inside the white rectangle in Fig. 5.3. The black line is a fit of the finesse values with losses from equation (5.2). The modulation of the finesse values between high-finesse air-like modes and low-finesse diamond-like modes is visible. The diamond thickness values that correspond to an air-like (diamond-like) mode are indicated by the bright blue (purple) axis ticks, determined by equation (5.1). By determining the mean and standard deviation of the finesse values in 10 nm segments (see text), we also give an upper (yellow) and lower finesse curve (bright green) for both devices. More than 60 % of the finesse values lie between the two curves. The diamond thickness measurement by the cavity dispersion is performed for the displayed first air-like mode for both samples (see Appendix Fig. 5.10). (a) Finesse measured on the laser-cut diamond microdevice (*Vincent Vega*). (b) Finesse measured on the EBL diamond microdevice (*Pai Mei*). Note that the black fit is lowered due to the higher spread in finesse values.

5.3.3 Frequency Splitting of the Polarization Cavity Modes

In addition to the finesse, the frequency splitting of the two orthogonal polarization modes of the microcavity is studied. Strain-induced birefringence in the diamond microdevice can cause a splitting of the horizontal and vertical polarization cavity mode [60]. In general, diamond color centers couple differently to these modes depending on their electric dipole overlap with the electric field of the cavity. These polarization modes are used in cross-polarization resonant excitation and detection schemes, and the magnitude of polarization splitting becomes relevant for excitation laser power considerations [28].

We investigate the polarization splitting of the fundamental modes within the same scan used for the finesse measurements. To measure the splitting, the cavity is resonantly probed using laser light with frequency-modulated sidebands, generated by a phase electro-optic modulator. The cavity length is scanned around the fundamental mode, and a typical measurement is shown in 5.7.6. The spacing of the sidebands is set by the modulator driving frequency and is used to determine the frequency splitting of the polarization modes.

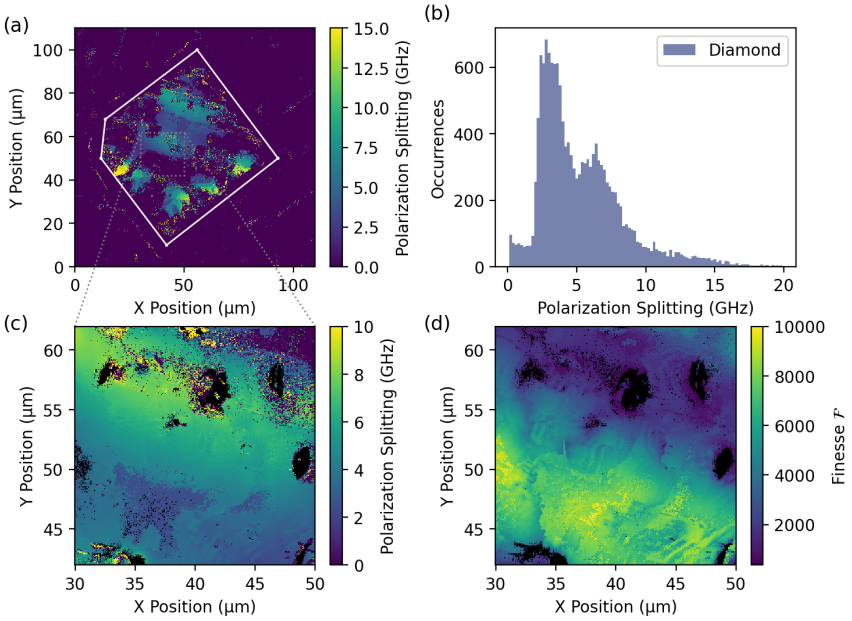

Figure 5.5: Polarization splitting on the laser-cut diamond microdevice (*Vincent Vega*). (a) Polarization splitting is measured on the bare mirror and the diamond device. Data is taken within the same scan as shown in Fig. 5.3 (a). (b) Histogram of the polarization splitting measured on the diamond device inside the white rectangle in (a). Around half of the measured lateral points do not show a polarization splitting (zero bin not included in the histogram). The bin size is 0.2 GHz. (c) Polarization splitting, seperately measured with a 70 nm resolution in the $(20 \times 20)\,\mu m^2$ area indicated in (a). (d) Corresponding finesse values of the same area as shown in (c). The air-like modes with a higher finesse show a smaller polarization splitting compared to the diamond-like modes.

Figure 5.5 (a) shows the polarization splitting measured on and around the laser-cut microdevice. On the bare mirror, no polarization splitting is measured, while on the diamond device, polarization splittings up to 15 GHz can be observed (histogram shown in Fig. 5.5 (b)). It seems that regions with higher polarization splitting in Fig. 5.5 (a) are closer to the device edges, which can be explained by higher strain, possibly induced by the damage of the laser-cutting. Figure 5.5 (c) shows a selected part of the device with the corresponding finesse scan in Fig. 5.5 (d). It is observed that the polarization splitting is higher in the low-finesse, diamond-like mode part (upper area in the scan). This can be explained by the higher electric field intensity inside the diamond for diamond-like modes, leading to a more pronounced effect of the birefringence [58].
For the EBL microdevices presented here, we do not observe significant polarization splitting beyond the cavity linewidth. However, we have also seen polarization splittings up to 10 GHz on other EBL-fabricated devices. To understand the origin of the different strain values, further investigations are needed.

5.4 Optically Coherent Color Centers

For quantum network applications, the color centers in the diamond microdevices must show a (close to) transform-limited optical emitter linewidth. Noise in the environment of the color center (such as fluctuating charges) broadens the emitter linewidth. We can decompose the linewidth broadening into a slow noise contribution, spectral diffusion, and a fast noise contribution, pure dephasing [61]. The former leads to a Gaussian broadening and can be mitigated by active tracking and feedback on the emitter transition frequency [62–65]. Whereas pure dephasing leads to a Lorentzian broadening with a more fundamental influence, as it directly determines the indistinguishability in a two-photon quantum interference experiment of color centers [66, 67] and limits the achievable remote entanglement fidelity in emission-based entanglement protocols [61, 68]. Moreover, the pure dephasing linewidth enters the coherent cooperativity determining fidelities of quantum information protocols [69].

We study the optical emitter linewidth of the color centers in our diamond microdevices with photoluminescence excitation (PLE) measurements. These measurements are performed in a home-built confocal microscope setup, where the samples are mounted in a closed-cycle helium cryostat. In the PLE measurements, a resonant laser is scanned over the zero-phonon line (ZPL) of the color center, and the fluorescence is detected in the phonon sideband.

Figure 5.6 (a) shows a confocal scan of the laser-cut diamond microdevice hosting SnV centers. Note that this device is a different microdevice than shown before, but it originated from the same fabrication run and parent membrane (*Vincent Vega*). For the PLE measurements, an off-resonant, 515 nm laser is used before each resonant laser scan to initialize the SnV center in its negatively charged state. The application of a green laser pulse is known to change the charge environment of the color center, resulting in spectral diffusion. We acquire 100 of these scans on three different SnV centers (Fig. 5.6 (b)) and average all scans to get a measure of the spectral diffusion linewidth. In some of these measurements, a bistability of the SnV center transition frequency is observed. These discrete jumps between two spectral positions separated by about 100 MHz might be caused by a charge trap near the SnV center [70, 71].

To quantify the pure dephasing linewidth, scans that show a complete Lorentzian fluorescence peak are manually selected (more than 50 %), fitted, and centered before averaging. The SnV centers of Fig. 5.6 (b) show good optical coherence with pure dephasing linewidths close to the transform limit around 32 MHz. The corresponding excited state lifetime was determined in previous work [31], which also demonstrated the coherent cavity coupling of a single SnV center in a device obtained from the same diamond membrane. These results demonstrate that coherent SnV centers are created in the laser-cut microdevices.

Figure 5.6 (c) shows the confocal scan of an EBL diamond microdevice hosting NV centers. Note that this device is fabricated in a second run with the EBL method (device originated from parent membrane named *Mr. Orange*). For NV centers, we probe the spin-conserving E_x or E_y emitter transition of the ZPL, which involves the application of intermediate off-resonant, 515 nm, laser pulses at every resonant laser scan frequency to mitigate spin state pumping. These off-resonant laser pulses initialize the NV center predominantly in the negatively charged and spin ground state [72]. Because of the intermediate application of green laser pulses, we can experimentally not measure spectral diffusion and pure

dephasing linewidth separately. We thus analyze the emitter fluorescence peaks by fitting a Voigt profile, which is a convolution of a Gaussian and a Lorentzian function. In the fit routine, the Lorentzian linewidth is lower bound to the transform-limited linewidth of 13 MHz of the NV center [73]. Typical scan results with their corresponding Voigt fits are shown in Fig. 5.6 (d).
We analyze 20 different NV centers at several lateral diamond microdevice positions and find linewidths between 38 MHz and 130 MHz with a median linewidth of 62 MHz (statistics shown in Appendix Fig. 5.12). These results are in line with former work with larger $(2 \times 2)\,\mathrm{mm}^2$ thinned-down diamond membranes [26], indicating that the much tighter lateral dimensions do not induce additional optical decoherence.

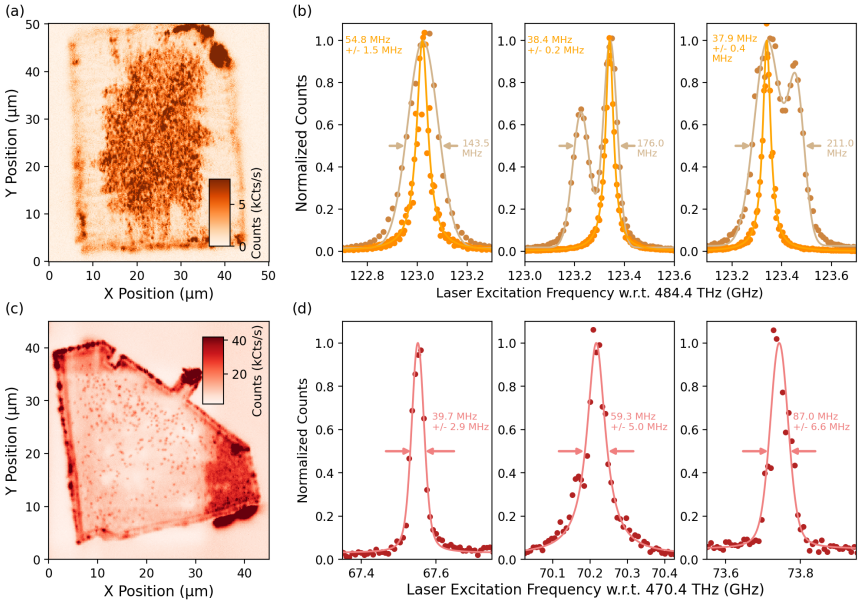

Figure 5.6: Optical properties of SnV centers inside a laser-cut diamond microdevice (*Vincent Vega*) and NV centers inside an EBL patterned diamond device (*Mr. Orange*). The emitter linewidth measurements are performed at ~ 4 K with a confocal microscope. (a) A map of the SnV device with off-resonant, 515 nm excitation. The fluorescence is filtered with a 620 nm bandpass filter (full-width half maximum of 10 nm) to detect predominantly fluorescence of SnV centers. A high SnV center density is observed in the center of the device, while the SnV center layer is removed at the wedged edges. Note that this map is measured in a room-temperature scanning confocal microscope. (b) Typical PLE laser scans of SnV centers, fitted with a Gaussian (ocher) and Lorentzian (orange) function to obtain the spectral diffusion and dephasing linewidth, respectively. (c) Confocal map of the electron-beam patterned device, showing individual, spatially separated NV centers. (d) Typical PLE laser scans of NV centers, fitted with a Voigt function to extract the linewidth. To initialize the NV center into the bright state, a green laser pulse is applied in every repetition. The relevant measurement parameters for the scans in (b) and (d) can be found in 5.7.7.

5.5 Conclusion

We present a method for patterning high-quality micrometer-thin diamond devices utilizing laser-cutting. This method significantly simplifies the fabrication process compared to previously reported methods. Also, the process step of laser-cutting can be readily outsourced. We show that these microdevices can be successfully bonded to a dielectric cavity Bragg sample mirror using a micromanipulator. SCM scans reveal a high surface quality of the fabricated devices, reflected by high cavity finesse values. In addition, we demonstrate that the devices host coherent color centers, which are suitable for quantum optical experiments and applications.

For quantum spin-photon interfaces, the expected microdevice performance in microcavities can be estimated with the measured finesse of 9000 (2000) in the air-like (diamond-like) mode. With the 17.3 µm radius of curvature of the used fiber mirror, these values translate to a maximum Purcell factor of about 30 (39) for a NV center and, with adjusted mirror coatings, also for a SnV center. The Purcell enhancement would be combined with a high outcoupling efficiency through the sample mirror of 40 % (51 %) for the air-like (diamond-like) modes and the used mirror coatings. The performance values could be further improved by using a fiber tip mirror that shows lower additional losses [74–76]. Combined with the integrated gold striplines on the sample mirror for microwave control of the spin qubits [32, 77, 78], the presented approach can enable the realization of an efficient spin-photon interface with diamond color centers.

5.6 Acknowledgment

The authors thank Alexander Stramma for proofreading the manuscript. Furthermore, the authors thank the Quentin Tarantino movie universe for providing the sample names.
The authors acknowledge financial support from the Dutch Research Council (NWO) by the Spinoza prize 2019 (project number SPI 63-264) and from the Dutch Ministry of Economic Affairs and Climate Policy (EZK), as part of the Quantum Delta NL programme. The authors gratefully acknowledge that this work was partially supported by the joint research program “Modular quantum computers” by Fujitsu Limited and Delft University of Technology, co-funded by the Netherlands Enterprise Agency under project number PPS2007. This research was supported by the Early Research Program of the Netherlands Organisation for Applied Scientific Research (TNO) and by the Top Sector High Tech Systems and Materials.

5.6.1 Author Contributions

Y. H., J. M. B., and J. F. contributed equally to this work. M. R. and N. C. developed the EBL fabrication process used in this work. N. d. J. contributed to developing the laser-cutting method. J. M. B., C. S., and Y. H. fabricated the diamond devices. C. S. and L. G. C. W. characterized the devices with the white light interferometer. J. F., Y. vd. G., C. F. J. W., and S. S. built the cavity characterization setup. S. S. measured the two-dimensional cavity scans and characterized the cavity fiber. C. S., Y. H., J. M. B., and J. F. characterized the color centers. R. M. fabricated the cavity fiber. J. F. derived the used cavity loss model. Y. H., J. F., and S. S. analyzed the data. Y. H., J. M. B., J. F., S. S., and R. H. wrote the manuscript with

input from all authors. R. H. supervised the experiments.

5.6.2 Data Availability

The datasets of this study and the Python software for analysis and plotting are publicly available on 4TU.ResearchData under Ref. [55].

5.7 Appendix

5.7.1 Outline of Fabrication

The detailed steps of both fabrication methods are summarized in table 5.1.

Fab. Step	Electron-Beam Lithography (EBL)	Laser-Cutting
I. Cleaning	Fuming nitric acid (1): 10 min in HNO_3 (65 %) at room temperature	
(II. Strain Relief Etch, Implantation, Annealing)	Strain relief etch as described in Section 5.2.2, followed by tri-acid clean, implantation, annealing, and a post-anneal tri-acid clean as detailed in Subsection 5.2.3	-
III. Application of Protection Mask	PECVD ~ 320 nm silicon nitride Si_xN_y	Application of PVA layer (2)
IV. Spin Coating	Sample mounted with PMMA495 A4 on silicon piece, resist CSAR-13 (AR-P 6200.13), 3500 rpm (thickness of ~ 430 nm), bake 3 min at 150 °C Spin coat Electra 92 (AR-PC 5090), 4000 rpm (thickness of ~ 30 nm), bake 2 min at 90 °C	-
V. Exposure	Electron-beam: Dose of 400 uC/cm^2 with 3 nm spot size	-
VI. Development	Remove Electra 92 with 1 min deionized water, blow dry with nitrogen. CSAR-13 development: 1 min in pentylacetate, 5 s in ortho-xylene, 1 min in IPA, blow dry with nitrogen	-
VII. Patterning Hard Mask	Si_xN_y etch with plasma composed of CHF_3/O_2 [79]	-
VIII. Resist Removal	PRS 3000 for 2 h at 80 °C, followed by overnight PRS 3000 at room temperature	-
IX. Cleaning	Double Piranha clean: Mixture with ratio 3:1 of H_2SO_4 (95 %) : H_2O_2 (31 %) at 80 °C for 20 min	-
X. Transfer Pattern into Diamond	Anisotropic ICP/RIE: Sample mounted with PMMA495 A4 on fused quartz carrier wafer, 30 min O_2 plasma chemistry	Laser-cutting (3) with a femtosecond pulsed laser
XI. Cleaning	Removal of the Si_xN_y hard mask: Hydrofluoric (HF) acid (40 %) clean 15 min at room temperature	Removal of PVA: Ultrasonic bath in de-ionized water and acetone for 10 min, each at room temperature (4), followed by Piranha clean
(XII. Strain Relief Etch, Implantation, Annealing)	-	Strain relief etch (5) as described in Section 5.2.2, followed by tri-acid clean, implantation (6), annealing (7), and post-anneal tri-acid clean as detailed in Section 5.2.3
XIII. Release Etch	ICP/RIE (8): Membrane protected by fused quartz mask with central opening, 45 min Ar/Cl_2. Multiple rounds of O_2 etch until individual microdevices are released. Etch rates can be found in Ruf et al. [26].	
XIV. Cleaning	HF clean	
XV. Bonding	Micromanipulator (9)	

Table 5.1: Detailed fabrication steps and process parameters of the two fabrication methods to obtain diamond microdevices, starting with ~ 50 µm membranes. All wet processing steps are followed by a dip in acetone and IPA and blow-drying with a nitrogen gun. The numbers in brackets for the laser-cutting refer to Fig. 5.1 (c) of the main text. Fabrication step II. (XII.) of the EBL (laser-cutting) method is used to create SnV centers. In the case of NV centers, the color centers are created in the bulk diamond, before slicing into membranes, as described in Section 5.2.3.

5.7.2 Bonding of Microdevices to Cavity Mirror

Figure 5.7 (a) shows the breaking out of individual microdevices by a micromanipulator. Supplementary Video 1 (Ref. [55]) shows the process with devices from a second laser-cut membrane. We observe that up to 30 % of the devices bond fully to the cavity mirror. Figure 5.7 (b) and (c) show diamond devices that are not fully bonded to the mirror. When approached by the cavity fiber, such devices can be moved or picked up accidentally.

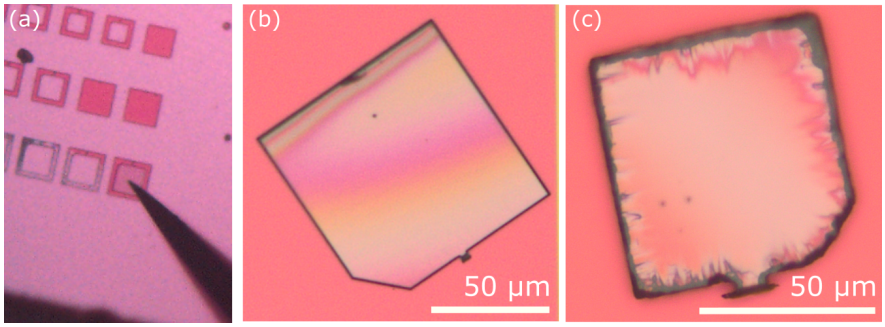

Figure 5.7: Bonding of diamond microdevices to the cavity mirror. (a) Released, thinned-down diamond devices above the cavity mirror. Individual devices can be broken out with the tip of a micromanipulator. An ill-bonded device fabricated by EBL (*Pai Mei*) in (b) and by laser-cutting (*Vincent Vega*) in (c). Both devices show interference fringes and an opaque color.

5.7.3 Experimental Setup: Room Temperature Microcavity

The cavity sample mirror with the microdevices (Fig. 5.8 (a)) is mounted on a piezo nanopositioning stage (Physik Instrumente P-542.2SL) with a range of 200 µm in both the X- and Y-direction. The other cavity mirror is a coated, laser-ablated fiber tip [74], which can be moved in the axial direction by a high-precision objective scanner (Physik Instrumente P-721) to change the cavity length along the Z-direction.

Figure 5.8 (b) shows a sketch of the optical setup and the microcavity. The cavity can be probed with resonant 637 nm light (Newport New Focus Velocity TLB-6300-LN) or with a white light supercontinuum source (NKT Photonics SC-450-2), spectrally filtered for 600 nm to 700 nm. The excitation light is combined in fiber and sent via the fiber side into the cavity. The transmitted light is collimated with an objective (100X Mitutoyo Plan Apochromat Objective) and collected on a photodiode (Thorlabs APD130A2) or sent via fiber to a spectrometer (Princeton Instruments SP-2500i). In addition, the microcavity can be imaged from the sample mirror side by a lamp and a camera for lateral alignment. Supplementary Video 2 (Ref. [55]) shows a two-dimensional cavity finesse scan over an exemplary device recorded with the camera.

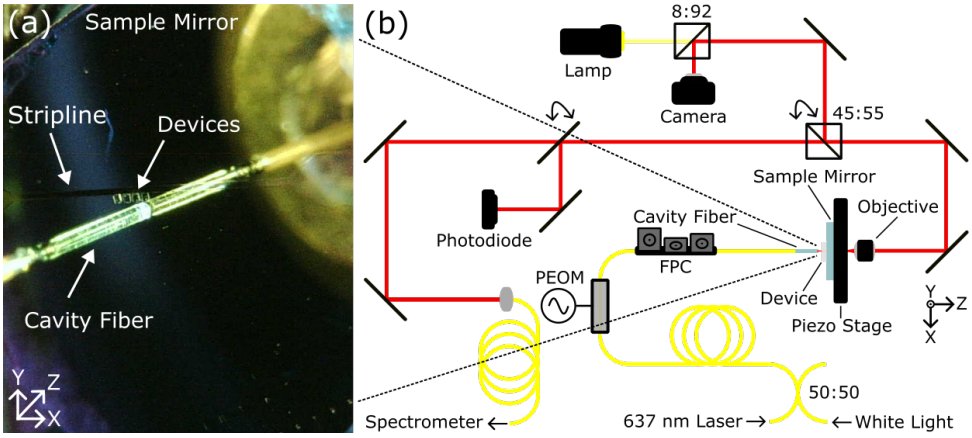

Figure 5.8: (a) Microscope picture of the microcavity with exemplary microdevices on the sample mirror next to a gold stripline. The cavity fiber can be seen on the left side, while the reflection in the mirror is on the right side. (b) Sketch of the home-built SCM setup. Excitation light (resonant laser or white light) is sent into the cavity via the fiber. The light can be modulated with a phase electro-optic modulator (PEOM), and the polarization is set manually with a 3-paddle fiber polarization controller (FPC). The outcoupled detection beam is collimated with an objective and sent either to a photodiode or coupled into a single-mode fiber for the spectrometer.

5

5.7.4 Experimental Methods: Finesse Measurements and Cavity Fiber Properties

To measure the finesse, the cavity is probed with a resonant 637 nm laser, and the transmission signal is recorded on the photodiode. We record the time trace of the photodiode voltage with an oscilloscope (Picotech Picoscope 3403). The cavity length is scanned by a triangular voltage with a frequency of 300 Hz over approximately five fundamental modes to ensure that the middle of these modes is not affected by nonlinearities occurring at the edges of the scanning range. The middle modes are fitted with Lorentzian functions, resulting in a measured cavity finesse defined as the ratio of the mode distance to the linewidth in time. An exemplary trace with two fundamental modes is shown in Fig. 5.9 (a). The resonance peak with the higher coefficient of determination (R^2) is used to determine the finesse. The data is filtered by requiring the mode distance to be within an acceptance range to ensure that only the fundamental modes are fitted.

As discussed in the main text, birefringence in diamond microdevices can cause polarization splitting, which is observed as a frequency splitting of the fundamental cavity mode. To correctly fit these modes in the finesse measurements, two Lorentzian functions are fitted (see Fig. 5.11 (a)).

The same cavity fiber is used for all the presented measurements. From an interferometric measurement of the concave fiber tip, we extract a spherical radius of curvature ROC of 17.3 µm with an asymmetry of 7.8 %. To determine the range in which the fiber exhibits a stable finesse, we measure the cavity length-dependent finesse in Fig. 5.9 (b) on the bare mirror. The cavity length is determined by taking white light transmission spectra, which directly yield the cavity free spectral range and thereby the cavity length. For longer cavity lengths L_{cav} clipping losses $\mathcal{L}_{clip}$ emerge which dependent on the diameter of the concave

feature D_d and the *ROC* of the fiber mirror and can be calculated by [56]:

$$\mathcal{L}_{clip} = e^{\left(-2\left(\frac{D_d}{2\omega_m}\right)^2\right)}. \tag{5.5}$$

In this formula, ω_m denotes the cavity beam width on the fiber mirror and can be calculated by the beam waist on the sample cavity mirror ω_0 [80]:

$$\omega_m = \omega_o \sqrt{1+\left(\frac{L_{cav}\lambda}{\pi n \omega_0^2}\right)^2}, \qquad \omega_0 = \sqrt{\frac{\lambda}{\pi}}\,(L_{cav}(ROC - L_{cav}))^{1/4}. \tag{5.6}$$

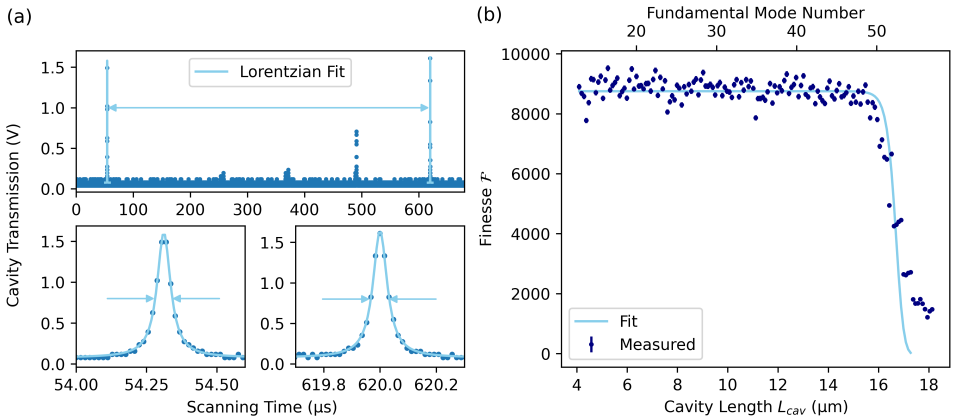

Figure 5.9: (a) Typical cavity finesse measurement recorded with an oscilloscope. The cavity length is scanned with a triangular voltage, and two fundamental modes with a few higher-order modes are visible in the upper panel. The peaks of the fundamental modes are fitted with a Lorentzian function, yielding the cavity linewidth in time. The free spectral range in time is given by the spacing of the fundamental modes. From the shown measurement, a finesse of 9500 is determined. (b) Cavity length-dependent measured finesse of the fiber used to characterize the diamond microdevices. The coating limited finesse is 19000 with 330 ppm losses. A clear plateau of finesse values of ~ 8700 is reached for a cavity length smaller than 15 µm.

We fit the measured finesse values in Fig. 5.9 (b), with the losses determined by equation (5.2) plus the clipping losses $\mathcal{L}_{clip}$. Like in Section 5.3.2 of the main text, we set $t_d = 0\,\mu$m and leave the additional losses and the diameter of the concave feature as free parameters. The radius of curvature is set to the measured value as stated above.
Note that the finesse values measured on the plateau in Fig. 5.9 (b) are a bit higher than the average bare cavity finesse values due to a local optimization on the lateral spot and reveal additional losses of 390 ppm determined by the fit.

5.7.5 Experimental Methods: Hybrid Cavity Modes

To determine the cavity length and the thickness of incorporated devices, we probe the cavity with broadband white light and send the transmitted light to a spectrometer. The cavity length is changed by applying a voltage to the objective scanner, which holds the cavity fiber.
For the broadband white light, the cavity acts as a spectral filter, and fundamental modes

appear as bright lines. We fit the fundamental modes with an analytic formula [10], yielding the length of the air gap and the device thickness. The measurements are shown in Fig. 5.10.

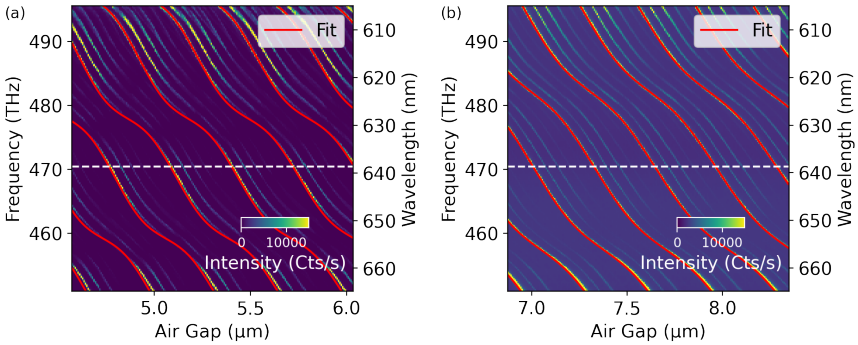

Figure 5.10: Cavity dispersion measured by transmission spectra of a broadband light source. (a) On the EBL microdevice (*Pai Mei*), we measure a device thickness of 3.31 µm. (b) On the laser-cut microdevice (*Vincent Vega*), the fit determines a thickness of 2.51 µm. Both devices are probed in the air-like mode (steeper slope) at 637 nm, indicated by the white, dashed line. The positions on the devices of these measurements are indicated in Fig. 5.3 (a) and (c) with a red cross.

5

5.7.6 Experimental Methods: Polarization Splitting

To measure the cavity polarization splitting, a second trace of the resonance peaks is measured at each lateral scan point with the resonant 637 nm laser, modulated by sidebands. The sidebands are imprinted by a phase electro-optic modulator (Jenoptik PM635) with a microwave source (Rohde & Schwarz SGS100A) at a frequency of 6 GHz. The obtained modes are fitted with three (or six) Lorentzian peaks, and the sidebands are used to convert the polarization splitting from scanning time to frequency. The data are filtered by requiring $R^2 > 0.95$ to ensure the fit succeeded. An example measurement is shown in Fig. 5.11.

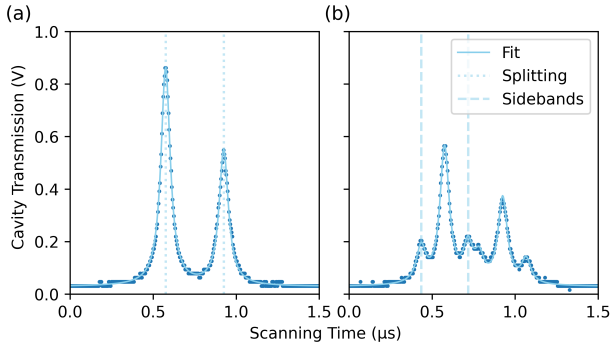

Figure 5.11: Exemplary measurement of the polarization splitting of the two orthogonal cavity modes on the diamond device. The cavity length is scanned with a triangular voltage over the fundamental mode, and the transmission is measured on a photodiode. (a) The length-dependent polarization splitting of the fundamental mode. (b) The same measurement with the sideband modulation. The fixed distance of the sidebands (indicated by the dashed lines) is used to determine the cavity linewidth and polarization splitting in frequency. In this measurement, a linewidth of 2.9 GHz and polarization splitting of 14.9 GHz (dotted lines in (a)) is extracted.

5.7.7 Experimental Methods: PLE Scans

Measurements are performed in a home-built, cryogenic confocal microscope, whose excitation and detection path can be adapted for the measurements of SnV and NV centers. Details about the low-temperature setup and the measurement methods are described in the Supplementary Information of Brevoord et al. [63] and Ruf et al. [26].
The parameters for the SnV center measurements shown in Fig. 5.6 (b) are: 1 µW green repump for 100 ms and 0.5 nW to 1 nW resonant laser excitation power for 10 ms integration. The resonant laser is detuned in steps between 10 MHz to 20 MHz with a speed of ~ 2 GHz/s.

The parameters of the NV center measurements in Fig. 5.6 (d) are: 40 µW green repump for 10 µs and 40 nW resonant laser excitation power for 20 µs integration. At each frequency step between 8 MHz to 20 MHz, a sequence of repump, waiting of 10 µs, and readout is repeated for a total time of 200 ms. The statistics of the NV center measurements can be found in Fig. 5.12.

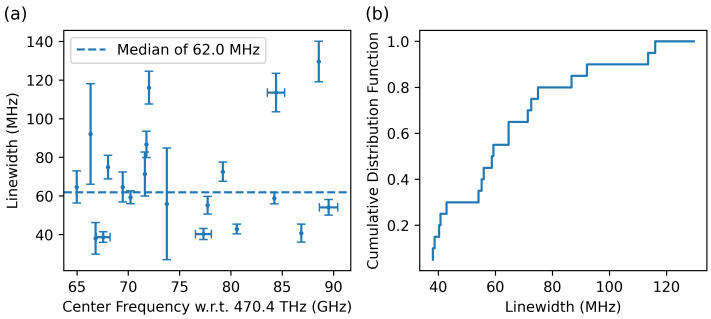

Figure 5.12: Statistics of the optical coherence of 20 different NV centers in an EBL patterned diamond microdevice (*Mr. Orange*), measured at ~ 4 K with a confocal microscope. (a) ZPL center frequencies and linewidth values, obtained by a Voigt fit to the individual NV center resonances (see Fig. 5.6 for exemplary data and fit). The errors are also obtained by the fit. (b) The linewidth values are plotted as a cumulative distribution function (CDF). The measurement parameters can be found in 5.7.7.

5.7.8 Measurements on the Laser-cut Microdevice

An overview of all measurements performed on the laser-cut microdevice (*Vincent Vega*) is shown in Fig. 5.13.

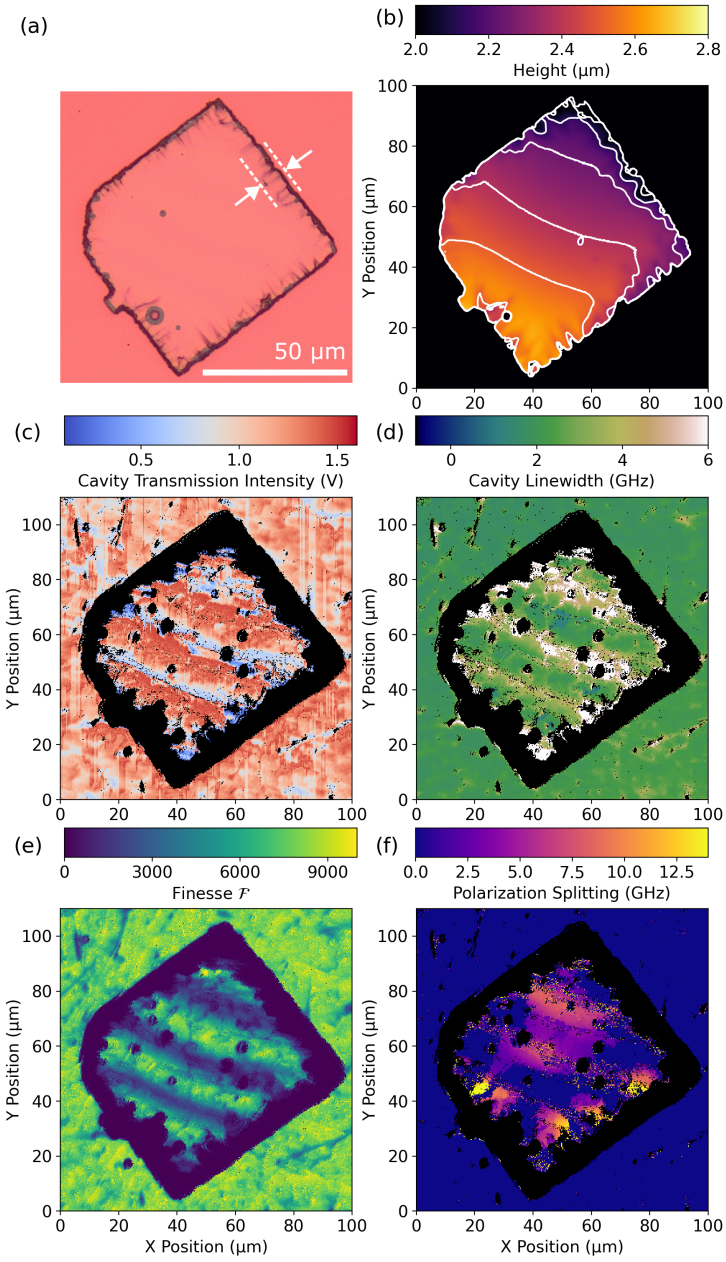

Figure 5.13: Summary of different measurements of the laser-cut diamond microdevice (*Vincent Vega*). (a) Light microscope image. (b) Height map measured by a white light interferometer. (c)-(f) Scanning cavity microscopy. All data is measured within one scan and by probing the cavity with a resonant laser. (c) Cavity transmission intensity is measured on a photodiode. Note that the laser power is varied during the measurement. (d) Cavity linewidth. (e) Cavity finesse. (f) Cavity polarization splitting.

References

[1] E. Janitz, M. K. Bhaskar, and L. Childress, *Cavity quantum electrodynamics with color centers in diamond,* Optica **7**, 1232 (2020).

[2] S. Mi, M. Kiss, T. Graziosi, and N. Quack, *Integrated photonic devices in single crystal diamond,* Journal of Physics: Photonics **2**, 042001 (2020).

[3] M. Ruf, N. H. Wan, H. Choi, D. Englund, and R. Hanson, *Quantum networks based on color centers in diamond,* Journal of Applied Physics **130**, 070901 (2021).

[4] P. K. Shandilya, S. Flagan, N. C. Carvalho, E. Zohari, V. K. Kavatamane, J. E. Losby, and P. E. Barclay, *Diamond Integrated Quantum Nanophotonics: Spins, Photons and Phonons,* Journal of Lightwave Technology **40**, 7538 (2022).

[5] J. Riedrich-Möller, L. Kipfstuhl, C. Hepp, E. Neu, C. Pauly, F. Mücklich, A. Baur, M. Wandt, S. Wolff, M. Fischer, S. Gsell, M. Schreck, and C. Becher, *One- and two-dimensional photonic crystal microcavities in single crystal diamond,* Nature Nanotechnology **7**, 69 (2012).

[6] J. C. Lee, A. P. Magyar, D. O. Bracher, I. Aharonovich, and E. L. Hu, *Fabrication of thin diamond membranes for photonic applications,* Diamond and Related Materials **33**, 45 (2013).

[7] A. Faraon, C. Santori, Z. Huang, K.-M. C. Fu, V. M. Acosta, D. Fattal, and R. G. Beausoleil, *Quantum photonic devices in single-crystal diamond,* New Journal of Physics **15**, 025010 (2013).

[8] S. W. Ding, M. Haas, X. Guo, K. Kuruma, C. Jin, Z. Li, D. D. Awschalom, N. Delegan, F. J. Heremans, A. A. High, and M. Loncar, *High-Q cavity interface for color centers in thin film diamond,* Nature Communications **15**, 6358 (2024).

[9] P. Fuchs, T. Jung, M. Kieschnick, J. Meijer, and C. Becher, *A cavity-based optical antenna for color centers in diamond,* APL Photonics **6**, 086102 (2021).

[10] E. Janitz, M. Ruf, M. Dimock, A. Bourassa, J. Sankey, and L. Childress, *Fabry-Perot microcavity for diamond-based photonics,* Physical Review A **92**, 043844 (2015).

[11] S. Bogdanović, S. B. van Dam, C. Bonato, L. C. Coenen, A.-M. J. Zwerver, B. Hensen, M. S. Z. Liddy, T. Fink, A. Reiserer, M. Lončar, and R. Hanson, *Design and low-temperature characterization of a tunable microcavity for diamond-based quantum networks,* Applied Physics Letters **110**, 171103 (2017).

[12] D. Riedel, I. Söllner, B. J. Shields, S. Starosielec, P. Appel, E. Neu, P. Maletinsky, and R. J. Warburton, *Deterministic Enhancement of Coherent Photon Generation from a Nitrogen-Vacancy Center in Ultrapure Diamond,* Physical Review X **7**, 031040 (2017).

[13] D. Riedel, D. Rohner, M. Ganzhorn, T. Kaldewey, P. Appel, E. Neu, R. J. Warburton, and P. Maletinsky, *Low-Loss Broadband Antenna for Efficient Photon Collection from a Coherent Spin in Diamond,* Physical Review Applied **2**, 064011 (2014).

[14] A. Butcher, X. Guo, R. Shreiner, N. Delegan, K. Hao, P. J. I. Duda, D. D. Awschalom, F. J. Heremans, and A. A. High, *High-Q Nanophotonic Resonators on Diamond Membranes using Templated Atomic Layer Deposition of TiO2,* Nano Letters **20**, 4603 (2020).

[15] X. Guo, M. Xie, A. Addhya, A. Linder, U. Zvi, S. Wang, X. Yu, T. D. Deshmukh, Y. Liu, I. N. Hammock, Z. Li, C. T. DeVault, A. Butcher, A. P. Esser-Kahn, D. D. Awschalom, N. Delegan, P. C. Maurer, F. J. Heremans, and A. A. High, *Direct-bonded diamond membranes for heterogeneous quantum and electronic technologies,* Nature Communications **15**, 8788 (2024).

[16] A. M. Boyce, H. Li, N. C. Wilson, D. Acil, A. Shams-Ansari, S. Chakravarthi, C. Pederson, Q. Shen, N. Yama, K.-M. C. Fu, M. Loncar, and M. H. Mikkelsen, *Plasmonic Diamond Membranes for Ultrafast Silicon Vacancy Emission,* Nano Letters **24**, 3575 (2024).

[17] S. Asif, H. Chen, J. Cremer, S. Ravan, J. Támara-Isaza, S. Lamsal, R. Ebadi, Y. Li, L.-J. Zhou, C.-Z. Chang, J. Q. Xiao, A. Yacoby, R. L. Walsworth, and M. J. H. Ku, *Diamond micro-chip for quantum microscopy,* AVS Quantum Science **6**, 044405 (2024).

[18] Y. Schlussel, T. Lenz, D. Rohner, Y. Bar-Haim, L. Bougas, D. Groswasser, M. Kieschnick, E. Rozenberg, L. Thiel, A. Waxman, J. Meijer, P. Maletinsky, D. Budker, and R. Folman, *Wide-Field Imaging of Superconductor Vortices with Electron Spins in Diamond,* Physical Review Applied **10**, 034032 (2018).

[19] J. J. Carmiggelt, I. Bertelli, R. W. Mulder, A. Teepe, M. Elyasi, B. G. Simon, G. E. W. Bauer, Y. M. Blanter, and T. Van Der Sar, *Broadband microwave detection using electron spins in a hybrid diamond-magnet sensor chip,* Nature Communications **14**, 490 (2023).

[20] T. S. Ghiasi, M. Borst, S. Kurdi, B. G. Simon, I. Bertelli, C. Boix-Constant, S. Mañas-Valero, H. S. J. Van Der Zant, and T. Van Der Sar, *Nitrogen-vacancy magnetometry of CrSBr by diamond membrane transfer,* npj 2D Materials and Applications **7**, 62 (2023).

[21] M. Borst, P. H. Vree, A. Lowther, A. Teepe, S. Kurdi, I. Bertelli, B. G. Simon, Y. M. Blanter, and T. Van Der Sar, *Observation and control of hybrid spin-wave–Meissner-current transport modes,* Science **382**, 430 (2023).

[22] J. Zhou, G. Q. Yan, M. Huang, N. J. McLaughlin, C. R. Du, and H. Wang, *Quantum sensing of local stray field environment of micron-scale magnetic disks,* Applied Physics Letters **123**, 024003 (2023).

[23] R. Albrecht, A. Bommer, C. Deutsch, J. Reichel, and C. Becher, *Coupling of a Single Nitrogen-Vacancy Center in Diamond to a Fiber-Based Microcavity,* Physical Review Letters **110**, 243602 (2013).

[24] H. Kaupp, C. Deutsch, H.-C. Chang, J. Reichel, T. W. Hänsch, and D. Hunger, *Scaling laws of the cavity enhancement for nitrogen-vacancy centers in diamond,* Physical Review A **88**, 053812 (2013).

[25] S. Johnson, P. R. Dolan, T. Grange, A. A. P. Trichet, G. Hornecker, Y. C. Chen, L. Weng, G. M. Hughes, A. A. R. Watt, A. Auffèves, and J. M. Smith, *Tunable cavity coupling of the zero phonon line of a nitrogen-vacancy defect in diamond,* New Journal of Physics **17**, 122003 (2015).

[26] M. Ruf, M. IJspeert, S. van Dam, N. de Jong, H. van den Berg, G. Evers, and R. Hanson, *Optically Coherent Nitrogen-Vacancy Centers in Micrometer-Thin Etched Diamond Membranes,* Nano Letters **19**, 3987 (2019).

[27] V. Yurgens, A. Corazza, J. A. Zuber, M. Gruet, M. Kasperczyk, B. J. Shields, R. J. Warburton, Y. Fontana, and P. Maletinsky, *Spectrally stable nitrogen-vacancy centers in diamond formed by carbon implantation into thin microstructures,* Applied Physics Letters **121**, 234001 (2022).

[28] V. Yurgens, Y. Fontana, A. Corazza, B. J. Shields, P. Maletinsky, and R. J. Warburton, *Cavity-assisted resonance fluorescence from a nitrogen-vacancy center in diamond,* npj Quantum Information **10**, 112 (2024).

[29] R. Zifkin, C. D. Rodríguez Rosenblueth, E. Janitz, Y. Fontana, and L. Childress, *Lifetime Reduction of Single Germanium-Vacancy Centers in Diamond via a Tunable Open Microcavity,* PRX Quantum **5**, 030308 (2024).

[30] R. Berghaus, S. Sachero, G. Bayer, J. Heupel, T. Herzig, F. Feuchtmayr, J. Meijer, C. Popov, and A. Kubanek, *Cavity-enhanced emission and absorption of color centers in a diamond membrane with selectable strain,* Physical Review Applied **23**, 034050 (2025).

[31] Y. Herrmann, J. Fischer, J. M. Brevoord, C. Sauerzapf, L. G. C. Wienhoven, L. J. Feije, M. Pasini, M. Eschen, M. Ruf, M. J. Weaver, and R. Hanson, *Coherent Coupling of a Diamond Tin-Vacancy Center to a Tunable Open Microcavity,* Physical Review X **14**, 041013 (2024).

[32] S. Bogdanović, M. S. Z. Liddy, S. B. van Dam, L. C. Coenen, T. Fink, M. Lončar, and R. Hanson, *Robust nano-fabrication of an integrated platform for spin control in a tunable microcavity,* APL Photonics **2**, 126101 (2017).

[33] P. Tamarat, T. Gaebel, J. R. Rabeau, M. Khan, A. D. Greentree, H. Wilson, L. C. L. Hollenberg, S. Prawer, P. Hemmer, F. Jelezko, and J. Wrachtrup, *Stark Shift Control of Single Optical Centers in Diamond,* Physical Review Letters **97**, 083002 (2006).

[34] N. R. Parikh, J. D. Hunn, E. McGucken, M. L. Swanson, C. W. White, R. A. Rudder, D. P. Malta, J. B. Posthill, and R. J. Markunas, *Single-crystal diamond plate liftoff achieved by ion implantation and subsequent annealing,* Applied Physics Letters **61**, 3124 (1992).

[35] A. H. Piracha, P. Rath, K. Ganesan, S. Kühn, W. H. P. Pernice, and S. Prawer, *Scalable Fabrication of Integrated Nanophotonic Circuits on Arrays of Thin Single Crystal Diamond Membrane Windows,* Nano Letters **16**, 3341 (2016).

[36] B. A. Fairchild, P. Olivero, S. Rubanov, A. D. Greentree, F. Waldermann, R. A. Taylor, I. Walmsley, J. M. Smith, S. Huntington, B. C. Gibson, D. N. Jamieson, and S. Prawer, *Fabrication of Ultrathin Single-Crystal Diamond Membranes,* Advanced Materials **20**, 4793 (2008).

[37] X. Guo, N. Delegan, J. C. Karsch, Z. Li, T. Liu, R. Shreiner, A. Butcher, D. D. Awschalom, F. J. Heremans, and A. A. High, *Tunable and Transferable Diamond Membranes for Integrated Quantum Technologies,* Nano Letters **21**, 10392 (2021).

[38] A. Faraon, P. E. Barclay, C. Santori, K.-M. C. Fu, and R. G. Beausoleil, *Resonant enhancement of the zero-phonon emission from a colour centre in a diamond cavity,* Nature Photonics **5**, 301 (2011).

[39] B. J. M. Hausmann, B. Shields, Q. Quan, P. Maletinsky, M. McCutcheon, J. T. Choy, T. M. Babinec, A. Kubanek, A. Yacoby, M. D. Lukin, and M. Lončar, *Integrated Diamond Networks for Quantum Nanophotonics,* Nano Letters **12**, 1578 (2012).

[40] P. Ovartchaiyapong, L. M. A. Pascal, B. A. Myers, P. Lauria, and A. C. Bleszynski Jayich, *High quality factor single-crystal diamond mechanical resonators,* Applied Physics Letters **101**, 163505 (2012).

[41] P. Appel, E. Neu, M. Ganzhorn, A. Barfuss, M. Batzer, M. Gratz, A. Tschöpe, and P. Maletinsky, *Fabrication of all diamond scanning probes for nanoscale magnetometry,* Review of Scientific Instruments **87**, 063703 (2016).

[42] M. Ruf, *Cavity-enhanced quantum network nodes in diamond*, Ph.D. thesis, Delft University of Technology (2021).

[43] Y. Tao, J. M. Boss, B. A. Moores, and C. L. Degen, *Single-crystal diamond nanomechanical resonators with quality factors exceeding one million,* Nature Communications **5**, 3638 (2014).

[44] J. Heupel, M. Pallmann, J. Körber, D. Hunger, J. P. Reithmaier, and C. Popov, *Fabrication of High-Quality Thin Single-Crystal Diamond Membranes with Low Surface Roughness,* Physica Status Solidi A **220**, 2200465 (2023).

[45] M. J. Burek, N. P. de Leon, B. J. Shields, B. J. M. Hausmann, Y. Chu, Q. Quan, A. S. Zibrov, H. Park, M. D. Lukin, and M. Lončar, *Free-Standing Mechanical and Photonic Nanostructures in Single-Crystal Diamond,* Nano Letters **12**, 6084 (2012).

[46] B. Khanaliloo, M. Mitchell, A. C. Hryciw, and P. E. Barclay, *High-Q/V Monolithic Diamond Microdisks Fabricated with Quasi-isotropic Etching,* Nano Letters **15**, 5131 (2015).

[47] J. S. Hodges, L. Li, M. Lu, E. H. Chen, M. E. Trusheim, S. Allegri, X. Yao, O. Gaathon, H. Bakhru, and D. Englund, *Long-lived NV^- spin coherence in high-purity diamond membranes,* New Journal of Physics **14**, 093004 (2012).

[48] C. Toninelli, Y. Delley, T. Stöferle, A. Renn, S. Götzinger, and V. Sandoghdar, *A scanning microcavity for in situ control of single-molecule emission,* Applied Physics Letters **97**, 021107 (2010).

[49] M. Mader, J. Reichel, T. W. Hänsch, and D. Hunger, *A scanning cavity microscope,* Nature Communications **6**, 7249 (2015).

[50] J. Benedikter, T. Moosmayer, M. Mader, T. Hümmer, and D. Hunger, *Transverse-mode coupling effects in scanning cavity microscopy,* New Journal of Physics **21**, 103029 (2019).

[51] S. M. Eaton, J. P. Hadden, V. Bharadwaj, J. Forneris, F. Picollo, F. Bosia, B. Sotillo, A. N. Giakoumaki, O. Jedrkiewicz, A. Chiappini, M. Ferrari, R. Osellame, P. E. Barclay, P. Olivero, and R. Ramponi, *Quantum Micro–Nano Devices Fabricated in Diamond by Femtosecond Laser and Ion Irradiation,* Advanced Quantum Technologies **2**, 1900006 (2019).

[52] R. A. Norte, J. P. Moura, and S. Gröblacher, *Mechanical Resonators for Quantum Optomechanics Experiments at Room Temperature,* Physical Review Letters **116**, 147202 (2016).

[53] J. F. Ziegler, M. Ziegler, and J. Biersack, *SRIM – The stopping and range of ions in matter (2010),* Nuclear Instruments and Methods in Physics Research Section B: Beam Interactions with Materials and Atoms **268**, 1818 (2010).

[54] S. B. Van Dam, M. Walsh, M. J. Degen, E. Bersin, S. L. Mouradian, A. Galiullin, M. Ruf, M. IJspeert, T. H. Taminiau, R. Hanson, and D. R. Englund, *Optical coherence of diamond nitrogen-vacancy centers formed by ion implantation and annealing,* Physical Review B **99**, 161203 (2019).

[55] Y. Herrmann, J. M. Brevoord, J. Fischer, S. Scheijen, C. Sauerzapf, N. Codreanu, L. G. C. Wienhoven, Y. M. Q. van der Graaf, C. F. J. Wolfs, R. Méjard, M. Ruf, N. de Jong, and R. Hanson, *Data and software underlying the publication "Laser-cut Patterned, Micrometer-thin Diamond Membranes with Coherent Color Centers for Open Microcavities",* 4TU.ResearchData (2025), `https://www.doi.org/10.4121/a8e32e27-5a91-4a4a-abfc-e5bd884317ae`.

[56] S. B. van Dam, M. Ruf, and R. Hanson, *Optimal design of diamond-air microcavities for quantum networks using an analytical approach,* New Journal of Physics **20**, 115004 (2018).

[57] A. M. Zaitsev, *Optical Properties of Diamond* (Springer Berlin Heidelberg, Berlin, Heidelberg, 2001).

[58] J. Körber, M. Pallmann, J. Heupel, R. Stöhr, E. Vasilenko, T. Hümmer, L. Kohler, C. Popov, and D. Hunger, *Scanning Cavity Microscopy of a Single-Crystal Diamond Membrane,* Physical Review Applied **19**, 064057 (2023).

[59] I. Friel, S. L. Geoghegan, D. J. Twitchen, and G. A. Scarsbrook, *Development of high quality single crystal diamond for novel laser applications,* in *Optics and Photonics for Counterterrorism and Crime Fighting VI and Optical Materials in Defence Systems Technology VII*, edited by C. Lewis, D. Burgess, R. Zamboni, F. Kajzar, and E. M. Heckman (Toulouse, France, 2010) p. 783819.

[60] D. Howell, *Strain-induced birefringence in natural diamond: a review,* European Journal of Mineralogy **24**, 575 (2012).

[61] H. K. Beukers, M. Pasini, H. Choi, D. Englund, R. Hanson, and J. Borregaard, *Remote-Entanglement Protocols for Stationary Qubits with Photonic Interfaces,* PRX Quantum **5**, 010202 (2024).

[62] B. Hensen, H. Bernien, A. E. Dréau, A. Reiserer, N. Kalb, M. S. Blok, J. Ruitenberg, R. F. L. Vermeulen, R. N. Schouten, C. Abellán, W. Amaya, V. Pruneri, M. W. Mitchell, M. Markham, D. J. Twitchen, D. Elkouss, S. Wehner, T. H. Taminiau, and R. Hanson, *Loophole-free Bell inequality violation using electron spins separated by 1.3 kilometres,* Nature **526**, 682 (2015).

[63] J. M. Brevoord, L. De Santis, T. Yamamoto, M. Pasini, N. Codreanu, T. Turan, H. K. Beukers, C. Waas, and R. Hanson, *Heralded initialization of charge state and optical-transition frequency of diamond tin-vacancy centers,* Physical Review Applied **21**, 054047 (2024).

[64] J. M. Brevoord, L. G. C. Wienhoven, N. Codreanu, T. Ishiguro, E. van Leeuwen, M. Iuliano, L. De Santis, C. Waas, H. K. C. Beukers, T. Turan, C. Errando-Herranz, K. Kawaguchi, and R. Hanson, *Large-range tuning and stabilization of the optical transition of diamond tin-vacancy centers by in situ strain control,* Applied Physics Letters **126**, 174001 (2025).

[65] G. L. Van De Stolpe, L. J. Feije, S. J. H. Loenen, A. Das, G. M. Timmer, T. W. De Jong, and T. H. Taminiau, *Check-probe spectroscopy of lifetime-limited emitters in bulk-grown silicon carbide,* npj Quantum Information **11**, 31 (2025).

[66] H. Bernien, L. Childress, L. Robledo, M. Markham, D. Twitchen, and R. Hanson, *Two-Photon Quantum Interference from Separate Nitrogen Vacancy Centers in Diamond,* Physical Review Letters **108**, 043604 (2012).

[67] A. Sipahigil, K. D. Jahnke, L. J. Rogers, T. Teraji, J. Isoya, A. S. Zibrov, F. Jelezko, and M. D. Lukin, *Indistinguishable Photons from Separated Silicon-Vacancy Centers in Diamond,* Physical Review Letters **113**, 113602 (2014).

[68] H. Bernien, B. Hensen, W. Pfaff, G. Koolstra, M. S. Blok, L. Robledo, T. H. Taminiau, M. Markham, D. J. Twitchen, L. Childress, and R. Hanson, *Heralded entanglement between solid-state qubits separated by three metres,* Nature **497**, 86 (2013).

[69] J. Borregaard, A. S. Sørensen, and P. Lodahl, *Quantum Networks with Deterministic Spin–Photon Interfaces,* Advanced Quantum Technologies **2**, 1800091 (2019).

[70] Z. Li, X. Guo, Y. Jin, F. Andreoli, A. Bilgin, D. D. Awschalom, N. Delegan, F. J. Heremans, D. Chang, G. Galli, and A. A. High, *Atomic optical antennas in solids,* Nature Photonics **18**, 1113 (2024).

[71] G. Pieplow, C. G. Torun, C. Gurr, J. H. D. Munns, F. M. Herrmann, A. Thies, T. Pregnolato, and T. Schröder, *Quantum electrometer for time-resolved material science at the atomic lattice scale,* Nature Communications **16**, 6435 (2025).

[72] D. M. Irber, F. Poggiali, F. Kong, M. Kieschnick, T. Lühmann, D. Kwiatkowski, J. Meijer, J. Du, F. Shi, and F. Reinhard, *Robust all-optical single-shot readout of nitrogen-vacancy centers in diamond,* Nature Communications **12**, 532 (2021).

[73] S. L. N. Hermans, M. Pompili, L. D. Santos Martins, A. R-P Montblanch, H. K. C. Beukers, S. Baier, J. Borregaard, and R. Hanson, *Entangling remote qubits using the single-photon protocol: an in-depth theoretical and experimental study,* New Journal of Physics **25**, 013011 (2023).

[74] D. Hunger, T. Steinmetz, Y. Colombe, C. Deutsch, T. W. Hänsch, and J. Reichel, *A fiber Fabry–Perot cavity with high finesse,* New Journal of Physics **12**, 065038 (2010).

[75] M. Uphoff, M. Brekenfeld, G. Rempe, and S. Ritter, *Frequency splitting of polarization eigenmodes in microscopic Fabry–Perot cavities,* New Journal of Physics **17**, 013053 (2015).

[76] P. Maier, S. Rupp, N. Lettner, J. H. Denschlag, and A. Kubanek, *Fabrication of customized low-loss optical resonators by combination of FIB-milling and CO_2 laser smoothing,* Optics Express **33**, 19205 (2025).

[77] X. Guo, A. M. Stramma, Z. Li, W. G. Roth, B. Huang, Y. Jin, R. A. Parker, J. Arjona Martínez, N. Shofer, C. P. Michaels, C. P. Purser, M. H. Appel, E. M. Alexeev, T. Liu, A. C. Ferrari, D. D. Awschalom, N. Delegan, B. Pingault, G. Galli, F. J. Heremans, M. Atatüre, and A. A. High, *Microwave-Based Quantum Control and Coherence Protection of Tin-Vacancy Spin Qubits in a Strain-Tuned Diamond-Membrane Heterostructure,* Physical Review X **13**, 041037 (2023).

[78] Y. Herrmann, J. Fischer, S. Scheijen, C. F. J. Wolfs, J. M. Brevoord, C. Sauerzapf, L. G. C. Wienhoven, L. J. Feije, M. Eschen, M. Ruf, M. J. Weaver, and R. Hanson, *A low-temperature tunable microcavity featuring high passive stability and microwave integration,* AVS Quantum Science **6**, 041401 (2024).

[79] M. Ruf, M. Weaver, S. van Dam, and R. Hanson, *Resonant Excitation and Purcell Enhancement of Coherent Nitrogen-Vacancy Centers Coupled to a Fabry-Perot Microcavity,* Physical Review Applied **15**, 024049 (2021).

[80] S. van Dam, *Optical cavities, coherent emitters, and protocols for diamond-based quantum networks*, Ph.D. thesis, Delft University of Technology (2019).

6

Coherent Coupling of a Diamond Tin-Vacancy Center to a Tunable Open Microcavity

Y. Herrmann*, J. Fischer*, J. M. Brevoord, C. Sauerzapf, L. G. C. Wienhoven, L. J. Feije, M. Pasini, M. Eschen, M. Ruf, M. J. Weaver and R. Hanson

Efficient coupling of optically active qubits to optical cavities is a key challenge for solid-state-based quantum optics experiments and future quantum technologies. Here we present a quantum photonic interface based on a single tin-vacancy center in a micrometer-thin diamond membrane coupled to a tunable open microcavity. We use the full tunability of the microcavity to selectively address individual tin-vacancy centers within the cavity mode volume. Purcell enhancement of the tin-vacancy center optical transition is evidenced both by optical excited state lifetime reduction and by optical linewidth broadening. As the emitter selectively reflects the single-photon component of the incident light, the coupled emitter-cavity system exhibits strong quantum nonlinear behavior. On resonance, we observe a transmission dip of 50 % for low incident photon number per Purcell-reduced excited state lifetime, while the dip disappears as the emitter is saturated with higher photon number. Moreover, we demonstrate that the emitter strongly modifies the photon statistics of the transmitted light by observing photon bunching. This work establishes a versatile and tunable platform for advanced quantum optics experiments and proof-of-principle demonstrations on quantum networking with solid-state qubits.

The results of this chapter have been published in Physical Review X **14**, 041013 (2024).
* Equally contributed authors.

6.1 Introduction

Coherent interactions between photons and two-level matter systems are a central building block in quantum optics and quantum information science, with potential application in future quantum networks for communication and computation [1, 2]. To achieve significant light-matter interaction, optical resonators (cavities) are widely employed [3–6]. In the past years, tunable open microcavities have emerged as a versatile tool to explore and enhance the optical interface for a variety of solid-state emitters like rare-earth ions [7, 8], quantum dots [9–12], two-dimensional materials [13, 14], and dye molecules embedded in organic crystals [15]. These experiments capitalize on the combination of spatial flexibility, large spectral tunability, full optical accessibility, and simple hybrid integration with emitter hosts. Moreover, the mirror parameters can be tailored to a desired application, including native fiber coupling by mirrors fabricated on the tip of optical fibers [16].

Much work with open microcavities has focused on diamond color centers [17–26], which have been the main workhorse for early quantum network nodes [27–29]. The electron spin of those color centers functions as a good communication qubit thanks to the combination of excellent quantum coherence [30] and spin-dependent optical transitions. Furthermore, the center's native nuclear spin [31, 32] as well as surrounding nuclear spins [33] can be utilized as additional qubits, enabling network experiments with multi-qubit nodes [34–36]. Recent experiments on coupling color centers to open microcavities have demonstrated Purcell enhancement [21], resonant excitation and detection [24] and optical addressing of the spin [26]. However, access to the coherent coupling regime, where the color center significantly alters the cavity transmission as well as the photon statistics of the transmitted light, has so far remained elusive.

In this work, we demonstrate the coherent coupling of individual diamond tin-vacancy (SnV) centers to a fiber-based Fabry-Pérot microcavity. We capitalize on the excellent spatial and spectral tunability of the open microcavity to select a well-coupled SnV center, which is characterized through the reduced excited state lifetime and the broadened emitter linewidth. Compared to previous implementations with nitrogen-vacancy centers [21, 24], we achieve an improvement in coherent cooperativity of nearly two orders of magnitude through the combination of SnV centers and a high-quality, stable microcavity. We then exploit the coherent coupling to observe a strong reduction of cavity transmission by the emitter on resonance and study the dependence on detuning and on incident photon number. Finally, we explicitly demonstrate the nonlinearity of the light-emitter interaction by measuring changes in the photon statistics of the transmitted light induced by the emitter.

6.2 Experimental Setup

We use a fiber-based Fabry-Pérot microcavity, that is schematically depicted in Fig. 6.1 (a). The microcavity is formed by a laser-ablated concave fiber tip input mirror with a radius of curvature of 15.7 µm and a macroscopic flat output mirror [16], where thin diamond samples are bonded via Van der Waals forces. The used diamond device hosts implanted SnV centers and has a thickness of about 3.72 µm in the region of the cavity. SnV centers have recently emerged among solid-state color centers as a promising qubit platform with demonstrations of excellent optical and spin coherence [37–41]. The inset of Fig. 6.1

(a) shows the energy level structure of the negatively charged SnV center in diamond, including the zero-phonon line (ZPL) C and D transition at 619 nm and 620 nm, respectively. These transitions connect the lower branch of the excited states (ES) to the ground states (GS).

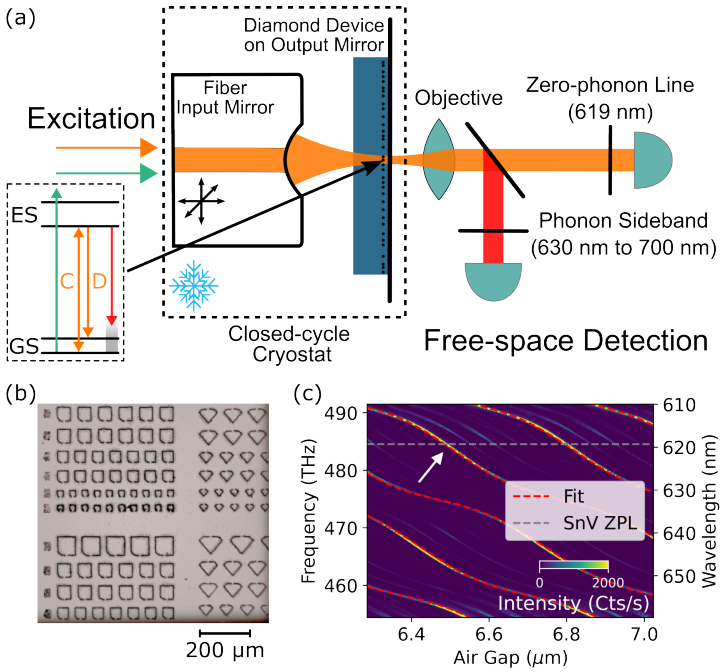

Figure 6.1: Schematical experimental setup, diamond devices, and air-diamond hybrid cavity operation. (a) On- and off-resonant excitation light is sent into the cavity via the fiber input mirror, and the outcoupled Gaussian beam is collimated with an objective, sent to a spectrometer after free-space filtering, or split into zero-phonon line and phonon sideband light and fiber-coupled to single-photon detectors (see Appendix 6.8.1 for details). SnV centers are hosted in the micrometer-thin diamond devices. The inset shows the energy level structure of the negatively charged SnV center in diamond. (b) Light microscope image of the diamond devices in their holding structure. (c) Cavity transmission spectra of a broadband, white light supercontinuum source depending on the cavity air gap, which shows the mode dispersion of the air-diamond hybrid cavity. The dashed red lines display a fit using a one-dimensional hybrid cavity model [42]. The white arrow indicates the operation point of the cavity at an air gap of 6.50 µm and a diamond thickness of 3.72 µm matching the SnV center zero-phonon line wavelength.

The sample fabrication starts with an approximately 50 µm thick and top-facing ⟨100⟩ oriented diamond membrane, obtained by laser cutting and polishing [43]. In the next step, $25\,\mathrm{x}\,25\,\mu m^2$ squares with support bars are patterned into the diamond, followed by tin ion implantation and subsequent annealing at 1200 °C. With the implantation energy of 350 keV (implantation dose of 3×10^{10} ions/cm^2 under an angle of 7°) SnV centers in the range of the first intracavity electric field antinode located about 64 nm away from the output mirror are created. The membranes are further thinned down to a few micrometers using a fused quartz mask and reactive ion etching [43, 44]. Figure 6.1 (b) shows a light microscope image of the membrane after this step. Individual small diamond devices are

broken out with a micromanipulator and bonded to the output mirror [21].

The input and output mirror transmittance is specified with 80 ppm and 2000 ppm (diamond termination), respectively. A piezo positioning system moves the fiber across multiple diamond devices and changes cavity position and length in situ. As illustrated in Fig. 6.1 (c) we operate the cavity at an air gap of 6.50 µm (mode number $q = 50$ of the air-diamond hybrid cavity) matching the resonance of the SnV center ZPL wavelength of 619 nm and showing an air-like mode character with a local dispersion slope of 46 MHz/pm. By measuring the cavity mode in transmission with a resonant 619 nm laser a Lorentzian linewidth of (6.86 ± 0.05) GHz is determined (see Appendix 6.8.2, Fig. 6.7), resulting in a cavity quality factor Q of about 7×10^4. Using a transfer matrix model we estimate an effective cavity length $L_{\text{eff}} = 10.8\,\mu\text{m}$ and a beam waist of $\omega_0 = 1.24\,\mu\text{m}$, leading to a mode volume of $V = 55\ \lambda^3$ (see Appendix 6.8.2 for details) [45]. The estimated total cavity losses read 7500 ppm (Finesse $\mathcal{F} = 830$). Comparing with the mirror transmittance values, we find additional losses that we attribute to residual scattering at the refractive index interfaces of our hybrid cavity. With these cavity parameters we calculate a Purcell factor of $F_P = 6.9$ following the definition

$$F_P = \frac{3}{4\pi^2}\left(\frac{\lambda}{n}\right)^3 \frac{Q}{V}, \tag{6.1}$$

with the cavity resonance wavelength λ, the refractive index of diamond n, the cavity quality factor Q and the cavity mode volume V.

The microcavity is cooled by a closed-cycle optical cryostat to a device temperature of about 8 K. We measure cavity length fluctuations of 27 pm over the full cryostat cold head cycle, a five times improvement over our previous work [24] (extended technical details of the cryostat setup can be found in Ref. [46]). For the SnV center measurements, excitation laser light is inserted into the cavity via the fiber input mirror. We use free-space optics to collect the light exiting the cavity through the output mirror for detection (see Fig. 6.1 (a)). In combination with the asymmetric mirror transmittance values, this enables the efficient coupling of the cavity mode signal into a single-mode fiber.

All power and photons per lifetime values stated in this work refer to the values after the output mirror of the microcavity. Moreover, the reported uncertainties correspond to one standard deviation confidence intervals.

6.3 Coupling of Individual SnV Centers to the Microcavity

With the cavity resonance set close to the SnV center ZPL we explore the coupling of SnV centers in the diamond device to the optical cavity. We excite the emitters with continuous wave, off-resonant 515 nm excitation through the input mirror and detect the light that is leaving the cavity through the output mirror. The cavity resonance frequency is tuned by applying a voltage to the piezo positioning system, on which the fiber input mirror is mounted. The cavity coating is almost transparent for (525 ± 15) nm light, which renders the emitter excitation independent of the cavity resonance frequency. In this measurement, we directly send the outcoupled light to a spectrometer after filtering out the excitation laser with a 600 nm longpass filter. When the cavity comes in resonance with an emitter, cavity-coupled SnV center light emission is expected to appear. Figure 6.2 (a) shows the

resulting spectra as a function of relative cavity air gap displacement. As expected for SnV centers at cryogenic temperatures, two prominent regions of high emission are observed around 619 nm and 620 nm. We attribute these regions to the C and D transition of multiple SnV centers, corresponding to the optical transitions from the lower branch of the excited state to the two ground states (see energy level structure in Fig. 6.1 (a)).

To analyze the emission with the spectral resolution of the cavity (vibration averaged linewidth 8.0 GHz) we scan the cavity mode over the emission lines and measure the intensity in the ZPL detection path with a single-photon detector under pulsed, off-resonant 532 nm excitation (see Fig. 6.2 (b)). The ZPL detection path is equipped with a (620 ± 5) nm bandpass filter and polarization optics, which are already adjusted to the emission line investigated below. In the resulting spectrum, a group of multiple SnV center emission lines around 619 nm and 620 nm is observed together with individual, spectrally isolated emission lines.

In the following, we focus on the isolated 619 nm emission line indicated by the arrow in Fig. 6.2 (b). We additionally filter the ZPL light with an angle-tunable etalon with a full width at half maximum linewidth (FWHM) of ≈ 45 GHz to further reduce background counts. This background emission may originate from parasitic light created by the green excitation laser in the cavity input fiber and in the output mirror substrate. We verify that the selected emission line corresponds to a single SnV center coupled to the cavity by measuring the $g^{(2)}(\tau)$ correlation function of the ZPL light under pulsed, off-resonant 532 nm excitation (inset of Fig. 6.2 (b)). We find $g^{(2)}(0) \ll 0.5$ without background subtraction, showing that indeed this emission is dominated by a single SnV center.

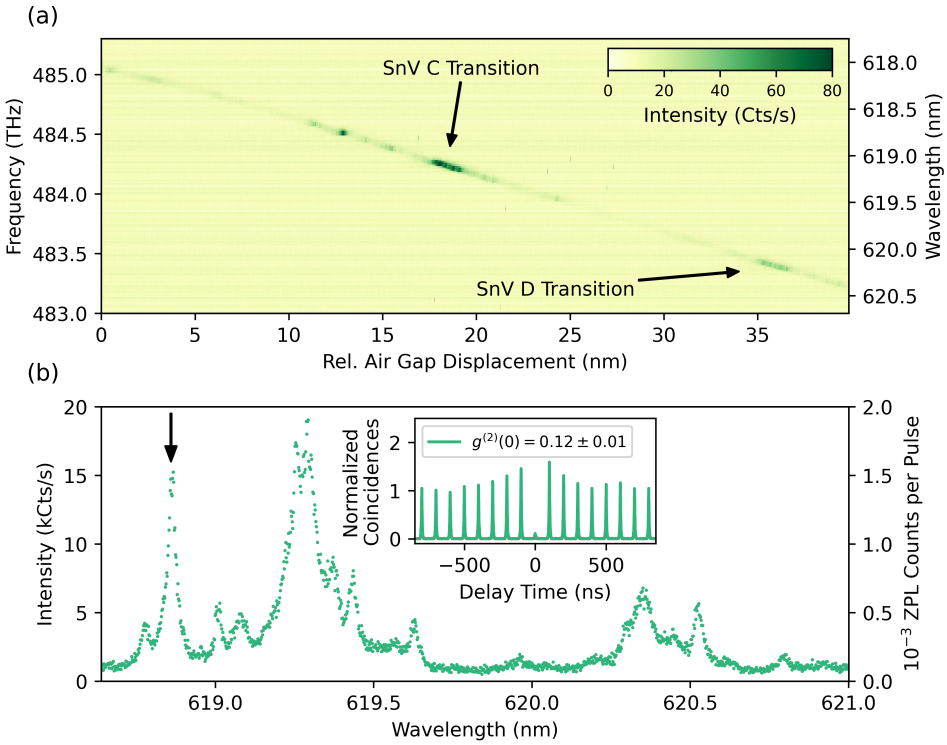

Figure 6.2: Coupling SnV centers to the microcavity under off-resonant excitation. (a) Analyzing the detection with a spectrometer, after filtering out the excitation light with a 600 nm longpass filter. High emission is observed when the cavity mode (straight line) becomes resonant with the C or D transition of a SnV center. (b) The detection path light is sent to a single-photon detector, after filtering with a (620 ± 5) nm bandpass filter and polarization optics. The left and right y-axis show the count rate and the corresponding photon detection probability per pulse (laser repetition rate $f_{\mathrm{rep}} = 10\,\mathrm{MHz}$), respectively. We tune the cavity to the isolated line, which is marked with an arrow. The inset shows a normalized $g^{(2)}(\tau)$ correlation measurement of the ZPL fluorescence, which is additionally filtered with an etalon (measurement time 20 min, count rate per detector 7 kHz, background count rate 200 Hz).

6.4 Characterization of the Emitter-Cavity System

After selecting an isolated SnV center emission line, we quantify the coupling of the SnV center to the cavity. We make use of the tunability of our microcavity, which enables us to switch the coupling on and off by tuning the cavity on and off resonance with the emitter. For emitters with a coupling strength to the cavity field comparable to other decay channels, the emission is significantly altered. In particular, the excited state lifetime is reduced via the Purcell effect. The coupling strength to the cavity can thus be estimated by comparing the excited state lifetimes for the cases where the cavity is on resonance and off resonance with the emitter.

Figure 6.3 (a) shows excited state lifetime measurements of the SnV center at the C transition for different cavity frequency detunings. The emitter is excited by pulsed, off-resonant 532 nm excitation. Each cavity frequency detuning is set by matching the cavity resonance to a frequency-stabilized reference laser before starting the lifetime measurement. When the cavity is fully on resonance with the SnV center, we measure a detector count rate of 15 kHz and a Purcell-reduced excited state lifetime of $\tau_P = (2.55 \pm 0.01)$ ns (see Fig. 6.3 (b)). The emitter's natural lifetime of $\tau = (5.0 \pm 0.1)$ ns (corresponding to a lifetime-limited linewidth of $\gamma = 1/2\pi\tau = 32$ MHz) is determined at large cavity detuning, where the Purcell enhancement is negligible.

As expected qualitatively, the measured emitter count rate in Fig. 6.3 (a) decreases with increasing cavity frequency detuning. However, the range over which the decrease occurs does not quantitatively match the previously characterized cavity linewidth (vibration-averaged 8 GHz). We attribute this to random emission frequency jumps (spectral diffusion) of the SnV center, due to changes in the environment caused by the strong pulsed, off-resonant 532 nm excitation light (see Appendix 6.8.8 for details). The presence of this spectral diffusion in the individual lifetime measurements leads to an averaging of the Purcell enhancement. Thus, the Purcell-reduced excited state lifetime only yields a lower bound on the cooperativity, which we calculate to be $C \geq \tau/\tau_P - 1 = 0.96 \pm 0.05$.

We note that we observe Purcell-reduced lifetimes on several other SnV centers in this device, with the shortest lifetime measured to be (1.78 ± 0.01) ns (see Appendix 6.8.6, Fig. 6.9 and Fig. 6.12). Differences between measured Purcell-reduced lifetimes are likely due to differences in the cavity quality factor at different lateral positions and due to emitters being at different depths in the diamond device, leading to a different overlap with the cavity field.

The Purcell-reduction of the excited state lifetime also reflects in a broadening of the emitter linewidth, which presents an alternative approach to measure the emitter-cavity coupling. Since spectral diffusion is expected to be strongly reduced in linewidth measurements using resonant excitation, the coupling can be more precisely determined. Figure 6.3 (c) shows such photoluminescence excitation (PLE) measurements using phonon sideband (PSB) detection. We define the emitter linewidth for the case that the cavity is on resonance as $\gamma_P'/2\pi$ and for a far-detuned cavity as $\gamma'/2\pi$. On cavity resonance, we measure $\gamma_P'/2\pi = (126 \pm 4)$ MHz, and for a large emitter-cavity detuning of > 100 GHz an emitter linewidth of $\gamma'/2\pi = (77.6 \pm 0.8)$ MHz (see Appendix 6.8.7 for details about the PLE measurements). From these measurements we calculate a cooperativity of $C = 1.7 \pm 0.2$ (see Appendix 6.8.4 for details about the employed vibration correction) and conclude the full set of emitter-cavity parameters $\{g, \kappa, \gamma\}/2\pi = \{0.30, 6.86, 0.032\}$GHz, with the single photon

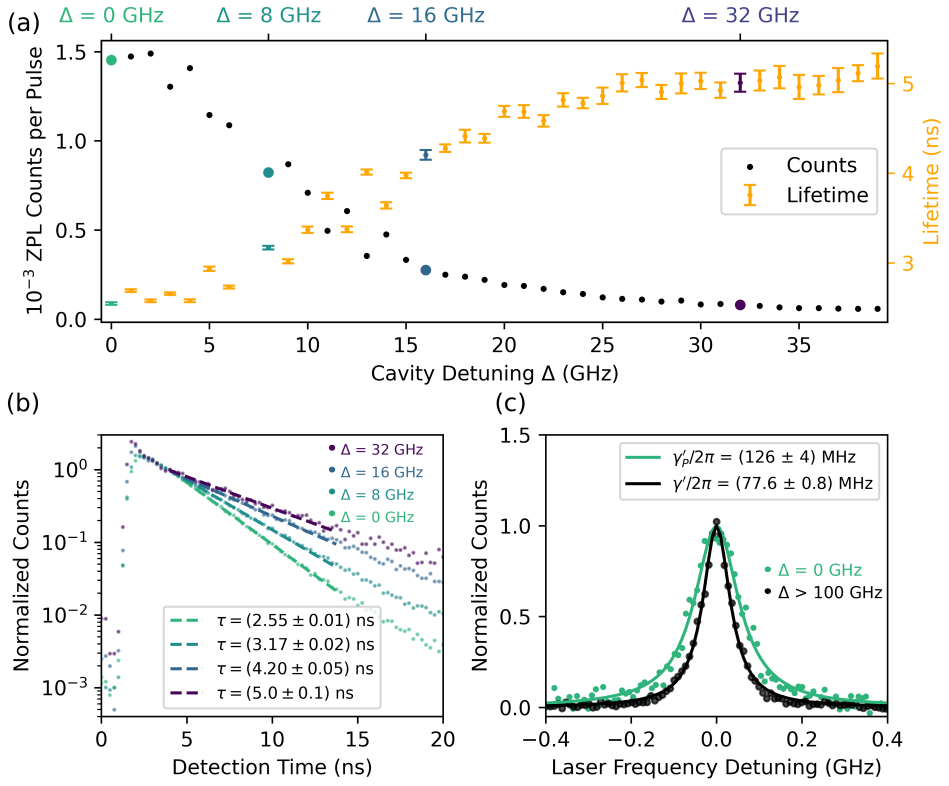

Figure 6.3: Quantifying the emitter-cavity coupling. (a) SnV center fluorescence and excited state lifetime for different cavity detunings with respect to the SnV center. Off-resonant, pulsed excitation ($P \approx 5\,\mathrm{mW}$, $f_{\mathrm{rep}} = 10\,\mathrm{MHz}$) is used to excite the SnV center independently of the cavity resonance. The colored data points indicate the lifetime measurements plotted in (b). The complete dataset is shown in Appendix 6.8.6, Fig. 6.10. The error bars represent one standard deviation confidence intervals of the fit. (b) Individual lifetime measurements (integration time of 30 s) of four different cavity detunings of (a), varying from fully on resonance to off resonance. The dashed lines show the fits to a monoexponential decay in a 10 ns fit window. The lifetime measurements without normalization are shown in Appendix 6.8.6, Fig. 6.11. (c) On and off cavity resonance PLE linewidth measurement of the SnV center. For the off resonance measurement, the cavity is detuned by $> 100\,\mathrm{GHz}$ with respect to the SnV center.

Rabi frequency g and the total cavity loss rate κ. The determined cooperativity, to our knowledge, the highest reported for color centers in microcavities, puts the emitter-cavity system in the coherent coupling regime in which quantum nonlinear behavior dominates the dynamics.

Since our cavity system is characterized and understood in detail, the measured cooperativity also allows us to draw conclusions about the SnV center properties, when considering the cooperativity definition

$$C = F_P \, \beta_0 \, \eta \, \alpha \, \zeta \, \epsilon, \tag{6.2}$$

with the SnV center Debye-Waller factor β_0, quantum efficiency η, branching ratio between C and D transition α, overlap of cavity polarization with the emitter dipole ζ and the spatial overlap of cavity mode and emitter ϵ. For our implementation $\zeta = \cos^2(35^\circ)$ due to the $\langle 100 \rangle$ diamond crystal orientation. In addition, the SnV center Debye-Waller factor of $\beta_0 = 0.57 \pm 0.01$ [47] is reported. Since the spatial overlap is bounded by unity ($\epsilon \leq 1$) a lower bound for the product of branching ratio and quantum efficiency $\alpha \, \eta \geq 0.64 \pm 0.06$ is calculated. This value represents an important figure of merit to estimate the performance of future SnV-cavity implementations and is consistent with reported estimates $\eta \approx 0.8$ [48] and $\alpha \approx 0.8$ [49].

While the cooperativity quantifies the efficiency of the spin-photon interface, the coherent cooperativity ultimately determines the fidelity of protocols [50]. The investigated emitter exhibits contributions of nonradiative broadening above its lifetime-limited linewidth, likely due to phonon dephasing because of finite temperature effects [51, 52]. Accounting for these contributions a vibration-corrected coherent cooperativity of $C_{\mathrm{coh}} = C\gamma/\gamma' = 0.69 \pm 0.07$ is evaluated.

6.5 Quantum Nonlinear Behavior of the Emitter-Cavity System

For an emitter coherently coupled to a cavity, resonant light entering the cavity is significantly modulated by coherent scattering. Due to destructive interference of the incident light with light scattered by the emitter in the forward direction, the transmission through the cavity can be strongly reduced [53]. We probe this effect by scanning the frequency of a weak coherent laser and measuring the cavity transmission with a single-photon detector. Figure 6.4 (a) depicts transmission measurements for different cavity detunings. These measurements exhibit transmission dips at the emitter frequency, with a contrast on resonance reaching 50 %. As the detuning is increased, the transmission dip shape changes from absorptive to dispersive.

We model the emitter-cavity system with a Lindblad master equation approach [54], which allows for quantitative numerical simulations of the cavity transmission as well as photon correlations (see Appendix 6.8.5 for details). All simulation input parameters are determined through independent measurements. The solid lines in Fig. 6.4 (a) and (b) show the predicted, simulated transmission curves, which are in good agreement with the data and confirm our quantitative understanding of the emitter-cavity system.

The coherent scattering observed here is a highly nonlinear quantum effect as it results from the light interacting with a single two-level system. In Fig. 6.4 (c) we plot

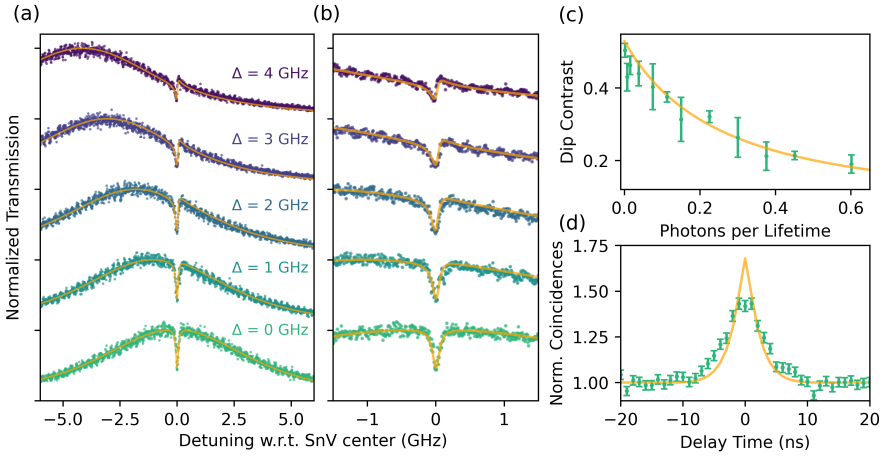

Figure 6.4: Nonlinear quantum effects of the emitter-cavity system. The dots are measured values, while the solid lines are modeled with a Lindblad master equation approach using the previously measured parameters of the emitter-cavity system. (a) Exemplary transmission dip measurements for increasing emitter-cavity detuning in steps of about 1 GHz and weak coherent probe laser power ($P = 260\,\mathrm{fW}$). (b) Zoom in on the data and simulated graphs presented in (a). (c) Cavity transmission dip contrast depending on photons per Purcell-reduced excited state lifetime. The evaluation of the transmission dip contrast and error is described in Appendix 6.8.9. (d) Measured $g^{(2)}(\tau)$ correlation function of the transmitted cavity light on emitter resonance, showing photon bunching as a quantum nonlinear effect. For the measured and simulated correlation function, a binning of 1 ns is used. The error bars represent one standard deviation confidence intervals of the data.

the transmission dip contrasts for different light intensities, expressed in photons per Purcell-reduced excited state lifetime measured after the cavity. For the cooperativity $C = 1.7$ of our emitter-cavity system the Purcell-reduced lifetime reads 1.85 ns. For very weak incident light intensity, the emitter acts as an efficient scatterer, whereas the emitter saturates for light intensities on the order of a photon per excited state lifetime.

The nonlinearity of the coherent coupling fundamentally modifies the statistical properties of the transmitted light. To show this quantum nonlinear behavior, we measure the $g^{(2)}(\tau)$ correlation function of the transmitted light when the cavity is on resonance with the SnV center (see Fig. 6.4 (d)). The observed photon bunching $g^{(2)}(0) \approx 1.5$ evidences the modified statistics resulting from the selective reflection of the single-photon component of the incident weak coherent light.

The measured photon bunching time scale, which is related to the Purcell-reduced excited state lifetime, is slightly larger than predicted by our theoretical model (solid line). We attribute this to a residual emitter-cavity detuning during the measurement time, which leads to a slightly longer excited state lifetime (less Purcell-reduction) and thereby to a larger bunching time constant.

6.6 Conclusion and Outlook

Our work establishes a versatile tunable platform for exploring light-matter interactions with individual diamond color centers, showing coherent coupling that modifies the cavity

transmission intensity and photon statistics. These results constitute the first demonstration of these quantum nonlinear effects for any color center in a hybrid cavity. Furthermore, the methods used here can be directly extended to other color centers such as diamond nitrogen-vacancy and silicon-vacancy centers as well as color centers in other materials such as silicon carbide [55, 56].

Our results open up near-term opportunities along several directions. First, our cavity performance may be improved by an order of magnitude as finesse values exceeding 10,000 were shown with reduced losses from the diamond sample in comparable systems [23, 57–59]. Furthermore, SnV centers in waveguides and thin membranes have shown near lifetime-limited linewidths at liquid helium temperatures [38, 41], leading to an improved coherent cooperativity.

Moreover, this system can be complemented with the recently established coherent control over the SnV center ground state spin [40, 41]. Striplines to deliver microwaves can be fabricated onto the diamond membrane [41] or embedded into the mirror [60]. Combining the light-matter interface with spin control would enable a versatile spin-photon interface for advanced quantum optics experiments and proof-of-principle demonstrations towards cavity-enhanced quantum networking with solid-state qubits.

6.7 Acknowledgment

We thank Nina Codreanu for help in the cleanroom, Henri Ervasti for software support and Lorenzo De Santis for proofreading the manuscript. We thank Johannes Borregaard, Anders Søndberg Sørensen, Robert Berghaus and Gregor Bayer for helpful discussions.

We acknowledge financial support from the Dutch Research Council (NWO) through the Spinoza prize 2019 (project number SPI 63-264) and from the Dutch Ministry of Economic Affairs and Climate Policy (EZK), as part of the Quantum Delta NL programme. We gratefully acknowledge that this work was partially supported by the joint research program "Modular quantum computers" by Fujitsu Limited and Delft University of Technology, co-funded by the Netherlands Enterprise Agency under project number PPS2007.

6.7.1 Author Contributions

Y. H. and J. F. conducted the experiments and analyzed the data. M. R. developed parts of the device fabrication process and designed together with M. J. W., Y. H. and J. F. the setup. Y. H., J. F., L. J. F. and M. J. W. built the setup. J. M. B., C. S. and Y. H. fabricated the diamond devices. M. E. fabricated the cavity fibers. L. G. C. W. characterized the diamond devices and the cavity fiber. J. F. and M. P. developed the simulations. Y. H., J. F. and R. H. wrote the manuscript with input from all authors. R. H. supervised the experiments.

6.7.2 Data Availability

The datasets that support this work are available at 4TU.ResearchData [61].

6.8 Appendix

6.8.1 Experimental Setup

Experimental sequences are orchestrated with a real-time microcontroller (Jäger Adwin Pro II) and time-resolved measurements are recorded with a single photon counting module (Picoquant Hydraharp 400). The setup is controlled and measurements are performed with a PC and the Python 3 framework QMI 0.37 [62]. We use quantify-core [1] for data handling and analysis.

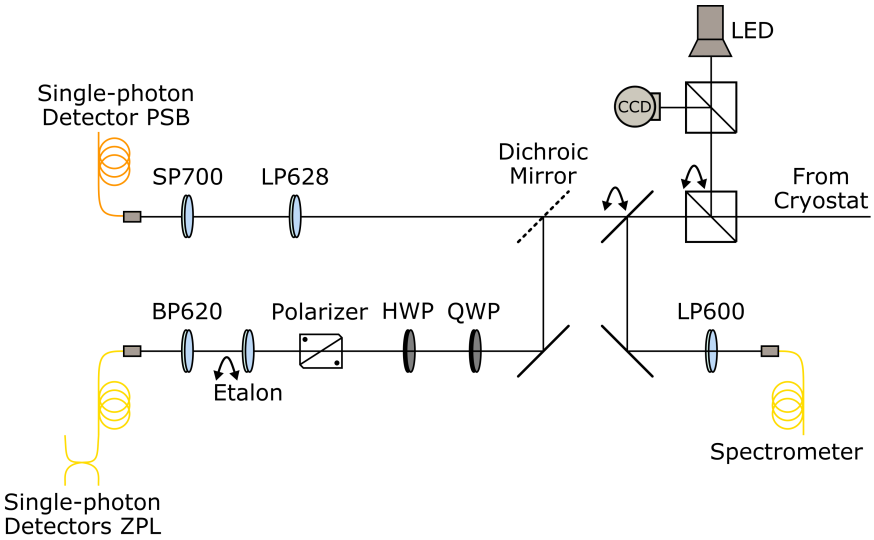

Figure 6.5: Schematic of the detection setup. The collimated cavity beam comes from the right-hand side and is split into ZPL and PSB detection. Alternatively, the cavity light can be sent with a flip mirror to a fiber-coupled spectrometer. Further, a 50:50 pellicle beam splitter can be inserted to image the cavity with an LED and a CCD camera. Spectral filtering is performed with various shortpass (SP), longpass (LP), and bandpass (BP) filters (see main text for details).

The excitation path consists of a frequency-doubled tunable diode laser (619 nm, Toptica TA-SHG pro), which is frequency stabilized to a wavemeter (High Finesse WS-U) and intensity-controlled with a fiber-based amplitude acousto-optic modulator (Gooch and Housego Fiber-Q 633 nm). After free-space launching, we fix the polarization with a Glan-Thompson polarizer (Thorlabs GTH10M-A), after which half- (HWP) and quarter-wave (QWP) plates are used for polarization control. For off-resonant excitation, a continuous wave laser (515 nm, Hübner Photonics Cobolt MLD515) and a pulsed laser (532 nm, 230 ps pulse duration, (5 – 12) MHz repetition rate, NKT Photonics Katana-05HP) are combined with a 30:70 beam splitter and overlapped with the 619 nm diode laser via a dichroic mirror. The light is coupled into one port of a 4x1 single-mode fiber switch (Agiltron custom version), whose output port is connected to the cavity fiber (single mode, 5 µm mode field diameter, IVG CU600). A different input port of the fiber switch is connected to a white

[1] Available at `https://gitlab.com/quantify-os/quantify-core`.

light supercontinuum source (NKT Photonics SC-450-2), which is spectrally filtered for (600 – 700) nm to measure the cavity dispersion.

We use a floating stage helium-free optical cryostat (Montana Instruments HILA) with an off-table cold head design and a base temperature of 6 K. A detailed description of the design and operation of the full setup is presented in Ref. [46]. The fiber can be placed and fine-tuned in situ with a piezo positioning stage (JPE CPSHR1-a), which is mounted on a passive vibration isolator (JPE CVIP1). The output beam of the cavity is collimated with a room temperature objective (100x magnification, 0.75 numerical aperture, 4 mm working distance, Zeiss LD EC Epiplan-Neofluar), which is positioned by three linear piezo stages (Physik Instrumente Q-545) in a tripod configuration.

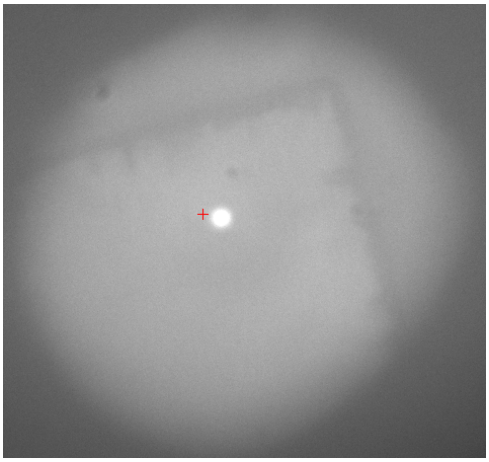

Figure 6.6: Micrograph of the hybrid cavity imaged through the output mirror, showing the diamond device. Off-resonant 515 nm laser light is inserted over the input mirror, illuminating the lateral cavity position used in the experiments.

The collimated cavity beam leaves free-space the cryostat vacuum chamber to the detection path shown in Fig. 6.5. We illuminate and monitor the cavity with an LED lamp and a CCD camera to position the fiber with respect to the sample (see Fig. 6.6 for the exact cavity spot on the diamond device). To measure the cavity dispersion or SnV center fluorescence, the light can be sent to a fiber-coupled spectrometer (Princeton Instruments SP-2500i). For all other measurements, the light is split into the ZPL and PSB path with a longpass filter (Asahi Spectra LP 630 nm). The PSB path is spectrally filtered with two longpass (Semrock VersaChrome Edge TLP01-628) and a shortpass filter (Thorlabs FES700) and fiber-coupled into a multimode fiber (25 µm core size, 0.1 numerical aperture, Thorlabs FG025LJA) with an objective (10x magnification, 0.1 numerical aperture, 10.6 mm working distance, Olympus RMS10X). The PSB light is measured with a single-photon detector (Laser Components COUNT-10C-FC). The ZPL light is filtered for polarization with a quarter- and half-wave plate and a Glan-Thompson polarizer (Thorlabs GTH10M-A) and spectrally with a bandpass filter (Thorlabs FBH620-10). We additionally filter the light for some experiments with an angle-tunable free-space etalon (full width at half maximum ≈ 45 GHz, free spectral range ≈ 2.7 THz, LightMachinery custom coating). The ZPL light is fiber-coupled into a

single-mode fiber ($3.6-5.3\,\mu m$ mode field diameter, $0.1-0.14$ numerical aperture, Thorlabs SM600) with an objective (Olympus RMS10X). For the correlation measurements, a 50:50 single-mode fiber beam splitter (Thorlabs TW630R5A2) is used. The ZPL light is measured with a single-photon detector (Picoquant Tau-SPAD-20).

6.8.2 Hybrid Cavity Characterization and Simulation

Figure 6.7 shows a cavity transmission measurement used to determine the cavity linewidth. In this measurement, a resonant laser is scanned over the cavity resonance, while the transmission is detected with a single-photon detector in the ZPL path. To this transmission signal, a Voigt fit with a fixed Gaussian contribution of 2.92 GHz is applied. This Gaussian contribution accounts for the 27 pm root mean square (RMS) value of cavity length fluctuation. The Voigt fit yields a Lorentzian contribution of (6.86 ± 0.05) GHz, which corresponds to the Lorentzian cavity linewidth.

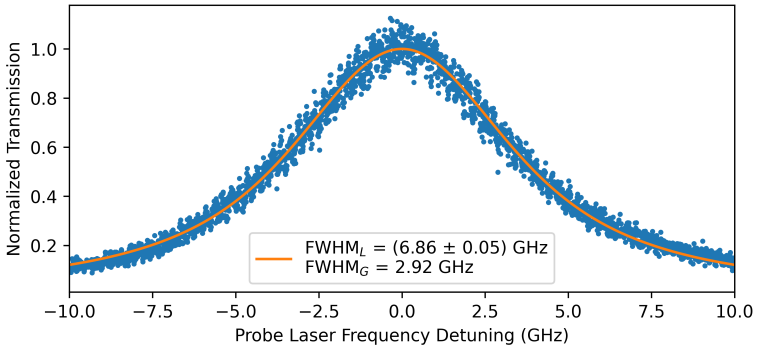

Figure 6.7: Linewidth characterization of the air-diamond hybrid cavity. Extracted from a resonant cavity transmission scan fit, the cavity shows a total Voigt linewidth of 8 GHz, composed of a Lorentzian cavity linewidth of (6.86 ± 0.05) GHz and a Gaussian contribution of 2.92 GHz ($= 27\,\text{pm} \cdot 46\,\text{MHz/pm} \cdot 2\sqrt{2\ln 2}$) accounting for 27 pm RMS cavity length fluctuations.

To calculate the cavity mode volume of our microcavity, the electric field distribution inside the cavity is simulated in Fig. 6.8 [45]. The electric field is confined between the dielectric input and output mirrors and spreads over the air and diamond part in between. From simulations, an effective cavity length $L_{\text{eff}} = 10.8\,\mu m$ is calculated, which leads with the cavity beam waist $\omega_0 = 1.24\,\mu m$ to a cavity mode volume of 55 λ^3.

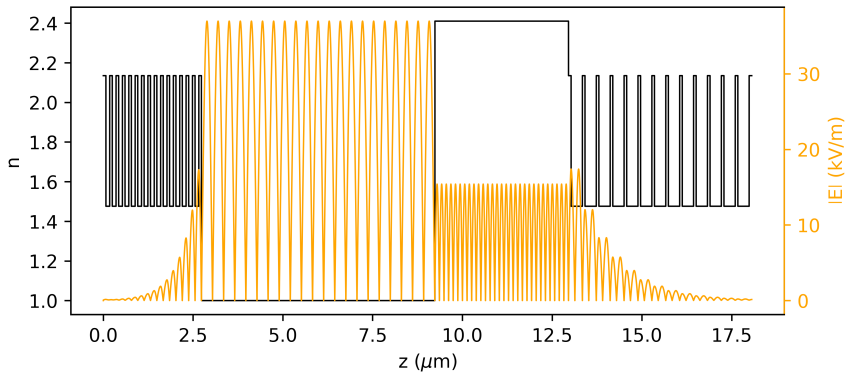

Figure 6.8: Simulation of the electric field distribution inside the microcavity. The solid black line displays the refractive index n over the extent of our microcavity, and the yellow solid line shows the simulated electric field strength $|E|$. The dielectric input and output mirrors are shown on the left and right sides. In between, the air gap of 6.50 µm and the diamond of thickness 3.72 µm are modeled with a refractive index of $n = 1$ and $n = 2.41$, respectively. An effective cavity length of $L_{\text{eff}} = 10.8\,\mu\text{m}$ is numerically calculated.

6.8.3 Vibration Model

The cavity length fluctuations of our microcavity lead to vibration averaging in measurements, which we take into account in simulations and when stating vibration-corrected quantities. We model a Gaussian distribution of cavity length fluctuations that translate over a local linear cavity mode dispersion into cavity frequency detunings $\Delta\nu$. The probability density function is given by [24]

$$f(\Delta\nu) = \frac{1}{\sqrt{2\pi\sigma^2}} e^{-\Delta\nu^2/2\sigma^2}, \tag{6.3}$$

with the RMS value σ of the cavity frequency fluctuations. We perform the vibration averaging by discretizing the probability density function and integrating numerically.

6.8.4 Cooperativity Definitions and Vibration Correction

The efficiency of a spin-photon interface is quantified by the cooperativity [50]

$$C = \frac{4g^2}{\kappa\,(\gamma_{\mathrm{rad}} + \gamma_{\mathrm{nonrad}})}, \tag{6.4}$$

with the single photon Rabi frequency g and the emitter decay rate $\gamma = \gamma_{\mathrm{rad}} + \gamma_{\mathrm{nonrad}}$ with its radiative and nonradiative component. For the SnV center, the radiative component is composed of a ZPL and a PSB part $\gamma_{\mathrm{rad}} = \gamma_{\mathrm{ZPL}} + \gamma_{\mathrm{PSB}}$. Further, the ZPL component splits up into the SnV center C and D transition $\gamma_{\mathrm{ZPL}} = \gamma_{\mathrm{C}} + \gamma_{\mathrm{D}}$.

In this study, we couple a narrow-linewidth SnV center via its C transition to a spectrally broad cavity ($\kappa \gg \gamma$). The cavity-induced increase in the C transition decay rate with respect to its initial value γ_{C} is determined by the Purcell factor times the spatial ϵ as well as polarization ζ overlap between emitter and cavity mode. Hence, the Purcell-enhanced emitter decay rate reads

$$\gamma_P = F_P\,\epsilon\,\zeta\,\gamma_{\mathrm{C}} + \gamma. \tag{6.5}$$

This Purcell-enhanced decay rate can be expressed as a function of the cooperativity by introducing the branching ratio between C and D transition $\alpha = \gamma_{\mathrm{C}}/\gamma_{\mathrm{ZPL}}$, the Debye-Waller factor $\beta_0 = \gamma_{\mathrm{ZPL}}/\gamma_{\mathrm{rad}}$ and the quantum efficiency $\eta = \gamma_{\mathrm{rad}}/\gamma$. Equation (6.5) transforms to

$$\gamma_P = F_P\,\epsilon\,\zeta\,\alpha\,\beta_0\,\eta\,\gamma + \gamma = \gamma(C+1), \tag{6.6}$$

with the cooperativity C as defined in equation (6.2) of the main text.

Following equation (6.6) the cooperativity

$$C = (\gamma_P - \gamma)/\gamma = \tau/\tau_P - 1, \tag{6.7}$$

can be determined by measuring the Purcell-reduced excited state lifetime τ_P and the natural excited state lifetime τ. In the case of a linewidth-broadened emitter $\gamma' = \gamma + \gamma_{\mathrm{dp}}$ with pure dephasing rate γ_{dp} the cooperativity

$$C = (\gamma_P' - \gamma')/\gamma, \tag{6.8}$$

can be calculated by measuring the emitter linewidth γ' and the Purcell-enhanced linewidth γ_P' together with the lifetime-limited linewidth $\gamma = 1/2\pi\tau$ deduced from a lifetime measurement.

The coherent cooperativity that takes emitter coherence into account reads [50]

$$C_{\mathrm{coh}} = C\frac{\gamma}{\gamma'} = \frac{\gamma'_P}{\gamma'} - 1, \tag{6.9}$$

and hence can be determined by measuring the emitter linewidth and the Purcell-enhanced linewidth only.

Moreover, the emitter-cavity coupling, described by the cooperativity C, depends on the spectral overlap between emitter and cavity. In the regime where the emitter linewidth is much smaller than the cavity linewidth, the cooperativity is given by [45]

$$C_{\mathrm{overlap}}(\nu_e, \nu_c) = \frac{C}{1 + 4Q^2(\nu_e/\nu_c - 1)^2}, \tag{6.10}$$

with the maximal cooperativity C on emitter-cavity resonance, the cavity quality factor Q, the cavity resonance frequency ν_c and the emitter transition frequency ν_e. Note that this dependency needs to be generally considered for emitter-cavity detunings and also vibration averaging. Using equation (6.10) and (6.3), a ratio of 0.90 between measured (vibration averaged) and maximal cooperativity on emitter-cavity resonance is calculated for our RMS vibration level of 27 pm. We take this factor into account when stating vibration-corrected cooperativity values.

6.8.5 Modeling SnV Centers in Optical Cavities

The investigated emitter-cavity system under resonant excitation is described by an atomic system and a driven optical cavity, modeling the SnV center and the probed microcavity, respectively. For sample temperatures of about 8 K, the SnV center in diamond is well approximated by a two-level atomic system, considering only the lower branches of the excited and ground states that are linked via the SnV center C transition.

The population in the upper branch states of the ground state can be calculated by the ratio of the fast electron-phonon transition rates between the ground state branches γ_+ and γ_- [51]. The ratio γ_+/γ_- is determined by the thermal population of the corresponding phonon mode, which for the SnV center ground state splitting of ≈ 850 GHz and temperature of 8 K is well approximated by the Maxwell-Boltzmann distribution. In this regime, the population of the upper branch states follows the Maxwell-Boltzmann distribution as well and is with $< 1\,\%$ very low, allowing to disregard this state. Note that the SnV center Debye-Waller factor, quantum efficiency, and branching ratio are included in the cooperativity of the emitter-cavity system.

The dynamics of the emitter-cavity system are modeled with a Lindblad master equation approach, where the Hamiltonian of the system in the rotating frame of the probe frequency reads [54]

$$\hat{H} = \Delta_e |e\rangle\langle e| + \Delta_c \hat{a}^\dagger \hat{a} + i\xi\left(\hat{a}^\dagger - \hat{a}\right) + ig\left(\hat{a}|e\rangle\langle g| - \hat{a}^\dagger |g\rangle\langle e|\right) \tag{6.11}$$

with $\Delta_e/2\pi = \nu_e - \nu_p$, $\Delta_c/2\pi = \nu_c - \nu_p$, where ν_e is the emitter transition frequency between excited state $|e\rangle$ and ground state $|g\rangle$ and ν_c the resonance frequency of the cavity. The cavity field is described by the bosonic photon annihilation operator $\hat{a}$. The single photon Rabi frequency g determines the coupling strength between the two atomic levels and the cavity field via the Jaynes-Cummings interaction. The weak coherent probe laser field

at frequency ν_p has a photon flux amplitude of $\xi/\sqrt{\kappa_{in}}$ at the cavity input mirror. The Lindblad operators of the system are

$$\begin{aligned}\hat{L}_1 &= \sqrt{\gamma}\,|g\rangle\langle e|,\\ \hat{L}_2 &= \sqrt{\gamma_{\mathrm{dp}}}\,|e\rangle\langle e|,\\ \hat{L}_3 &= \sqrt{\kappa}\hat{a},\end{aligned} \tag{6.12}$$

with the decay rate γ from the state $|e\rangle$ to $|g\rangle$, the dephasing rate γ_{dp} and the total cavity loss rate κ. The Linblad master equation for the system density matrix ρ reads

$$\dot{\rho} = -\left[\hat{H},\rho\right] + \sum_{x=1}^{3} \hat{L}_x \rho \hat{L}_x^\dagger - \frac{1}{2}\left(\hat{L}_x^\dagger \hat{L}_x \rho + \rho \hat{L}_x^\dagger \hat{L}_x\right). \tag{6.13}$$

In the weak driving regime ($\xi \ll \kappa$), the Hilbert space can be truncated, and we assume at most two excitations in our system, which results in the basis

$$\{|0,g\rangle, |0,e\rangle, |1,g\rangle, |1,e\rangle, |2,g\rangle\}. \tag{6.14}$$

To calculate the cavity transmission and intensity correlation function of the transmitted light, the steady state of the system is considered. The cavity transmission is given by

$$T = \frac{\kappa_{out}\langle \hat{a}^\dagger \hat{a}\rangle}{\langle \hat{a}_{in}^\dagger \hat{a}_{in}\rangle} = \frac{\kappa_{out}\kappa_{in}}{\xi^2}\langle \hat{a}^\dagger \hat{a}\rangle, \tag{6.15}$$

with the loss rate of the output mirror κ_{out} and the input photon flux $\langle \hat{a}_{in}^\dagger \hat{a}_{in}\rangle = \xi^2/\kappa_{in}$. The normalized intensity correlation function of the transmitted light is given by

$$g_T^{(2)}(\tau) = \frac{\langle \hat{a}^\dagger(0)\hat{a}^\dagger(\tau)\hat{a}(\tau)\hat{a}(0)\rangle}{\langle \hat{a}^\dagger \hat{a}\rangle^2}, \tag{6.16}$$

with the correlation time delay τ.

We use the Python toolbox qutip [63] to solve for the operator expectation values. To calculate the photon field expectation values of the correlation functions, we increase the photon Hilbert space to eight excitations for numerical stability.

6.8.6 Further Data on SnV-Cavity Coupling

To identify SnV centers exhibiting large cavity coupling strengths within the cavity mode volume, we tune the cavity resonance over a large range by sweeping the piezo voltage of the fiber positioning system. We simultaneously excite with a pulsed, off-resonant 532 nm laser and monitor the counts in the ZPL detection. Once a certain count rate is exceeded, the sweep is paused and a lifetime measurement (usually 10 s to 60 s integration time) is performed to extract the excited state lifetime. The measurement and analysis are fully automated, and the best coupled SnV centers are found efficiently. For the cavity used in this work, an exemplary sweep is shown in Fig. 6.9, where the SnV center used in this study is located at a piezo voltage of 0.12 V with a Purcell-reduced excited state lifetime of about 2.5 ns as indicated by the black arrow.

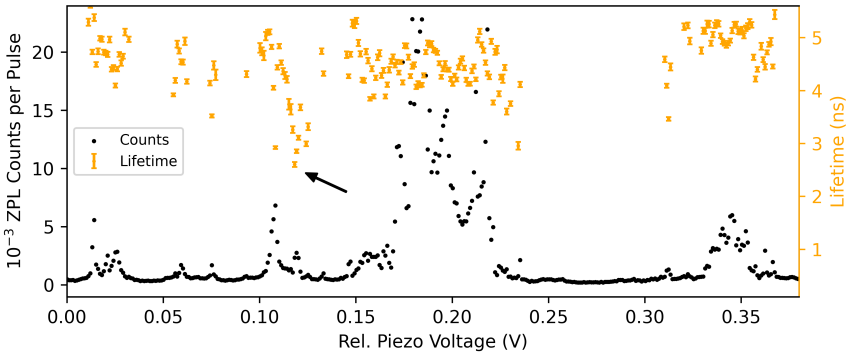

Figure 6.9: Detuning of the cavity resonance from about 617 nm to 621 nm with a lifetime measurement triggered on a predefined count rate threshold of 7 kCts (background of 2 kCts). The ZPL path is filtered with a (620 ± 5) nm bandpass filter only. We attribute the clustered peaks around 0.2 V and 0.35 V to the C and D transition of multiple SnV centers. The SnV center used in this study is indicated by the black arrow with a Purcell-reduced excited state lifetime of about 2.5 ns. The error bars represent one standard deviation confidence intervals of the fit.

After finding a SnV center with a good coupling strength to the cavity, an etalon filter (full width at half maximum $\approx$ 45 GHz) is added to the ZPL path to further reduce the background and the polarization detection is optimized on the emitter counts under pulsed, off-resonant 532 nm excitation. The coupling is then quantified via cavity detuning-dependent lifetime measurements as reported in Fig. 6.3 (a) and (b). Figure 6.10 depicts the full dataset, which is used in Fig. 6.3 (a). The investigated emission line is located at around 455 GHz (with respect to 484 THz), whereas at around 430 GHz another weaker coupled emission line is present. We choose to analyze the data for frequencies $\geq$ 455 GHz only, where leakage of the 430 GHz emission line is very small. Note that these measurements under pulsed, off-resonant 532 nm excitation were performed last and caused the emitter frequency to jump from the initial 484.558 THz to 484.455 THz. We attribute this jump to the extensive irradiation of the diamond device with high power ($\approx$ 5 mW) pulsed 532 nm light.

The lifetime measurements of Fig. 6.3 (b) are shown without normalization in Fig. 6.11 together with the monoexponential fits, which are used to extract the lifetime.

The lifetime measurement of a different SnV center with a larger lifetime reduction is shown in Fig. 6.12. Note that this is measured at a different lateral cavity position with a better cavity quality factor.

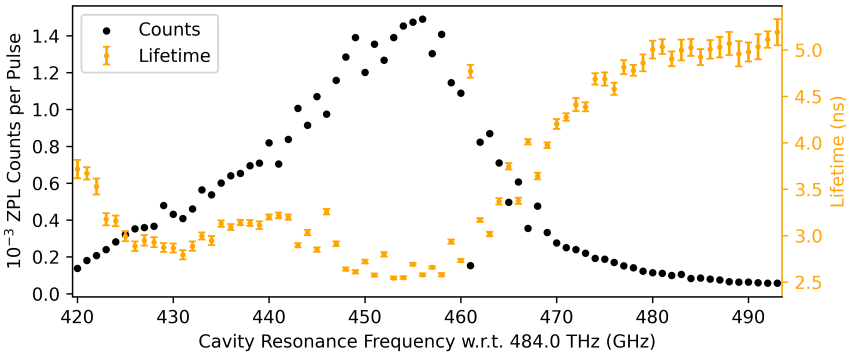

Figure 6.10: Full dataset of the cavity detuning measurement presented in Fig. 6.3 (a). The cavity frequency, which is matched to a frequency-stabilized reference laser, is stated in absolute values. Note that in the lifetime measurement of frequency 461 GHz, the cavity is not set to the correct resonance frequency, which leads to a wrong lifetime value. The error bars represent one standard deviation confidence intervals of the fit.

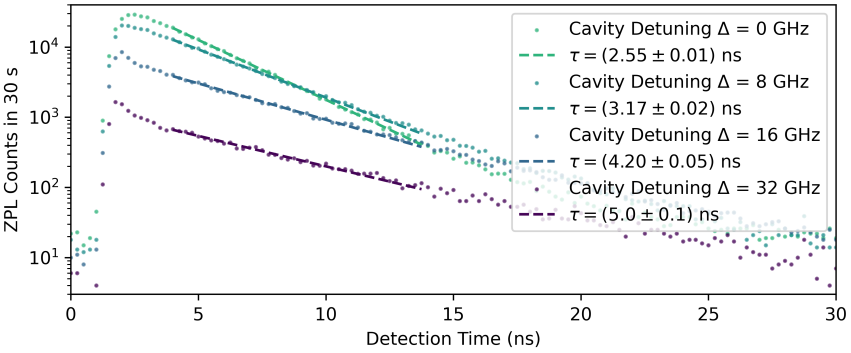

Figure 6.11: Lifetime measurements and fits (dashed lines) of the data presented in Fig. 6.3 (b) without normalization. The signal of the SnV center is reduced for larger cavity detuning. Here, an additional fast-decaying signal can be observed for short detection times. We attribute this to background fluorescence, which could stem from the cavity fiber, the mirror coating, or the output mirror substrate. The fit window is chosen to exclude this fast decay. A binning of 0.25 ns is used.

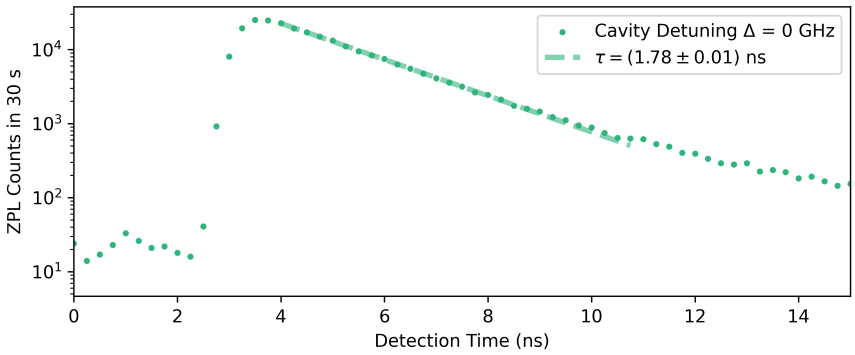

Figure 6.12: Lifetime measurement of the SnV center, which shows the largest lifetime reduction. This is measured at a different lateral position on the diamond device with a better cavity quality factor of about 8×10^4 and a comparable mode volume. Note that, in this measurement, the ZPL signal is filtered in a 10 nm window. The change in the exponential slope for longer detection times could stem from weaker coupled SnV centers or not filtered slow-decaying background fluorescence. A binning of 0.25 ns is used.

6.8.7 PLE Measurements of SnV Centers with the Microcavity

The investigated SnV center shows spectral diffusion and emitter ionization. In the PLE measurements, a conditional off-resonant 515 nm laser pulse is applied before scanning the resonant laser over the emission line. This sequence measures the emitter linewidth without contributions of spectral diffusion, and the SnV center is likely found in its negative charge state. The usage of the 515 nm pulse is conditioned on the detected emitter counts of the previous scan. If a specified peak contrast is not reached, the emitter is likely ionized, and a 10 μW 515 nm laser pulse is applied for 50 ms to repump the charge state. The resonant laser is scanned with about 180 MHz/s, while we integrate the emitter counts for 50 ms at each frequency step. Phonon sideband detection is utilized to filter out residual resonant excitation laser after the microcavity. The microcavity itself strongly filters the PSB emission of the emitter, resulting in a low PSB photon collection rate. Therefore, individual PLE scans are postselected and averaged to get a good estimate of the emitter linewidth.

Cavity On Resonance PLE Measurement Analysis

For the cavity on resonance, PLE scans a low excitation power corresponding to 260 fW is used. This enables the acquisition of the ZPL counts next to the PSB counts with single-photon detectors in the detection. These ZPL count traces are equivalent to transmission dip measurements, which show a significantly better signal-to-noise than the PSB count traces. We use the transmission dips for postselecting PLE measurements. First, we only consider measurements that exhibit a transmission dip and where the cavity mode is resonant with the laser scan range. Next, each transmission dip is fitted with a Lorentzian function, and further postselection is performed on the resulting fit parameters. The transmission dip, and therewith the emission frequency, has to be in the range $(558-559)$ GHz in the center of the laser scan. In addition, a Lorentzian width > 100 MHz and a dip contrast $> 50\,\%$ are required, which sorts out scans where emitter ionization occurred. The selected PLE scans are centered using the Lorentzian fit center frequencies and finally averaged. For the data presented in Fig. 6.3 (c), where the cavity is on resonance with the emitter, the average is performed with 170 individual scans.

Cavity Off Resonance PLE Measurement Analysis

For cavity off resonance PLE scans, the propagation of the scanned resonant laser light into the cavity is highly suppressed. To achieve similar PSB emitter count rates, the excitation laser power is increased by a factor of 400. In postselection, we use the knowledge if a conditional repump is applied to select scans where no ionization occurred and additionally require a certain emission peak contrast. Then, each PLE scan is fitted with a Lorentzian peak, and further postselection is performed based on the resulting fitting parameters. A Lorentzian center frequency in the range of $(558-559)$ GHz and the linewidth in the range of $(30-500)$ MHz is required. Moreover, we select on the Lorentzian peak amplitude as a criterion for a successful fit. The selected PLE scans are centered using the Lorentzian fit center frequencies and finally averaged. For the data presented in Fig. 6.3 (c), where the cavity is off resonance with the emitter, the average is performed with 307 individual scans.

6.8.8 Cavity Transmission Dip Measurements

The cavity transmission dip measurements are performed by scanning a weak coherent laser over the cavity resonance and detecting the transmitted laser signal with a single-photon detector in the ZPL path. These transmission scans exhibit a good signal-to-noise ratio, allowing to scan the laser faster than in the PLE measurements, which is beneficial to lower the chance of emitter ionization. The measurements depicted in Fig. 6.4 (a) and (b) were conducted with a laser power of 260 fW, a laser scan speed of about 350 MHz/s and an integration time of 20 ms for each frequency step. A 50 uW off-resonant 515 nm laser pulse is applied for 50 ms before each scan. Figure 6.13 depicts successively acquired cavity transmission dip measurements. These reveal the effect of spectral diffusion of the investigated SnV center. In individual measurements, the SnV center exhibits its narrow emitter linewidth, whereas between measurements, spectral diffusion on the order of GHz is observed. We attribute these frequency jumps to changes in the SnV center environment due to the application of the off-resonant 515 nm laser before each measurement. Without the application of the off-resonant 515 nm laser, the frequency jumps between successive measurements are on the order of the emitter linewidth.

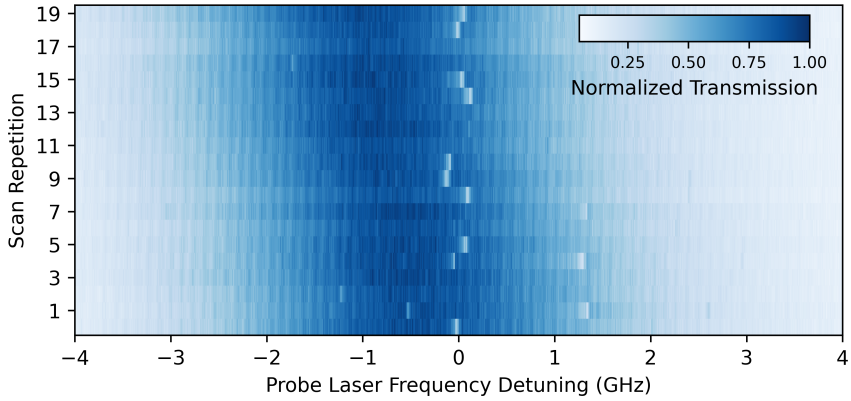

Figure 6.13: Successively acquired cavity transmission dip measurements. The cavity resonance is not actively controlled during these measurements.

6.8.9 Transmission Dip Contrast Measurements

The transmission dip contrasts, depending on photons per Purcell-reduced excited state lifetime, are determined by performing transmission dip measurements with different laser powers. In all of these measurements, we use a scan range of 1.8 GHz and apply an off-resonant 515 nm laser pulse before each scan. The laser scan speed and the frequency step integration time are adjusted for each laser power to acquire transmission dips before they vanish due to emitter ionization. An exemplary transmission dip contrast analysis is shown in Fig. 6.14. For each power value, we analyze four scans and take the mean contrast value with standard deviation as the dip contrast displayed in Fig. 6.4 (c).

The experimental data of Fig. 6.4 (c) is fit to the simulations by scaling the used excitation powers to the simulated photons per lifetime, which maps the experimentally set laser

power to the actual laser power leaving the cavity. A set laser power of 1.0 nW measured in our excitation setup corresponds to 0.015 photons per lifetime and a power of 2.6 pW after the cavity. This power ratio originates from an initial free space to fiber coupling efficiency, fiber and fiber splice losses, fiber mode to cavity mode matching efficiency, and cavity transmission. The cavity transmission is calculated to be 2.4 %, and an achievable fiber mode to cavity mode efficiency of 47 % is calculated for the used cavity geometry. The determined power ratio is used to state the resonant laser power values. By comparing the detector count rate with the expected photons per lifetime after the cavity, we estimate a cavity mode collection efficiency of about 12 %. An independent measurement of the collection efficiency confirms this value.

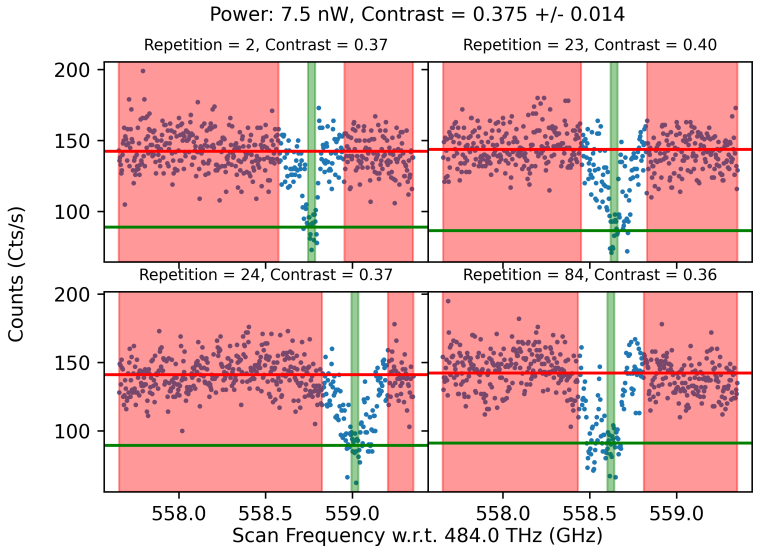

Figure 6.14: Exemplary analysis of the cavity transmission dip contrasts shown in Fig. 6.4 (c) for a set laser power of 7.5 nW, corresponding to about 0.1 photons per lifetime. Four individual scans of the resonant cavity transmission measurements, where a clear dip is visible, are selected. We use a running average of the count rate to automatically identify the position of the dip. 12 data points inside the dip are taken as an average to define the dip depth (green area). Excluding 50 data points to both sides of the dip, the remaining points are averaged to calculate the cavity transmission peak height (red area).

6.8.10 Photon Statistics Measurement of the Cavity Transmission on Emitter Resonance

The measurement, depicted in Fig. 6.4 (d), shows the photon statistics of the light that is transmitted through the cavity on emitter resonance. The transmitted light is collected by a single-mode fiber in the ZPL path and guided by a 50:50 fiber beam splitter to two single-photon detectors, which are connected to time-tagging electronics. In this measurement, a probe laser power of 2.6 pW, a scan speed of about 1.8 GHz/s, and a frequency step integration time of 5 ms is used. To exclusively acquire data on emitter resonance, we only trigger the time tagging electronics to record for the next 5 ms if the transmission dip

contrast is > 35 % in the previous frequency step. Before each scan a 10 uW off-resonant 515 nm laser pulse is applied for 50 ms. In the simulated graph of Fig. 6.4 (d), the detunings between emitter and probe laser due to the transmission dip trigger threshold of 35 % are taken into account. Emitter-cavity detunings due to spectral diffusion and small cavity drift during the course of the experiment are not captured by the measurement routine nor by the simulations.

6.8.11 Summary of System Parameters

An overview of measured, estimated, and simulated values of this work is summarized in Tab. 6.1.

Table 6.1: Overview of system parameters.

Parameter	Value
Input mirror radius of curvature	15.7 µm
Cavity air gap	6.50 µm
Diamond thickness	3.72 µm
Hybrid cavity mode number q	50
Effective cavity length L_{eff} [45]	10.8 µm
Estimated cavity beam waist ω_0 [45]	1.24 µm
Estimated cavity mode volume V [45]	55 λ^3
Cavity Lorentzian linewidth $\kappa/2\pi$	(6.86 ± 0.05) GHz
Root mean square cavity length fluctuations	27 pm
Cavity mode dispersion slope	46 MHz/pm
Cavity quality factor Q	7×10^4
Cavity finesse $\mathcal{F}$	830
Calculated Purcell factor F_P [45]	6.9
Calculated cavity transmission	2.4 %
SnV center natural lifetime τ	(5.0 ± 0.1) ns
SnV center lifetime-limited linewidth $\gamma/2\pi$	32 MHz
SnV center linewidth $\gamma'/2\pi$	(77.6 ± 0.8) MHz
Purcell-enhanced emitter linewidth $\gamma'_P/2\pi$	(126 ± 4) MHz
Vibration-corrected cooperativity C	1.7 ± 0.2
Vibration-corrected coherent cooperativity C_{coh}	0.69 ± 0.07
Single photon Rabi frequency g	(300 ± 20) MHz

References

[1] H. J. Kimble, *The quantum internet,* Nature **453**, 1023 (2008).

[2] S. Wehner, D. Elkouss, and R. Hanson, *Quantum internet: A vision for the road ahead,* Science **362**, eaam9288 (2018).

[3] K. J. Vahala, *Optical microcavities,* Nature **424**, 839 (2003).

[4] A. Reiserer and G. Rempe, *Cavity-based quantum networks with single atoms and optical photons,* Reviews of Modern Physics **87**, 1379 (2015).

[5] E. Janitz, M. K. Bhaskar, and L. Childress, *Cavity quantum electrodynamics with color centers in diamond,* Optica **7**, 1232 (2020).

[6] M. Ruf, N. H. Wan, H. Choi, D. Englund, and R. Hanson, *Quantum networks based on color centers in diamond,* Journal of Applied Physics **130**, 070901 (2021).

[7] B. Merkel, A. Ulanowski, and A. Reiserer, *Coherent and Purcell-Enhanced Emission from Erbium Dopants in a Cryogenic High- Q Resonator,* Physical Review X **10**, 041025 (2020).

[8] B. Casabone, C. Deshmukh, S. Liu, D. Serrano, A. Ferrier, T. Hümmer, P. Goldner, D. Hunger, and H. De Riedmatten, *Dynamic control of Purcell enhanced emission of erbium ions in nanoparticles,* Nature Communications **12**, 3570 (2021).

[9] A. Muller, E. B. Flagg, M. Metcalfe, J. Lawall, and G. S. Solomon, *Coupling an epitaxial quantum dot to a fiber-based external-mirror microcavity,* Applied Physics Letters **95**, 173101 (2009).

[10] T. Herzog, M. Sartison, S. Kolatschek, S. Hepp, A. Bommer, C. Pauly, F. Mücklich, C. Becher, M. Jetter, S. L. Portalupi, and P. Michler, *Pure single-photon emission from In(Ga)As QDs in a tunable fiber-based external mirror microcavity,* Quantum Science and Technology **3**, 034009 (2018).

[11] D. Najer, I. Söllner, P. Sekatski, V. Dolique, M. C. Löbl, D. Riedel, R. Schott, S. Starosielec, S. R. Valentin, A. D. Wieck, N. Sangouard, A. Ludwig, and R. J. Warburton, *A gated quantum dot strongly coupled to an optical microcavity,* Nature **575**, 622 (2019).

[12] N. Tomm, A. Javadi, N. O. Antoniadis, D. Najer, M. C. Löbl, A. R. Korsch, R. Schott, S. R. Valentin, A. D. Wieck, A. Ludwig, and R. J. Warburton, *A bright and fast source of coherent single photons,* Nature Nanotechnology **16**, 399 (2021).

[13] S. Häußler, G. Bayer, R. Waltrich, N. Mendelson, C. Li, D. Hunger, I. Aharonovich, and A. Kubanek, *Tunable Fiber-Cavity Enhanced Photon Emission from Defect Centers in hBN,* Advanced Optical Materials **9**, 2002218 (2021).

[14] S. Vadia, J. Scherzer, H. Thierschmann, C. Schäfermeier, C. Dal Savio, T. Taniguchi, K. Watanabe, D. Hunger, K. Karraï, and A. Högele, *Open-Cavity in Closed-Cycle Cryostat as a Quantum Optics Platform,* PRX Quantum **2**, 040318 (2021).

[15] D. Wang, H. Kelkar, D. Martin-Cano, T. Utikal, S. Götzinger, and V. Sandoghdar, *Coherent Coupling of a Single Molecule to a Scanning Fabry-Perot Microcavity,* Physical Review X **7**, 021014 (2017).

[16] D. Hunger, T. Steinmetz, Y. Colombe, C. Deutsch, T. W. Hänsch, and J. Reichel, *A fiber Fabry–Perot cavity with high finesse,* New Journal of Physics **12**, 065038 (2010).

[17] R. Albrecht, A. Bommer, C. Deutsch, J. Reichel, and C. Becher, *Coupling of a Single Nitrogen-Vacancy Center in Diamond to a Fiber-Based Microcavity,* Physical Review Letters **110**, 243602 (2013).

[18] S. Johnson, P. R. Dolan, T. Grange, A. A. P. Trichet, G. Hornecker, Y. C. Chen, L. Weng, G. M. Hughes, A. A. R. Watt, A. Auffèves, and J. M. Smith, *Tunable cavity coupling of the zero phonon line of a nitrogen-vacancy defect in diamond,* New Journal of Physics **17**, 122003 (2015).

[19] H. Kaupp, T. Hümmer, M. Mader, B. Schlederer, J. Benedikter, P. Haeusser, H.-C. Chang, H. Fedder, T. W. Hänsch, and D. Hunger, *Purcell-Enhanced Single-Photon Emission from Nitrogen-Vacancy Centers Coupled to a Tunable Microcavity,* Physical Review Applied **6**, 054010 (2016).

[20] J. Benedikter, H. Kaupp, T. Hümmer, Y. Liang, A. Bommer, C. Becher, A. Krueger, J. M. Smith, T. W. Hänsch, and D. Hunger, *Cavity-Enhanced Single-Photon Source Based on the Silicon-Vacancy Center in Diamond,* Physical Review Applied **7**, 024031 (2017).

[21] D. Riedel, I. Söllner, B. J. Shields, S. Starosielec, P. Appel, E. Neu, P. Maletinsky, and R. J. Warburton, *Deterministic Enhancement of Coherent Photon Generation from a Nitrogen-Vacancy Center in Ultrapure Diamond,* Physical Review X **7**, 031040 (2017).

[22] M. Salz, Y. Herrmann, A. Nadarajah, A. Stahl, M. Hettrich, A. Stacey, S. Prawer, D. Hunger, and F. Schmidt-Kaler, *Cryogenic platform for coupling color centers in diamond membranes to a fiber-based microcavity,* Applied Physics B **126**, 131 (2020).

[23] R. Høy Jensen, E. Janitz, Y. Fontana, Y. He, O. Gobron, I. P. Radko, M. Bhaskar, R. Evans, C. D. Rodríguez Rosenblueth, L. Childress, A. Huck, and U. Lund Andersen, *Cavity-Enhanced Photon Emission from a Single Germanium-Vacancy Center in a Diamond Membrane,* Physical Review Applied **13**, 064016 (2020).

[24] M. Ruf, M. Weaver, S. van Dam, and R. Hanson, *Resonant Excitation and Purcell Enhancement of Coherent Nitrogen-Vacancy Centers Coupled to a Fabry-Perot Microcavity,* Physical Review Applied **15**, 024049 (2021).

[25] F. Feuchtmayr, R. Berghaus, S. Sachero, G. Bayer, N. Lettner, R. Waltrich, P. Maier, V. Agafonov, and A. Kubanek, *Enhanced spectral density of a single germanium vacancy center in a nanodiamond by cavity integration,* Applied Physics Letters **123**, 024001 (2023).

[26] G. Bayer, R. Berghaus, S. Sachero, A. B. Filipovski, L. Antoniuk, N. Lettner, R. Waltrich, M. Klotz, P. Maier, V. Agafonov, and A. Kubanek, *Optical driving, spin initialization*

and readout of single SiV^- centers in a Fabry-Perot resonator, Communications Physics **6**, 300 (2023).

[27] H. Bernien, B. Hensen, W. Pfaff, G. Koolstra, M. S. Blok, L. Robledo, T. H. Taminiau, M. Markham, D. J. Twitchen, L. Childress, and R. Hanson, *Heralded entanglement between solid-state qubits separated by three metres,* Nature **497**, 86 (2013).

[28] P. C. Humphreys, N. Kalb, J. P. J. Morits, R. N. Schouten, R. F. L. Vermeulen, D. J. Twitchen, M. Markham, and R. Hanson, *Deterministic delivery of remote entanglement on a quantum network,* Nature **558**, 268 (2018).

[29] M. K. Bhaskar, R. Riedinger, B. Machielse, D. S. Levonian, C. T. Nguyen, E. N. Knall, H. Park, D. Englund, M. Lončar, D. D. Sukachev, and M. D. Lukin, *Experimental demonstration of memory-enhanced quantum communication,* Nature **580**, 60 (2020).

[30] M. H. Abobeih, J. Cramer, M. A. Bakker, N. Kalb, M. Markham, D. J. Twitchen, and T. H. Taminiau, *One-second coherence for a single electron spin coupled to a multi-qubit nuclear-spin environment,* Nature Communications **9**, 2552 (2018).

[31] T. Van Der Sar, Z. H. Wang, M. S. Blok, H. Bernien, T. H. Taminiau, D. M. Toyli, D. A. Lidar, D. D. Awschalom, R. Hanson, and V. V. Dobrovitski, *Decoherence-protected quantum gates for a hybrid solid-state spin register,* Nature **484**, 82 (2012).

[32] P.-J. Stas, Y. Q. Huan, B. Machielse, E. N. Knall, A. Suleymanzade, B. Pingault, M. Sutula, S. W. Ding, C. M. Knaut, D. R. Assumpcao, Y.-C. Wei, M. K. Bhaskar, R. Riedinger, D. D. Sukachev, H. Park, M. Lončar, D. S. Levonian, and M. D. Lukin, *Robust multi-qubit quantum network node with integrated error detection,* Science **378**, 557 (2022).

[33] C. E. Bradley, J. Randall, M. H. Abobeih, R. C. Berrevoets, M. J. Degen, M. A. Bakker, M. Markham, D. J. Twitchen, and T. H. Taminiau, *A Ten-Qubit Solid-State Spin Register with Quantum Memory up to One Minute,* Physical Review X **9**, 031045 (2019).

[34] N. Kalb, A. A. Reiserer, P. C. Humphreys, J. J. W. Bakermans, S. J. Kamerling, N. H. Nickerson, S. C. Benjamin, D. J. Twitchen, M. Markham, and R. Hanson, *Entanglement distillation between solid-state quantum network nodes,* Science **356**, 928 (2017).

[35] S. L. N. Hermans, M. Pompili, H. K. C. Beukers, S. Baier, J. Borregaard, and R. Hanson, *Qubit teleportation between non-neighbouring nodes in a quantum network,* Nature **605**, 663 (2022).

[36] C. M. Knaut, A. Suleymanzade, Y.-C. Wei, D. R. Assumpcao, P.-J. Stas, Y. Q. Huan, B. Machielse, E. N. Knall, M. Sutula, G. Baranes, N. Sinclair, C. De-Eknamkul, D. S. Levonian, M. K. Bhaskar, H. Park, M. Lončar, and M. D. Lukin, *Entanglement of nanophotonic quantum memory nodes in a telecom network,* Nature **629**, 573 (2024).

[37] M. E. Trusheim, B. Pingault, N. H. Wan, M. Gündoğan, L. De Santis, R. Debroux, D. Gangloff, C. Purser, K. C. Chen, M. Walsh, J. J. Rose, J. N. Becker, B. Lienhard, E. Bersin, I. Paradeisanos, G. Wang, D. Lyzwa, A. R.-P. Montblanch, G. Malladi,

H. Bakhru, A. C. Ferrari, I. A. Walmsley, M. Atatüre, and D. Englund, *Transform-Limited Photons From a Coherent Tin-Vacancy Spin in Diamond,* Physical Review Letters **124**, 023602 (2020).

[38] A. E. Rugar, C. Dory, S. Aghaeimeibodi, H. Lu, S. Sun, S. D. Mishra, Z.-X. Shen, N. A. Melosh, and J. Vučković, *Narrow-Linewidth Tin-Vacancy Centers in a Diamond Waveguide,* ACS Photonics **7**, 2356 (2020).

[39] J. Arjona Martínez, R. A. Parker, K. C. Chen, C. M. Purser, L. Li, C. P. Michaels, A. M. Stramma, R. Debroux, I. B. Harris, M. Hayhurst Appel, E. C. Nichols, M. E. Trusheim, D. A. Gangloff, D. Englund, and M. Atatüre, *Photonic Indistinguishability of the Tin-Vacancy Center in Nanostructured Diamond,* Physical Review Letters **129**, 173603 (2022).

[40] E. I. Rosenthal, C. P. Anderson, H. C. Kleidermacher, A. J. Stein, H. Lee, J. Grzesik, G. Scuri, A. E. Rugar, D. Riedel, S. Aghaeimeibodi, G. H. Ahn, K. Van Gasse, and J. Vučković, *Microwave Spin Control of a Tin-Vacancy Qubit in Diamond,* Physical Review X **13**, 031022 (2023).

[41] X. Guo, A. M. Stramma, Z. Li, W. G. Roth, B. Huang, Y. Jin, R. A. Parker, J. Arjona Martínez, N. Shofer, C. P. Michaels, C. P. Purser, M. H. Appel, E. M. Alexeev, T. Liu, A. C. Ferrari, D. D. Awschalom, N. Delegan, B. Pingault, G. Galli, F. J. Heremans, M. Atatüre, and A. A. High, *Microwave-Based Quantum Control and Coherence Protection of Tin-Vacancy Spin Qubits in a Strain-Tuned Diamond-Membrane Heterostructure,* Physical Review X **13**, 041037 (2023).

[42] E. Janitz, M. Ruf, M. Dimock, A. Bourassa, J. Sankey, and L. Childress, *Fabry-Perot microcavity for diamond-based photonics,* Physical Review A **92**, 043844 (2015).

[43] M. Ruf, M. IJspeert, S. van Dam, N. de Jong, H. van den Berg, G. Evers, and R. Hanson, *Optically Coherent Nitrogen-Vacancy Centers in Micrometer-Thin Etched Diamond Membranes,* Nano Letters **19**, 3987 (2019).

[44] P. Appel, E. Neu, M. Ganzhorn, A. Barfuss, M. Batzer, M. Gratz, A. Tschöpe, and P. Maletinsky, *Fabrication of all diamond scanning probes for nanoscale magnetometry,* Review of Scientific Instruments **87**, 063703 (2016).

[45] S. B. van Dam, M. Ruf, and R. Hanson, *Optimal design of diamond-air microcavities for quantum networks using an analytical approach,* New Journal of Physics **20**, 115004 (2018).

[46] Y. Herrmann, J. Fischer, S. Scheijen, C. F. J. Wolfs, J. M. Brevoord, C. Sauerzapf, L. G. C. Wienhoven, L. J. Feije, M. Eschen, M. Ruf, M. J. Weaver, and R. Hanson, *A low-temperature tunable microcavity featuring high passive stability and microwave integration,* AVS Quantum Science **6**, 041401 (2024).

[47] J. Görlitz, D. Herrmann, G. Thiering, P. Fuchs, M. Gandil, T. Iwasaki, T. Taniguchi, M. Kieschnick, J. Meijer, M. Hatano, A. Gali, and C. Becher, *Spectroscopic investigations of negatively charged tin-vacancy centres in diamond,* New Journal of Physics **22**, 013048 (2020).

[48] T. Iwasaki, Y. Miyamoto, T. Taniguchi, P. Siyushev, M. H. Metsch, F. Jelezko, and M. Hatano, *Tin-Vacancy Quantum Emitters in Diamond,* Physical Review Letters **119**, 253601 (2017).

[49] A. E. Rugar, S. Aghaeimeibodi, D. Riedel, C. Dory, H. Lu, P. J. McQuade, Z.-X. Shen, N. A. Melosh, and J. Vučković, *Quantum Photonic Interface for Tin-Vacancy Centers in Diamond,* Physical Review X **11**, 031021 (2021).

[50] J. Borregaard, A. S. Sørensen, and P. Lodahl, *Quantum Networks with Deterministic Spin–Photon Interfaces,* Advanced Quantum Technologies **2**, 1800091 (2019).

[51] K. D. Jahnke, A. Sipahigil, J. M. Binder, M. W. Doherty, M. Metsch, L. J. Rogers, N. B. Manson, M. D. Lukin, and F. Jelezko, *Electron–phonon processes of the silicon-vacancy centre in diamond,* New Journal of Physics **17**, 043011 (2015).

[52] P. Wang, L. Kazak, K. Senkalla, P. Siyushev, R. Abe, T. Taniguchi, S. Onoda, H. Kato, T. Makino, M. Hatano, F. Jelezko, and T. Iwasaki, *Transform-Limited Photon Emission from a Lead-Vacancy Center in Diamond above 10 K,* Physical Review Letters **132**, 073601 (2024).

[53] R. J. Thompson, G. Rempe, and H. J. Kimble, *Observation of normal-mode splitting for an atom in an optical cavity,* Physical Review Letters **68**, 1132 (1992).

[54] A. Sipahigil, R. E. Evans, D. D. Sukachev, M. J. Burek, J. Borregaard, M. K. Bhaskar, C. T. Nguyen, J. L. Pacheco, H. A. Atikian, C. Meuwly, R. M. Camacho, F. Jelezko, E. Bielejec, H. Park, M. Lončar, and M. D. Lukin, *An integrated diamond nanophotonics platform for quantum-optical networks,* Science **354**, 847 (2016).

[55] D. M. Lukin, M. A. Guidry, and J. Vučković, *Integrated Quantum Photonics with Silicon Carbide: Challenges and Prospects,* PRX Quantum **1**, 020102 (2020).

[56] J. Heiler, J. Körber, E. Hesselmeier, P. Kuna, R. Stöhr, P. Fuchs, M. Ghezellou, J. Ul-Hassan, W. Knolle, C. Becher, F. Kaiser, and J. Wrachtrup, *Spectral stability of V2 centres in sub-micron 4H-SiC membranes,* npj Quantum Materials **9**, 34 (2024).

[57] S. Bogdanović, S. B. van Dam, C. Bonato, L. C. Coenen, A.-M. J. Zwerver, B. Hensen, M. S. Z. Liddy, T. Fink, A. Reiserer, M. Lončar, and R. Hanson, *Design and low-temperature characterization of a tunable microcavity for diamond-based quantum networks,* Applied Physics Letters **110**, 171103 (2017).

[58] S. Flågan, D. Riedel, A. Javadi, T. Jakubczyk, P. Maletinsky, and R. J. Warburton, *A diamond-confined open microcavity featuring a high quality-factor and a small mode-volume,* Journal of Applied Physics **131**, 113102 (2022).

[59] J. Körber, M. Pallmann, J. Heupel, R. Stöhr, E. Vasilenko, T. Hümmer, L. Kohler, C. Popov, and D. Hunger, *Scanning Cavity Microscopy of a Single-Crystal Diamond Membrane,* Physical Review Applied **19**, 064057 (2023).

[60] S. Bogdanović, M. S. Z. Liddy, S. B. van Dam, L. C. Coenen, T. Fink, M. Lončar, and R. Hanson, *Robust nano-fabrication of an integrated platform for spin control in a tunable microcavity,* APL Photonics **2**, 126101 (2017).

[61] Y. Herrmann, J. Fischer, J. M. Brevoord, C. Sauerzapf, L. G. C. Wienhoven, L. J. Feije, M. Pasini, M. Eschen, M. Ruf, M. J. Weaver, and R. Hanson, *Data underlying the publication "Coherent Coupling of a Diamond Tin-Vacancy Center to a Tunable Open Microcavity",* 4TU.ResearchData (2023), https://doi.org/10.4121/421a26ac-4e92-411f-bb0a-5e6af21cf426.

[62] I. T. Raa, H. K. Ervasti, P. J. Botma, L. C. Visser, R. Budhrani, J. F. van Rantwijk, S. P. Cadot, J. Vermeltfoort, M. Pompili, A. J. Stolk, M. J. Weaver, K. L. van der Enden, D. de Leeuw Duarte, M. Teng, J. van Zwieten, and F. Grooteman, *QMI - Quantum Measurement Infrastructure, a Python 3 framework for controlling laboratory equipment,* 4TU.ResearchData (2023), https://data.4tu.nl/datasets/6d39c6db-2f50-4a49-ad60-5bb08f40cb52.

[63] J. Johansson, P. Nation, and F. Nori, *QuTiP: An open-source Python framework for the dynamics of open quantum systems,* Computer Physics Communications **183**, 1760 (2012).

7

Spin-Photon Correlations from a Purcell-enhanced Diamond Nitrogen-Vacancy Center Coupled to an Open Microcavity

J. Fischer*, Y. Herrmann*, C. F. J. Wolfs, S. Scheijen, M. Ruf and R. Hanson

An efficient interface between a spin qubit and single photons is a key enabling system for quantum science and technology. We report on a coherently controlled diamond nitrogen-vacancy center electron spin qubit that is optically interfaced with an open microcavity. Through Purcell enhancement and an asymmetric cavity design, we achieve efficient collection of resonant photons, while on-chip microwave lines allow for spin qubit control at a 10 MHz *Rabi frequency. With the microcavity tuned to resonance with the nitrogen-vacancy center's optical transition, we use excited state lifetime measurements to determine a Purcell factor of* 7.3 ± 1.6. *Upon pulsed resonant excitation, we find a coherent photon detection probability of* 0.5 % *per pulse. Although this result is limited by the finite excitation probability, it already presents an order of magnitude improvement over the solid immersion lens devices used in previous quantum network demonstrations. Furthermore, we use resonant optical pulses to initialize and read out the electron spin. By combining the efficient interface with spin qubit control, we generate two-qubit and three-qubit spin-photon states and measure heralded Z-basis correlations between the photonic time-bin qubits and the spin qubit.*

The results of this chapter have been published in Nature Communications **16**, 11680 (2025).

7.1 Introduction

Optically active solid-state qubits are promising physical systems for quantum networking [1–4]. Among several candidates [5–8], the nitrogen-vacancy (NV) center in diamond is one of the most-studied, with the realization of qubit teleportation [9] across a multi-node quantum network [10] and metropolitan-scale heralded entanglement [11]. Furthermore, efficient quantum frequency conversion to telecom wavelength [12, 13] and hybrid entanglement of photons and nuclear spins [14, 15] have been demonstrated. The NV center offers excellent spin qubit properties [16] and the nitrogen nuclear spin [17] together with nearby carbon-13 spins [18] can function as a multi-qubit register [19, 20] to store [21–23] and process [24–26] quantum states with high fidelities [27]. The main challenges for the generation of spin-photon states with the NV center are the relatively low zero-phonon line (ZPL) emission of $\sim 3\,\%$ [28] and the reduced optical coherence in the presence of charge noise hindering integration into nanophotonic devices [29–32]. State-of-the-art quantum network nodes [9] are thus realized with solid immersion lenses (SIL) [33], in which the NV center retains lifetime-limited optical linewidth [34]. In practice, such systems have shown ZPL detector click probabilities around 5×10^{-4} upon pulsed resonant excitation [9, 10, 35, 36].

In this work, we realize the integration of a NV center into a fiber-based Fabry-Pérot microcavity [37, 38] in combination with coherent microwave spin control, enabling the generation of spin-photon states. This platform features bulk-like optical coherence of the NV center by incorporating a micrometer-thin diamond membrane into the cavity [39, 40] and a Purcell-enhanced emission into the ZPL combined with an efficient photon extraction. We quantify the coupling of the NV center's readout transition to the cavity modes with the Purcell factor by measuring the reduction of the excited state lifetime. Further, we investigate the cavity-coupled readout transition with a photoluminescence excitation (PLE) measurement to determine the optical linewidth, a Hanbury Brown and Twiss (HBT) experiment to verify single-photon emission, and a saturation measurement, which reveals a ZPL detector click probability that is an order of magnitude higher compared to standard solid immersion lens systems. Moreover, we demonstrate coherent control of the NV center's electron spin and characterize its coherence properties in a Ramsey and a Hahn-Echo measurement. Finally, we use our platform to generate spin-photon states of the electron spin qubit with one and two time-bin encoded ZPL photon qubits. We herald on the photon detection in their time-bin states and observe the correlation with the corresponding spin qubit readout.

7.2 Interfacing Diamond Nitrogen-Vacancy Center Spin Qubits with an Optical Microcavity

In this section, we conceptually outline the optical interfacing of NV centers which are coupled to a fiber-based Fabry-Pérot microcavity as schematically depicted in Fig. 7.1(a). At its heart, a sample mirror with a bonded diamond membrane faces a laser-ablated spherical mirror on the tip of an optical fiber forming the microcavity [38]. Using the experimental setup presented in Fig. 7.1(b), the cavity-coupled NV centers are optically addressed via

* Equally contributed authors.

the microcavity, which is mounted inside a closed-cycle optical cryostat. Details about the low-vibration cryogenic microcavity setup can be found in Ref. [41], and the fabrication of the thinned-down diamond membrane, which is also used in earlier work [40], is reported in Ref. [39].

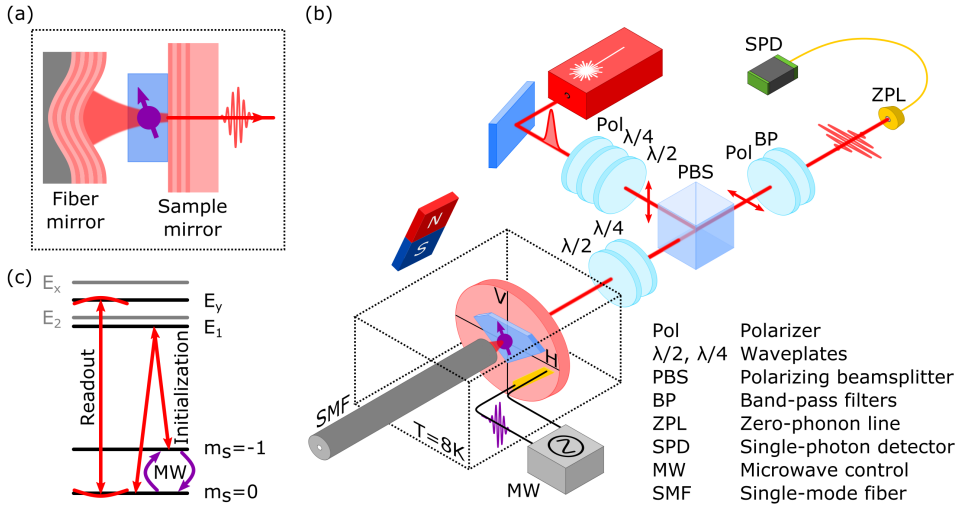

Figure 7.1: (a) Schematic of the fiber-based Fabry-Pérot microcavity. The NV center is hosted in a diamond membrane bonded to a planar sample mirror that faces a spherical mirror on the tip of an optical fiber, forming the cavity. The cavity mirrors are dielectric Bragg mirrors. (b) Schematic experimental setup to efficiently interface a NV center qubit with an optical microcavity. The cavity-coupled NV center spin qubit is controlled with microwave signals, which are delivered via a gold stripline that is embedded into the sample mirror. Outside the cryostat, a permanent magnet is mounted to apply a static magnetic field to the qubit. The optical readout of the cavity-coupled NV center is achieved using free-space cross-polarized resonant excitation and detection via the sample mirror side. Additional lasers for charge repump, spin initialization, and cavity locking are deployed in fiber via the fiber mirror side. (c) Energy diagram showing the investigated levels of the cavity-coupled NV center. The microwave qubit control, as well as the optical interface for readout and spin initialization, is depicted. The cavity is on resonance with the NV center E_y transition for readout.

For the experiments in this study, the two orthogonal, linear polarization modes of the microcavity must be considered. Due to birefringence in the diamond membrane, the frequency degeneracy of these cavity modes is lifted, which is identified as a polarization mode splitting in the optical cavity response. In our lab frame, the low frequency (LF) and high frequency (HF) cavity mode is referred to as horizontal and vertical polarization cavity modes, respectively. The NV center's optical dipole of the readout transition around 637 nm couples to both polarization cavity modes, enabling resonant excitation and detection in a cross-polarized fashion [42]. Nanosecond optical excitation pulses are coupled into the vertical polarization cavity mode through the sample mirror via the reflection of a polarizing beamsplitter. Upon excitation, the NV center ZPL emission into the horizontal polarization cavity mode is coupled out through the sample mirror and detected by a fiber-coupled single-photon detector in transmission of the polarizing beamsplitter. This cross-polarization filtering reaches high suppression values of the excitation laser and

is actively optimized during the experiments via piezo rotation mounted waveplates. In addition, a cavity lock laser at 637 nm is launched over the optical fiber mirror into the horizontal polarization cavity mode and is detected in cavity transmission by the same single-photon detector. This signal is used in the experiments to run a side-of-fringe lock that feedbacks on the piezo that is controlling the fiber mirror position to maintain a constant cavity length. More details about the experimental setup and the methods to maintain a high excitation laser suppression and to lock the cavity are described in Appendix 7.8.1.

To prepare the NV center in its negatively charged state an off-resonant 515 nm charge repump laser is deployed over the fiber mirror next to a second, 637 nm laser to initialize the NV center in its $m_s = 0$ spin ground state via the E_1 transition (see Fig. 7.1(c)). A permanent magnet outside the cryostat creates a static magnetic field at the position of the NV center, which Zeeman-splits the NV center's $m_s = \pm 1$ spin states, allowing us to define a qubit subspace consisting of the $m_s = 0$ and $m_s = -1$ states. Microwave pulses for qubit control are delivered via a gold stripline, which is embedded into the sample mirror [43].

All reported uncertainties in this work correspond to one standard deviation confidence intervals.

7.3 Coupling a Single Nitrogen-Vacancy Center to the Microcavity

With the full spatial and spectral tunability of the microcavity [44], we select a position on the diamond membrane that is close to the mirror-embedded gold stripline, exhibits a high cavity quality factor, and a well-coupled NV center. At the selected position, a frequency splitting between the horizontal and vertical polarization cavity mode of (9.56 ± 0.02) GHz is observed, which we attribute to birefringence due to the presence of strain in the diamond membrane. The individual cavity polarization mode shows a linewidth of (1.69 ± 0.02) GHz, which corresponds to a quality factor of 280×10^3. With the determined cavity geometry, a cavity mode volume of 86 λ^3 is simulated. Accounting for our residual cavity vibration level of 22 pm, this results in a maximal vibration-averaged Purcell factor of 12 for a NV center that is perfectly coupled to a single cavity mode [45]. In addition, a cavity mode outcoupling efficiency through the sample mirror of 39 % is calculated by taking the mirror coating transmission losses into account (see Appendix 7.8.2 for the cavity characterization details).

For the investigated cavity, we find a NV center that is coupled with its E_y transition (readout transition) at a frequency of 470.377 THz (−23.34 GHz with respect to 470.4 THz). Figure 7.2(a) shows a PLE measurement of this transition in the LF cavity mode, resulting in a linewidth of (45 ± 3) MHz determined by a Gaussian fit. We attribute the additional broadening above the expected linewidth of $1/2\pi\tau_{P,\mathrm{LF}} \approx 20$ MHz for the Purcell-reduced lifetime $\tau_{P,\mathrm{LF}}$ in the LF cavity mode as stated below to spectral diffusion. The determined transition linewidth is typical for NV centers with bulk-like optical properties and the used experimental PLE sequence involving 515 nm repump laser pulses [39]. Furthermore, we find the NV center's E_x transition at a frequency of 10 GHz. This corresponds to a transverse strain with E_x - E_y excited state splitting of ~ 33 GHz, which is larger compared to typical bulk samples. We note that we also find NV centers with less strain in the diamond

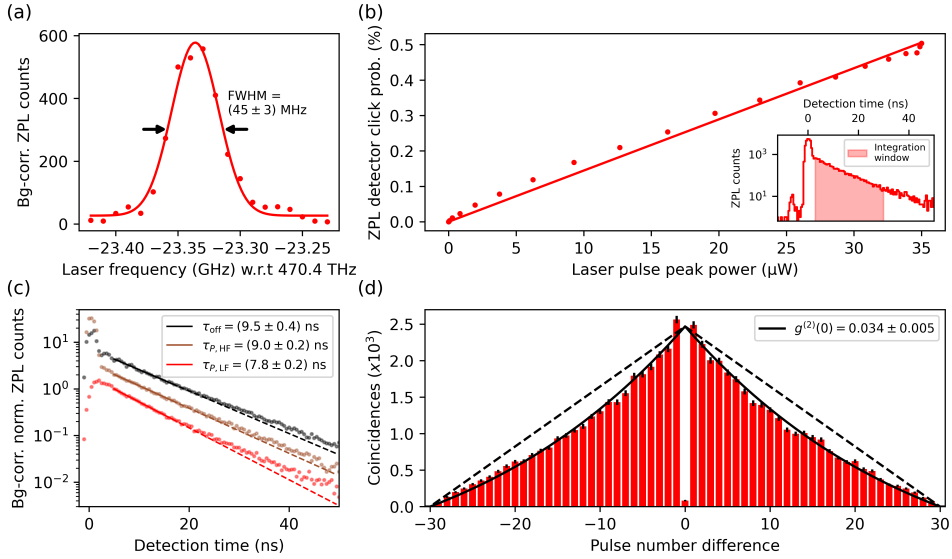

Figure 7.2: Characterization of the optical interface of the cavity-coupled NV center. (a) PLE measurement of the NV center's E_y transition (readout transition) in the LF cavity mode with a Gaussian fit (solid line). Details about the PLE measurement sequence and the applied background correction are presented in Appendix 7.8.3. (b) Pulsed resonant saturation measurement of the readout transition in the LF cavity mode, together with a linear fit as a guide for the eye. The inset shows the time-resolved detector counts for a laser pulse peak power of 35 µW measured free-space before the objective and the used integration window from 3 ns to 30 ns with respect to the excitation pulse center. The small peak at a detection time of about −5 ns is light of the excitation pulse that is backscattered into the free-space detection before reaching the cryostat. (c) Lifetime measurements of the NV center's E_y excited state on cavity resonance in the LF and HF cavity modes, as well as off resonance in the LF mode. Details about the applied background correction are outlined in Appendix 7.8.5. The fit windows of 5 ns to 18 ns are represented by the length of the solid lines of the monoexponential fits. The data is offset for visual clarity. (d) Second-order correlation measurement of the readout transition in the LF cavity mode for a pulse train of 30 consecutive short resonant excitation pulses. In this measurement, the integration window of (b) is used. The triangular function capturing the finite pulse train (black dashed line) is shown next to the fit function that also includes the spin flipping process (black solid line).

membrane. Next to these NV center transitions associated with the $m_s = 0$ spin state, we find emission lines at −26.0 GHz as well as −24.5 GHz that are associated with the $m_s = \pm 1$ spin states. We attribute these to the NV center's E_1 and E_2 transitions, where we use the former as our spin initialization transition. In all measurements, a static magnetic field of about 37.5 G is present along the NV center crystal axis. See Appendix 7.8.3 and 7.8.10 for the PLE measurements of the other transitions and details about the used sequences of the here studied and another cavity-coupled NV center.

In the sequences of all following measurements, we start by applying a 515 nm charge repump laser pulse to prepare the NV center with high probability in its negatively charged state, and a spin initialization laser pulse to initialize the NV center in its $m_s = 0$ spin state (see Appendix 7.8.7 for details). Figure 7.2(c) shows lifetime measurements of the NV center's E_y excited state using 2 ns short resonant excitation pulses (see Appendix 7.8.4 for details about the excitation pulse). The Purcell-reduced lifetime is measured in the LF and

HF cavity modes with the cavity being on resonance with the readout transition. An off resonance lifetime is determined in the LF mode by detuning the cavity from the readout transition by −4 GHz. The lifetime measurement data is fitted with monoexponential curves. We observe that the data start to deviate from a monoexponential behavior for detection times $\gtrsim 20$ ns. We attribute this to the detected fluorescence of other (weaker coupled) NV centers and therefore restrict the fit window size. Details about the applied background subtraction and the influence of the fit window are further outlined in Appendix 7.8.5. From the monoexponential fit, we determine an off resonance lifetime of $\tau_{\text{off}} = (9.5 \pm 0.4)$ ns and a Purcell-reduced lifetime of $\tau_{P,\text{LF}} = (7.8 \pm 0.2)$ ns and $\tau_{P,\text{HF}} = (9.0 \pm 0.2)$ ns for the LF and HF cavity mode, respectively. The off resonance lifetime differs from the expected excited state lifetime of 12.4 ns for low-strained NV centers [34]. We attribute this to strain-induced mixing in excited states [46, 47]. In Appendix 7.8.5 we show a complementary investigation of this mechanism with time-resolved detection during continuous wave resonant excitation. The determined lifetimes allow to calculate the Purcell factor

$$F_P = \frac{1}{\beta_0}\left(\frac{\tau_{\text{off}}}{\tau_P} - 1\right), \tag{7.1}$$

with the NV center Debye-Waller factor $\beta_0 = 0.03$ [28]. The Purcell factors for the LF and HF cavity mode are $F_{P,\text{LF}} = 7.3 \pm 1.6$ and $F_{P,\text{HF}} = 2.0 \pm 1.4$. In all the following measurements, we use the stronger coupling to the LF cavity mode to enhance the NV center emission and the HF cavity mode for excitation. Based on the determined Purcell factor the NV center coherently emits $\beta_{\text{LF}} = \beta_0 F_{P,\text{LF}}/(\beta_0 F_{P,\text{LF}} + 1) \approx 18\,\%$ into the LF cavity mode, which corresponds to a cavity outcoupled ZPL emission of about 7 % and a maximal detector click probability of about 1.4 % per excitation pulse for our setup efficiency and detection time window (see Appendix 7.8.11 for details).

In Figure 7.2(b), the saturation behavior of the NV center readout transition is studied. For that, the peak power of the short excitation pulse is varied, and the ZPL detector click probability after the first excitation pulse is measured. A ZPL detector click probability of 0.5 % per pulse is determined for the highest power applied, which outperforms the standard NV center quantum network node setups based on solid immersion lenses by an order of magnitude [9, 10, 35, 36]. In addition, the detector click probability still increases linearly for the investigated laser power regime showing that higher detector click probabilities can be reached if more laser power is applied. In the experiments, we are limited to the here investigated laser power regime due to the efficiency of our short optical pulse generation setup.

Furthermore, we confirm single-photon emission by performing a pulsed resonant HBT experiment on the readout transition. In the experiment, we perform in total 55×10^6 measurement sequence repetitions in which we apply a train of short excitation pulses with a consecutive time separation of 126 ns. Figure 7.2(d) shows the second-order correlation function for 30 consecutive excitation pulses. The second-order correlation function exhibits clear antibunching at zero pulse number difference. Further, it shows two bunching-like features, which we attribute to the spin flipping probability into the $m_s = \pm 1$ states for larger pulse number differences and the probability to decay back into the $m_s = 0$ state from the intersystem crossing singlet state for small pulse number differences. We fit the data with a triangular function as expected for the finite pulse train multiplied

by a monoexponential function capturing the spin flipping process (see Appendix 7.8.6 for details)). The exponential decay for small pulse number differences is not included, since the amount of affected data points is insufficient for a reliable fit. We quantify an antibunching value of $g^{(2)}(0) = 0.034 \pm 0.005$ by the ratio of measured coincidences in the zero bin to the triangular fit amplitude.

7.4 Coherent Microwave Control of the Nitrogen-Vacancy Center Spin Qubit

The NV center electron spin is coherently manipulated with microwave pulses, that are delivered via an about 10 µm distant gold stripline. Before microwave spin manipulation a 515 nm charge repump laser pulse prepares the NV center with high probability in its negatively charged state and the spin is optically initialized in its $m_s = 0$ ground state with a spin initialization laser pulse and a fidelity of $(93.5 \pm 0.9)\,\%$ (see Appendix 7.8.7 for details about the initialization and qubit readout analysis). The applied magnetic field along the NV center crystal axis splits the $m_s = \pm 1$ states by about 210 MHz, enabling selective driving of the $m_s = 0$ and $m_s = -1$ qubit subsystem. After spin manipulation, the qubit is read out via the readout transition using the short excitation pulses and the same integration window as introduced in Fig. 7.2(b). Figure 7.3(a) shows the statistics of detected photons for our spin qubit readout after spin initialization in the $m_s = \pm 1$ or $m_s = 0$ state. This measurement is used as a readout fidelity calibration, and its dependency on the number of used short readout pulses is presented in the inset. The average fidelity F_{avg} of the $m_s = \pm 1$ readout fidelity $F_{\pm 1}$ and the $m_s = 0$ readout fidelity F_0 plateaus for larger readout pulse numbers and is optimal around 200 pulses, which is used in the following experiments. These readout fidelities are used for qubit readout correction, where the finite spin state initialization fidelity is also taken into account. We note that the average readout fidelity is not limited by laser power, but rather the average number of emitted photons before the studied NV center spin flips. The outcoupled ZPL emission of about 7 % for our system is comparable to the collected non-coherent phonon sideband (PSB) emission used for readout in a SIL setup, rendering high-fidelity qubit readout possible [48].

In Figure 7.3(b), coherent Rabi oscillations with a Rabi frequency of $\Omega = (10.73 \pm 0.02)$ MHz are shown for our spin qubit at a microwave frequency of 2.773 GHz. Based on the fitted contrast of the Rabi oscillations and correcting for the finite spin state initialization fidelity, a microwave π pulse fidelity of $(83 \pm 9)\,\%$ is extracted.

For the next experiments, a π pulse and a $\pi/2$ pulse are calibrated by varying the amplitude of five consecutively applied π pulses that minimize the probability to readout $m_s = 0$. The π pulse duration is fixed to 64 ns, and half of that duration is used for the $\pi/2$ pulse. As depicted in Fig. 7.3(c), the qubit coherence is probed in a Ramsey experiment with an artificial detuning of 50 MHz by applying a delay time-dependent phase shift to the second $\pi/2$ pulse. The observed beating signature is attributed to the hyperfine coupling of the nitrogen nuclear spin, which is included in the fit model (see Appendix 7.8.8 for details). By fitting the measurement data, a free-induction decay time of $T_2^* = (170 \pm 20)$ ns is determined, which is short compared to typical T_2^* times for these diamond membranes (see Appendix 7.8.10 for additional data).

Using a Hahn-Echo experiment as presented in Fig. 7.3(d), the qubit coherence can be

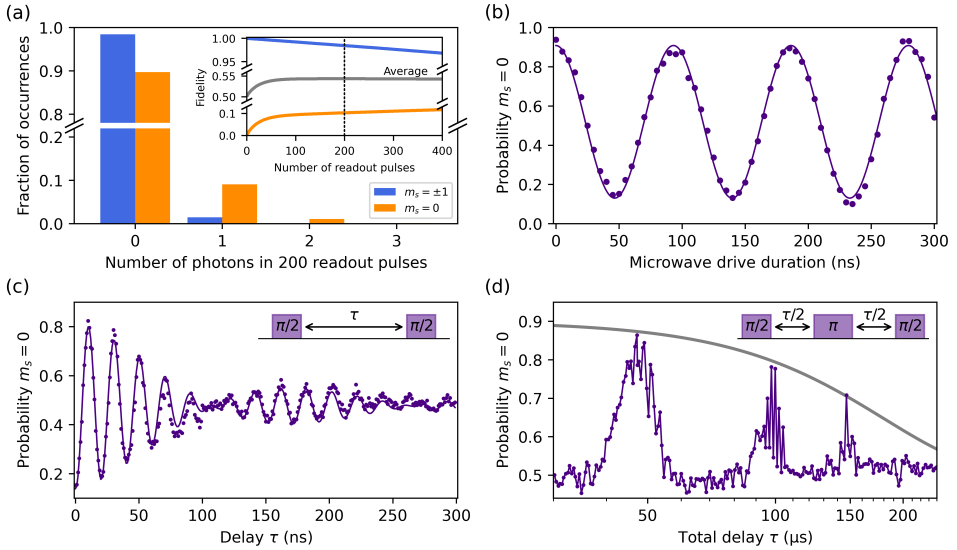

Figure 7.3: Characterization of the NV center electron spin qubit. (a) Statistics of detected photons for our spin qubit readout after spin initialization in the $m_s = \pm 1$ or $m_s = 0$ state. The inset presents the corresponding readout fidelities depending on the number of used short excitation pulses. For the experiments 200 short readout pulses are used, which leads to fidelities of $F_{\pm 1} = 98.4\,\%$, $F_0 = 10.3\,\%$ and $F_{\text{avg}} = 54.4\,\%$ for the shown calibration. (b) Coherent Rabi oscillations with a fit (solid line) showing a Rabi frequency of $\Omega = (10.73 \pm 0.02)\,\text{MHz}$. The error bars are within the dot size. (c) Ramsey measurement with an artificial detuning of 50 MHz. The inset shows the used microwave pulse sequence, where a delay time-dependent phase is applied to the second pulse to generate the artificial detuning. The fit (solid line) captures a beating signature of $(2.68 \pm 0.05)\,\text{MHz}$ which is attributed to the coupled nitrogen nuclear spin and the free-induction decay of $T_2^* = (170 \pm 20)\,\text{ns}$ with an exponent of $n = 1.0 \pm 0.2$. The error bars are within the dot size. (d) Hahn-Echo measurement with its microwave pulse sequence in the inset. The grey solid line is a guide for the eye of a Gaussian decay curve with an amplitude of 0.9 and a decay time of 180 μs. The error bars are within the dot size.

largely recovered by choosing an appropriate total delay time τ, which mitigates quasi-static magnetic field fluctuations. In this measurement, three revivals are observed and a Gaussian decay curve with a time constant of 180 μs is displayed as a guide for the eye in Fig. 7.3(d). The revivals occur around decoupling interpulse delay times $\tau/2$ that correspond to integer multiples of the bare Larmor period of the carbon-13 nuclear spin bath of about 25 μs ($\gamma_{C13} = 1.0705\,\text{kHz/G}$ and $B = 37.5\,\text{G}$) [49].

7.5 Generation of Spin-Photon States

In this section, we use our system to generate two-qubit and three-qubit spin-photon states and measure heralded correlations between the photonic and spin states. Figure 7.4(a) depicts the used pulse sequence, which combines spin qubit microwave control with the short resonant excitation pulses to generate spin-dependent photonic time-bin qubits. After optical initialization, the spin qubit is brought into equal superposition with a $\pi/2$ microwave pulse, followed by two resonant excitation pulses with an intermediate microwave π pulse. This generates the Bell state $|\text{NV spin}, \text{photon}\rangle = (|1, \text{E}\rangle + |0, \text{L}\rangle)/\sqrt{2}$ between the

spin qubit states $m_s = 0$ ($|0\rangle$) and $m_s = -1$ ($|1\rangle$) and the photonic qubit in the time-bin basis of early ($|\mathrm{E}\rangle$) and late ($|\mathrm{L}\rangle$) as used for remote entanglement generation in quantum network demonstrations [5, 35, 50]. The generated photon is measured by a single-photon detector, which heralds an early or late detection event. The spin qubit is optically read out in its Z-basis by 200 short readout pulses. The qubit readout probabilities conditioned on a photon heralding event in the early or late time-bin are shown in Fig. 7.4(b) (see Appendix 7.8.7 for details about the applied qubit readout correction and Appendix 7.8.9 for an X-basis spin qubit readout). A photon detection event in the late time-bin heralds the qubit in its expected $|0\rangle$ state. For an early time-bin photon detection event, the spin is read out with a probability of 82 % in its expected $|1\rangle$ state. We attribute the lower readout probability of the $|1\rangle$ state to our limited microwave π pulse fidelity and an imperfect pulse calibration. In the Bell state correlation measurement, we record 27143 photon heralding events in 5×10^6 attempts, which corresponds to a probability of 0.54 % per attempt.

Furthermore, the Greenberger–Horne–Zeilinger (GHZ) state $|\mathrm{NV\ spin, photon, photon}\rangle = (|0,\mathrm{E},\mathrm{L}\rangle + |1,\mathrm{L},\mathrm{E}\rangle)/\sqrt{2}$ can be generated by repeating the center sequence with the two short resonant excitation pulses before readout (see case $N = 2$ in Fig. 7.4(a)). The correlations after a successful double photon heralding event are displayed in Fig. 7.4(c). After heralding a correct two-photon state, the expected spin state is read out with similar probabilities as in the Bell state measurement. In total, we measure 5242 two-photon heralding events in 220×10^6 attempts, which corresponds to a probability of 2.4×10^{-5} per attempt.

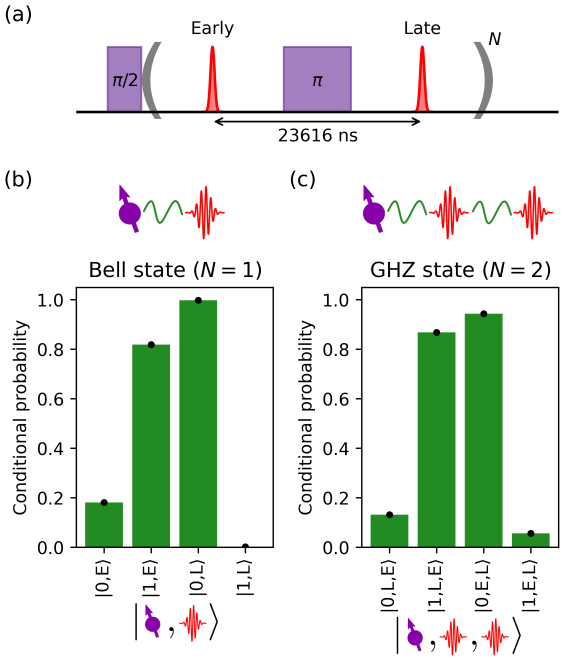

Figure 7.4: Spin-photon correlation measurements. (a) Pulse sequence to generate spin-photon states involving microwave pulses (in purple) for qubit control and short excitation pulses (in red) to generate spin-dependent time-bin photons. In the experiments, a microwave decoupling interpulse delay time of $\tau/2 = 23568\,\text{ns}$ is used. (b) Conditional probabilities of the spin qubit readout in the Z-basis after successful heralding an early ($|\text{E}\rangle$) or late ($|\text{L}\rangle$) photon of the spin-photon Bell state. The error bars are within the black dot size. (c) Conditional probabilities of the spin qubit readout in the Z-basis after a successful double heralding event of the photonic state $|\text{L},\text{E}\rangle$ or $|\text{E},\text{L}\rangle$ of the spin-photon GHZ state. The error bars are within the black dot size.

7

7.6 Discussion

We have equipped a coherent NV center spin qubit with an efficient spin-photon interface by coupling it to an open microcavity. Coherent qubit control is realized with microwave pulses, and qubit initialization as well as qubit readout are achieved with optical pulses in a cross-polarized resonant excitation and detection scheme. Moreover, we have demonstrated the quantum networking capabilities of our system by generating two-qubit and three-qubit spin-photon states and measuring heralded correlations between the photonic time-bin and the spin qubit states.

For the presented system, we project a saturation ZPL detector click probability of 1.4 % per pulse, by improving the excitation efficiency without modifying the microcavity. Furthermore, improving the device quality to eliminate additional cavity losses suggests a ZPL detector click probability of about 5 %, which corresponds to a cavity outcoupled ZPL emission of 26 %. Moreover, the system can be further optimized by implementing a charge-resonant check procedure of the optical transitions to mitigate spectral diffusion, improving charge state and qubit initialization fidelities [51], as well as microwave pulse shaping for high-fidelity qubit control [27].

Our work opens up opportunities to explore quantum networking with Purcell-enhanced NV centers, promising remote entanglement generation with higher rates and fidelities. Furthermore, we expect that the here developed methods provide guidance for other solid-state qubits to realize efficient spin-photon interfaces based on microcavities for quantum network applications [45, 52–55].

7.7 Acknowledgment

We thank Raymond Vermeulen for designing and building the standalone pulse generator used to modulate the electro-optical amplitude modulator. We thank Martin Eschen for laser-ablating the fiber mirror. We thank Jiwon Yun, Kai-Niklas Schymik, Conor Bradley, Alexander Stramma, and Mariagrazia Iuliano for helpful discussions. We thank Alexander Stramma for feedback on the manuscript.

We acknowledge financial support from the Dutch Research Council (NWO) through the Spinoza prize 2019 (project number SPI 63-264) and from the EU Flagship on Quantum Technologies through the project Quantum Internet Alliance (EU Horizon 2020, grant agreement no. 820445).

7.7.1 Author Contributions

J. F. and Y. H. contributed equally to this work. J. F. and Y. H. conducted the experiments and analyzed the data. J. F., Y. H., and S. S. developed and built the cross-polarization filtering setup. J. F. developed the cavity lock and the polarization suppression control. J. F., Y. H., and C. F. J. W. developed and built the short optical laser pulse generation setup. J. F. and C. F. J. W. developed the microwave qubit control. S. S. characterized the cavity fiber. M. R. fabricated the diamond membrane. J. F., Y. H., and R. H. wrote the manuscript with input from all authors. R. H. supervised the experiments.

7.7.2 Data Availability

The datasets that support this manuscript are available at 4TU.ResearchData [56].

7.8 Appendix

7.8.1 Experimental Setup

We use a floating stage closed-cycle optical cryostat (Montana Instruments HILA) with a base temperature of about 6 K and a sample mirror holder temperature of about 8 K. The spherical fiber mirror, that faces the sample mirror, is made out of a single-mode optical fiber with a pure silica core and a polyimide protection coating (Coherent FUD-4519, S630-P) and is mounted on a cryo-compatible positioning stage (JPE CPSHR1-a). A room temperature objective (Zeiss LD EC Epiplan-Neofluar), which is thermally shielded, is used to optically interface the sample mirror side of the cavity. The objective is positioned with three linear nanopositioning stages (Physik Instrumente Q-545) in a tripod configuration. A permanent neodymium disc magnet (Supermagnete S-70-35-N), which is mounted on the lid of the cryostat, is used to create a static magnetic field at the position of the sample mirror. Further details about the cryogenic setup can be found in Ref. [41].

The setup is operated with a computer and the Python-based software QMI version

0.44 [57]. The data is stored and analyzed with the Python framework quantify-core. The actual measurement sequences are timed and executed by an interplay between a microcontroller (Jäger Computergesteuerte Messtechnik Adwin Pro II) and an arbitrary waveform generator (Tektronix AWG5014C). Microwave pulses are generated with a single sideband modulated vector signal generator (Rohde & Schwarz SMBV100A), amplified by a microwave amplifier (Mini-Circuits ZHL-50W-63+) and delivered to the cryostat via a home-built microwave switch. At the qubit frequency of 2.773 GHz we measure about 26 dB transmission loss through the cryostat. Further details about the microwave wiring and a picture of the sample mirror with mirror-embedded gold striplines can be found in Ref. [41].

Laser Pulse Generation and Delivery

We use one 637 nm continuous wave diode laser each for cavity locking (Newport Newfocus Velocity TLB-6300-LN) and spin initialization (Toptica DL Pro 637 nm). To modulate the laser intensity and generate microsecond-long optical pulses with high on/off ratios, two cascaded in-fiber acousto-optic modulators (AOM, Gooch and Housego Fiber-Q 633 nm) are used. Both lasers are combined free-space by a 50:50 non-polarizing beamsplitter (Thorlabs BS016). Then, a Glan-Taylor polarizer (Thorlabs GT10-A) and a half-wave and quarter-wave plate (Thorlabs WPH05M-633 and WPQ05M-633) are used to set and control the polarization. Finally, the 637 nm lasers are overlapped with the 515 nm repump laser (Hübner Photonics Cobolt 06-MLD) by a dichroic mirror (Semrock Di01-R532) and coupled into a single-mode fiber, which is connected to the cavity fiber.

A frequency-doubled, high-power tunable diode laser (Toptica TA-SHG Pro 637 nm) is used for readout as well as for cross-polarization control. For that, the laser is split by a 50:50 fiber beamsplitter (Thorlabs PN635R5A2) into two in-fiber paths. In the path for cross-polarization control, two in-fiber AOMs are used for modulation, whereas in the readout laser path, a temperature-stabilized electro-optical amplitude modulator (EOM, Jenoptik AM635) is deployed additionally. This allows for faster intensity modulation and the generation of nanosecond-short resonant excitation pulses. The EOM is DC biased by a programmable bench power supply (Tenma 72-13360) using a bias-tee (Mini-Circuits ZX85-12G-S+) and a DC block (Mini-Circuits BLK-89-S+) to control a constant transmission level. In addition, fast electrical pulses are generated with a home-built standalone pulse generator [58] and applied to the EOM via the RF input of the bias-tee to generate nanosecond-short excitation pulses (see Appendix 7.8.4 for their characterization). Finally, both in-fiber paths are combined with a 75:25 fiber beamsplitter (Thorlabs PN635R3A2) whose 75 % output is connected to a polarization-maintaining fiber (Thorlabs P3-630PM-FC-2) before free-space launching. The 25 % output is connected to a power meter (Thorlabs PM100USB with head S130VC) for laser power monitoring. To preserve a high polarization extinction ratio in both paths, in-line fiber polarizers (Thorlabs ILP630PM-APC) are used. All 637 nm lasers are stabilized on a wave meter (HighFinesse WS-U).

Free-space Cross-polarization Optics

The cavity is interfaced from the sample mirror side with free-space cross-polarization optics as depicted in Fig. 7.1(b). The collimated beam leaving the cryostat chamber is guided by broadband dielectric mirrors (Thorlabs BB03-E03) on the optical table and is reflected off a dichroic mirror (Semrock Di02-R635) before reaching the polarization optics. Next,

the beam passes through half-wave and quarter-wave plates (Thorlabs WPH05M-633 and WPQ05M-633), which are mounted in piezo rotation stages (Newport AG-PR100 controlled by Newport AG-UC8). These wave plates map the excitation and detection polarization of the polarizing beamsplitter cube (PBS, Thorlabs PBS202) to the cavity polarization modes.

In the excitation path of the PBS the readout laser is launched from the polarization-maintaining fiber into free-space (Thorlabs KT120 with objective RMS10X) and passes a Glan-Thompson polarizer (Thorlabs GTH10M-A), followed by a quarter-wave and half-wave plate, which are mounted in piezo rotation stages as well.

In the detection path of the PBS, the light is filtered by a Glan-Thompson polarizer (Thorlabs GTH10M-A), an angle-tunable etalon (Light Machinery custom coating, $\approx 100\,\mathrm{GHz}$ full width at half maximum (FWHM) at 637 nm), and a bandpass filter (Thorlabs FBH640-10). Finally, the light is coupled (Thorlabs KT120 with objective RMS10X) into a single-mode fiber (Thorlabs P3-630A-FC-2) and detected by a single-photon detector (Picoquant Tau-SPAD-20). For the HBT experiment shown in Fig. 7.2(d), a 50:50 fiber beamsplitter (Thorlabs TW630R5A2) is added, and a second single-photon detector (Laser Components Count-10C-FC) is used. The detectors are connected to a single-photon counting module (Picoquant Hydraharp 400) and the counter module of the microcontroller. The gating of the single-photon detectors is used to protect them against blinding during the application of the spin initialization laser.

Microcavity Operation

For the resonant cross-polarization excitation and detection scheme used in this work, it is essential to keep the cavity on resonance with the NV center and to maintain a high excitation laser suppression during the measurements. To ensure these operational conditions, we probe the cavity resonance as well as the excitation laser suppression interleaved with the experimental sequences and stream the data to a computer in real-time to run an optimization routine next to the measurement. In both cases, the probe laser light is detected with the ZPL single-photon detector and recorded with the counter module of the microcontroller. This technique allows for live feedback on the order of Hertz, which is sufficient to compensate for drifts of the cavity resonance and the cross-polarization filtering. With the methods outlined in the following, it is possible to run measurements remotely for days.

To keep the cavity on resonance with the readout transition of the NV center, a side-of-fringe lock is deployed. For that, the cavity lock laser is frequency-tuned to the fringe of the cavity mode, and the single-photon detector counts are recorded during interleaved 100 µs long probe laser pulses. The recorded counts are streamed to a computer that uses a proportional control loop programmed in Python to optimize on a specified set value. The proportional control loop feedbacks on the piezo that is controlling the fiber mirror position and, by that, locks the cavity on resonance. The cavity lock laser power is adjusted such that a count rate of about 700 kHz is measured when the cavity is on resonance with the cavity lock laser. For every specified set value, the cavity lock laser frequency can be slightly adjusted to fine-tune the cavity resonance on the NV center.

For the cross-polarization filtering, interleaved 10 nW probe pulses of the cross-polarization control laser are applied for 400 µs while recording the single-photon detector counts. These counts represent the current excitation laser suppression and are streamed to a computer

that runs a hill-climbing type algorithm programmed in Python. The algorithm makes iterative changes to the four piezo rotation-mounted wave plates as introduced in Fig. 7.1(b) to minimize the recorded counts. With this polarization suppression control loop, typical long-term count rates are < 2 kHz for 10 nW probe pulses, which corresponds to excitation laser suppression values > 60 dB.

7.8.2 Hybrid Cavity Characterization

All measurements presented in the main text are performed at the same cavity length and lateral cavity position. By measuring the cavity mode dispersion as shown in Fig. 7.5, we extract an air gap of 6.39 µm and a diamond thickness of 6.20 µm, which corresponds to an air-like cavity mode [59] with hybrid cavity mode number 67. Due to a non-uniform bond, there might be a bond gap between the sample mirror and the diamond membrane. Further, a cavity mode dispersion slope of 34 MHz/pm and an effective cavity length of 13.2 µm is estimated [60]. Together with the 21.4 µm radius of curvature of the fiber mirror, a cavity beam waist of 1.46 µm and a cavity mode volume of 86 λ^3 is calculated.

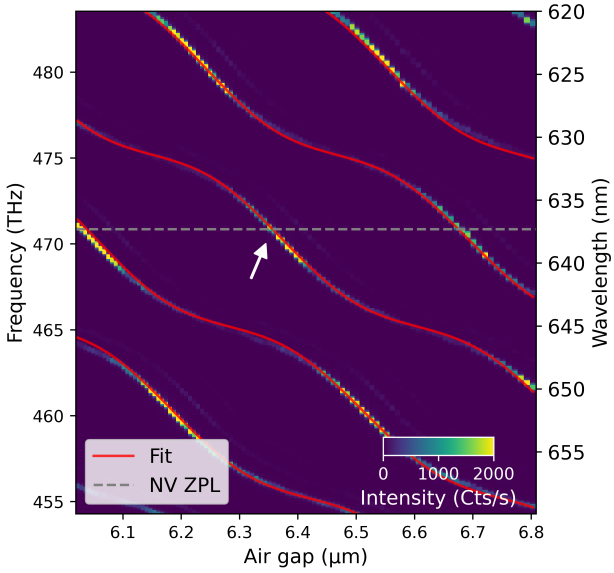

Figure 7.5: Cavity mode dispersion measurement of the hybrid air-diamond cavity. The cavity transmission of a broadband white light source spanning from 600 nm to 700 nm is measured on a spectrometer depending on the air gap. The bright fundamental modes are extracted and fitted by an analytical equation [59] to determine the air gap and the diamond thickness. In all measurements, the cavity is operated in the air-like mode at 637 nm as indicated by the white arrow.

To determine the FWHM Lorentzian linewidth of the cavity mode, we scan a laser over the cavity resonance as shown in Fig. 7.6. In this measurement, the linewidth of the cavity is broadened due to cavity length fluctuations. An independent measurement (as described in Ref. [41]) yields a vibration level of 22 pm root mean square of the cavity length fluctuations. Modeling these vibrations with a Gaussian distribution results in a

Gaussian contribution of $\mathrm{FWHM_G} = 22\,\mathrm{pm} \times 34\,\mathrm{MHz/pm} \times 2\,\sqrt{2\ln 2}$ next to the Lorentzian cavity linewidth. By fitting a Voigt function with the determined Gaussian contribution, an intrinsic cavity linewidth of $\mathrm{FWHM_L} = (1.69 \pm 0.02)\,\mathrm{GHz}$ is obtained. This corresponds to a cavity quality factor of 280×10^3 and, for our cavity geometry, to a cavity finesse of 2800. The cavity mirrors are both coated with dielectric Bragg mirrors (Laseroptik), that are optimized for maximum reflectivity at 637 nm. At this wavelength, the fiber mirror (sample mirror) exhibits a transmission value of 50 ppm (875 ppm) for air (diamond) termination. With the determined finesse, total cavity losses of 2260 ppm are calculated, which reveal additional losses of 1260 ppm. We attribute these additional losses to residual scattering at the interface of different refractive indices in the microcavity. Considering these losses, an outcoupling efficiency through the sample mirror of about 39 % is estimated, which reflects our asymmetric cavity design.

The inset of Fig. 7.6 shows another resonant laser scan, which is used to determine the frequency splitting between the LF and the HF cavity mode of $(9.56 \pm 0.02)\,\mathrm{GHz}$. For the used spherical fiber mirror, we do not observe a significant mode splitting on the bare mirror and hence attribute it mainly to the birefringence of the diamond membrane.

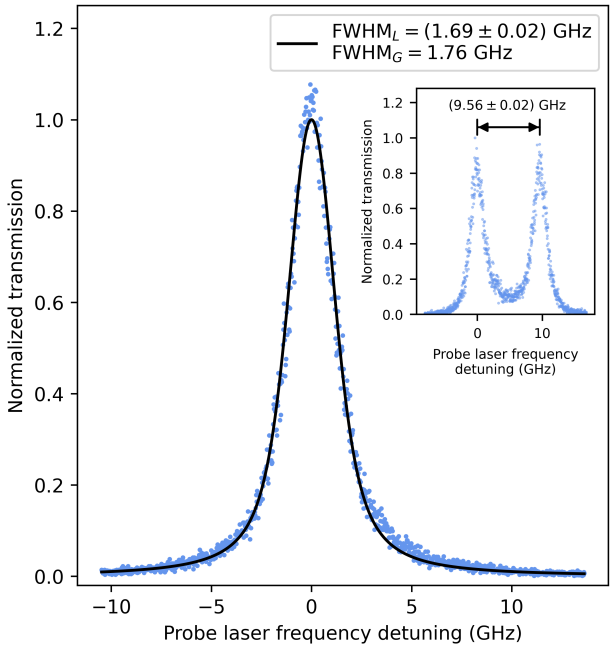

Figure 7.6: Resonant laser frequency scan over the cavity resonance to determine the cavity linewidth. The polarization of the laser is aligned to the LF cavity mode. The cavity transmission is measured on the ZPL single-photon detector. A Voigt function with a fixed Gaussian $\mathrm{FWHM_G}$ contribution, set by the vibration level, is used to fit the data (see text). The fit yields the cavity linewidth $\mathrm{FWHM_L}$ as the Lorentzian contribution. The inset shows a laser frequency scan, where a laser polarization is used that illuminates both cavity modes. This measurement reveals a frequency splitting between the LF and HF cavity mode of $(9.56 \pm 0.02)\,\mathrm{GHz}$.

7.8.3 NV Center PLE measurements

The power values of the lasers that are deployed via the cavity fiber mirror are stated as measured in transmission after the cavity (on cavity resonance), whereas the power values of the lasers deployed via the sample mirror side are measured free-space before entering the cryostat. All PLE measurements of the NV center are performed by repetitively running a certain PLE sequence for every swept excitation laser frequency. The number of repetitions and the exact PLE sequences for the different PLE measurements are outlined in the following subsections. All PLE sequences start with a 515 nm repump pulse, that prepares the NV center with high probability in its negatively charged state and predominantly in its $m_s = 0$ spin ground state. This pulse consists of a 50 µs long and 60 µW strong 515 nm repump laser pulse followed by a 5 µs wait time.

PLE Sequence of the NV Center E_y Transition

In the PLE measurement of the NV center E_y transition, shown in Fig. 7.2(a), the following PLE sequence is applied 200×10^3 times per excitation laser frequency. The sequence starts with the above-described repump pulse followed by a 100 µs long 0.2 nW spin initialization laser pulse on the E_1 transition to initialize the NV center in the $m_s = 0$ spin ground state. Then a free-space 1 nW excitation laser pulse is applied for 200 µs, while simultaneously measuring the ZPL signal of the NV center in the cross-polarized detection. The ZPL counts are acquired time-resolved, which results in an exponential decaying signal as can be seen exemplarily in Fig. 7.11(a) after averaging the repetitions for each excitation laser frequency. For the used excitation laser power of 1 nW, the decay is described well by a monoexponential fit on top of a constant offset level, which is determined by excitation laser leakage into the cross-polarized detection. Thus, the monoexponential fit amplitudes resemble a background-corrected measure of the ZPL counts, which are plotted in Fig. 7.2(a). In this measurement, the NV center is excited via the HF cavity mode, and fluorescence is detected in the LF cavity mode. In addition, the LF mode is kept on resonance with the excitation laser frequency by the cavity lock.

PLE Sequence of the NV Center E_1 and E_2 Transition

In the PLE measurement of the NV center E_1 and E_2 transition, shown in Fig. 7.7(a), the following PLE sequence is applied 100×10^3 times per excitation laser frequency. The sequence starts with the above-described repump pulse followed by 300 short excitation pulses on the NV center E_y transition to prepare the NV center in the $m_s = \pm 1$ spin ground states (see Fig. 7.12(a)). Then a 0.01 nW excitation laser pulse is applied for 100 µs via the cavity fiber, followed by 30 short excitation pulses to read out the NV center $m_s = 0$ spin state (as used in the main text). If the excitation laser is resonant with a transition associated with the $m_s = \pm 1$ spin states, some population is optically pumped back into the $m_s = 0$ spin ground state, and the ZPL signal is detected by the readout as shown in Fig. 7.7(a). This technique is used since the direct ZPL signal acquisition of the weaker coupled NV transitions in cross-polarized resonant excitation and detection is inefficient. In this measurement, the LF cavity mode is used for readout and kept on resonance with the NV center E_y transition by the cavity lock.

In the acquired PLE measurement shown in Fig. 7.7(a), two additional peaks with a splitting of about 200 MHz that overlap with the E_1 transition are observed. We attribute these peaks to the transitions between the Zeeman-split $m_s = \pm 1$ ground states and the

excited E_y state. This observation reveals a finite strength of these transitions for the investigated NV center.

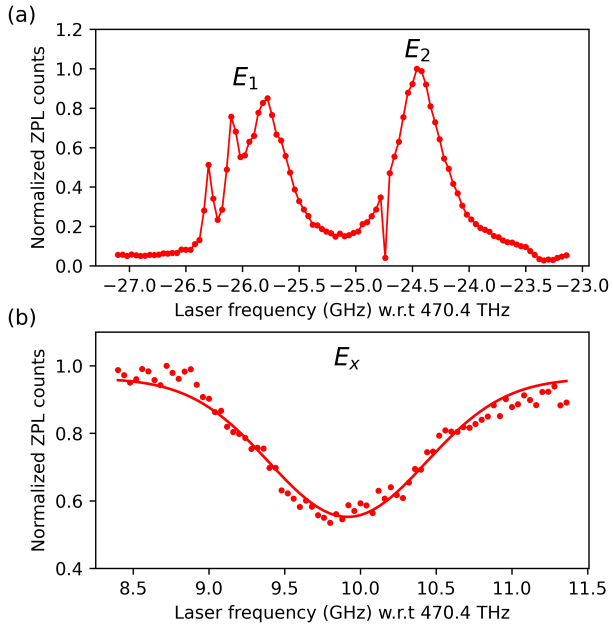

Figure 7.7: Further PLE measurements of the NV center used in the main text. (a) NV center E_1 and E_2 transition. For the laser frequency of −24.74 GHz, we suspect that our spin initialization laser did not switch on, resulting in ZPL counts on the background level. (b) NV center E_x transition with a Gaussian fit as a guide for the eye.

7

PLE Sequence of the NV Center E_x Transition

In the PLE measurement of the NV center E_x transition, shown in Fig. 7.7(b), the following PLE sequence is applied 100×10^3 times per excitation laser frequency. The sequence starts with the above-described repump pulse. Then a 200 µs long 50 nW excitation laser pulse is applied via the cavity fiber, followed by 30 short excitation pulses to read out the NV center $m_s = 0$ spin state. If the excitation laser is resonant with a transition associated with the $m_s = 0$ spin state, some population is optically pumped into the $m_s = \pm 1$ spin ground states, and a reduction of ZPL signal is detected by the readout as shown in Fig. 7.7(b). This technique is used since the direct ZPL acquisition of the weaker coupled NV transitions in cross-polarized resonant excitation and detection is inefficient. In this measurement, the LF cavity mode is used for readout and kept on resonance with the NV center E_y transition by the cavity lock.

7.8.4 Pulsed Resonant Excitation

Figure 7.8(a) shows the temporal shape of the short excitation pulse used throughout the study.

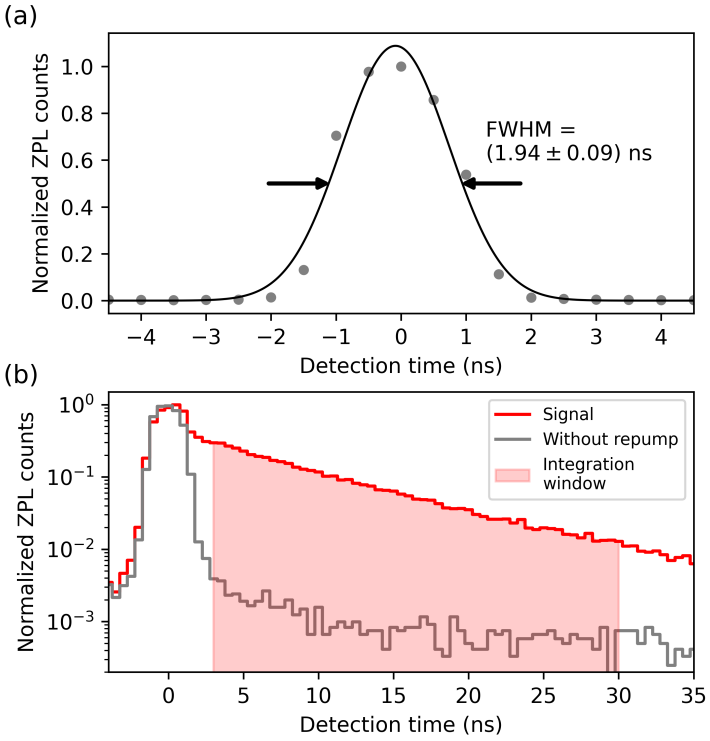

Figure 7.8: (a) Temporal shape of the short excitation pulse used in this study. (b) Short excitation pulse next to a time-resolved NV center readout signal. For the short excitation pulse measurement, the NV center is 'switched off' by not applying the charge repump pulse at the start of the measurement sequence.

A FWHM value of (1.94 ± 0.09) ns is determined by a Gaussian fit. In addition, Fig. 7.8(b) shows the same short excitation pulse next to a time-resolved pulsed readout measurement of the NV center E_y transition. The short excitation pulse is declined before the integration window, from 3 ns to 30 ns with respect to the excitation pulse center, starts. The integration window includes about 75 % of the studied Purcell-enhanced NV center emission, assuming the NV center population inversion is completed 1 ns after the excitation pulse center.

7.8.5 NV Center Excited State Lifetime Measurements

The NV center excited state lifetime measurement sequences used in Fig. 7.2(c) start with a 515 nm repump pulse, that prepares the NV center with high probability in its negatively charged state. This pulse consist of a 50 µs long and 60 µW strong 515 nm repump laser pulse followed by a 5 µs wait time. Subsequently, a 0.2 nW spin initialization laser pulse is applied for 100 µs (20 µs) on the E_1 transition to initialize the NV center in the LF (HF) cavity mode in its $m_s = 0$ spin ground state. Then 100 short excitation pulses are used in the sequence to excite the NV center, followed by time-resolved detection of the ZPL signal. To correct for background, we make use of the pumping into the NV center $m_s = \pm 1$ spin

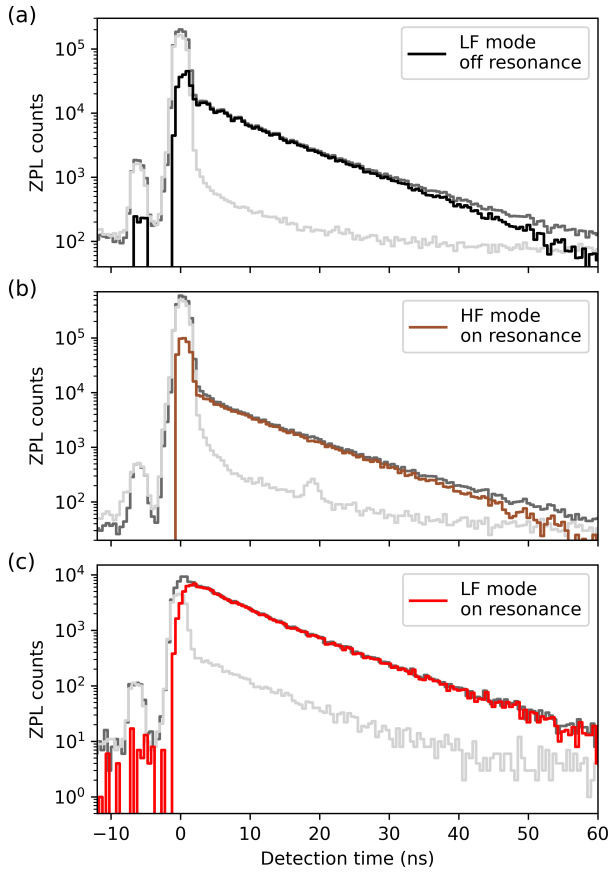

Figure 7.9: Background correction of the NV center E_y excited state lifetime measurement. Data in dark (light) gray shows the ZPL signal of the first (last) 5 short excitation pulses of the in total applied 100 pulses. The small peak at a detection time of about −5 ns is light of the excitation pulse that is backscattered into the free-space detection before reaching the cryostat. (a) Background correction of the lifetime measurement in the LF mode with a cavity detuning of −4 GHz from the E_y transition. (b) Background correction of the lifetime measurement in the HF mode and the cavity on resonance with the E_y transition. (c) Background correction of the lifetime measurement in the LF mode and the cavity on resonance with the E_y transition.

ground states with more applied short excitation pulses (see Fig. 7.12(a)). This allows to take the high signal-to-noise part of the first 5 short excitation pulses and subtract the last 5, which corrects for constant background contributions. The data underlying the background subtraction is shown in Fig. 7.9 and leads to the lifetime measurement data used in the main text Fig. 7.2(c).

Despite the background subtraction, we see that the data deviates from a monoexponential behavior with increasing detection time, which is also observed in the extracted lifetimes for different fit windows shown in Fig. 7.10. This hints towards a time-dependent background contribution of fluorescence that might stem from other weaker coupled NV

centers in the diamond membrane or the cavity mirror materials.

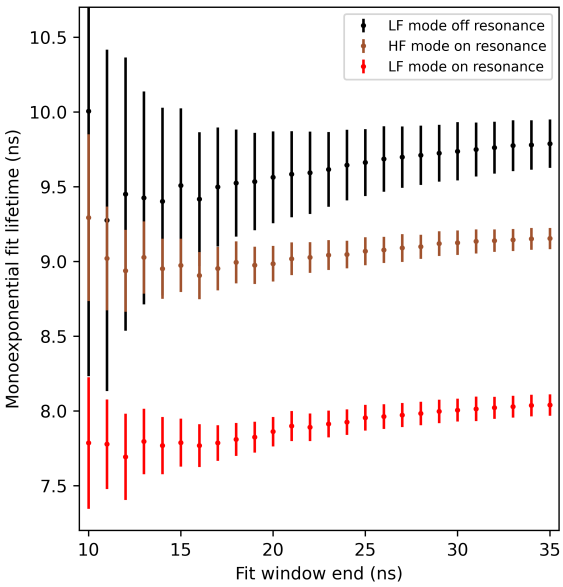

Figure 7.10: Extracted excited state lifetime from a monoexponential fit on the lifetime measurement data of main text Fig. 7.2(c). The fit window start is set to 5 ns while the fit window end is varied.

Furthermore, an off resonance lifetime of $\tau_{\text{off}} = (9.5 \pm 0.4)$ ns is measured for the NV center E_y excited state in the main text, which deviates from the expected about 12.4 ns lifetime in bulk samples [34]. This reveals a larger excited state decay rate of the studied NV center, which we attribute to strain-induced mixing in the excited states [46, 47]. In Fig. 7.11(b), we conduct a continuous wave saturation measurement of the NV center E_y transition using 32 µs long resonant pulses and detect the ZPL signal time-resolved as shown in Fig. 7.11(a). The ZPL signal fits well to a double exponential fit with a constant offset accounting for excitation laser leakage into the cross-polarized detection. The summed amplitudes resemble a measure for the saturating ZPL counts, while the exponential time constants give insights into the decay dynamics of the studied NV center. We attribute the fast decay time constant to additional decay from the excited state, next to the decay into the $m_s = 0$ spin ground state. Assuming that saturating the NV center with high excitation power leads to an average excited state population of 50 %, half of the fitted fast decay time constant 110 ns/2 (see Fig. 7.11(b)) determines the additional decay rate. With that additional decay, the predicted lifetime of the excited state is about 10 ns, which matches with the value of the off resonance lifetime measurement.

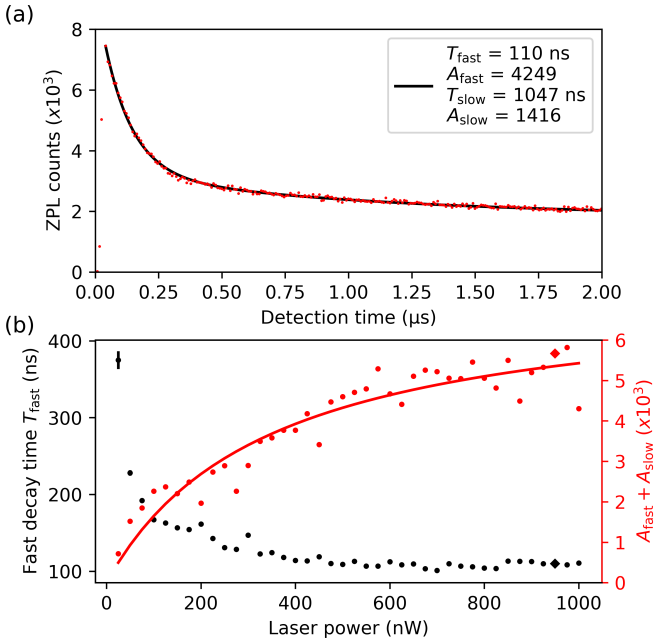

Figure 7.11: (a) Exemplary time-resolved ZPL signal of the NV center E_y transition saturation measurement. In this measurement, a resonant laser power of 950 nW is used, and the black solid line is a double exponential fit with offset to the data. The fast decay for short detection times is described with the time constant T_{fast} while the slow decay is captured by T_{slow}. (b) NV center E_y transition saturation measurement with extracted fit parameters. The total fit amplitude $A_{\text{fast}} + A_{\text{slow}}$ resembles the saturating ZPL counts, and T_{fast} is the fast exponential decay time constant. The total fit amplitudes that depend on the laser power P are fitted to a function proportional to $P/(P+2P_{\text{sat}})$ as a guide for the eye. The individual measurement shown in (a) is indicated by the diamond-shaped data point.

7

7.8.6 NV Center Second-order Correlation Measurement

The second-order correlation measurement of the E_y transition (readout transition) in Fig. 7.2(d) is fitted by the following function

$$g^{(2)}(n) = A\left|1-\frac{|n|}{N}\right|\exp\left(-\frac{|n|}{B}\right) \quad \forall \quad 0<|n|<N, \tag{7.2}$$

with the amplitude A, the spin flipping constant B and the number of consecutive short resonant excitation pulses N. In our experiments, the parameter B takes the spin flipping process into the $m_s = \pm 1$ states into account, where $1-\exp(-1/B)$ is the probability per excitation pulse to spin flip. The consequence of a spin flip is that the NV center stops emitting photons with excitation pulses addressing the readout transition.

7.8.7 NV Center Spin Initialization and Readout

All measurement sequences used in Fig. 7.3 and Fig. 7.4 start with a 515 nm repump pulse, which prepares the NV center with high probability in its negatively charged state. This pulse consist of a 50 µs long and 60 µW strong 515 nm repump laser pulse followed by a 5 µs

wait time. Subsequently, and if not stated otherwise, a 100 µs long 0.2 nW spin initialization laser pulse on the E_1 transition is applied to initialize the NV center in its $m_s = 0$ spin ground state. Then the actual measurement sequence, composed of microwave (and individual short resonant excitation) pulses, is played, followed by a series of short excitation pulses to read out the NV center qubit state. If at least one photon is detected during the readout, the $m_s = 0$ qubit state is measured; otherwise, the $m_s = -1$ qubit state is assigned. Since these outcomes are subject to measurement errors like photon loss as well as dark or background photon detection events, a readout correction is used to recover the measurement statistics. For this purpose, the initialization fidelity in the $m_s = 0$, as well as $m_s = \pm 1$ spin state and their corresponding readout fidelities, are determined, and the correction formalism as outlined in Ref. [61] is used.

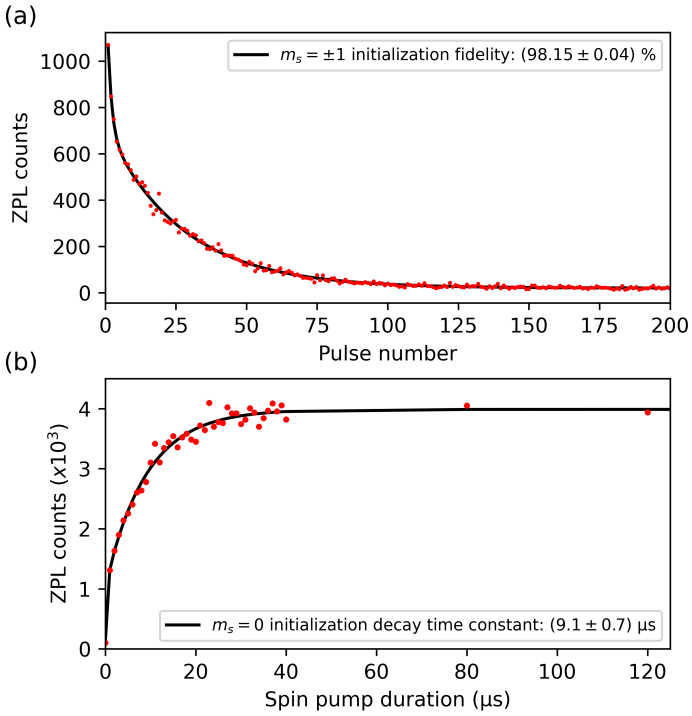

Figure 7.12: (a) Spin initialization measurement in the $m_s = \pm 1$ spin states by optical pumping with short excitation pulses on the NV center E_y transition. Before the short excitation pulses are applied, a 0.2 nW spin initialization pulse is applied for 120 µs on the E_1 transition. (b) Indirect spin initialization measurement in the $m_s = 0$ spin state by optical pumping on the NV center E_1 transition and readout by 5 short excitation pulses. In this measurement, a spin initialization pulse power of 0.2 nW is used, while the spin initialization pulse duration is varied.

The initialization in the $m_s = \pm 1$ spin states is performed using the short excitation pulses that are resonant with the NV center readout transition. The detected ZPL counts in the integration window of 3 ns to 30 ns after each short excitation pulse are shown in Fig. 7.12(a). The ZPL counts, depending on the pulse number, follow a double exponential

behavior similar to the second-order correlation measurement in Fig. 7.2(d). The measurement shows that after about 200 short excitation pulses, a constant ZPL count level is reached. Comparing the total ZPL count amplitude with the offset determined by fitting an initialization fidelity of $(98.15 \pm 0.04)\,\%$ is determined.

The initialization in the $m_s = 0$ spin state is performed by optical pumping on the NV center E_1 transition. To investigate the spin initialization behavior, the NV center is first prepared in the $m_s = \pm 1$ spin states by 600 short excitation pulses, and then a 0.2 nW spin initialization laser pulse is applied for different durations, followed by 5 short excitation pulses for readout. The measured readout ZPL counts depending on the spin initialization pulse duration are shown in Fig. 7.12(b). For longer spin initialization pulse durations, the detected ZPL counts increase until they settle exponentially. From a double exponential fit, a slow decay time constant of $(9.1 \pm 0.7)\,\mu s$ is determined. This indirect spin initialization measurement via the NV center readout transition gives insights about the required spin initialization pulse durations for the used laser power, but does not allow us to determine an initialization fidelity in the $m_s = 0$ spin state.

To estimate the $m_s = 0$ initialization fidelity, the NV center $m_s = 0$ spin state is first heralded by measuring a photon after a single short excitation pulse and then read out with 200 short excitation pulses. This results in the maximal readout probability, since the $m_s = 0$ spin state is heralded just before the readout. After this first readout, further short excitation pulses are used to initialize the NV center in the $m_s = \pm 1$ states followed by a 0.2 nW spin initialization laser pulse on the E_1 transition for 100 µs and another readout with 200 short excitation pulses. This results in a second readout probability, which is set by the optical pumping performance of the initialization laser pulse. Comparing the second to the first readout yields an initialization fidelity in the $m_s = 0$ spin state of $(93.5 \pm 0.9)\,\%$. To exclude NV center ionization, a third iteration is performed, leading to the same result as the second readout.

Moreover, this experiment reveals the combined probability that the initial repump and spin initialization pulse prepares the NV center in its negatively charged and $m_s = 0$ state by comparing the probability of the first readout with and without the described heralding. From this, a probability of $(72.8 \pm 0.6)\,\%$ is found, which is considered in the readout of the heralded measurements in Fig. 7.4. Further, we note that an initialization laser pulse duration of 20 µs instead of 100 µs is used in the GHZ state measurement of Fig. 7.4(c).

7.8.8 NV Center Ramsey Measurement

The Ramsey fringes measured in Fig. 7.3(c) are determined by the hyperfine coupling of the nitrogen-14 nuclear spin ω_{hf}, the free-induction decay time T_2^*, and the used artificial detuning Δ. The artificial detuning is implemented by applying a phase of $\tau\Delta$ to the second $\pi/2$ pulse in the Ramsey sequence. The data is well fitted by the following function

$$P_{m_s=0}(\tau) = c - \exp\left(-\left(\frac{\tau}{T_2^*}\right)^n\right) \cdot \sum_{k=-1,0,+1} P_k \cos\left((\Delta + k\omega_{\mathrm{hf}})\tau + \phi\right), \tag{7.3}$$

with the offset c, the decay exponent n, the nitrogen nuclear spin amplitudes P_k and a common phase ϕ. The amplitudes P_k take partial polarization of the nitrogen nuclear spin

into account, and the common phase ϕ accounts for a phase offset between the two applied $\pi/2$ pulses.

7.8.9 Bell State Spin-photon Correlations with Spin Qubit Readout in X-Basis

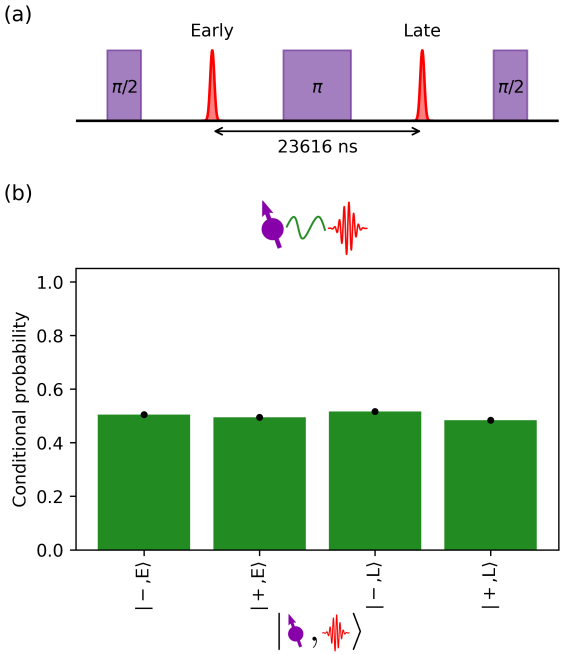

Figure 7.13: (a) Pulse sequence to generate a spin-photon Bell state and a spin qubit readout in the X-basis. In the experiment, a microwave decoupling interpulse delay time of $\tau/2 = 23568\,\text{ns}$ is used. (b) Conditional probabilities of the spin qubit readout in the X-basis after successful heralding an early ($|\text{E}\rangle$) or late ($|\text{L}\rangle$) photon of the spin-photon Bell state. The error bars are within the black dot size.

In addition to the Bell state spin-photon correlation measurement of Fig. 7.4(b), where the spin qubit is read out in its Z-basis, we perform an X-basis spin qubit readout in Fig. 7.13(b). The used pulse sequence is depicted in Fig. 7.13(a), which exhibits another $\pi/2$ pulse after the Bell state generation to perform the qubit readout in the X-basis. As in the main text, 200 short excitation pulses are used for readout.

In the X-basis measurement, the spin is measured with equal probability in one of the qubit states. In total we record 24456 photon heralding events in 5×10^6 attempts, which corresponds to a probability of 0.49 % per attempt.

7.8.10 Additional Data of a Second Cavity-coupled NV Center

At a different lateral position on the diamond membrane, a second NV center coupled to the cavity is investigated. For this cavity position a frequency splitting of the two polarization cavity modes of about 10.7 GHz is observed and a NV center coupled with its E_y transition at a frequency of about 36.8 GHz (with respect to 470.4 THz) is found. The frequency splitting of the polarization cavity modes ~ 10 GHz is observed for all cavity spots in the investigated range of ~ 100 µm along the gold stripline. The E_x transition of the NV center is identified with a frequency of about 48.8 GHz, resulting in a lower transverse strain with E_x - E_y excited state splitting of ~ 12 GHz compared to the NV center studied in the main text. The corresponding PLE measurements are shown in Fig. 7.14. The absolute transition frequencies as well as the transverse strain level are comparable to NV centers in solid immersion lens devices, which have also been used to demonstrate high-fidelity readout [48]. This shows that low-strained NV centers, similar to solid immersion lens devices, are found in the diamond membrane.

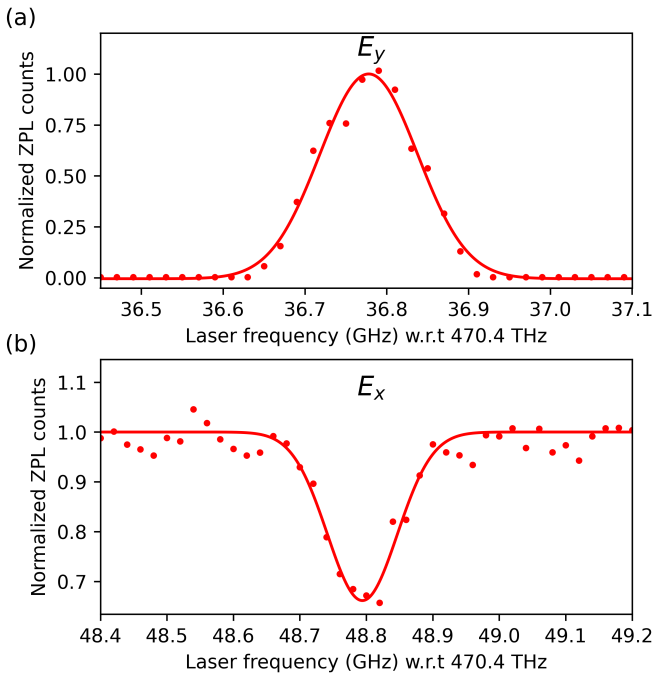

Figure 7.14: PLE measurements of a second cavity-coupled NV center at a different lateral position on the diamond membrane. (a) NV center E_y transition. (b) NV center E_x transition. For both measurements, 200 short readout pulses are used.

In addition, the spin coherence of this NV center is measured in a Ramsey experiment as shown in Fig. 7.15(b). Compared to the Ramsey experiment shown in Fig. 7.3(c) of the main text, only the $m_I = 0$ spin resonance of the coupled nitrogen nuclear spin is driven. This transition is identified beforehand in an electron spin resonance measurement as

shown in Fig. 7.15(a). The resulting Ramsey fringes are well fitted by the function

$$P_{m_s=0}(\tau) = c - A \exp\left(-\left(\frac{\tau}{T_2^*}\right)^n\right) \cdot \sum_{k=-1,+1} \cos((\Delta + k\omega_c/2)\tau + \phi), \tag{7.4}$$

with the amplitude A and the carbon-13 nuclear spin coupling frequency ω_c. Fitting the Ramsey experiment yields a free-induction decay time of $T_2^* = (3.7 \pm 0.4)\,\mu s$ with a decay exponent of $n = 1.1 \pm 0.3$ and a beating with a frequency of $(218 \pm 4)\,kHz$, which we attribute to the coupling of a carbon-13 nuclear spin. To summarize, NV centers with electron spin coherence times similar to diamond bulk samples can be observed [5].

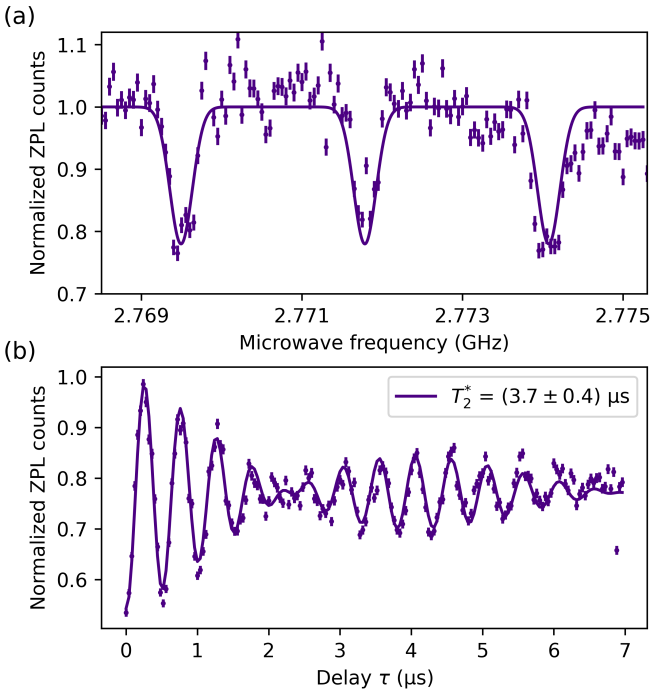

Figure 7.15: (a) Electron spin resonance measurement. The NV center is initialized in its $m_s = 0$ state, then a microwave pulse of 10 µs is applied, and finally the NV center $m_s = 0$ state is read out with 50 short excitation pulses. The microwave frequency is swept over the $m_s = -1$ electron spin state, and for each nitrogen nuclear spin resonance ($m_I = -1, 0, +1$), a decrease in ZPL counts is observed. The fit with three Gaussian dips is a guide for the eye. (b) Ramsey experiment at the $m_I = 0$ nitrogen nuclear spin resonance frequency with an artificial detuning of 2 MHz. In this measurement, a microwave $\pi/2$ pulse duration of 350 ns is used.

7.8.11 Summary of System Parameters

Next to the parameters of the emitter-cavity system, the efficiency of the free-space cross-polarization setup determines the total efficiency of the short excitation pulse excitation and detection scheme. The photon collection efficiency into the ZPL single-mode fiber comprising all the optics after the microcavity amounts to about 39 %, and the used single-photon detectors are specified with 70 %. Including the integration time window used for short excitation pulse readout with a collected fraction of about 75 %, the total ZPL setup efficiency is estimated to be about 20 %. Considering the ZPL emission into the LF mode of about 18 % together with the cavity outcoupling efficiency of 39 %, a detector click probability of about 1.4 % per pulse is estimated upon NV center excitation as stated in the main text.

An overview of measured, estimated, and simulated values of this work is summarized in Table 7.1.

Table 7.1: Overview of system parameters.

Parameter	Value
Fiber mirror radius of curvature	21.4 µm
Cavity air gap	6.39 µm
Diamond thickness	6.20 µm
Hybrid cavity mode number q	67
Effective cavity length L_{eff} [60]	13.2 µm
Estimated cavity beam waist ω_0 [60]	1.46 µm
Estimated cavity mode volume V [60]	86 λ^3
Cavity Lorentzian linewidth $\kappa/2\pi$	(1.69 ± 0.02) GHz
Root mean square cavity length fluctuations	22 pm
Cavity mode dispersion slope	34 MHz/pm
Cavity quality factor Q	280×10^3
Cavity finesse $\mathcal{F}$	2800
Cavity outcoupling efficiency	39 %
Calculated cavity transmission	8 %
Calculated vibration-averaged Purcell factor [45]	12
NV center Debye-Waller factor β_0	0.03 [28]
Measured Purcell factor LF mode $F_{P,\text{LF}}$	7.3 ± 1.6
Measured Purcell factor HF mode $F_{P,\text{HF}}$	2.0 ± 1.4
Measured cooperativity LF mode $\beta_0 F_{P,\text{LF}}$	0.22 ± 0.05
Measured cooperativity HF mode $\beta_0 F_{P,\text{HF}}$	0.06 ± 0.04
ZPL emission into LF mode β_{LF}	18 %
Cavity outcoupled ZPL emission LF mode	7 %
ZPL detector click probability per pulse LF mode (end-to-end efficiency at saturation)	1.4 %

References

[1] H. J. Kimble, *The quantum internet,* Nature **453**, 1023 (2008).

[2] S. Wehner, D. Elkouss, and R. Hanson, *Quantum internet: A vision for the road ahead,* Science **362**, eaam9288 (2018).

[3] M. Ruf, N. H. Wan, H. Choi, D. Englund, and R. Hanson, *Quantum networks based on color centers in diamond,* Journal of Applied Physics **130**, 070901 (2021).

[4] E. Janitz, M. K. Bhaskar, and L. Childress, *Cavity quantum electrodynamics with color centers in diamond,* Optica **7**, 1232 (2020).

[5] H. Bernien, B. Hensen, W. Pfaff, G. Koolstra, M. S. Blok, L. Robledo, T. H. Taminiau, M. Markham, D. J. Twitchen, L. Childress, and R. Hanson, *Heralded entanglement between solid-state qubits separated by three metres,* Nature **497**, 86 (2013).

[6] C. M. Knaut, A. Suleymanzade, Y.-C. Wei, D. R. Assumpcao, P.-J. Stas, Y. Q. Huan, B. Machielse, E. N. Knall, M. Sutula, G. Baranes, N. Sinclair, C. De-Eknamkul, D. S. Levonian, M. K. Bhaskar, H. Park, M. Lončar, and M. D. Lukin, *Entanglement of nanophotonic quantum memory nodes in a telecom network,* Nature **629**, 573 (2024).

[7] A. Ruskuc, C.-J. Wu, E. Green, S. L. N. Hermans, W. Pajak, J. Choi, and A. Faraon, *Multiplexed entanglement of multi-emitter quantum network nodes,* Nature **639**, 54 (2025).

[8] F. Afzal, S. J. Beale, O. Bedroya, K. Bell, L. Bergeron, K. Bonsma-Fisher, P. Bychkova, Z. M. E. Chaisson, C. Chartrand, C. Clear, A. Darcie, A. DeAbreu, C. DeLisle, L. A. Duncan, C. D. Smith, J. Dunn, A. Ebrahimi, N. Evetts, D. F. Pinheiro, P. Fuentes, T. Georgiou, B. Guha, R. Haenel, D. Higginbottom, D. M. Jackson, N. Jahed, A. Khorshidahmad, P. K. Shandilya, A. T. K. Kurkjian, N. Lauk, N. R. Lee-Hone, E. Lin, R. Litynskyy, D. Lock, L. Ma, I. MacGilp, E. R. MacQuarrie, A. Mar, A. M. Khah, A. Matiash, E. Meyer-Scott, C. P. Michaels, J. Motira, N. K. Noori, E. Ospadov, E. Patel, A. Patscheider, D. Paulson, A. Petruk, A. L. Ravindranath, B. Reznychenko, M. Ruether, J. Ruscica, K. Saxena, Z. Schaller, A. Seidlitz, J. Senger, Y. S. Lee, O. Sevoyan, S. Simmons, O. Soykal, L. Stott, Q. Tran, S. Tserkis, A. Ulhaq, W. Vine, R. Weeks, G. Wolfowicz, and I. Yoneda, *Distributed Quantum Computing in Silicon,* arXiv:2406.01704 (2024), `https://arxiv.org/abs/2406.01704`.

[9] S. L. N. Hermans, M. Pompili, H. K. C. Beukers, S. Baier, J. Borregaard, and R. Hanson, *Qubit teleportation between non-neighbouring nodes in a quantum network,* Nature **605**, 663 (2022).

[10] M. Pompili, S. L. N. Hermans, S. Baier, H. K. C. Beukers, P. C. Humphreys, R. N. Schouten, R. F. L. Vermeulen, M. J. Tiggelman, L. dos Santos Martins, B. Dirkse, S. Wehner, and R. Hanson, *Realization of a multinode quantum network of remote solid-state qubits,* Science **372**, 259 (2021).

[11] A. J. Stolk, K. L. Van Der Enden, M.-C. Slater, I. Te Raa-Derckx, P. Botma, J. Van Rantwijk, J. J. B. Biemond, R. A. J. Hagen, R. W. Herfst, W. D. Koek, A. J. H. Meskers, R. Vollmer, E. J. Van Zwet, M. Markham, A. M. Edmonds, J. F. Geus, F. Elsen, B. Jungbluth, C. Haefner, C. Tresp, J. Stuhler, S. Ritter, and R. Hanson, *Metropolitan-scale heralded entanglement of solid-state qubits,* Science Advances **10**, eadp6442 (2024).

[12] A. Tchebotareva, S. L. N. Hermans, P. C. Humphreys, D. Voigt, P. J. Harmsma, L. K. Cheng, A. L. Verlaan, N. Dijkhuizen, W. de Jong, A. Dréau, and R. Hanson, *Entanglement between a Diamond Spin Qubit and a Photonic Time-Bin Qubit at Telecom Wavelength,* Physical Review Letters **123**, 063601 (2019).

[13] J. F. Geus, F. Elsen, S. Nyga, A. J. Stolk, K. L. Van Der Enden, E. J. Van Zwet, C. Haefner, R. Hanson, and B. Jungbluth, *Low-noise short-wavelength pumped frequency downconversion for quantum frequency converters,* Optica Quantum **2**, 189 (2024).

[14] J. Javadzade, M. Zahedian, F. Kaiser, V. Vorobyov, and J. Wrachtrup, *Efficient nuclear spin–photon entanglement with optical routing,* Physical Review Applied **24**, 024059 (2025).

[15] X.-Y. Chang, P.-Y. Hou, W.-G. Zhang, X.-Q. Meng, Y.-F. Yu, Y.-N. Lu, Y.-Q. Liu, B.-X. Qi, D.-L. Deng, and L.-M. Duan, *Hybrid entanglement and bit-flip error correction in a scalable quantum network node,* Nature Physics **21**, 583 (2025).

[16] M. H. Abobeih, J. Cramer, M. A. Bakker, N. Kalb, M. Markham, D. J. Twitchen, and T. H. Taminiau, *One-second coherence for a single electron spin coupled to a multi-qubit nuclear-spin environment,* Nature Communications **9**, 2552 (2018).

[17] T. Van Der Sar, Z. H. Wang, M. S. Blok, H. Bernien, T. H. Taminiau, D. M. Toyli, D. A. Lidar, D. D. Awschalom, R. Hanson, and V. V. Dobrovitski, *Decoherence-protected quantum gates for a hybrid solid-state spin register,* Nature **484**, 82 (2012).

[18] L. Childress, M. V. Gurudev Dutt, J. M. Taylor, A. S. Zibrov, F. Jelezko, J. Wrachtrup, P. R. Hemmer, and M. D. Lukin, *Coherent Dynamics of Coupled Electron and Nuclear Spin Qubits in Diamond,* Science **314**, 281 (2006).

[19] C. E. Bradley, J. Randall, M. H. Abobeih, R. C. Berrevoets, M. J. Degen, M. A. Bakker, M. Markham, D. J. Twitchen, and T. H. Taminiau, *A Ten-Qubit Solid-State Spin Register with Quantum Memory up to One Minute,* Physical Review X **9**, 031045 (2019).

[20] G. L. Van De Stolpe, D. P. Kwiatkowski, C. E. Bradley, J. Randall, M. H. Abobeih, S. A. Breitweiser, L. C. Bassett, M. Markham, D. J. Twitchen, and T. H. Taminiau, *Mapping a 50-spin-qubit network through correlated sensing,* Nature Communications **15**, 2006 (2024).

[21] A. Reiserer, N. Kalb, M. S. Blok, K. J. M. Van Bemmelen, T. H. Taminiau, R. Hanson, D. J. Twitchen, and M. Markham, *Robust Quantum-Network Memory Using Decoherence-Protected Subspaces of Nuclear Spins,* Physical Review X **6**, 021040 (2016).

[22] C. E. Bradley, S. W. De Bone, P. F. W. Möller, S. Baier, M. J. Degen, S. J. H. Loenen, H. P. Bartling, M. Markham, D. J. Twitchen, R. Hanson, D. Elkouss, and T. H. Taminiau, *Robust quantum-network memory based on spin qubits in isotopically engineered diamond,* npj Quantum Information **8**, 122 (2022).

[23] H. P. Bartling, M. H. Abobeih, B. Pingault, M. J. Degen, S. J. H. Loenen, C. E. Bradley, J. Randall, M. Markham, D. J. Twitchen, and T. H. Taminiau, *Entanglement of Spin-Pair Qubits with Intrinsic Dephasing Times Exceeding a Minute,* Physical Review X **12**, 011048 (2022).

[24] T. H. Taminiau, J. Cramer, T. van der Sar, V. V. Dobrovitski, and R. Hanson, *Universal control and error correction in multi-qubit spin registers in diamond,* Nature Nanotechnology **9**, 171 (2014).

[25] N. Kalb, A. A. Reiserer, P. C. Humphreys, J. J. W. Bakermans, S. J. Kamerling, N. H. Nickerson, S. C. Benjamin, D. J. Twitchen, M. Markham, and R. Hanson, *Entanglement distillation between solid-state quantum network nodes,* Science **356**, 928 (2017).

[26] M. H. Abobeih, Y. Wang, J. Randall, S. J. H. Loenen, C. E. Bradley, M. Markham, D. J. Twitchen, B. M. Terhal, and T. H. Taminiau, *Fault-tolerant operation of a logical qubit in a diamond quantum processor,* Nature **606**, 884 (2022).

[27] H. Bartling, J. Yun, K. Schymik, M. Van Riggelen, L. Enthoven, H. Van Ommen, M. Babaie, F. Sebastiano, M. Markham, D. Twitchen, and T. Taminiau, *Universal high-fidelity quantum gates for spin qubits in diamond,* Physical Review Applied **23**, 034052 (2025).

[28] D. Riedel, I. Söllner, B. J. Shields, S. Starosielec, P. Appel, E. Neu, P. Maletinsky, and R. J. Warburton, *Deterministic Enhancement of Coherent Photon Generation from a Nitrogen-Vacancy Center in Ultrapure Diamond,* Physical Review X **7**, 031040 (2017).

[29] A. Faraon, C. Santori, Z. Huang, V. M. Acosta, and R. G. Beausoleil, *Coupling of Nitrogen-Vacancy Centers to Photonic Crystal Cavities in Monocrystalline Diamond,* Physical Review Letters **109**, 033604 (2012).

[30] T. Ishikawa, K.-M. C. Fu, C. Santori, V. M. Acosta, R. G. Beausoleil, H. Watanabe, S. Shikata, and K. M. Itoh, *Optical and Spin Coherence Properties of Nitrogen-Vacancy Centers Placed in a 100 nm Thick Isotopically Purified Diamond Layer,* Nano Letters **12**, 2083 (2012).

[31] I. Lekavicius, T. Oo, and H. Wang, *Diamond Lamb wave spin-mechanical resonators with optically coherent nitrogen vacancy centers,* Journal of Applied Physics **126**, 214301 (2019).

[32] T. Jung, J. Görlitz, B. Kambs, C. Pauly, N. Raatz, R. Nelz, E. Neu, A. M. Edmonds, M. Markham, F. Mücklich, J. Meijer, and C. Becher, *Spin measurements of NV centers coupled to a photonic crystal cavity,* APL Photonics **4**, 120803 (2019).

[33] J. P. Hadden, J. P. Harrison, A. C. Stanley-Clarke, L. Marseglia, Y.-L. D. Ho, B. R. Patton, J. L. O'Brien, and J. G. Rarity, *Strongly enhanced photon collection from diamond defect centers under microfabricated integrated solid immersion lenses,* Applied Physics Letters **97**, 241901 (2010).

[34] S. L. N. Hermans, M. Pompili, L. D. Santos Martins, A. R-P Montblanch, H. K. C. Beukers, S. Baier, J. Borregaard, and R. Hanson, *Entangling remote qubits using the single-photon protocol: an in-depth theoretical and experimental study,* New Journal of Physics **25**, 013011 (2023).

[35] B. Hensen, H. Bernien, A. E. Dréau, A. Reiserer, N. Kalb, M. S. Blok, J. Ruitenberg, R. F. L. Vermeulen, R. N. Schouten, C. Abellán, W. Amaya, V. Pruneri, M. W. Mitchell, M. Markham, D. J. Twitchen, D. Elkouss, S. Wehner, T. H. Taminiau, and R. Hanson, *Loophole-free Bell inequality violation using electron spins separated by 1.3 kilometres,* Nature **526**, 682 (2015).

[36] P. C. Humphreys, N. Kalb, J. P. J. Morits, R. N. Schouten, R. F. L. Vermeulen, D. J. Twitchen, M. Markham, and R. Hanson, *Deterministic delivery of remote entanglement on a quantum network,* Nature **558**, 268 (2018).

[37] K. J. Vahala, *Optical microcavities,* Nature **424**, 839 (2003).

[38] D. Hunger, T. Steinmetz, Y. Colombe, C. Deutsch, T. W. Hänsch, and J. Reichel, *A fiber Fabry–Perot cavity with high finesse,* New Journal of Physics **12**, 065038 (2010).

[39] M. Ruf, M. IJspeert, S. van Dam, N. de Jong, H. van den Berg, G. Evers, and R. Hanson, *Optically Coherent Nitrogen-Vacancy Centers in Micrometer-Thin Etched Diamond Membranes,* Nano Letters **19**, 3987 (2019).

[40] M. Ruf, M. Weaver, S. van Dam, and R. Hanson, *Resonant Excitation and Purcell Enhancement of Coherent Nitrogen-Vacancy Centers Coupled to a Fabry-Perot Microcavity,* Physical Review Applied **15**, 024049 (2021).

[41] Y. Herrmann, J. Fischer, S. Scheijen, C. F. J. Wolfs, J. M. Brevoord, C. Sauerzapf, L. G. C. Wienhoven, L. J. Feije, M. Eschen, M. Ruf, M. J. Weaver, and R. Hanson, *A low-temperature tunable microcavity featuring high passive stability and microwave integration,* AVS Quantum Science **6**, 041401 (2024).

[42] V. Yurgens, Y. Fontana, A. Corazza, B. J. Shields, P. Maletinsky, and R. J. Warburton, *Cavity-assisted resonance fluorescence from a nitrogen-vacancy center in diamond,* npj Quantum Information **10**, 112 (2024).

[43] S. Bogdanović, M. S. Z. Liddy, S. B. van Dam, L. C. Coenen, T. Fink, M. Lončar, and R. Hanson, *Robust nano-fabrication of an integrated platform for spin control in a tunable microcavity,* APL Photonics **2**, 126101 (2017).

[44] S. Bogdanović, S. B. van Dam, C. Bonato, L. C. Coenen, A.-M. J. Zwerver, B. Hensen, M. S. Z. Liddy, T. Fink, A. Reiserer, M. Lončar, and R. Hanson, *Design and low-temperature characterization of a tunable microcavity for diamond-based quantum networks,* Applied Physics Letters **110**, 171103 (2017).

[45] Y. Herrmann, J. Fischer, J. M. Brevoord, C. Sauerzapf, L. G. C. Wienhoven, L. J. Feije, M. Pasini, M. Eschen, M. Ruf, M. J. Weaver, and R. Hanson, *Coherent Coupling of a Diamond Tin-Vacancy Center to a Tunable Open Microcavity,* Physical Review X **14**, 041013 (2024).

[46] N. B. Manson, J. P. Harrison, and M. J. Sellars, *Nitrogen-vacancy center in diamond: Model of the electronic structure and associated dynamics,* Physical Review B **74**, 104303 (2006).

[47] M. L. Goldman, M. W. Doherty, A. Sipahigil, N. Y. Yao, S. D. Bennett, N. B. Manson, A. Kubanek, and M. D. Lukin, *State-selective intersystem crossing in nitrogen-vacancy centers,* Physical Review B **91**, 165201 (2015).

[48] L. Robledo, L. Childress, H. Bernien, B. Hensen, P. F. A. Alkemade, and R. Hanson, *High-fidelity projective read-out of a solid-state spin quantum register,* Nature **477**, 574 (2011).

[49] C. A. Ryan, J. S. Hodges, and D. G. Cory, *Robust Decoupling Techniques to Extend Quantum Coherence in Diamond,* Physical Review Letters **105**, 200402 (2010).

[50] W. Pfaff, B. J. Hensen, H. Bernien, S. B. van Dam, M. S. Blok, T. H. Taminiau, M. J. Tiggelman, R. N. Schouten, M. Markham, D. J. Twitchen, and R. Hanson, *Unconditional quantum teleportation between distant solid-state quantum bits,* Science **345**, 532 (2014).

[51] J. M. Brevoord, L. De Santis, T. Yamamoto, M. Pasini, N. Codreanu, T. Turan, H. K. Beukers, C. Waas, and R. Hanson, *Heralded initialization of charge state and optical-transition frequency of diamond tin-vacancy centers,* Physical Review Applied **21**, 054047 (2024).

[52] G. Bayer, R. Berghaus, S. Sachero, A. B. Filipovski, L. Antoniuk, N. Lettner, R. Waltrich, M. Klotz, P. Maier, V. Agafonov, and A. Kubanek, *Optical driving, spin initialization and readout of single SiV^- centers in a Fabry-Perot resonator,* Communications Physics **6**, 300 (2023).

[53] R. Zifkin, C. D. Rodríguez Rosenblueth, E. Janitz, Y. Fontana, and L. Childress, *Lifetime Reduction of Single Germanium-Vacancy Centers in Diamond via a Tunable Open Microcavity,* PRX Quantum **5**, 030308 (2024).

[54] J. Hessenauer, J. Körber, M. Ghezellou, J. Ul-Hassan, G. V. Astakhov, W. Knolle, J. Wrachtrup, and D. Hunger, *Cavity enhancement of V2 centers in 4H-SiC with a fiber-based Fabry–Perot microcavity,* Optica Quantum **3**, 175 (2025).

[55] A. Ulanowski, J. Früh, F. Salamon, A. Holzäpfel, and A. Reiserer, *Spectral Multiplexing of Rare-Earth Emitters in a Co-Doped Crystalline Membrane,* Advanced Optical Materials **12**, 2302897 (2024).

[56] J. Fischer, Y. Herrmann, C. F. J. Wolfs, S. Scheijen, M. Ruf, and R. Hanson, *Data underlying the publication "Spin-Photon Correlations from a Purcell-enhanced Diamond Nitrogen-Vacancy Center Coupled to an Open Microcavity",* 4TU.ResearchData (2025), https://doi.org/10.4121/6f8031ae-dd61-4b4f-adf4-d20bc88ed9ac.

[57] I. T. Raa, H. K. Ervasti, P. J. Botma, L. C. Visser, R. Budhrani, J. F. van Rantwijk, S. P. Cadot, J. Vermeltfoort, M. Pompili, A. J. Stolk, M. J. Weaver, K. L. van der Enden, D. de Leeuw Duarte, M. Teng, J. van Zwieten, and F. Grooteman, *QMI - Quantum Measurement Infrastructure, a Python 3 framework for controlling laboratory equipment,* 4TU.ResearchData (2023), https://data.4tu.nl/datasets/6d39c6db-2f50-4a49-ad60-5bb08f40cb52.

[58] R. F. L. Vermeulen, *Pulse generator and method for generating pulses,* (2020), https://research.tudelft.nl/en/publications/pulse-generator-and-method-for-generating-pulses.

[59] E. Janitz, M. Ruf, M. Dimock, A. Bourassa, J. Sankey, and L. Childress, *Fabry-Perot microcavity for diamond-based photonics,* Physical Review A **92**, 043844 (2015).

[60] S. B. van Dam, M. Ruf, and R. Hanson, *Optimal design of diamond-air microcavities for quantum networks using an analytical approach,* New Journal of Physics **20**, 115004 (2018).

[61] M. Pompili, *Multi-Node Quantum Networks with Diamond Qubits*, Ph.D. thesis, Delft University of Technology (2021).

8

Conclusion and Outlook

8.1 Summary of Results

This thesis investigates open microcavities as efficient spin-photon interfaces for nitrogen-vacancy (NV) and tin-vacancy (SnV) centers in diamond and explores their potential as next-generation quantum network nodes. Therefore, a cryogenic and a room temperature open microcavity setup as well as a novel patterning method for fabricating diamond membranes are developed. These developments form the basis for the quantum optics experiments with NV and SnV centers. The experimental results of this thesis are summarized in the following.

In Chapter 4, we report on the realization of a cryogenic open microcavity that reproducibly achieves low passive cavity length fluctuation levels around 25 pm over the complete cryostat cycle. This passive stability level is approximately a sixfold improvement over our previous implementation and enables advanced quantum optics experiments with diamond color centers. In this regard, microwave lines are added to the setup and used to drive the electron spin of a cavity-coupled NV center in optically detected magnetic resonance measurements.

In Chapter 5, we utilize laser-cutting as a novel patterning method for the fabrication of micrometer-thin diamond membranes for open microcavity applications. Diamond microdevices are successfully fabricated and bonded to dielectric mirrors, which are then mounted in our room temperature open microcavity setup to perform scanning cavity microscopy measurements. These measurements reveal the finesse and the cavity polarization mode splitting across the full diamond device. Finesse values measured in length of 9000 in air-like and 2000 in diamond-like modes are reached, which corresponds to additional scattering losses in diamond-like modes of about 390 ppm. With these finesse values, we predict Purcell factors of 30 for an air-like and 39 for a diamond-like mode. Finally, optically coherent SnV and NV centers in micrometer-thin diamond membranes are found with emitter linewidth measurements at cryogenic temperatures.

In Chapter 6, we demonstrate the coherent coupling of a single SnV center to our cryogenic

open microcavity. The SnV center is optically coupled with its C transition to the cavity, and emitter linewidth measurements with the cavity on and off resonance reveal a vibration-corrected coherent cooperativity of 0.69 ± 0.07. Accounting for the pure dephasing rate of the emitter leads to a vibration-corrected cooperativity of 1.7 ± 0.2. Using this quantity and a careful analysis of the cavity parameters, we can bound the product of the quantum efficiency and branching ratio to $\geq 0.64 \pm 0.06$ for the SnV center. In the final experiments, we study nonlinear quantum effects of the emitter-cavity system in the coherent coupling regime by probing the cavity transmission with a laser. We observe dips in the cavity transmission due to coherent interactions with the cavity-coupled SnV center, and changes in the photon statistics of the transmitted light, showing photon bunching.

In Chapter 7, we use a Purcell-enhanced NV center in our cryogenic open microcavity to generate spin-photon states and measure heralded correlations between the photonic and the spin qubit states. Through the Purcell effect and high cavity outcoupling, we achieve an efficient spin-photon interface, with a coherent photon detection efficiency of 0.5 % per resonant excitation pulse. Despite being limited by available laser power, this already represents an order of magnitude improvement compared to NV centers in state-of-the-art solid immersion lens devices. In addition, coherent control of the NV center electron spin is achieved using microwave pulses, which are used to investigate the spin qubit coherence in Ramsey and Hahn-Echo experiments. Ultimately, we combine the efficient optical interface with the coherent qubit control to play sequences for the generation of spin-photon Bell and Greenberger–Horne–Zeilinger states between the spin qubit and time-bin encoded photonic qubits. We herald the detection of the photonic qubits and observe their correlations with the spin qubit in the Z-basis.

8.2 Next Experiments with Nitrogen-Vacancy Centers

The proposed experiments and suggested improvements in the following subsections build on the results of Chapter 7.

8.2.1 Spin-Photon Entanglement

The generation of spin-photon entangled states is the basis for remote spin-spin entanglement generation. In Chapter 7, we show the efficient generation of spin-photon states with a microcavity-enhanced NV center and the observation of their correlations in the Z-basis. The determination of the spin-photon Bell state fidelity requires measuring correlations, which also entail qubit readouts in the X- and Y-basis. These measurements can be realized with a phase-stabilized imbalanced interferometer for the photonic time-bin qubits and phase-shifted microwave pulses for the spin qubit [1]. For that, implementing a charge-resonance (CR) check procedure [2, 3] is an enabling step, as it mitigates spectral diffusion and prepares the NV center to be on resonance with the readout laser. Both of which are important to achieve a high interference contrast for the photonic qubit readout. In addition, a CR check procedure can improve the initialization fidelity of the spin qubit as optical pumping is ensured. The capability of driving the NV center electron spin qubit with phase-shifted microwave pulses can be implemented using the hardware of Chapter 7.

However, fidelity improvements are desired, as they translate into the fidelity of the generated spin-photon entangled state as well. The application of microwave pulse shaping can drive the electron spin more uniformly, improving qubit control fidelity [4]. In addition, the cryostat's microwave delivery can be upgraded to enable higher Rabi frequencies and faster qubit control.

These improvements suggest the generation and verification of spin-photon Bell states with an end-to-end efficiency of up to 1.4 %. Furthermore, if additional cavity losses can be eliminated, an end-to-end efficiency of about 5 % can be reached. In addition, careful mode matching of the detection fiber coupling to the cavity mode, together with highly efficient superconducting nanowire single-photon detectors, can further improve the efficiency by a factor of ~ 3. Moreover, the increased end-to-end efficiency benefits qubit readout fidelity.

8.2.2 Remote Spin-Spin Entanglement

In addition to the improvements outlined in the previous section, a mechanism to tune multiple NV centers on resonance is desired for remote spin-spin entanglement generation. This has been realized via the DC Stark shift using gate electrodes [5, 6] and could be implemented similarly in open microcavity systems. The reachable end-to-end efficiencies of our system are two orders of magnitude higher than those of NV centers in state-of-the-art solid immersion lens devices. This improvement factor is proportional to the achievable remote entanglement generation rate for the single photon protocol [7] and squared proportional for the two photon protocol [2]. In this regime, the delivery of an on average entangled state can be deterministic in a quantum network [6] with a realistic number of 1000 entanglement generation attempts [8] and projected rates of hundreds of Hz. This would improve the active link efficiency above 1, which is a key enabling condition for scaling quantum networks [9].

For quantum network applications requiring memory qubits, carbon-13 nuclear spins in the environment of the NV center can be used. To realize robust memory qubits under remote entanglement generation attempts high magnetic fields are desired [10], which may necessitate mounting permanent magnets or coils close to the sample inside the cryostat.

8.3 Future Experiments and Research Directions

8.3.1 Optical Multiplexed Entanglement Generation

In open microcavity systems, multiple color centers can be coupled to the same cavity and hence addressed via the same optical mode. This enables the use of multiple color centers with different ZPL emission wavelengths at each quantum network node and multiplexed entanglement generation protocols [11]. Furthermore, piezoelectric actuators with demonstrated bandwidths up to 44 kHz [12] can be used to rapidly tune the cavity on resonance with different ZPL emission wavelengths. Moreover, each communication qubit can exhibit nuclear spins in the environment, which can be used as memory qubits and may enable further multiplexing.

8.3.2 Diamond-Air Microcavity Designs

Multiple research groups have reported the fabrication of high-quality micrometer-thin diamond membranes for open microcavities [13–15]. These diamond devices feature

very low surface roughness, which is characterized by low additional scattering losses in diamond-like modes. This development paves the way to operate microcavities in diamond-like modes, where the maximum attainable Purcell factor is about a factor of 5.8 higher than in air-like modes, considering cavity length fluctuations.

Furthermore, progress has been made on the fabrication of homogeneously flat diamond membranes with very low surface roughness [16, 17], thereby relaxing the requirement for open microcavity setups with large spatial tunability. This promises cavity designs with higher mechanical resonances and higher vibration stability. In addition, the footprint of microcavities can be as small as the 125 µm cavity fiber diameter, and fiber arrays could be used to scale to multiple microcavities per quantum network node [18]. Moreover, the direct coupling efficiency of the cavity mode into the cavity fiber can be improved by integrating mode-matching optics [19].

8.3.3 Heterogeneous Integration

For open microcavity applications, diamond membranes are typically bonded to flat dielectric Bragg mirrors, which are fabricated on top of fused silica substrates. These mirrors could be equipped with various electrical structures, such as microwave striplines [20], or potentially photonic structures, such as waveguides. Furthermore, intentional gaps between the diamond membrane and the mirror can be introduced to isolate these structures, which might also facilitate the bonding of larger membranes. Small gaps between the diamond membrane and the mirror of multiple $\lambda_0/2n_a$ leave the achievable Purcell enhancement almost unchanged. Moreover, buried striplines have recently been demonstrated with bonded diamond membranes [21].

8.3.4 Quantum Networking with Tin-Vacancy Centers

This section focuses on SnV centers in open microcavities and their potential for future quantum networks. The feature of the SnV center to preserve good optical coherence in very thin diamond membranes [22] allows to boost the coherent cooperativity in microcavities by operating at very short cavity lengths and *ROC* of a few μm [23, 24]. This can enable cooperativities for SnV centers in open microcavities above one hundred. In addition, SnV centers in thin diamond membranes, featuring uniform tensile strain, have been used to demonstrate coherent microwave qubit control at temperatures of up to 4 K [22]. Similar diamond devices might be compatible with open microcavities and could be used to explore different entanglement protocols that utilize spin-dependent amplitude [25, 26] or phase [27] reflection.

Moreover, micro-electro-mechanically mediated strain control has shown to tune the optical transitions of SnV centers in waveguides [28]. This technique could be adapted to the microcavity platform by using waveguide-like diamond structures with dimensions larger than the cavity beam diameter, which are bonded to the mirror surface with an intentional gap. Figure 8.1 shows a schematic of a cavity sample mirror featuring structures to apply strain as well as microwave and static electric signals to a microcavity-coupled diamond color center. This design underlines the potential of heterogeneous integration and could be realized via transfer printing [29].

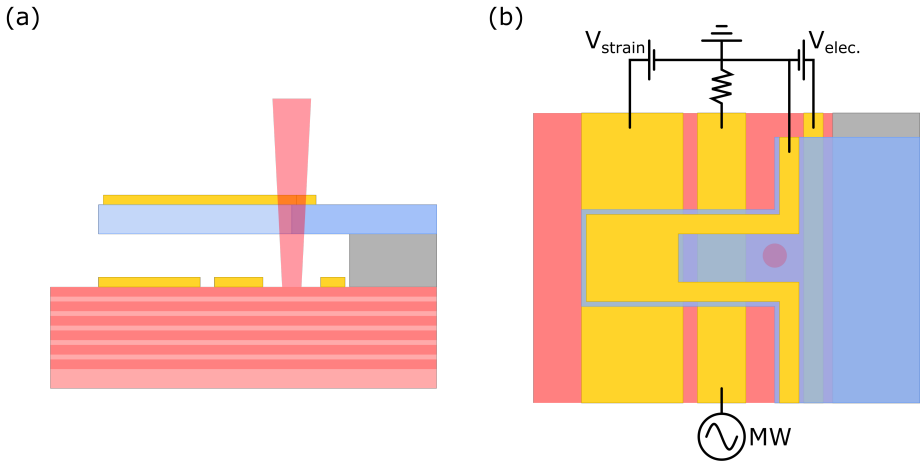

Figure 8.1: Schematic cavity sample mirror featuring strain, electric field, and microwave application. (a) Shows a cross-section and (b) the top view, next to an exemplary electronic circuit delivering the control voltages. On top of the sample mirror (light red layers), three electrical lines (yellow) and a spacer (gray) are depicted. The latter holds the diamond membrane and introduces a gap between the sample mirror surface and the membrane. On top of the diamond membrane, another electric line is deposited to apply micro-electro-mechanical strain via capacitive forces to the corresponding electric line on the sample mirror. The two other electrical lines are for the delivery of microwave signals and the application of static electric fields. The lateral cavity position, close to the hinge point of the diamond membrane lever, is indicated with a red cone-shaped cavity mode.

8.4 Epilogue

The bare data acquisition time for the results presented in this thesis amounts to a few days. It takes measurement phases of several weeks to record these final datasets. And none of that is possible without building and preparing measurement setups for many months. Figure 8.2 visualizes this journey with documented timelines of my PhD categorized by thesis chapters. In addition, the cryostat temperature is monitored to present its operational status.

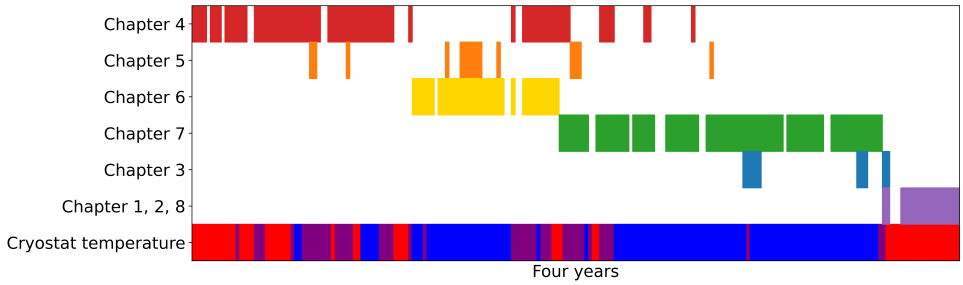

Figure 8.2: Timelines of my PhD categorized by thesis chapters. The cryostat temperature is shown in red when at room temperature, in blue when at base temperature, and in purple when temperature cycled.

There are just a few chapters, but a whole journey to celebrate.

References

[1] A. Tchebotareva, S. L. N. Hermans, P. C. Humphreys, D. Voigt, P. J. Harmsma, L. K. Cheng, A. L. Verlaan, N. Dijkhuizen, W. de Jong, A. Dréau, and R. Hanson, *Entanglement between a Diamond Spin Qubit and a Photonic Time-Bin Qubit at Telecom Wavelength,* Physical Review Letters **123**, 063601 (2019).

[2] H. Bernien, B. Hensen, W. Pfaff, G. Koolstra, M. S. Blok, L. Robledo, T. H. Taminiau, M. Markham, D. J. Twitchen, L. Childress, and R. Hanson, *Heralded entanglement between solid-state qubits separated by three metres,* Nature **497**, 86 (2013).

[3] J. M. Brevoord, L. De Santis, T. Yamamoto, M. Pasini, N. Codreanu, T. Turan, H. K. Beukers, C. Waas, and R. Hanson, *Heralded initialization of charge state and optical-transition frequency of diamond tin-vacancy centers,* Physical Review Applied **21**, 054047 (2024).

[4] H. Bartling, J. Yun, K. Schymik, M. Van Riggelen, L. Enthoven, H. Van Ommen, M. Babaie, F. Sebastiano, M. Markham, D. Twitchen, and T. Taminiau, *Universal high-fidelity quantum gates for spin qubits in diamond,* Physical Review Applied **23**, 034052 (2025).

[5] P. Tamarat, T. Gaebel, J. R. Rabeau, M. Khan, A. D. Greentree, H. Wilson, L. C. L. Hollenberg, S. Prawer, P. Hemmer, F. Jelezko, and J. Wrachtrup, *Stark Shift Control of Single Optical Centers in Diamond,* Physical Review Letters **97**, 083002 (2006).

[6] M. Pompili, S. L. N. Hermans, S. Baier, H. K. C. Beukers, P. C. Humphreys, R. N. Schouten, R. F. L. Vermeulen, M. J. Tiggelman, L. dos Santos Martins, B. Dirkse, S. Wehner, and R. Hanson, *Realization of a multinode quantum network of remote solid-state qubits,* Science **372**, 259 (2021).

[7] P. C. Humphreys, N. Kalb, J. P. J. Morits, R. N. Schouten, R. F. L. Vermeulen, D. J. Twitchen, M. Markham, and R. Hanson, *Deterministic delivery of remote entanglement on a quantum network,* Nature **558**, 268 (2018).

[8] S. L. N. Hermans, M. Pompili, H. K. C. Beukers, S. Baier, J. Borregaard, and R. Hanson, *Qubit teleportation between non-neighbouring nodes in a quantum network,* Nature **605**, 663 (2022).

[9] C. E. Bradley, S. W. De Bone, P. F. W. Möller, S. Baier, M. J. Degen, S. J. H. Loenen, H. P. Bartling, M. Markham, D. J. Twitchen, R. Hanson, D. Elkouss, and T. H. Taminiau, *Robust quantum-network memory based on spin qubits in isotopically engineered diamond,* npj Quantum Information **8**, 122 (2022).

[10] M. Pompili, *Multi-Node Quantum Networks with Diamond Qubits*, Ph.D. thesis, Delft University of Technology (2021).

[11] A. Ruskuc, C.-J. Wu, E. Green, S. L. N. Hermans, W. Pajak, J. Choi, and A. Faraon, *Multiplexed entanglement of multi-emitter quantum network nodes,* Nature **639**, 54 (2025).

[12] E. Janitz, M. Ruf, Y. Fontana, J. Sankey, and L. Childress, *High mechanical bandwidth fiber-coupled Fabry-Perot cavity,* Optics Express **25**, 20932 (2017).

[13] S. Bogdanović, S. B. van Dam, C. Bonato, L. C. Coenen, A.-M. J. Zwerver, B. Hensen, M. S. Z. Liddy, T. Fink, A. Reiserer, M. Lončar, and R. Hanson, *Design and low-temperature characterization of a tunable microcavity for diamond-based quantum networks,* Applied Physics Letters **110**, 171103 (2017).

[14] S. Flågan, D. Riedel, A. Javadi, T. Jakubczyk, P. Maletinsky, and R. J. Warburton, *A diamond-confined open microcavity featuring a high quality-factor and a small mode-volume,* Journal of Applied Physics **131**, 113102 (2022).

[15] J. Körber, M. Pallmann, J. Heupel, R. Stöhr, E. Vasilenko, T. Hümmer, L. Kohler, C. Popov, and D. Hunger, *Scanning Cavity Microscopy of a Single-Crystal Diamond Membrane,* Physical Review Applied **19**, 064057 (2023).

[16] X. Guo, M. Xie, A. Addhya, A. Linder, U. Zvi, S. Wang, X. Yu, T. D. Deshmukh, Y. Liu, I. N. Hammock, Z. Li, C. T. DeVault, A. Butcher, A. P. Esser-Kahn, D. D. Awschalom, N. Delegan, P. C. Maurer, F. J. Heremans, and A. A. High, *Direct-bonded diamond membranes for heterogeneous quantum and electronic technologies,* Nature Communications **15**, 8788 (2024).

[17] A. Corazza, S. Ruffieux, Y. Zhu, C. A. Jaramillo Concha, Y. Fontana, C. Galland, R. J. Warburton, and P. Maletinsky, *Homogeneous Free-Standing Nanostructures from Bulk Diamond over Millimeter Scales for Quantum Technologies,* Nano Letters **25**, 14526 (2025).

[18] C. Derntl, M. Schneider, J. Schalko, A. Bittner, J. Schmiedmayer, U. Schmid, and M. Trupke, *Arrays of open, independently tunable microcavities,* Optics Express **22**, 22111 (2014).

[19] G. K. Gulati, H. Takahashi, N. Podoliak, P. Horak, and M. Keller, *Fiber cavities with integrated mode matching optics,* Scientific Reports **7**, 5556 (2017).

[20] S. Bogdanović, M. S. Z. Liddy, S. B. van Dam, L. C. Coenen, T. Fink, M. Lončar, and R. Hanson, *Robust nano-fabrication of an integrated platform for spin control in a tunable microcavity,* APL Photonics **2**, 126101 (2017).

[21] D. Riedel, T. Graziosi, Z. Wang, C. De-Eknamkul, A. Abulnaga, J. Dietz, A. Mucchietto, M. Haas, M. Sutula, P. Barral, M. Pompili, C. Robens, J. Ha, D. Sukachev, D. Levonian, M. Bhaskar, M. Markham, and B. Machielse, *A scalable photonic quantum interconnect platform,* arXiv:2508.06675 (2025), `https://arxiv.org/abs/2508.06675`.

[22] X. Guo, A. M. Stramma, Z. Li, W. G. Roth, B. Huang, Y. Jin, R. A. Parker, J. Arjona Martínez, N. Shofer, C. P. Michaels, C. P. Purser, M. H. Appel, E. M. Alexeev, T. Liu, A. C. Ferrari, D. D. Awschalom, N. Delegan, B. Pingault, G. Galli, F. J. Heremans, M. Atatüre, and A. A. High, *Microwave-Based Quantum Control and Coherence Protection of Tin-Vacancy Spin Qubits in a Strain-Tuned Diamond-Membrane Heterostructure,* Physical Review X **13**, 041037 (2023).

[23] A. A. P. Trichet, P. R. Dolan, D. M. Coles, G. M. Hughes, and J. M. Smith, *Topographic control of open-access microcavities at the nanometer scale,* Optics Express **23**, 17205 (2015).

[24] D. Najer, M. Renggli, D. Riedel, S. Starosielec, and R. J. Warburton, *Fabrication of mirror templates in silica with micron-sized radii of curvature,* Applied Physics Letters **110**, 011101 (2017).

[25] C. M. Knaut, A. Suleymanzade, Y.-C. Wei, D. R. Assumpcao, P.-J. Stas, Y. Q. Huan, B. Machielse, E. N. Knall, M. Sutula, G. Baranes, N. Sinclair, C. De-Eknamkul, D. S. Levonian, M. K. Bhaskar, H. Park, M. Lončar, and M. D. Lukin, *Entanglement of nanophotonic quantum memory nodes in a telecom network,* Nature **629**, 573 (2024).

[26] P.-J. Stas, Y.-C. Wei, M. Sirotin, Y. Q. Huan, U. Yazlar, F. A. Arias, E. Knyazev, G. Baranes, B. Machielse, S. Grandi, D. Riedel, J. Borregaard, H. Park, M. Lončar, A. Suleymanzade, and M. D. Lukin, *Entanglement Assisted Non-local Optical Interferometry in a Quantum Network,* arXiv:2509.09464 (2025), `https://arxiv.org/abs/2509.09464`.

[27] S. Daiss, S. Langenfeld, S. Welte, E. Distante, P. Thomas, L. Hartung, O. Morin, and G. Rempe, *A quantum-logic gate between distant quantum-network modules,* Science **371**, 614 (2021).

[28] J. M. Brevoord, L. G. C. Wienhoven, N. Codreanu, T. Ishiguro, E. van Leeuwen, M. Iuliano, L. De Santis, C. Waas, H. K. C. Beukers, T. Turan, C. Errando-Herranz, K. Kawaguchi, and R. Hanson, *Large-range tuning and stabilization of the optical transition of diamond tin-vacancy centers by in situ strain control,* Applied Physics Letters **126**, 174001 (2025).

[29] J. A. Smith, D. Jevtics, B. Guilhabert, M. D. Dawson, and M. J. Strain, *Hybrid integration of chipscale photonic devices using accurate transfer printing methods,* Applied Physics Reviews **9**, 041317 (2022).

Acknowledgments

The last four years have been a fantastic journey, during which many people supported me in various ways. On the following pages, I try to express my gratitude, although it is difficult to put into words.

Ronald, thank you for giving me the opportunity to do my PhD with you! You are an excellent scientist and supervisor, and with your clear vision you have created a truly special team. I am very happy to be in this environment, where I have grown as a researcher and had a lot of fun with a fantastic group of people. In addition, I want to thank you for your great support in presenting our results at conferences and for connecting with the scientific community during various trips. I am very grateful for the PhD time and excited to see the results of your future endeavors! I wish you all the best! **Tim**, thank you for taking over my co-supervision. Your fascination about spin systems is truly inspiring! I learned a lot about spins and their control in the networks meetings, which helped me a lot to set up the microwave control in the microcavity setup. I am looking forward to the advances your group will make! **Alexander Kubanek**, thank you very much for hosting us on our cavity tour through Germany and for the opportunity to visit your labs and share our research! I look forward to all the great research on open microcavities that your group will conduct! **Stefanie Barz**, thank you for sparking the excitement about quantum technologies in your Hauptseminar, which I very much enjoyed following in my master's studies. Further, it was great to visit your labs on our way from Delft to the DPG SAMOP conference in Freiburg! **Sander Otte**, you followed the open microcavity efforts through some defenses of our bachelor students, which was always a great opportunity to discuss the project. In addition, it was great to visit your labs, which left me amazed by the stability of cryogenic STMs. **Massimiliano Rossi**, it is exciting to see a new lab starting at TU Delft working on macroscopic quantum mechanics. Good luck making quantum systems larger in mass and size! Thank you all for taking the time to be on my committee!

I want to thank my two paranymphs and very good friends for their great support during my PhD. **Yanik**, you welcomed me warmly to a new, well-organized lab, making my start a smooth ride! Quickly, we became "The Cavity Boys" and good friends, on the mission to build cavity-enhanced quantum network nodes. What followed were many exciting moments in the lab and wonderful trips to conferences, summer schools, and research groups. Thanks for sharing so much fun time with me! I will miss the "good coffees", "boosters", and evenings at Proeflokaal! I wish you all the best for your next step and hope our paths keep crossing! **Chris**, we were working on different projects and bonded over our passion for volleyball. Having you in the team is always a win, and playing the Beach Competitions was a blast! I also want to thank you for our many bike ride chats! You are a great listener and sharp thinker, always understanding my struggles and helping to sort my thoughts. I wish you all the best in München and look forward to visiting you there!

Next, I want to thank the cavity team, who supported me in so many ways and made working on my PhD so much fun! **Julia**, with your fabrication expertise, you quickly brought our master's student Colin up to speed. I learned a lot from you, and it is great how you keep an open ear and eye for your colleagues! Thanks for introducing me to all the Dutch culture, like De Dijk and TT Basse! It was also always a great time going to conferences and road trips with you! Good luck with your next big step! **Laurens**, you were still around as a research assistant in the cavity team when I started my PhD. Thanks for introducing me to the art of gluing cavity fibers and for training me on the setup in the calm, quiet early January! It was always a lot of fun having you around, and it is impressive how fast you set up a new lab during your PhD! Good luck with your final bits! **Colin**, I was just a few months into my PhD when you applied for a master's project with us, and it did not take long to figure out that you are a great fit! Co-supervised by Julia, you ramped up the diamond device fabrication and characterization in no time. Thanks for this significant contribution! It was a lot of fun having you around and exploring the Netherlands with you! Good luck with your PhD in Stuttgart! **Leo**, joining the cavity team for your bachelor's project was the start of a long career in Team Diamond. It is incredible how you strengthen the team in so many scientific aspects and beyond — your sprinting skills are impressive! Thanks for the fantastic time in the US, especially for all the extensive breakfasts at Denny's! Good luck with your PhD! **Boris**, you did your bachelor's project at the same time as Leo and built a full confocal microscopy setup to measure a very nice antibunching dip! Thanks for setting this up for the practicum! It is great to see you doing a PhD now as well! **Yuran**, I could not have wished for a better bachelor student for this project! Your dedication and precision when building the microcavity setup are unmatched! It was a great achievement of you to conduct the first automated device scans, paving the way for a scientific publication. Good luck with your master's! **Cees**, at the beginning of your master's project, a lot of new equipment needed to be set up, and it did not take long until you made the AWG your own. With your excellent programming and scientific skills, you advanced into unexplored domains and laid the groundwork for our optical and microwave qubit control. It was a lot of fun to work with such a quick learner as you are! Good luck with your professional software endeavors! **Stijn**, you started your master's project in the cavity team and turned into a key member as a research assistant. You became the fiber whisperer and grew into an independent researcher, bringing our device characterization to the next level! Thanks for sharing your passion for kapsalon, BBQ, and carnaval - it was a lot of fun! Good luck with your PhD in Eindhoven! **Matteo Jr.**, you were the expert on SnV centers in the cavity team, and my go-to for any question about their coupling to cavities and waveguides. Thanks for all the relaxed and always constructive discussions! Have fun at ICFO!

I want to extend my thanks to you, **Nina**, for taking me into the cleanroom and showing me all the machines you mastered in your research! It was great to have such a knowledgeable person around whom we could always consult regarding our microcavity device fabrication. It was a lot of fun being on a road trip with you and sharing offices! Good luck with your future endeavors! **Max**, thanks for welcoming me to Delft, although you already graduated! It was a lot of fun brewing beer and having some self-made Pizza! **Max**, **Suzanne**, **Stefan**, plus all the students and postdocs, thanks for all the hard work you put into the project before my PhD! Without your contributions, the results of this

thesis would not have been possible!

Moreover, I want to thank you, **Johannes**, for the co-supervision at the beginning of my PhD! You were always happy to discuss cQED systems and brought a great theoretical perspective to the mix. It was also fun TAing your quantum hardware course! Good luck in the US!

I was about halfway in my PhD when I joined the networks team, and I am very grateful for everything I learned from you! **MG**, thanks for your warm welcome to the team! It was great to work with you - the person who can actually make entanglement! I learned a lot from you and really enjoyed the evenings at Proefi and the road trips abroad! Thank you also for all the social events you were organizing! All the best in München! **Nic**, thanks for introducing me to your fascinating research about very coherent qubits! You are a very pleasant person, and I really enjoyed our chats! Good luck finishing your PhD! **Ben**, you are a very sharp thinker and always willing to help! Thanks a lot for supporting us with the RT2 measurements and for keeping Grafana up and running! Good luck with the final steps of your PhD! **Jiwon**, you are always approachable and happy to explain! Thanks for all our discussions on NV centers and their nuclear spin control. It was a lot of fun exploring Amsterdam during King's Day with you! **Alejandro**, thanks for introducing me to the network setup and all the fun! Thanks also to **Sophie**, **Matteo Sr.**, and **Hans** for setting up these impressive setups! And **Sophie**, good luck with your own research group in Delft!

A big thanks also to everyone who was working on "the other side of the curtain"! **Chris**, **Hans**, it was impressive to see you turning an empty lab into a fully functional optical cryostat setup. Thanks also for sharing the, at that point in time, probably most valuable resource - the new 619 nm laser - with us! **Hans**, you are a great person to bounce ideas with! Your sharp questions always help to understand, reflect, and learn from conversations. Thanks also for organizing the amazing sailing trip, and good luck at ETH! **Alex**, it was great to see a postdoc with so much knowledge, I readily made use, joining the team! Thanks for all your critical proofreading and feedback! **Timo**, it is great to see you continuing in the Hanson Lab! Thanks for all the event organization you already take over. Good luck with your PhD! And thank you all for making working in F-14 so much fun!

In addition, I was surrounded by many amazing people in the Hanson Lab, that worked on other projects and in different labs! **Arian**, you have the answer to every question! I really appreciate your willingness to always help and your genuine interest in how things are going! Thanks for all the great chats and beers at tpkv! I really enjoyed the road trip in the US with you! Good luck with your next endeavor! **Kian**, with your humorous nature, you make any conversation fun! Thanks for the great road trip in the US and for sharing your excitement about Bass Pro Shops with us! Thanks also for carrying the basketball match at the Diamond Cup and good luck with your new endeavor in Canada! **Christian**, you are the first Team Diamond member exploring silicon! And I am certain you will do great! It is always a lot of fun spending time with you and having a chat "over de belangrijke dingen van het leven - stopcontacten!". Good luck with your PhD! **Tim**, it was great to see the SnV results coming in from the small cavities! And it was a lot of fun rebuilding the setup and learning about waveguides from you! Good luck with your new setup! **Dani**, if you are around, there is always energy and joy! I really enjoyed all our discussions about cQED and sharing the office with you! And sorry again for roasting you,

but dude, five APDs! **Niv**, it was a lot of fun discussing theory and later also experimental work with! Your excitement about building quantum networks and all its smaller bits really added to the joy! I am sure you will do great in the lab as well! **Lorenzo**, you are one of our very experienced postdocs! Thanks for always taking the time for my questions! Good luck with your research at CNRS! **MC**, thanks for the great "Deutscher Abend" that you hosted at your beautiful place! And sorry **Josh**, that my German pronunciation made it hard for you to follow. All the best to you in Vienna!

During my time, Team Diamond continued to grow in the number of people and research groups, and even beyond diamond. Thanks to all the TimTams that I had the chance to meet! **Conor**, we just briefly met before you went to the US, and it is great to see you back in Delft! Thank you for sharing your experience and code on multi-tone driving with us! **Kai-Niklas**, thank you for sharing your insights about nuclear spin coherence measurements! It was a great time in Freiburg with you! **Hans**, you are the one and only ball-throwing champion! Good luck at TNO! **Sjoerd**, it was fantastic to establish the Diamond Cup with you! While you are very competitive on the field, I also really appreciate all our social interaction off the field. **Guido**, thanks for organizing the Diamond Cup with us - it was a blast! And thank you very much for showing us Stanford and its surroundings! **Anta**, it was great seeing you join Team Diamond and having you around a bit longer. Good luck at ICFO! **Christina**, I am very impressed by your research and the number of spins you control! Good luck with the measurements! **Margriet**, with a bright smile, you always share your excitement for NVs and GST! Keep that up, and you will do an excellent PhD! **Gerben**, it is impressive to see your fab developing and producing excellent results! I really enjoyed discussing cavities with you! Good luck with your PhD! **Jasper**, with you, another great force has joined the SiC project. Congratulations on your GO! **Tobi**, great to see you continuing at QuTech and building up a new setup! Good luck with your PhD! **Madhu**, utilizing nuclear spins is your thing, good luck doing quantum simulations! **Dan**, with your experience you are certainly strengthening the team! Good luck with your postdoc!

Thanks also to everyone from the Carlos Lab! **Carlos**, it was great meeting you at the March Meeting and then seeing you building up your research group in Delft. **Jan**, you are one of the most energetic people I know! It is great to see how this fuels your enthusiasm about building optical setups and organizing social events! Thanks for all the after-work activities and your introduction to Eierbacken! **Elena**, you are another great addition to the photonic integration efforts! Good luck with your PhD! **Matteo Jr. Jr.**, thanks for organizing the Diamond Cup with us! It was fun, and good luck with your PhD! **Lin**, it was great seeing your rapid ramp-up in Delft, and congratulations on your fellowship! I am sure you will do great! **Vicky**, hosted by the Carlos lab at the end, but office mates from day one! I really enjoyed our office conversations, especially those that began with a seemingly random question. Thanks for the great time, and keep up your excitement for satellites! Good luck in Spain!

A PhD is not nearly as much fun without all the students and interns who join for their projects. Thanks to all of you! **Sezer**, **Sarel**, **Otmar**, **Tijmen**, **Caroline**, **Adrià**, **Zarije**, **Elvis**, **Pepjin**, **Joan**, **Thomas**, **Constantijn**, **Miguel**, **Alexandre**, **Valentino**, **Sara**, **Rana**, **Charlotte**, **Noé**, **Kilian**, **Mark**, **Bram**, **Leanne**, **Jonas**, **August**, **Brian**, **Marta**.

QuTech would not be the same without all its social events. Among those, it was great

fun to organize the yearly QID Beach Day with a fantastic team. **Shannon**, **Sara**, **Sjoerd**, **Vicky**, **Thomas**, **Maurice**, **Francisco**, **Christian**, **Jan**, **Matteo**, **Niv**, **Tim**, thanks for repeatedly making the Beach Day such a great event!

QuTech is a very special place, especially because of our amazing staff! **Nico Alberts**, **Tim Hiep**, thanks for machining all our special cavity parts! **Siebe Visser**, **Vinod Narain**, **Roy Schoonenboom**, **Jelle Haanstra**, thanks for supporting us with our various needs in the lab. **Olaf Benningshof**, **Jason Mensingh**, **Tom Orton**, **Erik van der Wiel**, thanks for teaching me all the dos and don'ts in a cryogenic environment! **Raymond Schouten**, **Raymond Vermeulen**, **Roy Birnholtz**, **Berend Otto**, thanks for all the custom electronics and answering all my naive questions! **Henri Ervasti**, **Pieter Botma**, **Ravi Budhrani**, **Ingmar te Raa-Derckx**, thanks for providing this excellent software infrastructure! Without you, our experiments would not run nearly as smoothly! **Hitham Mahmoud Amin**, **Régis Méjard**, thanks for providing us with training and keeping our labs safe! **Sara Bedin**, **Esther Kruithof**, **Chantal Smith**, **Shannon de Groot-Finch**, thanks for making the administration so smooth for us! **Erik van den Biggelaar**, **Milan Verbrugge**, **Arthur Newton**, thank you for communicating our scientific results and advising us on our research data.

I very much acknowledge the support of our TNO colleagues on the cavity project. **Martin Eschen**, thanks for developing the laser-ablating process and shooting fibers for us! **Nick de Jong**, **Zahra Sadre Momtaz**, thanks for your help on the device fabrication!

I want to extend my thanks to **Bart van Bree** and **Huub Janssen** from JPE for the help on tackling the cavity vibrations, **Robert Janz** from Quantum Design for making sure the HILA runs without squeaking, and **Tobias Groß** from Laseroptik for all your expertise on mirror coatings.

I also thank my daily bachelor's and master's project supervisors, who introduced me to the exciting world of experimental quantum optics and supported me in starting a PhD. **Hüseyin**, thanks for your trust in starting the exploration of Rubidium vapor with me. You sparked my excitement for quantum optics, and I will never forget the time we spent in the lab performing manual spectroscopy scans! **Cornelius**, thanks for the freedom I had developing the optics to explore telecom quantum dots with you. I learned a lot from your structured, precise approach to work and had a lot of fun playing table football with you!

Moving to the Netherlands meant stopping Indiaca training. Luckily, I found an amazing volleyball team that included me right away and provided me with a great sporty and Dutch diversion. **Michiel**, **Martijn**, **Maarten**, **Cas**, **Alex**, **Xin**, **Bram**, **Chris**, **Amin**, **Tristan**, **Ioannis**, **Joost**, **Stach**, **Arik**, **Arjan**, **Myrthe**, **Vera**, **Leandra**, **Jens**, heel erg bedankt!

Ich möchte mich auch bei all denen bedanken die mich aus der Ferne unterstützt haben! Zunächst bei **Jojo**, **Jonas**, **Lukas** und **Felix** aus meiner alten WG. Danke, dass ich bei meinen Besuchen im Ländle jederzeit bei euch willkommen bin! Zudem bedanke ich mich bei meinen weiteren Wegbegleiter aus dem Studium **Manu**, **Rapha**, **Fabio**, **Luana**, **Aileen** und **Martin**. Danke für die Zoooooom calls und das persönliche Quatschen über die gute alte Studienzeit! Außerdem bin ich sehr dankbar für meine Schulfreunde **Dominic**, **Alex**, **Thomas**, **Steffen**, **Elia** und **Joshua**, die mich schon lange treu begleiten. Danke für die vielen tollen Feste und entspannten Zusammenkünfte! Indiaca ist noch stehts ein Bestandteil meiner Freizeit dank meinen CIND Leuten **Fabi**, **Timo**, **Achim** mit **CVJM Naila**, **Jule**, **Max**, **Steffen**, **Janina**, **Katha** und **Simon**. Danke für die coole Zeit, die wir

online, auf und neben dem Spielfeld verbringen!

Ich bedanke mich auch bei meiner Familie für die großartige Unterstützung über die vielen Jahre! **Matthias**, **Micha**, **Lilly** und **Lasse** mit eurem Besuch in Delft habt ihr euch hier für einen besonderen Platz qualifiziert! Danke für die gemeinsame Zeit! **Oma**, danke, dass sich ein Besuch bei dir immer wie Urlaub anfühlt! Zudem bin ich sehr dankbar für meine Geschwister **Miriam** mit **Martin**, **Tim** und **Felix**, **Moritz** und **Rafael**. Danke, dass ihr mich von klein auf begleitet und unterstützt! Und mein größter Dank gilt meinen Eltern. **Mama** und **Papa**, danke, dass ihr immer für mich da seid und mich bei allem unterstützt!

List of Publications

9. **J. Fischer***, Y. Herrmann*, C. F. J. Wolfs, S. Scheijen, M. Ruf, and R. Hanson, *Spin-photon correlations from a Purcell-enhanced diamond nitrogen-vacancy center coupled to an open microcavity*, Nature Communications **16**, 11680 (2025).

8. Y. Herrmann*, J. M. Brevoord*, **J. Fischer***, S. Scheijen, C. Sauerzapf, N. Codreanu, L. G. C. Wienhoven, Y. M. Q. van der Graaf, C. F. J. Wolfs, R. Méjard, M. Ruf, N. de Jong, and R. Hanson, *Laser-cut Patterned, Micrometer-thin Diamond Membranes with Coherent Color Centers for Open Microcavities*, Materials for Quantum Technology **5**, 035001 (2025).

7. C. D. Donne*, M. Iuliano*, B. van der Vecht*, G. M. Ferreira, H. Jirovská, T. J. W. van der Steenhoven, A. Dahlberg, M. Skrzypczyk, D. Fioretto, M. Teller, P. Filippov, A. R.-P. Montblanch, **J. Fischer**, B. van Ommen, N. Demetriou, D. Leichtle, L. Music, H. Ollivier, I. te Raa, W. Kozlowski, T. H. Taminiau, P. Pawełczak, T. E. Northup, R. Hanson, and S. Wehner, *Design and demonstration of an operating system for executing applications on quantum network nodes*, Nature **639**, 321-328 (2025).

6. Y. Herrmann*, **J. Fischer***, S. Scheijen, C. F. J. Wolfs, J. M. Brevoord, C. Sauerzapf, L. G. C. Wienhoven, L. J. Feije, M. Eschen, M. Ruf, M. J. Weaver, and R. Hanson, *A Low-Temperature Tunable Microcavity featuring High Passive Stability and Microwave Integration*, AVS Quantum Science **6**, 041401 (2024).

5. Y. Herrmann*, **J. Fischer***, J. M. Brevoord, C. Sauerzapf, L. G. C. Wienhoven, L. J. Feije, M. Pasini, M. Eschen, M. Ruf, M. J. Weaver, and R. Hanson, *Coherent Coupling of a Diamond Tin-Vacancy Center to a Tunable Open Microcavity*, Physical Review X **14**, 041013 (2024).

4. C. Nawrath*, R. Joos*, S. Kolatschek, S. Bauer, P. Pruy, F. Hornung, **J. Fischer**, J. Huang, P. Vijayan, R. Sittig, M. Jetter, S. L. Portalupi, and P. Michler, *Bright Source of Purcell-Enhanced, Triggered, Single Photons in the Telecom C-Band*, Advanced Quantum Technologies **6**, 2300111 (2023).

3. S. Bauer, D. Wang, N. Hoppe, C. Nawrath, **J. Fischer**, N. Witz, M. Kaschel, C. Schweikert, M. Jetter, S. L. Portalupi, M. Berroth, and P. Michler, *Achieving stable fiber coupling of quantum dot telecom C-band single-photons to an SOI photonic device*, Applied Physics Letters **119**, 211101 (2021).

2. S. Kolatschek*, C. Nawrath*, S. Bauer*, J. Huang, **J. Fischer**, R. Sittig, M. Jetter, S. L. Portalupi, and P. Michler, *Bright Purcell Enhanced Single-Photon Source in the Telecom O-Band Based on a Quantum Dot in a Circular Bragg Grating*, Nano Letters **21**, 7740-7745 (2021).

1. C. Nawrath, H. Vural, **J. Fischer**, R. Schaber, S. L. Portalupi, M. Jetter, and P. Michler, *Resonance fluorescence of single In(Ga)As quantum dots emitting in the telecom C-band*, Applied Physics Letters **118**, 244002 (2021).

Included in this thesis.

* Equally contributed authors.

Curriculum Vitæ

Julius Fischer

2021 – 2026	Ph.D. in Physics, *Technische Universiteit Delft* Thesis: *"Diamond Quantum Network Nodes with Open Microcavities"* Promotor: Prof. dr. ir. Ronald Hanson Copromotor: Dr. ir. Tim Taminiau Delft, The Netherlands
2019 – 2021	M.Sc. in Physics, *Universität Stuttgart* Thesis: *"Investigation of non-classical states of light from (quasi-)resonantly excited InAs/In(Ga)As quantum dots emitting in the telecom wavelength regime"* Advisor: Prof. dr. Peter Michler Stuttgart, Germany
2016 – 2019	B.Sc. in Physics, *Universität Stuttgart* Thesis: *"Two-photon spectroscopy of Rubidium vapor for an atom-quantum dot interface at telecom wavelengths"* Advisor: Prof. dr. Peter Michler Stuttgart, Germany
2013 – 2016	Secondary School, *Gottlieb-Daimler-Schule 1* Sindelfingen, Germany
1997/07/25	Born in Gießen, Germany

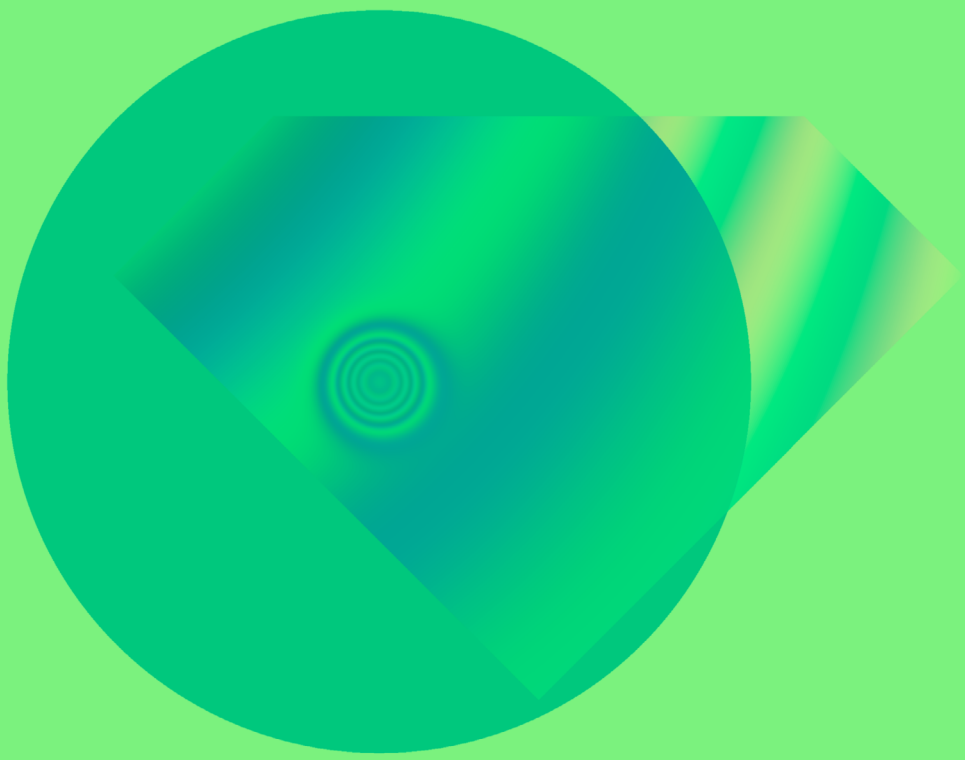

TU Delft

ISBN 978-94-6518-198-1

TEAM DIAMOND
EST. 2008 A.D.